# Journal of Turbomachinery

Published Quarterly by ASME

VOLUME 126 • NUMBER 2 • APRIL 2004





**Transactions of the ASME, Journal of Turbomachinery** (ISSN 0889-504X) is published quarterly (Jan., Apr., July, Oct.) by The American Society of Mechanical Engineers, Three Park Avenue, New York, NY 10016. Periodicals postage paid at New York, NY and additional mailing offices. POSTMASTER: Send address changes to Transactions of the ASME, Journal of Turbomachinery, c/o THE AMERICAN SOCIETY OF MECHANICAL ENGINEERS, 22 Law Drive, Box 2300, Fairfield, NJ 07007-2300.
**CHANGES OF ADDRESS** must be received at Society headquarters seven weeks before they are to be effective. Please send old label and new address.
**STATEMENT from By-Laws**. The Society shall not be responsible for statements or opinions advanced in papers or ... printed in its publications (B7.1, Par. 3).



**INDEXED** by Applied Mechanics Reviews and Engineering Information, Inc. Canadian Goods & Services Tax Registration #126148048


## TECHNICAL PAPERS




(**Contents continued on inside back cover**)



This journal is printed on acid-free paper, which exceeds the ANSI Z39.48-1992 specification for permanence of paper and library materials. ♾™
♻ 85% recycled content, including 10% post-consumer fibers.

## ANNOUNCEMENTS AND SPECIAL NOTES



The ASME Journal of Turbomachinery is abstracted and indexed in the following:

*Aluminum Industry Abstracts, Aquatic Science and Fisheries Abstracts, AMR Abstracts Database, Ceramics Abstracts, Chemical Abstracts, Civil Engineering Abstracts, Compendex (The electronic equivalent of Engineering Index), Corrosion Abstracts, Current Contents, Ei EncompassLit, Electronics & Communications Abstracts, Energy Information Abstracts, Engineered Materials Abstracts, Engineering Index, Environmental Science and Pollution Management, Excerpta Medica, Fluidex, Fuel and Energy Abstracts, INSPEC, Index to Scientific Reviews, Materials Science Citation Index, Mechanical & Transportation Engineering Abstracts, Mechanical Engineering Abstracts, METADEX (The electronic equivalent of Metals Abstracts and Alloys Index), Metals Abstracts, Oceanic Abstracts, Pollution Abstracts, Referativnyi Zhurnal, Shock & Vibration Digest, Steels Alert*

# Effect of Tip Gap and Squealer Geometry on Detailed Heat Transfer Measurements Over a High Pressure Turbine Rotor Blade Tip

**Hasan Nasir**

**Srinath V. Ekkad**
e-mail: ekkad@me.lsu.edu

**David M. Kontrovitz**

Mechanical Engineering Department,
Louisiana State University,
Baton Rouge, LA 70803

**Ronald S. Bunker**
GE Global R&D Center,
Niskayuna, NY

**Chander Prakash**
GE Aircraft Engines,
Cincinnati, OH

*The present study explores the effects of gap height and tip geometry on heat transfer distribution over the tip surface of a HPT first-stage rotor blade. The pressure ratio (inlet total pressure to exit static pressure for the cascade) used was 1.2, and the experiments were run in a blow-down test rig with a four-blade linear cascade. A transient liquid crystal technique was used to obtain the tip heat transfer distributions. Pressure measurements were made on the blade surface and on the shroud for different tip geometries and tip gaps to characterize the leakage flow and understand the heat transfer distributions. Two different tip gap-to-blade span ratios of 1% and 2.6% are investigated for a plane tip, and a deep squealer with depth-to-blade span ratio of 0.0416. For a shallow squealer with depth-to-blade span ratio of 0.0104, only 1% gap-to-span ratio is considered. The presence of the squealer alters the tip gap flow field significantly and produces lower overall heat transfer coefficients. The effects of different partial squealer arrangements are also investigated for the shallow squealer depth. These simulate partial burning off of the squealer in real turbine blades. Results show that some partial burning of squealers may be beneficial in terms of overall reduction in heat transfer coefficients over the tip surface.* [DOI: 10.1115/1.1731416]

## Introduction

In an attempt to increase thrust to weight ratio and efficiency of modern gas turbines, there is a push towards higher turbine operating temperatures. The benefits are attributed to the fact that higher temperature gases have a higher energy potential. However, the detrimental effects on the components along the hot gas path can offset the benefits of increasing the operating temperature. The high pressure turbine (HPT) first stage blade is subject to extremely harsh environments. The tip region through exposure to hot leakage gases leads to loss of performance and life through oxidation, erosion, rubbing against stationary outer casing, and high local thermal stresses.

The cause for tip failures is fairly well understood and can be explained as follows. A clearance gap between the rotating blade tip and stationary shroud is necessary to allow for the blade's mechanical and thermal growth during operation. Unfortunately, the gap allows for leakage flow from the pressure side to the suction side of the blade surface. The gas accelerates as it passes through the small gap. This leads to enhanced heat load to the blade tip region. Leakage flow, or clearance flow, also leads to undesirable aerodynamic losses. In fact, one third of the aerodynamic losses through the turbine section can be attributed to leakage flow. The effects of leakage flow are increased thermal loading and reduced aerodynamic performance, which affects durability and life of the component. At these elevated temperatures, the turbine blades are also at risk of undergoing oxidation, TBC spallation, thermal fatigue, and creep.

Bindon [1] studied tip clearance loss, using a linear cascade, and concluded that the losses varied linearly with gap size. Bindon separated the total tip clearance loss into three components, and remarked that each loss component made different contributions to the total loss: internal gap loss 39%, suction corner mixing loss 48%, endwall/secondary loss 13%. Using static pressure measurements and flow visualization, Bindon observed a separation bubble on the blade pressure edge that mixes with a high-speed leakage jet induced at midchord. However, Bindon presented results in an atmospheric linear cascade. The leakage flow was not pressure driven and this created a different type of leakage vortex than what would occur for a pressure driven leakage flow. Yaras et al. [2] also observed the presence of a separation bubble away from the leading edge and concluded that flow towards the leading edge had little effect on overall losses. In Yaras' study, a high-speed test rig was used. Yamamoto et al. [3] also found that leakage vortices were sensitive to incident angle and the blade tip gap height.

One of the earliest heat transfer studies on turbine blade tip models by Mayle and Metzger [4] established that the effects of relative motion between a blade model and the shroud have negligible effects on heat transfer data. Metzger et al. [5] and Chyu et al. [6] investigated the effects of varying the recess depth on the tip heat transfer of a blade tip model. It was determined that tip heat transfer was reduced under the presence of a cavity. The cavity simulated the squealer tip geometry. Leakage flow was reduced until the depth reached $D/W=0.2$.

Yang and Diller [7] were the first to perform heat transfer measurements on a realistic blade tip, with a recessed tip, in a blow-down cascade wind tunnel. They reported that convective heat transfer coefficients were not dependent on tip gap height or local Mach number; however, the conclusions were based on data taken with a single heat flux gage in one location on the tip. They based all their observations on a single measurement point. Bunker et al. [8] published the first study with detailed blade tip heat transfer measurements on actual blade tips. The measurements were made for a first-stage power generation blade using a steady-state liquid crystal technique. Bunker et al. [9] varied the curvature of the

Contributed by the Turbomachinery Division of THE AMERICAN SOCIETY OF MECHANICAL ENGINEERS for publication in the JOURNAL OF TURBOMACHINERY. Manuscript received by the ASME Turbomachinery Division, October 14, 2003; final revision, February 6, 2004. Editor: D. Wisler.

  

blade tip edges (rounded and sharp). The blades were exposed to a pressure ratio of 1.45 and had a total turning ratio of 110 deg. They found that the blade with a tip edge radius had greater leakage flow and higher heat transfer coefficients. Bunker et al. [9] also reported that an increase in freestream turbulence intensity increased the heat transfer coefficient. The authors observed an area of low heat transfer toward the blade leading edge, referred to as the sweet spot. Ameri and Bunker [10] used CFD simulations to reproduce the results for the same blade geometry shown by Bunker et al. [9]. They concluded that the assumption of periodic flow was invalid for tip heat transfer calculations because the entire passage had to be modeled. Their numerical results for the radiused edge showed better agreement with the experimental data than those of the sharp edge.

Recently, Azad et al. [11] performed an experiment in which three different clearance gaps ($C/H=1$, 1.5, 2.5%) were used. They used a GE-$E^3$ engine blade and a pressure ratio of 1.2 in a five-blade cascade. They measured heat transfer coefficients using the transient liquid crystal technique. The results of this experiment showed that a larger gap causes higher heat transfer coefficient on the tip. A second study by Azad et al. [12] investigated the effects of a recessed tip ($D/H=3.77\%$) on the heat transfer coefficient. It was determined that the squealer tip produced a lower overall heat transfer coefficient compared to the plain tip. The squealer redirected the airflow over the tip forcing the flow to move from the leading edge pressure side to the trailing edge suction side. It produced a different heat transfer pattern than that seen on a plain tip.

Bunker and Bailey [13] investigated the effectiveness of chordwise sealing strips to reduce leakage flow and heat transfer. Sealing strips increased resistance to leakage flow. Sealing strips also reduced flow when the gap between the strip and shroud was the same as that between the plain tip and shroud. The strip location affected the tip heat load distribution. Bunker and Bailey [14] continued the study with more complicated strip geometries: circumferential rub strips, 45 deg angled rub strips. The experiments showed that circumferential and angled strips increase heat loads by 20–25% and 10–15%, respectively.

Bunker and Bailey [15] also investigated the effect of squealer depth for a high-pressure turbine blade. They studied tip clearance-to-squealer cavity depth ratios of 0.67 and 2, and squealer depths of 1.02, 1.78, 2.54, and 3.05 mm. They found that a deeper tip cavity results in reduced heat transfer to the tip, although the distribution is nonuniform. They also studied the effect of squealer rim loss on heat transfer by studying partial squealers along the pressure and suction surfaces. They indicated rim loss along the pressure surface reduced overall tip heat transfer levels. Azad et al. [16] examined the benefits of six different squealers, including single and double squealers. The single squealer was a thin extension running from tip to tail, located on the camber line, pressure edge, or suction edge. The double squealer consists of two strips: a full perimeter strip, a pressure side strip from tip to tail and a short chord strip, and a suction-side strip from tip to tail and a short chord strip. The single squealer produced lower heat transfer coefficients on the tip than the double squealers. The midchord squealer produced the best leakage reduction. Dunn and Haldeman [17] presented time-averaged heat flux measurements on a recessed tip, the lip of the recess of a rotating blade in a full-scale rotating stage at transonic vane exit conditions. They made some localized measurements inside the recess, on the lip of the tip, and the platform of the blade. The results show that the recess had low heat flux values near the trailing edge compared to the leading edge.

Many parameters affect blade tip heat transfer. The total blade turning angle and general blade geometry, such as thickness, the presence of a squealer and edge radius, make a large contribution to the heat load distribution. Inlet Reynolds number and turbulence intensity can also affect the magnitude of the heat transfer coefficient. The present study explores the effects of gap height and tip squealer geometry on heat transfer distribution. This investigation focuses on a HPT blade tip profile with a different Mach number distribution, loading, and blade thickness compared to other studies. The pressure ratio (inlet total pressure to exit static pressure) used was 1.2, which is lower than the actual pressure ratio this blade sees in service ($PR=1.7$) but simulates similar relative Mach number distributions as for the blade under realistic conditions. A transient liquid crystal technique was used to obtain the tip heat transfer distributions similar to that used by Azad et al. [11]. Pressure measurements were made on the blade surface and on the shroud for different tip geometries and tip gaps to characterize the leakage flow and understand the heat transfer distributions. Also, partial squealer arrangements are investigated for the first time. In the real engine, it is anticipated that the full squealer rim will be subject to high thermal stresses and rubbing against the stationary shroud causing local loss of material resulting in partial squealer arrangements. In this study some partial squealer arrangements are investigated and compared to full squealer tips.

## Experimental Setup

This experiment uses a blow down test rig as illustrated in Fig. 1. The test rig was designed to produce the required pressure ratio across the blade for a short duration. An air compressor supplies dry air to a large tank capable of holding 2000 gallons of high pressure air at 20 atm (290 psig). This system is capable of generating a steady flowrate of 0.5 kg/s. The test section is part of an open loop blowdown setup, which is shown in Fig. 1. A gate valve isolates the entire wind tunnel from the supply tank. Downstream from that valve is a large pneumatically actuated control valve. A programmable controller regulates the pneumatic valve. The controller allows one to set the valve and maintain a specified valve opening and/or operating pressure in the test section. Air then passes through a rectangular diverging-converging section. This section is placed directly upstream from the test section. Its purpose is to settle the flow and make it more uniform before entering the test section. Boundary layer bleeds (slotted openings) along the test section inlet ensure the formation of a new boundary layer before the air enters the four-blade linear cascade test section. The exhaust area of the cascade is fitted with two tailboards. One tailboard is aligned with the pressure blade trailing edge and the other is aligned with the heat transfer blade. The movable tailboards can be used to back pressurize some passages and adjust the flow in all three passages. The tailboards are adjustable to help equalize pressure distribution in the passages adjacent to each blade and ensure periodic flow in all passages.

The test section is a linear cascade with four two-dimensional blades with the tip section profile. The blade profile was taken from the tip section of a General Electric HPT blade. Each blade is made of aluminum using an EDM machine, and bolted to a steel base plate that can easily be removed from the test section. The blade spacing ($S$) is 95.25 mm, and the axial chord ($C$) is 60.02 mm. The two outer blades guide airflow around the inner blades. Inner blades are used for pressure and heat transfer measurements. All blades have a span height from root to tip ($H$) of 76.2 mm. Figure 2 shows the four-blade linear cascade.

Pressure measurements are made on the blade surface in order to map the surface distribution and ensure that the flow conditions during heat transfer tests are correct. The ''pressure blade'' (Fig. 3($a$)) outer surface is lined with small tubes, extending from root to tip, that are set in recesses. The blade is then covered by a thin, strong tape to provide a smooth surface. Small tap holes are drilled in the tubes at the specified locations for the purpose of making static pressure measurements, 33.3, 86.7, 100% of the span from hub to tip (one hole per tube). The 100% span tap holes are exposed to the tip gap as shown in Fig. 3($a$) whereas the other two span locations measure the blade surface pressure distributions. Each alternate hole has a different spanwise location. A total of 96 taps are distributed among the three span locations. Pressure

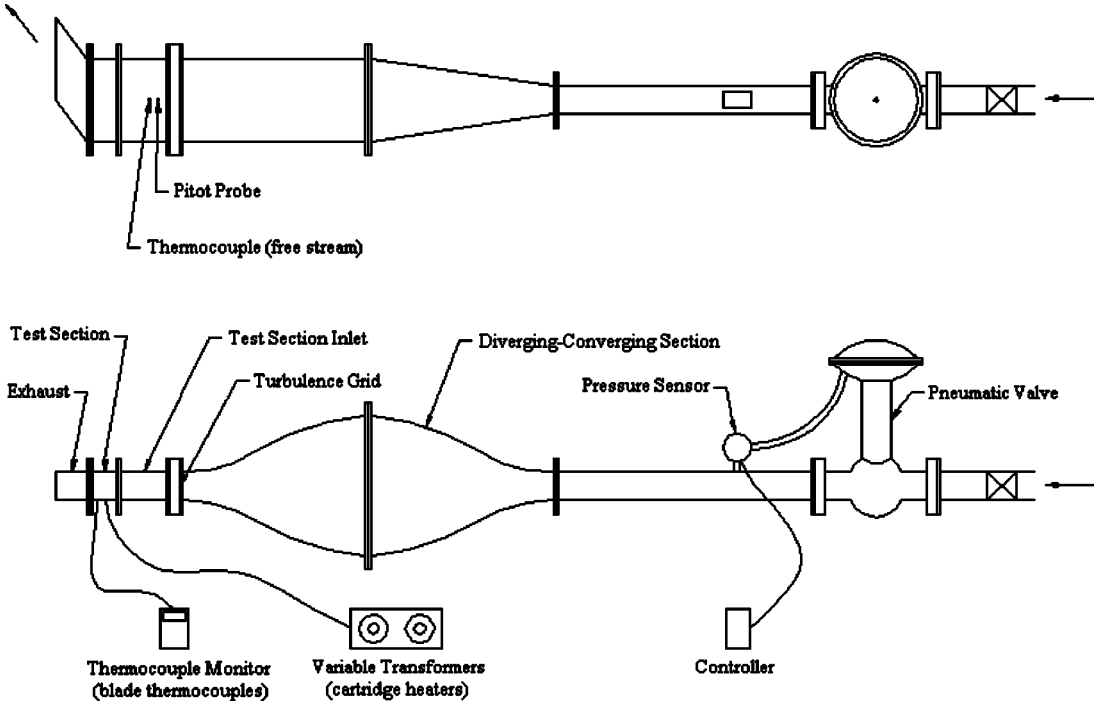


**Fig. 1 Illustration of the blow-down experimental setup**

measurements are also made on the shroud for each of the squealer tips and the flat tip cases as indicated in Fig. 3(*b*). A special top plate with holes 6.35 mm away from the suction side, 6.35 mm from the pressure side, and along the camber line, allows for static pressure measurements on the stationary shroud.

Figure 4 shows the full squealer and the four different partial squealer arrangements studied. The first geometry is the full squealer. The tip gap is measured from the tip of the squealer to the shroud. The first partial squealer geometry is called pressure side squealer (*PS*). The squealer rim exists along the pressure side edge of the blade only. The second partial squealer geometry is called suction side squealer (*SS*). The squealer rim exists along the suction side of the blade only. The third partial squealer geometry has the squealer rim on the pressure leading edge and along the suction side trailing edge (LEPS-TESS). The fourth partial squealer geometry has the squealer rim on the pressure side trailing edge and along the suction side leading edge (LESS-TEPS).

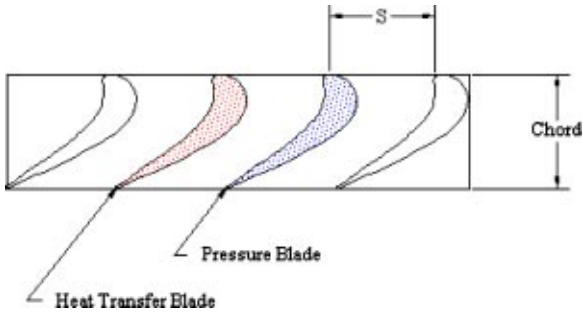


**Fig. 2 Cascade geometry**

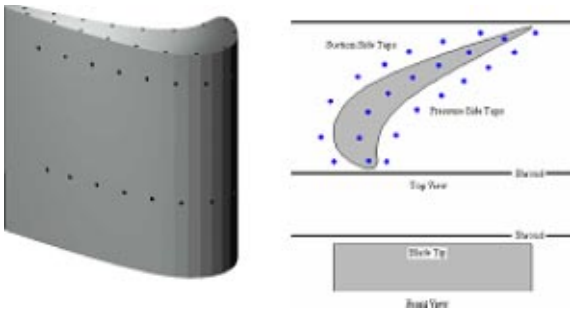

**Fig. 3 (*a*) Pressure test blade and (*b*) shroud plate with pressure taps**

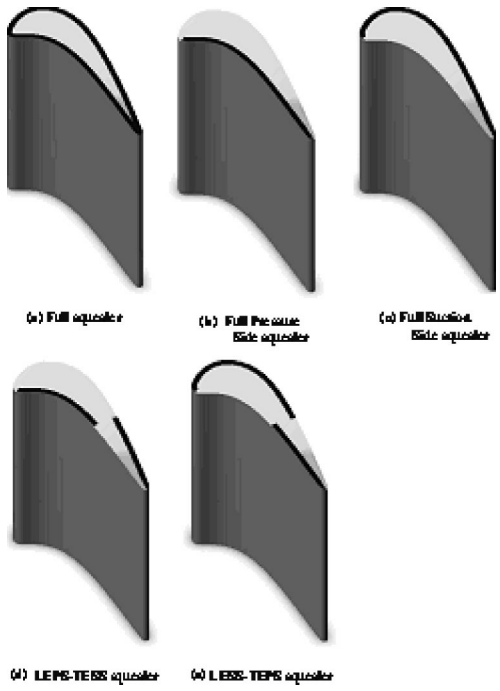

**Fig. 4 Different squealer geometries tested**

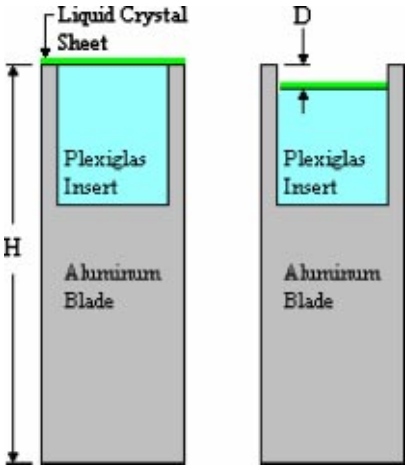


**Fig. 5 Heat transfer blade details; (*a*) plain tip, (*b*) blade with squealer**

A ''heat transfer blade'' is fabricated for heat transfer measurements (Fig. (5*a*,*b*)). Various Plexiglas inserts fit into the 25.4 mm recess and allow for variable groove depth. When the cavity is filled completely with a 25.4 mm insert, the result is the plain tip blade. Two squealer depths are investigated with other inserts to obtain depths, $D=0.79375$, 3.175 mm. The squealer rim, after machining the recess, is 1.5875 mm thick.

The experimental procedures involve heating the heat transfer blade to a high temperature then cooling it with compressed air in a blowdown mode. Two cartridge heaters are embedded in the blade aluminum core to heat the blade. These heaters have a length and diameter of 31 mm and 6.35 mm, respectively. Each heater connects to a variable transformer that allows the user to adjust the amount of current going into each heater and thereby controlling the blade temperature. A thermocouple is placed between the plexiglas insert and the aluminum blade monitors the aluminum-plexiglass contact temperature, and additional thermocouples are on the blade-tip monitor the liquid crystal temperature during the heating. The thermocouples are monitored and the heater input adjusted to ensure that a uniform blade temperature is maintained. A Hallcrest liquid crystal sheet (R30C5W; 30–35°C) is glued on the top of the Plexiglas insert. The sheet changes color, from green to red, as the blade cools during the blow-down test. A plexiglass top plate is used during the heat transfer experiments so that the RGB camera can view the blade tip surface and record the color changes. A RGB camera records the liquid crystal color change on the heat transfer blade. This camera, placed directly over the blade tip, connects to a 24-bit color frame grabber board in a PC. An image processing macro records the time at which the liquid crystal changes from green to red during the transient blow-down cooling experiment. It produces a time file, which provides the time of change for each pixel to turn red, i.e., 31.3°C during the blowdown test. The liquid crystal sheet was calibrated in-situ with a 36-gage thermocouple placed on the sheet that was monitored to obtain a red-green transition temperature to be 31.3°C.

## Procedure and Data Reduction

During a blow-down test the supply tank, which provides air to the test rig, empties into the test section. Therefore the inlet total pressure does not remain constant. A test was performed to determine the total pressure variation during the blow-down operation. Inlet total pressureis measured with a pitot probe (located 23 cm upstream of the test blades at midspan) and the NetScanner system.

**Pressure Tests.** Static pressure measurements are made on the shroud for each blade tip configuration. Measurements are also made on the pressure blade suction and pressure surfaces. Before each pressure test, moisture is blown from the pressure system data ports using the supply pressure. The data ports are calibrated and reset to zero, when necessary, to ensure accuracy. The pneumatic valve is then opened and air enters the test rig. The duration of all pressure tests matched that of the heat transfer tests. The pressure system reads surface gauge static pressures. Pressure ratios are computed based on the measured inlet total pressure at that instant.

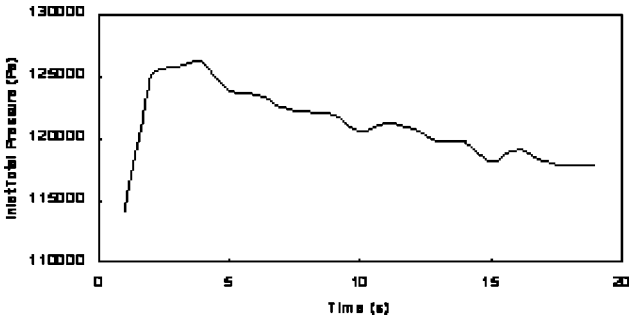


**Fig. 6 Blow-down test pressure during blow-down operation**

Figure 6 presents the inlet total pressure variation with time duration after the valve was opened. The majority of the liquid crystal color change takes place after the first 10 to 20 seconds of the heat transfer test. The total pressure peaks immediately after the valve opens within 1.5 seconds and then drops steadily for the duration of the test. The variation during the test of 30 seconds from highest to lowest absolute pressure is 3–5%. Before running any experiments, tests were run to equalize pressure distribution through the three passages. Equalizing the passages ensures that the flow field around the pressure and heat transfer blades is similar. Small holes are located on the shroud at identical locations above each passage. The tailboards were moved to achieve the equalization of pressure distribution in all three passages. Figure 7 presents the pressure $(P_s/P_o)$ distributions in the three passages. Results show that the pressure distributions are relatively similar through each of the passages but the levels are slightly different. The end passages show similar values compared to the middle passage. The middle passage lies between the heat transfer and the pressure blade.

**Heat Transfer Tests.** The heat transfer blade is heated for two hours to ensure that its temperature reaches steady-state before testing. During heating, thermocouples are used to monitor the internal and external temperature of the blade plexiglass insert. These thermocouples are checked every 5 minutes. Once the blade temperature reaches steady-state, the camera is focused on the heat transfer blade tip. The tip is illuminated with lighting to enable accurate capture of liquid crystal color changes. The heaters are switched off, and the pneumatic valve is then opened so that compressed air may enter the test rig. The time of appearance of red color at every pixel is measured from the initiation of the transient test. Typically, the initial temperature of the test section is set so that the first color change will be greater than 10 seconds.

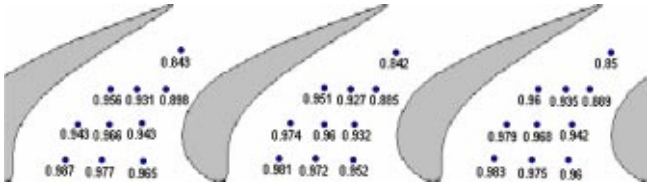


**Fig. 7 Pressure distributions on the shroud for all three passages**

The experiment takes 30–40 seconds to complete. The heat transfer coefficient is obtained by solving the one-dimensional transient conduction equation with convective boundary conditions for a semi-infinite solid.

$$\frac{T_r - T_i}{T_m - T_i} = 1 - \left[\exp\left(\frac{h^2 \alpha t}{k^2}\right)\right]\left[\operatorname{erfc}\left(\frac{h\sqrt{\alpha t}}{k}\right)\right]$$

The above equation is solved for every pixel location on the plexiglass tip where $T_i$ is the initial heated blade temperature before the transient is initiated; $T_m$ is the oncoming mainstream recovery temperature; $T_r$ is the temperature of the liquid crystal at red-green interface or the reference temperature during the transient test; $\alpha$ and $k$ are the thermal diffusivity and thermal conductivity of the plexiglass surface; and $t$ is the time required by each pixel to go from $T_i$ to $T_r$ during the transient test. All the above values are either known or measured during the test and the local heat transfer coefficient $(h)$ is calculated at every pixel location.

In order to verify the validity of the semi-infinite solid assumption, a two-dimensional transient analysis was performed with ANSYS. The model simulated the actual test blade with aluminum exterior and plexiglass insert. A direct contact was assumed between the two materials whereas a conducting adhesive was used during the real experiment. Blade geometry was generated for a location between the leading and trailing edges. The transient analysis was for 30 seconds, which corresponds to the average test duration. The finest mesh used for this analysis contained 12,659 elements. Boundary conditions were as follows: heat transfer coefficients of 800, 1000, 1300 W/m$^2$-K on the tip, pressure side, and suction side, respectively, freestream temperature was 373 K. The important result from the ANSYS analysis is that core temperatures of the plexiglass insert do not change during the transient cool down. Therefore no significant temperature penetration takes place. It also is important to note that during a typical heat transfer test, color change over most of the blade tip occurs within the first 20 seconds, so the calculations in the high heat transfer regions are unaffected by temperature penetration. The low heat transfer regions (test times $>$ 30 seconds) were typically in the middle of the blade tip relatively unaffected by two-dimensional conduction to the aluminum cavity.

A detailed uncertainty analysis was performed to evaluate the accuracy of the heat transfer coefficient measurement. The uncertainty analysis included the initial error in the blow-down pressure buildup, the error in accurately measuring the time of color change, the errors in temperature measurement, and the associated two-dimensional errors for corners. Based on the analysis, the average uncertainty in heat transfer coefficient was determined to be $\pm 7.5\%$. The highest uncertainty occurs for regions with very short color change times ($<5$ seconds) and for regions close to edges where two-dimensional effects are significant. These values can have errors up to $\pm 12.5\%$, [18]. Typically, these regions are 3–4 mm inward to the aluminum edges along the blade rim.

## Results and Discussion

The test flow conditions at inlet to cascade were measured using hot wire anemometry. The flow inlet velocity at cascade inlet was 60 m/s, which represents a cascade inlet Mach number of 0.16 The exit velocity to the cascade was 188 m/s, which is a Mach number of 0.54. The Reynolds number based on cascade exit velocity and blade axial chord is 861,000. Freestream turbulence intensity was also measured using the hot wire. The average freestream turbulence intensity at the cascade inlet was $Tu = 12.1\%$.

Figure 8 presents the blade pressure distribution at three different span locations for a tip gap of 1% of blade span. The measurement locations, for hub to tip are at locations along 33.3, 86.7, 100% of the blade span. The local static pressure is normalized by the cascade inlet total pressure $(P_s/P_{o,\text{inlet}})$. In the figure, curve $(a)$ represents the pressure side and curve $(b)$ represents the suction side. This plot clearly shows how the clearance gap affects leakage flow. At 33.3% blade height from hub, there is a large pressure differential between the pressure and suction surface which is the main driving potential for the leakage flow. At 86.7% of blade span closer to the tip gap, the pressure side distribution seems unaffected by the span location. However, the suction-side static pressures are higher than for 33.3% span location. It appears that the total pressure gradient is affected by the clearance gap. The pressure distributions in the tip gap along the blade edges are shown by the 100% case and are significantly affected by the leakage flow. In this case, the static pressure on the pressure side drops significantly from the 86.7% location values as the flow accelerates through the gap. The suction side pressure is not as significantly affected as the pressure side.

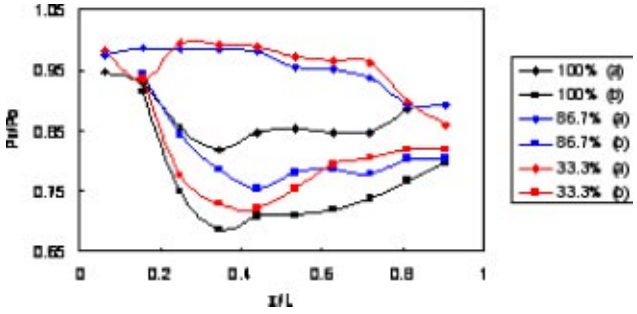


**Fig. 8 Surface pressure distributions on the blade surface and tip gap with 1% clearance gap; (*a*) pressure surface, (*b*) suction surface**

Figure 9 presents the pressure distributions on the shroud over a plain tip for tip gaps of 1.0% and 2.6% of the blade span. The local static pressure is again normalized by the cascade inlet total pressure $(P_s/P_t)$ as in Fig. 7. Measurements on the shroud are presented 6.35 mm ahead of the pressure side of the blade tip, 6.35 mm behind the suction side of the blade tip, and along the camber line (see inset); they are referred to as $a$, $b$, and $c$, respectively. Case 1 refers to the plain tip with 1.0% gap and Case 2 refers to plain tip with 2.6% gap. From the pressure distributions, it is evident that the air accelerates as it enters the clearance gap. This acceleration causes a drop in static pressure along the camber line. As the flow decelerates from the camber line to the suction side, there is a pressure recovery from the camber line to the suction side. Lowest static pressure occurs along the camber line. The levels of $P_s/P_o$ values are similar for both tip gaps. However, the tip gap with 2.6% clearance has a larger area and hence will allow more leakage flow.

Figure 10 presents the detailed tip heat transfer coefficients for the plain tip with 1.0% and 2.6% gap heights. A region of low heat transfer at the leading edge for both tip gaps occurs due to the low pressure gradient across this area. This region, referred to as the

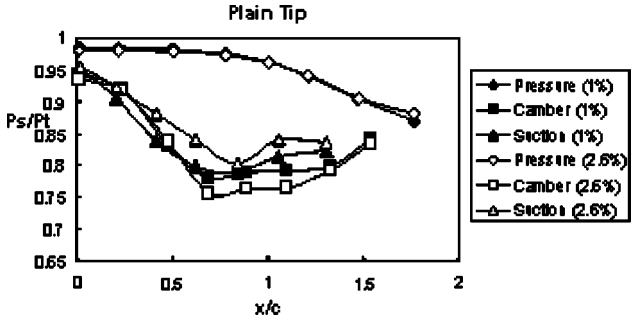


**Fig. 9 Pressure distributions on the shroud of a plain tip with 1% and 2.6% gaps**

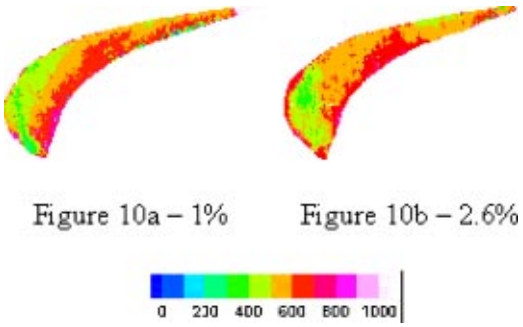


**Fig. 10 Detailed heat transfer coefficient distributions on plain tips**

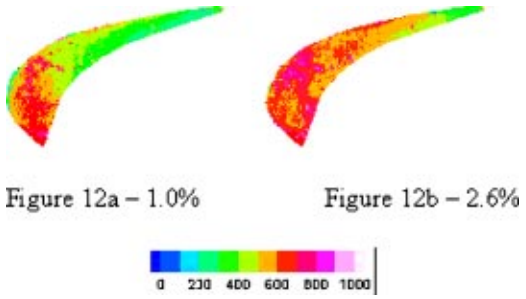


**Fig. 12 Detailed heat transfer coefficient distributions on shallow squealer tips**

"sweet spot," is larger and extends towards middle of the tip region for 1% and covers a smaller region for 2.6% gap.

Heat transfer coefficient values are significant along the trailing edge, close to pressure side. Flow separation occurs at the pressure side tip edge as the flow enters the clearance gap and then reattaches on the tip surface causing a low heat transfer region immediately behind the edge and a high heat transfer region in the reattachment region. The heat transfer coefficient values in the trailing edge region range from 800–1000 W/m$^2$-K for both the 1% gap height and 2% gap height. Notice that the high heat transfer area is much larger for 2.6% gap. As previously stated, a smaller gap height equates to reduced leakage flow over the plain tip, and this is the reason for lower heat transfer coefficients. The clearance gap flow Reynolds number is larger for the larger gap thus enhancing heat load.

Figure 11 presents the pressure distributions on the shroud over a tip with deep squealer for tip gaps of 1.0% and 2.6% of the blade span. The pressure distributions are significantly different for this tip geometry. The pressure side distributions are unaffected by both gap width and the tip geometry. The static pressure drops in the region around the leading edge region from $X/C = 0$ to 0.5. The camber line pressure is lower than the pressure on the pressure side before the gap. The flow decelerates as it expands into the squealer cavity and then accelerates through the clearance gap on the suction side. The camber line and suction side pressure are almost equal for regions where $X/C > 0.5$. It can be speculated that the bulk of the leakage flow occurs closer to the leading edge compared to the plain tip where the leakage flow occurred over the trailing edge of the blade.

Figure 12 presents the detailed tip heat transfer coefficients for the deep squealer tip with 1.0% and 2.6% gap heights. A region of high heat transfer coefficient occurs from $X/C = 0-0.5$ for both tip gaps due to the high pressure gradient across this area from pressure to camber line. This region, called the "hot spot," has values ranging from 600–800 W/m$^2$ K for the 1% gap height and 700–1000 W/m$^2$ K for the 2.6% gap height. The hot spot for 1% gap is smaller than that for 2.6% gap due to the reduced gap size. The red perimeter of high heat transfer along the edges of the squealer may be caused due to the corner conduction into the aluminum rim. This appears for both squealer geometries.

Heat transfer coefficient values are reduced along the trailing edge for the shallow squealer tip compared to the plain tip. This is especially true close to pressure side. As air flows over the pressure side rim there is a large separation zone, this is the "line" of decreased heat transfer. Behind that line, air reattaches to the recessed tip surface. The heat transfer coefficient values in the trailing edge region range from 200–500 W/m$^2$ K for the 1% gap height and 300–700 W/m$^2$ K for the 2.6% gap height. As was the case for the plain tip blade, a smaller gap height equates to reduced leakage flow over the squealer. The clearance gap flow Reynolds number is larger for the larger gap thus producing higher heat transfer coefficients.

Figure 13 presents the overall interpretation of the flow over the plain and squealer tip based on the pressure and heat transfer results. Most of the flow over the plain tip hugs the pressure side along the leading edge and crosses over after $X/C > 0.5$. The leakage flow is limited in the leading edge region due to the lower pressure gradient across the tip. This cause the low heat transfer region referred to as the "sweet spot." Towards the trailing edge, the pressure gradient across the tip increases causing a strong leakage flow and subsequently higher heat transfer coefficients. For the squealer tips, the leakage flow occurs in the region immediately after the leading edge. Flow enters the cavity reattaches to the recessed flow and then accelerates through the clearance gap on the suction side rim. The flow closer to the trailing edge hugs the blade surface and does not flow over the tip due to reduced pressure gradient. Also, the squealer depth to width ratio ($D/W$) effect as observed by Metzger et al. [5] is clearly evident comparing the two squealer depths in this study. The deeper depth creates a clear reattachment on the tip floor whereas the shallow squealer flow over the pressure side edge may be hitting the cavity wall on the suction side before rolling onto the cavity floor.

All the partial squealer geometries have been studied for a squealer depth to span ratio of 0.0104. Figure 14 presents the pressure distributions on the shroud over a tip for no squealer, full

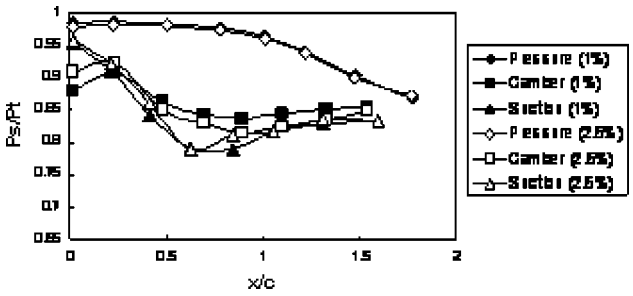


**Fig. 11 Pressure distributions on the shroud of a deep squealer tip with 1% and 2.6% gaps**

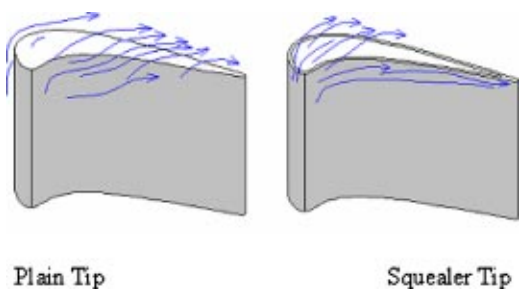


**Fig. 13 Illustration of tip leakage flows for plain tips and squealer tips based on pressure and heat transfer distributions**

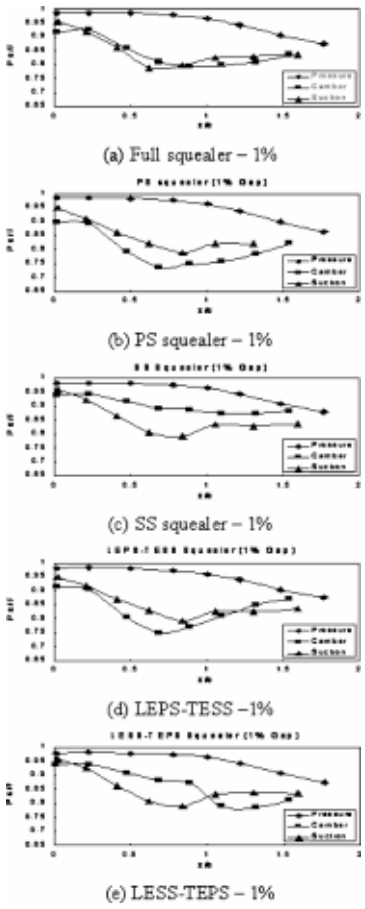


**Fig. 14 Shroud pressure distributions for different squealer configurations**

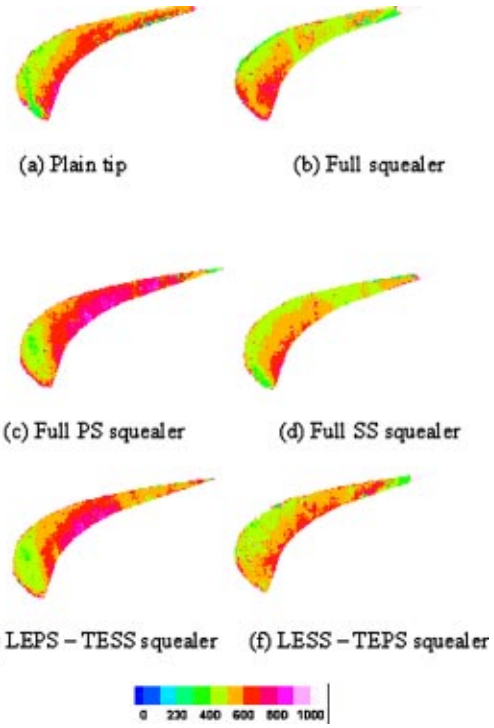


**Fig. 15 Detailed heat transfer distributions on tips with different squealer geometries**

squealer, full pressure side squealer, full suction-side squealer, the LEPS-TESS partial squealer, and the LESS-TEPS partial squealer for a tip gap of 1.0% of the blade span. The pressure gradient across the pressure side to the camberline indicates the strength of the leakage flow. It is clear that the suction side squealer reduces the pressure gradient more than other geometries. The LESS-TEPS squealer also reduces leakge flow from leading edge region to the midsection but then the pressure gradient flips due to the squealer on the pressure side. All other squealers show larger pressure gradient on the upstream side of the tip where the bulk of the leakage occurs across the tip.

Detailed heat transfer coefficient distributions are presented for different squealer cases in Fig. 15. As explained earlier, the full squealer reverses the heat transfer distributions on the tip surface. The higher heat transfer region moves towards the leading edge due to flow separation and reattachment phenomena. There also appears to be an overall reduction in heat transfer coefficient over the entire tip surface. The plain tip distributions are shown again for comparison.

With the full *PS* squealer, the heat transfer coefficients are enhanced compared to the plain tip. This may be due to the flow accelerating after entering the tip gap along the tip surface towards the *TE* due to the blockage at the entrance of the gap. There is stronger separation and reattachment over the entire tip surface. With the full *SS* squealer, the tip leakage flow does not see the overall pressure gradient across the tip gap. The leakage flow is accelerated into the tip gap but decelerates as it encounters the suction side squealer wall. There is very little flow separation due to the lack of the pressure side squealer wall. There appears some remnants of a sweet spot as in the case of the plain tip and reduced heat transfer at the *TE* due to the suction side squealer wall.

With the LEPS-TESS partial squealer, the sweet spot region is greatly enhanced but the flow separation along the pressure side wall is clearly higher. This causes higher heat transfer coefficient along the mid section of the tip surface. This squealer, although produces higher heat transfer coefficients than the plain tip, does perform better than the full *PS* squealer. With the LESS-TEPS partial squealer, the heat transfer coefficient along the pressure side edge is higher than the suction side edge. The flow appears to have a weak flow separation and reattachment along the leading edge and the presence of the squealer on the pressure side along the trailing edge reduces leakage flow. Overall this squealer configuration produces lower heat transfer coefficients than the plain tip but is still lower than the values obtained for the full *SS* squealer. Both Bunker and Bailey [15] and Azad et al. [16] show similar results for pressure-side squealer versus suction-side squealers.

Figure 16 presents the overall averaged heat transfer coefficients for the tip surface for different tip geometries. The heat transfer coefficients were averaged pixel to pixel to obtain the area-averaged heat transfer coefficients. The differences in heat transfer distributions on the surface are very different for each tip geometry, but the overall value can be used to obtain the total heat load to the tip surface. As seen from the plot, the plain tip is around 600 $W/m^2$ K. The full squealer provides the best reduction in heat transfer coefficients. The deeper squealer reduces heat transfer coefficient to around 400 $W/m^2$ K. The *PS* squealer increases overall heat transfer coefficient. Among all the partial squealers, the *SS* squealer is the only one that reduces heat transfer coefficient compared to the plain tip. The *PS* squealer, LEPS-TESS, and LESS-TEPS squealers either enhance or do not change the overall heat transfer coefficient compared to the plain tip. This indicates that the loss of squealer on the pressure side rim may actually benefit the tip surface. Any suction-side loss will cause increases in heat load.

## Conclusions

A blow-down test was performed to determine the heat transfer coefficients on the tip of a high pressure turbine blade with a plain

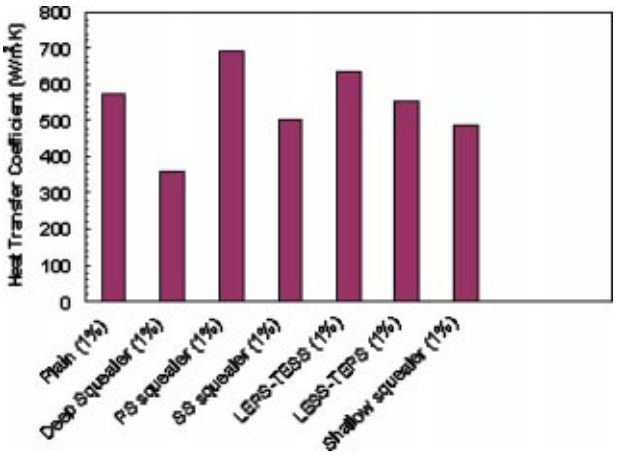


**Fig. 16 Overall averaged heat transfer coefficients for different tip geometries**

tip, two squealer depths ($D=0.79375$, 3.175 mm), and several partial squealer configurations. A transient liquid crystal measurement technique was used to obtain the detailed heat transfer coefficient distributions on the tip surface. Pressure measurements were presented over the shroud with a clearance gap and at different span locations on the blade surface. Results show that flow over the plain tip blade moves from the leading edge pressure side to the trailing edge suction side and flow over the squealer tip blades moves from the leading edge pressure side to the midpoint of the suction side. The plain tip produces relatively lower heat transfer coefficients downstream of the leading edge. This region is the typical ''sweet spot'' as indicated by several published studies. The trailing edge region for the plain tip has significantly higher heat transfer coefficients as most of the leakage flow crosses over the tip closer to the trailing edge. The squealers produce reduced leakage flow and associated heat transfer coefficients over the blade tip compared to the plain tip. The squealers show higher heat transfer in the region closer to the leading edge and lower heat transfer coefficients near the trailing edge. The trend is reverse to that of the plain tip. The deeper squealer produces lower heat transfer coefficients than the shallow squealer due to increased resistance to the leakage flow. Smaller gap height, 1.0%, produces reduced leakage flow over the blade tip than the larger 2.6% gap height and thus lower heat transfer coefficients.

The partial squealers represent squealer rim burn off. The results show that pressure side burn off is beneficial in reducing the overall heat transfer coefficient on the tip. However, suction-side rim loss may hurt the tip heat load. Partial losses on the suction and pressure-side rims produced very little effect on overall heat transfer coefficient but did affect local distributions on the tip surface.

## Acknowledgments

This work was supported through a grant from NSF under the GOALI program. Acknowledgements are due to the program managers Drs. A. Emery, S. Thynell, and R. Smith. Acknowledgments are also due to the industrial partners, General Electric Co., for their support of the project. Acknowledgements are also due to Dr. Sumanta Acharya, Dr. Huitao Yang, and Mr. Ryan Hebert for their help during this work.

## Nomenclature

$C$ = axial chord
$D$ = squealer depth
$h$ = convective heat transfer coefficient
$H$ = height of test blade
$k$ = thermal conductivity of plexiglas test surface
$M$ = Mach number
$P$ = pressure
$PR$ = inlet total-to-exit static pressure ratio
Re = freestream Reynolds number, $\rho VC_X/\mu$
$S$ = blade spacing
$t$ = time of color change
$T$ = temperature
$Tu$ = freestream turbulence intensity (%)
$V$ = freestream velocity
$W$ = width of squealer cavity
$x$ = axial distance

### Greek Symbols

$\alpha$ = thermal diffusivity of plexiglas test surface
$\rho$ = density of air
$\mu$ = viscosity of air

### Subscripts

$e$ = exit
$i$ = initial condition, inlet
$m$ = bulk flow or mainstream
$r$ = liquid crystal color red
$s$ = static
$t$ = total

## References

[1] Bindon, J. P., 1989, ''The Measurement and Formation of Tip Clearance Loss,'' ASME J. Turbomach., **111**, pp. 257–263.
[2] Yaras, M., Yingkang, Z., and Sjolander, S. A., 1989, ''Flow Field in the Tip Gap of a Planar Cascade of Turbine Blades,'' ASME J. Turbomach., **111**, pp. 276–283.
[3] Yamamoto, A., 1989, ''Endwall Flow/Loss Mechanisms in a Linear Turbine Cascade With Blade Tip Clearance,'' ASME J. Turbomach., **111**, pp. 264–275.
[4] Mayle, R. E., and Metzger, D. E., 1982, ''Heat Transfer at the Tip of an Unshrouded Turbine Blade,'' *Proceedings of the 7th International Heat Transfer Conference*, Hemisphere, Washington, DC, **3**, pp. 87–92.
[5] Metzger, D. E., Bunker, R. S., and Chyu, M. K., 1989, ''Cavity Heat Transfer on a Transverse Grooved Wall in a Narrow Flow Channel,'' ASME J. Heat Transfer, **111**, pp. 73–79.
[6] Chyu, M. K., Moon, H. K., and Metzger, D. E., 1989, ''Heat Transfer in the Tip Region of Grooved Turbine Blades,'' ASME J. Turbomach., **111**, pp. 131–138.
[7] Metzger, D. E., Dunn, M. G., and Hah, C., 1990, ''Turbine Tip and Shroud Heat Transfer,'' ASME Paper No. 90-GT-333.
[8] Yang, T. T., and Diller, T. E., 1995, ''Heat Transfer and Flow for a Grooved Turbine Blade Tip in a Transonic Cascade,'' ASME Paper No. 95-WA/HT-29.
[9] Bunker, R. S., Bailey, J. C., and Ameri, A. A., 1999, ''Heat Transfer and Flow on the First Stage Blade Tip of a Power Generation Gas Turbine: Part 1—Experimental Results,'' ASME J. Turbomach., **122**, pp. 263–271.
[10] Ameri, A. A., and Bunker, R. S., 1999, ''Heat Transfer and Flow on the First Stage Blade Tip of a Power Generation Gas Turbine: Part 2—Simulation Results,'' ASME J. Turbomach., **122**, pp. 272–277.
[11] Azad, Gm. S., Han, J. C., and Teng, S., 2000, ''Heat Transfer and Pressure Distributions on a Gas Turbine Blade Tip,'' ASME Paper No. 2000-GT-194.
[12] Azad, G. S., Han, J. C., and Boyle, R. J., 2000, ''Heat Transfer and Flow on the Squealer Tip of a Gas Turbine Blade,'' ASME Paper No. 2000-GT-195.
[13] Bunker, R. S., and Bailey, J. C., 2000, ''An Experimental Study of Heat Transfer and Flow on a Gas Turbine Blade Tip With Various Tip Leakage Sealing Methods,'' *Proceedings of the 4th HMT/ASME Heat and Mass Transfer Conference*, ASME, New York, Paper No. HMT2000-055, pp. 411–416.
[14] Bunker, R. S., and Bailey, J. C., 2000, ''Blade Tip Heat Transfer and Flow With Chordwise Sealing Strips,'' *International Symposium on Transport Phenomena and Dynamics of Rotating Machinery (ISROMAC)*, Honolulu, HI, pp. 548–555.
[15] Bunker, R. S., and Bailey, J. C., 2001, ''Effect of Squealer Cavity Depth and Oxidation on Turbine Blade Tip Heat Transfer,'' ASME Paper No. GT-2001-155.
[16] Azad, G. S., Han, J. C., Bunker, R. S., and Lee, C. P., 2001, ''Effect of Squealer Geometry Arrangement on Gas Turbine Blade Tip Heat Transfer,'' *Proceedings of the International Mechanical Engineering Congress and Exposition*, ASME, New York, Vol. IMECE2001/HTD-2431.
[17] Dunn, M. G., and Haldeman, C. W., 2000, ''Time-Averaged Heat Flux for a Recessed Tip, Lip and Platform of a Transonic Turbine Blade,'' ASME Paper No. 2000-GT-0197.
[18] Kline, S. J., and McClintock, F. A., 1953, ''Describing Uncertainties in Single Sample Experiments,'' Mech. Eng. (Am. Soc. Mech. Eng.), **75**, pp. 3–8.

# Experimental and Numerical Investigation of Trailing Edge Film Cooling by Circular Coolant Wall Jets Ejected From a Slot With Internal Rib Arrays

**P. Martini**

**A. Schulz**

Lehrstuhl und Institut für Thermische Strömungsmaschinen, Universität Karlsruhe (TH), Kaiserstr. 12, 76128 Karlsruhe, Germany

*The present study concentrates on the experimental and computational investigation of a cooled trailing edge in a modern turbine blade. The trailing edge features a pressure side cutback and a slot, stiffened by two rows of evenly spaced ribs in an inline configuration. Cooling air is ejected through the slot and forms a cooling film on the trailing edge cutback region. In the present configuration the lateral spacing of the ribs equals two times their width. The height of the ribs, i.e., the height of the slot equals their width. Since the ribs are provided with fillet radii of half the slot height in size, circular coolant jets are exiting the slot tangentially to the trailing edge cutback. The adiabatic wall temperature mappings on the trailing edge cutback indicate that strong three-dimensional flow interaction between the coolant jets and the hot main flow takes place in such a way that two or more coolant jets coalesce depending on the blowing ratio. Experimental and numerical data to be presented in the present study include adiabatic film cooling effectiveness on the trailing edge cutback, the pressure distribution along the internal ribbed passage as well as slot discharge coefficients for different blowing ratios ranging from $M=0.35$ to 1.1.* [DOI: 10.1115/1.1645531]

## Introduction

The enhancement of the overall efficiency is a major goal in the development of gas turbines. One possibility to improve thermal efficiency is to further increase process temperatures so that turbine inlet temperatures attain values of up to 2000 K in modern jet engines.

As this level is significantly beyond the maximum allowable temperatures for current blade materials, the application of appropriate cooling techniques is indispensable. Usually, the blades are cooled by a combination of convection and film cooling and, therefore, designed with internal cooling air passages which can be additionally provided with ribs, fins, and dimples to intensify internal heat transfer. In order to establish a cooling film on the surface the blades are locally perforated by cylindrical or shaped cooling holes.

One of the most critical, often life-limiting region of the turbine blade is its trailing edge, which, from an aerodynamic point of view, has to be as thin as possible. This causes an inherent conflict with cooling requirements as in the manufacturing process difficulties arise from the integration of internal cooling passages in the thin trailing edge region.

One state-of-the-art cooling technique, which leads to particularly thin trailing edges, is obtained by removing material from the pressure side of the trailing edge forming a characteristic step with a spanwise slot. Air can be ejected through the slot to generate a more or less uniform cooling film on the trailing edge cutback.

In order to increase the integrity of the trailing edge, the structure is stiffened by rib or pin-fin arrays in the cooling passage connecting the blade walls of the pressure and the suction side. Furthermore, these arrays work as turbulators to enhance the internal convective heat transfer in the cooling passage and control the blade cooling mass flow. **Fig. 1** shows a cross-sectional view of a typical turbine blade with pressure side trailing edge cutback.

It is evident, that the presence of rib or pin-fin arrays may have a significant influence on film cooling downstream of the ejection slot, especially if the rib-obstructed area is not negligible compared to the total slot area and the ribs are located close to the ejection slot. In that case, complex three-dimensional flow interaction occurs between the hot main flow and the coolant flow resulting in reduced film cooling effectiveness compared to an ideal, two-dimensional slot, i.e., cooling film.

Numerous experimental as well as numerical studies deal with two-dimensional film cooling through tangential slots (as predominantly found in combustor cooling applications). Here, the influence of geometric as well as flow related parameters are investigated in great detail and several correlations prescribing film cooling effectiveness downstream of the ejection slot are derived, [1–8].

Recent publications by Taslim et al. and Holloway et al. [9–11] concentrate on experimental and numerical investigation of special trailing edge cooling designs, e.g., slots which are disrupted by pieces of land. But in contrast to this work, they deal with an increased rib/land spacing resulting in a cooling film of a more two-dimensional nature than in the present study.

There only exist few publications concentrating on three-dimensional slot geometries similar to the present configuration. Sturgess et al. [12,13] investigate the influence of slot geometry effects on film cooling effectiveness. A nondimensional geometric parameter is derived to classify three-dimensional slot geometries with respect to their film cooling performance. The view is focused on practical combustor slots with circular coolant inlets followed by a lip overhang acting as a mixing chamber. In accordance to the findings in [12,13] it can be expected that for the present geometry with its relatively short lip overhang down-

Contributed by the International Gas Turbine Institute and presented at the International Gas Turbine and Aeroengine Congress and Exhibition, Atlanta, GA, June 16–19, 2003. Manuscript received by the IGTI December 2002; final revision March 2003. Paper No. 2003-GT-38157. Review Chair: H. R. Simmons.

  

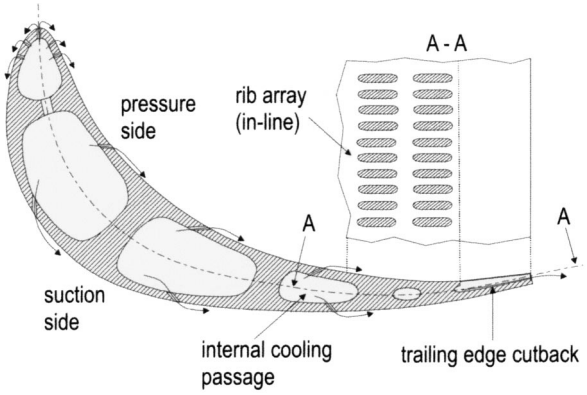


**Fig. 1 Cross-sectional view of a turbine blade with pressure side trailing edge cutback**

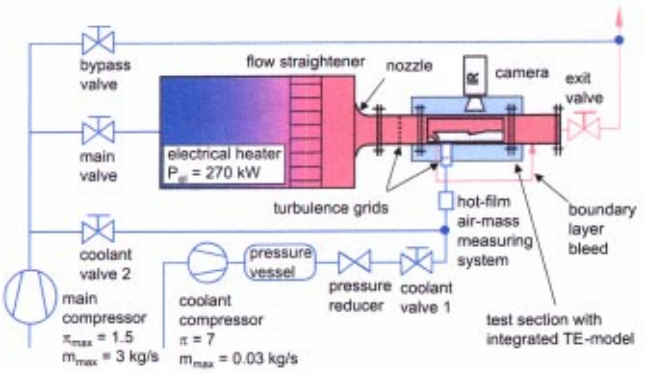


**Fig. 2 Schematic view of the atmospheric test facility**

stream of the last rib array the mixing between the coolant and the hot gas will be intensified due to the highly three-dimensional character of the coolant film.

Rastogi et al. [14] experimentally investigate the impervious wall effectiveness of three-dimensional slot geometries (circular coolant inlets without lip overhang) with respect to the influence of density ratio and characteristic geometrical parameters. They find that an increase of lip thickness and pitch to diameter ratio leads to a decrease in film effectiveness. Keeping the velocity ratio constant, an increased coolant density results in higher film effectiveness, whereas for a constant blowing ratio no explicit relationship between density ratio and effectiveness can be derived.

Similar studies are undertaken by Nina et al. [15]. They investigate the adiabatic film cooling effectiveness downstream of different slot geometries (circular coolant inlets with and without lip overhang) under constant density flow conditions. For certain flow conditions discrete hole injection results in substantial fluctuations of static and total pressure in the near slot region accompanied by a shift of velocity maxima indicating that neighboring jets are coalescing and uncoalescing in a random manner. They close with the statement that "*the extent to which this phenomenon is important in film cooling remains unknown.*"

The present paper, which continues a recent study on a similar trailing edge geometry with a larger aspect ratio (i.e., lateral spacing of the ribs) by Martini et al. [16], therefore concentrates on the experimental and computational investigation of such effects which turned out to have a severe impact on film cooling of the trailing edge cutback.

## Test Facility and Trailing Edge Model

The experimental work is carried out on a scaled-up trailing edge model integrated in an atmospheric hot wind channel. The main advantage of such a hot facility is that it easily allows for the investigation of film cooling under engine like density ratios between coolant and main flow. The test section of the hot wind channel has a width of 220 mm and a height of 105 mm. **Figure 2** shows a schematic view of the test facility.

The trailing edge model which is scaled up by a factor of 10 is integrated in the test section of the hot wind channel. It is composed of a double in-line rib array with each rib row consisting of 21 equally spaced ribs of 4 mm width. The pitch between two ribs is 8 mm. In contrast to the first rib row, it was decided to provide the ribs in the second row with fillets in order to determine the influence of the fillet radii on the flow field downstream of the ejection slot. The combination of rib spacing, width, and fillet radii leads to circular coolant inlets with a diameter of $D = 4$ mm. The ejection slot itself has a width of 180 mm and a height that equals the diameter of the circular coolant inlets.

**Figure 3** shows the geometric details of the investigated trailing edge cooling configuration. To establish an engine realistic boundary layer thickness of the main flow at the ejection slot plane, a variable boundary layer bleed is utilized upstream of the trailing edge model. Laminar/turbulent transition is achieved by means of a trip wire at the end of the nose region. This leads to a turbulent boundary layer having a thickness of $\delta/H \approx 1.25$ ($\delta_1/H \approx 0.15$) at the ejection slot plane.

A low conductive plastic material ($\lambda \approx 0.25$ W/(mK)) is used for the test plate in the pressure side cutback region to provide near adiabatic conditions for the determination of the film cooling effectiveness.

To obtain Biot number similarity between the real engine configuration and the investigated model, the ribs and the pressure side walls are fabricated from high-grade steel with a thermal conductivity of $\lambda \approx 16$ W/(mK). With respect to the pressure side, it is possible to obtain an engine representative temperature distribution of the coolant at the ejection slot. However, the surface equivalent of the suction side in $L1$ and $L2$ (see **Fig. 3**) is not explicitly heated in the experiment. Beside an increased complexity of the test section there is another important reason for this: a stepwise change of heat flux from a discrete value (inside the coolant cavity) to zero (on the adiabatic test plate) would disturb the equilibrium of the thermal boundary layer and affect the adiabatic wall temperatures in the near slot region. As such a stepwise change in heat flux does not exist in the real engine it should be avoided in the present experiment as well.

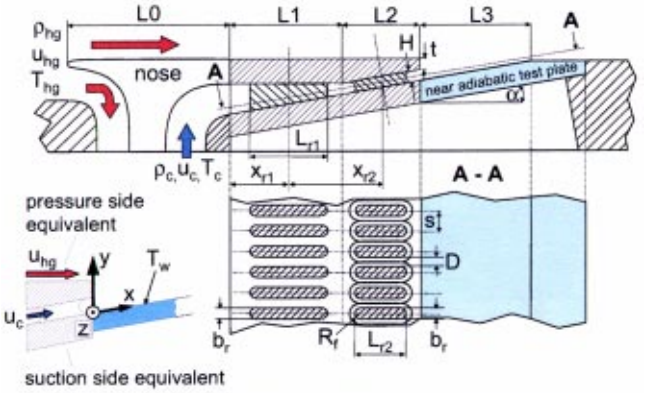


| L0 | L1 | L2 | L3 | H | t | α | $x_{r1}$ | $x_{r2}$ | $L_{r1}$ | $L_{r2}$ | $b_r$ | s | $R_f$ | D |
|---|---|---|---|---|---|---|---|---|---|---|---|---|---|---|
| 95 | 40 | 28 | 40 | 4 | 4 | 10 | 22 | 32 | 28 | 20 | 4 | 8 | 2 | 4 |

**Fig. 3 Schematic view of the trailing edge model with nomenclature (in (mm) or (deg))**

## Boundary Conditions and Measuring Technique

**Flow Conditions.** Due to the scale factor used for the trailing edge model, it is not possible to obtain engine representative Mach and Reynolds numbers at the same time. Therefore, it was decided to perform all tests at a realistic Reynolds number, $\mathrm{Re}_{hg}$, (using $L$ as characteristic length) of 250,000 as compressibility effects should be of minor importance compared to the influence of the Reynolds number.

The hot gas temperature is set to 500 K which leads to an engine representative temperature ratio of 0.65 (i.e., a density ratio of about 1.5). The static pressure in the hot main flow is slightly overatmospheric. At a Reynolds number of $\mathrm{Re}_{hg}=250{,}000$ the velocity of the main flow is 45 m/s ($\mathrm{Ma}=0.1$). To obtain an elevated turbulence level a square grid of square bars is placed upstream of the nose tip. Using this grid, a turbulence intensity of 7% at a macroscopic length scale of 10 mm is established on the trailing edge cutback in accordance to correlations suggested by Roach [17].

Six different blowing ratios ($M=(\rho_c u_c)/(\rho_{hg} u_{hg})$) between 0.35 and 1.1 are tested. $U_c$ is the mean velocity of the coolant in the second row ($L2$ region) leading to a Reynolds number, $\mathrm{Re}_c$, in the range of 2400 to 8200 (using $D$ as characteristic length).

As in case of the main flow, a turbulence grid is inserted in the rectangular coolant duct providing a turbulence intensity of around 5% and a macroscopic length scale of 1 mm at the inlet of $L1$. The coolant temperature is measured at two locations. At the first location, the inlet of $L1$, the temperature ranges from 294 K up to 316 K, depending on the coolant mass flow. The second location, the ejection slot, marks the starting point of film cooling. Therefore the coolant core temperature measured at the ejection slot in the centerline of a coolant jet is chosen as reference temperature for any film cooling effectiveness presented in this work.

Due to Biot number similarity the thermal boundary condition for the coolant flow inside the cavity is engine representative on the pressure side but as the coolant is not heated from the suction side the relationship between coolant core temperature and mixed bulk temperature at the ejection slot might deviate from the real engine. However, the overall film cooling effectiveness in the $L3$ region should not be affected as measurements performed with a traversable temperature probe at the slot exit indicate that only small temperature variations of around 5% exist between the coolant core flow and the internal near wall region of the pressure side. Therefore, a similar temperature variation on the suction side (caused by heating) would not significantly change the relationship between the coolant core and the mixed bulk temperature of the coolant flow.

**Infrared Measuring Technique.** In case of three-dimensional flows where two-dimensional temperature mapping on the film-cooled surface is of particular interest, IR-Thermography can be applied as a powerful means. The major advantage of IR-Thermography is its high spatial resolution. In the present study, the infrared scanner THERMOVISION 900 by AGEMA is utilized with a maximum resolution of $136\times272$ pixels. Each pixel represents a surface area of $0.56\times0.56\ \mathrm{mm}^2$. The frame rate of the scanner is 15 Hz. To eliminate scattering effects all temperature mappings derived by the scanner are averaged results based on 32 single frames. Good optical accessibility is provided by three sapphire windows integrated in the top channel wall. To increase accuracy, the infrared data is calibrated by several thermocouples embedded on the test plate. Applying this measurement technique a relative error of less than 1% of the surface temperature measurements can be achieved.

**Data Processing Scheme.** Since the material of the test plate is not perfectly adiabatic there still exists (albeit slight) heat transfer between the solid $L3$ test plate and the flow that has a non-negligible influence on the measured surface temperatures. To determine the adiabatic wall temperatures (i.e., the adiabatic film cooling effectiveness $\eta_{aw}$) from the measured (near adiabatic) wall temperatures the local wall heat flux on the trailing edge cutback must be known (see Eqs. (1) and (2)). In the present case a numerical simulation based on the finite volume (FV) approach is used to calculate local heat fluxes in the solid test plate according to the measured surface temperature distribution. For that simulation the calibrated IR-data serve as boundary condition for the upper surface, whereas 13 thermocouples provide sampling points for temperature interpolation on the remaining surfaces (front, end, and bottom). With the thermal conductivity of the test plate material the calculation provides the local heat fluxes inside the test plate as well as on its surface boundaries.

Due to significant temperature differences between the film cooled trailing edge cutback and the surrounding hot channel walls the influence of radiative heat transfer has to be considered as well. This is done by means of a numerical radiation model implemented in the commercial CFD-solver Fluent 6 that is also used for the computational work presented here. The model is based on the enclosure method and allows calculating surface to surface radiation depending on the temperatures and the emissivities of the participating walls. The resulting wall heat flux is the sum of convective and radiative heat transfer. For determination of the adiabatic film cooling effectiveness, only convective heat transfer is of interest.

$$q_{\mathrm{conv}}=q_w-q_{\mathrm{rad}}=h_f\cdot(T_{aw}-T_w) \tag{1}$$

where $h_f$ is the isoenergetic heat transfer coefficient of film cooling. Assuming constant flow properties it can be taken as the heat transfer coefficient resulting for the isoenergetic flow ($T_c/T_{hg}=1$). The adiabatic film cooling effectiveness can then be determined by

$$\eta_{aw}=\frac{T_{hg}-T_{aw}}{T_{hg}-T_c}=\eta-\frac{q_{\mathrm{conv}}}{h_f\cdot(T_{hg}-T_c)} \tag{2}$$

where $\eta$ is the diabatic film cooling effectiveness based on the actual measured wall temperatures $T_w$ instead of $T_{aw}$. As in the present experiments near adiabatic conditions are achieved, $\eta$ is not far from $\eta_{aw}$ (the deviation is typically in the range of 3 to 5%). The isoenergetic heat transfer coefficient $h_f$ is still unknown in Eq. (2). In accordance to Gritsch et al. [18] it can be derived from the principle of superposition for film cooling by performing a second experiment with an altered wall temperature (by heating or cooling the wall) for the same flow conditions. In the present case, the isoenergetic heat transfer coefficient is determined from a correlation for two-dimensional tangential slot ejection suggested by Bittlinger [19] as there are no data available in the open literature dealing with heat transfer in the range of $x/H<10$ for at least similar film cooling geometries. Although this correlation does not perfectly describe the present film cooling situation, it still makes sense to use it for the determination of $\eta_{aw}$ as even in case of (minor) deviations of the isoenergetic heat transfer coefficients $h_f$ the overall quality of the results will benefit from the correction procedure described in Eq. (2). An uncertainty study for the present near adiabatic conditions reveals that even for a 50% deviation in $h_f$ the relative error of the adiabatic film cooling effectiveness will be less than 2.5%.

## Experimental Results

**Discharge Coefficients.** The discharge coefficient $C_D$ quantifies the global pressure loss for the internal coolant passage (Eq. (3)). It is defined by the ratio of the measured coolant mass flux and the ideal mass flux resulting from an isentropic expansion from the total pressure $p_{1,t}$, measured upstream of the first rib row ($L1$ region), to the static pressure $p_2$ of the main flow. As reference area, the total area of the ejection slot, $A$, is chosen.

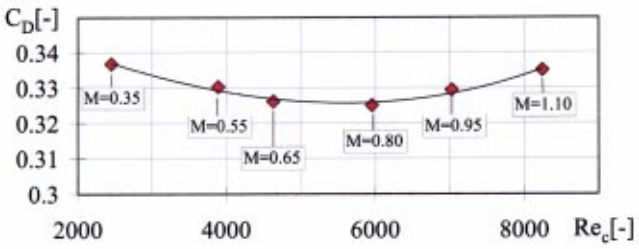


**Fig. 4 Measured discharge coefficient $C_D$ for varying $Re_c$ and $M$, respectively**

$$C_D = \frac{m_{c,\text{real}}}{m_{c,\text{ideal}}} = \frac{m_{c,\text{real}}}{p_{1,t}\cdot\left(\frac{p_2}{p_{1,t}}\right)^{\kappa+1/2\kappa}\cdot A\cdot\sqrt{\frac{2\kappa}{(\kappa-1)\cdot R\cdot T_{1,t}}\left[\left(\frac{p_{1,t}}{p_2}\right)^{\kappa-1/\kappa}-1\right]}} \tag{3}$$

All discharge coefficients are determined at main flow conditions described earlier. **Figure 4** shows the measured discharge coefficients for varying $Re_c$.

All discharge coefficients group around a value of $C_D \approx 0.33$. Usually, the discharge coefficient decreases as $Re_c$ is reduced so it is interesting to see that in the present configuration the $C_D$ value starts to increase again for $Re_c < 5000$. As this behavior was not observed without the presence of the main flow it is most likely that coolant is entrained by the high velocity main flow. As a consequence, the static pressure at the slot exit is reduced. For a blowing ratio of $M=0$, the described suction effects result in a static pressure which is significantly lower inside the coolant cavity than in the main flow.

**Adiabatic Film Cooling Effectiveness.** The surface temperature is mapped on the trailing edge cutback ($L3$-region in **Fig. 3**) by means of IR-Thermography and the data processing method described earlier is applied. **Figure 5** shows the adiabatic film cooling effectiveness, $\eta_{aw}$, downstream of the ejection slot for different blowing ratios, $M$.

The characteristic, two-dimensional distribution of $\eta_{aw}$ is a clear indication for a pronounced flow interaction between coolant and hot gas. Two neighboring coolant jets seem to coalesce resulting in a characteristic pattern of adiabatic film cooling effectiveness on the trailing edge cutback. This pattern of $\eta_{aw}$ is formed by peaks located on the centerlines of every second rib, and troughs on the centerlines of the two neighboring ribs caused by the expansion of hot gas in the wake region of these ribs.

For the present rib array with its 21 ribs and 22 coolant jets the coalescence of each two jets normally results in 11 peaks of adiabatic film cooling effectiveness on the trailing edge cutback with a central peak downstream of the symmetry-rib as shown in **Fig. 5** for $M>0.55$.

The maximum values of adiabatic film cooling effectiveness are less than unity and range from 0.82 for $M=0.35$ to 0.95 for $M=1.1$. This is mainly caused by hot gas entrainment in the wake region of the ribs, where recirculation and a high level of turbulence promote the mixing of the two flows. Another reason for a decreased maximum adiabatic film cooling effectiveness is the described nonuniformity of the coolant temperature at the ejection slot which is caused by heat conduction through the hot solid walls. In the present case this leads to an effective bulk temperature of the coolant which is slightly above the core temperature, $T_c$ used for the definition of $\eta_{aw}$.

It is interesting to note that for higher blowing ratios no unsteadiness can be identified with the IR scanner whereas especially at lower blowing ratios the interaction process is characterized by a permanent and random regrouping of coalescing jets. This leads to the characteristic shift of peaks and troughs of the adiabatic film cooling effectiveness in **Fig. 5** as $M$ changes from 0.65 to 0.55. The frequency of this phenomenon is highly dependent on the blowing ratio. In case of $M=0.65$ re-grouping takes place once within 10 minutes. For $M=0.5$ no steady condition can be achieved at all, as regrouping occurs every few seconds starting with a sudden separation of the cooling jets, which is probably induced by turbulent flow disturbances downstream of the lip. The state of separated jets is unstable and only exists for a few seconds. Then the jets randomly re-coalesce as shown in **Fig. 6(*a*).**

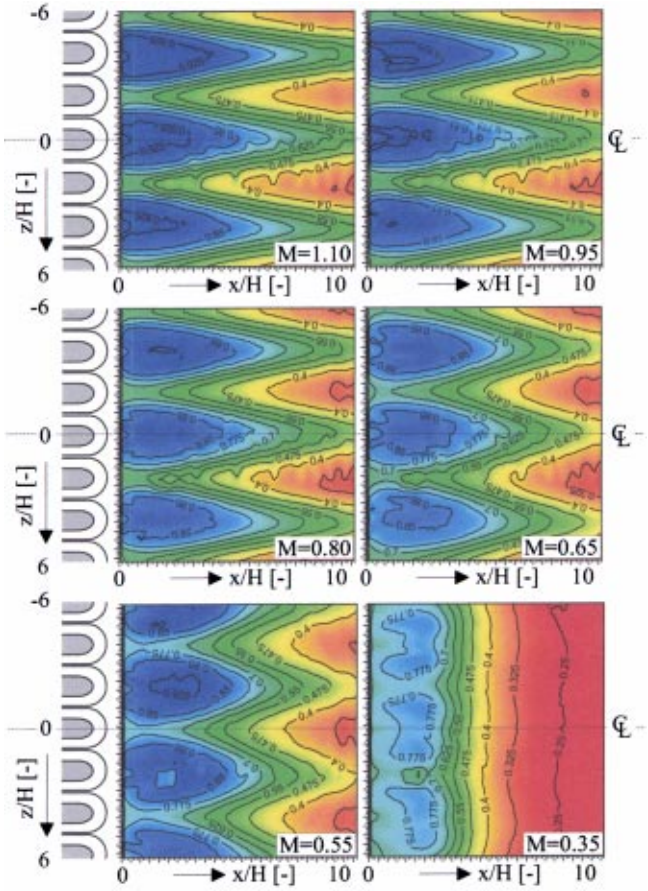


**Fig. 5 Adiabatic film cooling effectiveness $\eta_{aw}$ on the trailing edge cutback for different blowing rations $M$**

Although the normal case is groups of two attached coolant jets, sometimes also three jets are found to coalesce, e.g., as a result of a regrouping process, shifting the local peak of film cooling effectiveness from the rib centerline to the centerline of the central coolant jet. Whenever this phenomenon occurs, it is limited to one or two locations on the cutback region. The attachment of three jets is characterized by its relatively unstable nature and it sometimes induces a second mechanism of regrouping as shown in **Fig. 6(*b*)**: one of the two outer jets suddenly separates from the group and flaps to the neighboring two-jet group to participate in a new, laterally shifted, three-jet coalescence.

For blowing ratios of $M>1.1$ the groups of coalesced jets tend to re-separate probably due to their increased momentum. Then, the typical pattern of adiabatic film cooling effectiveness on the trailing edge cutback is replaced by an almost one-dimensional distribution of $\eta_{aw}$ due to turbulent mixing between the discrete coolant jets. The momentum-induced jet separation does not take place abruptly; furthermore separated as well as coalesced jets are found to coexist for a blowing ratio of $M=1.1$.

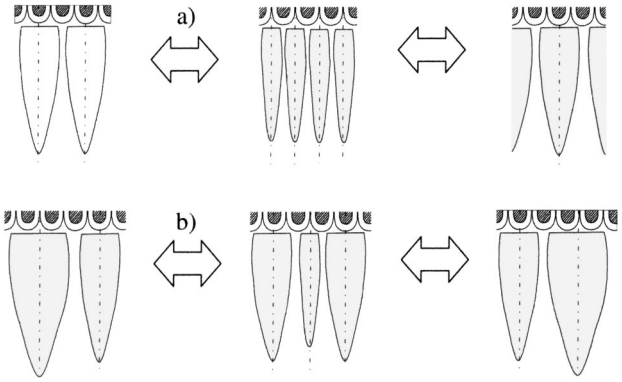


**Fig. 6 Observed regrouping mechanisms for (*a*) two-jet coalescence and (*b*) three-jet coalescence**

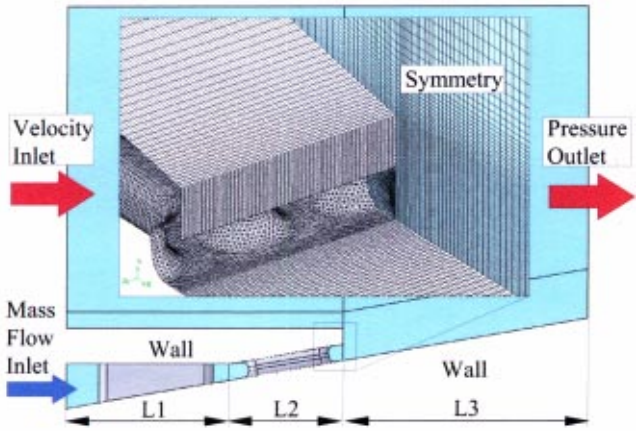


**Fig. 7 Computational domain with applied boundary types and example of a grid (*j*-2 model)**

There are some indications for the so-called Coanda effect being involved in the observed interaction phenomena. Due to this effect, two closely located parallel plane jets show the tendency to attach as the static pressure between them is reduced by entrainment of surrounding fluid into the jets.

It is important to emphasize that for the present configuration the coolant jets do not show any tendency to coalesce in the absence of a main flow.

In order to gain a more detailed insight in the flow field on the trailing edge cutback, computational studies are performed which will be presented in the following section.

## Computational Studies

Supporting three-dimensional steady and unsteady CFD studies are performed to gain a deeper insight into the flow field that is responsible for the observed coolant jet interaction on the trailing edge cutback. For the numerical investigation the commercial CFD-solver Fluent 6 is applied. Fluent 6 is based on an unstructured solver using a finite volume approach for the solution of the Reynolds averaged Navier-Stokes (RANS) equations and is especially well suited for parallel processing. By performing the simulations on up to ten nodes of an IBM RS/6000 SP supercomputer convergence is typically reached within one day.

**Geometry and Computational Grid.** Several models of the investigated cooling configuration are generated for the numerical studies. The computational domain of all models extends from the beginning of $L1$ to the end of $L3$ (see **Fig. 3**) and includes the main flow region as well as the whole internal coolant cavity. As several flow symmetries are indicated by the experiments the lateral extension of the trailing edge models can be reduced. For the numerical investigation of the experimentally observed interaction phenomena, meshes are generated for covering two (*j*-2 model) and six (*j*-6 model) coolant jets.

All modeling is performed in Gambit 2.04, the standard mesh generator of Fluent 6. Each computational grid is built by several blocks of different grid topology forming an unstructured hybrid mesh. In the main flow region hexahedrals are used whereas the coolant cavity is meshed by tetrahedral cells. Both meshes (*j*-2 and *j*-6 model) consist of approximately 1.3 million cells. **Figure 7** shows the domain and the chosen boundary types for one of the computational models.

In order to guarantee a $y^+$ of around 1 for the wall adjacent cell row, the mesh in the near wall region is either created by means of Gambit's boundary layer function or it is adaptively refined in Fluent.

**Turbulence Modeling.** The realizable $k$-$\varepsilon$ model is utilized for the present computations as its performance on shear flows including jets, mixing layers, and separated flows has been found to be substantially better than that of the standard $k$-$\varepsilon$ model.

The internal as well as the external flow field of the investigated trailing edge cooling design is highly influenced by the presence of surrounding walls. To predict such wall-bounded flows accurately, the near-wall region is described by means of a two-layer approach, which completely resolves the boundary layer all the way down to the viscous sublayer. Therefore, fine meshes have to be applied in the near-wall region with wall adjacent cell sizes of $y^+<5$.

## Computational Results

Main flow and coolant boundary conditions as well as the operating pressure are derived from the experiment.

For all computational studies second order discretization schemes are utilized. As convergence criterion of the iterative solution process a decrease of at least five orders of magnitude in all residuals is required.

Most of the simulations are done in an unsteady frame as recent publications by Holloway et al. [10,11] show that periodic vortex shedding can occur downstream of the lip. Furthermore, for the actual coolant Reynolds numbers, vortex street instabilities are likely to develop in the wake region behind the ribs.

**Pressure Distribution.** **Figure 8** shows the normalized static pressure $(p/p_{1t})$ inside the coolant cavity $(x/H<0)$ and downstream of the ejection slot along the center line of a coolant jet for three different blowing ratios. A good agreement is shown be-

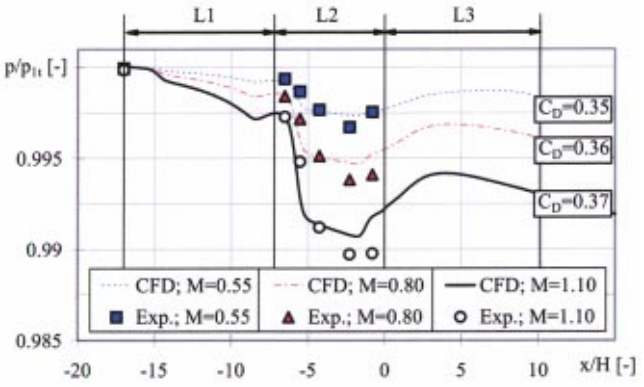


**Fig. 8 Comparison of measured and predicted pressure along the centerline of a coolant jet and resulting discharge coefficients for different *M***

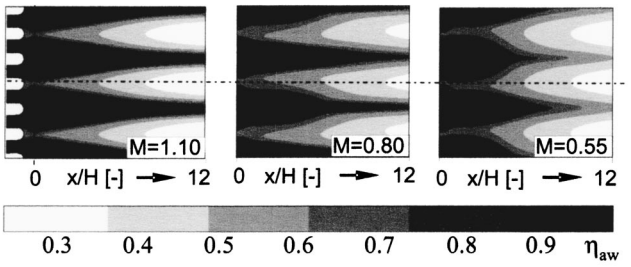


**Fig. 9 Predicted adiabatic film cooling effectiveness $\eta_{aw}$ for different blowing ratios $M$ ($j$-2 model)**

tween the pressure, measured on several locations inside coolant cavity and the numerical results. The plotted distribution in **Fig. 8** is characterized by a decrease of static pressure due to flow acceleration in the converging $L1$ region and, more pronounced, at the beginning of the second rib row.

Downstream of the ejection slot ($L3$ region, $x/H>0$) the static pressure increases as the main flow is decelerated behind the backward facing step of the film cooling configuration. After attaining a peak level, the static pressure starts to decrease again caused by flow acceleration on the converging trailing edge cutback. The resulting discharge coefficients are given in **Fig. 8** as well. In comparison to the experimental results shown in **Fig. 4**, a slight over-prediction can be noted. With respect to the very low pressure ratio which drives the coolant flow, these deviations, which are less than 10% seem to be acceptable.

**Adiabatic Film Cooling Effectiveness.** In **Fig. 9** the computational results of the adiabatic film cooling effectiveness are shown for three different blowing ratios. At a first glance the CFD predictions show the same characteristic temperature distribution on the trailing edge cutback as in the experiment.

**Figure 9** also indicates that especially for lower blowing ratios vortex street instabilities in the wake region of the ribs appear that cause periodic temperature fluctuations on the cooled surface. Nevertheless it can be stated that unsteady effects only seem to have a minor influence on the adiabatic film cooling effectiveness for the present configuration.

For a quantitative comparison between computational and experimental results, the adiabatic film cooling effectiveness is laterally averaged for three different blowing ratios and plotted in **Fig. 10**.

A surprisingly good agreement between experiment and CFD is found, which is especially true for $M=0.55$ where experimental and numerical results practically coincide. Nevertheless, it can be stated that with an increasing blowing ratio $M$, the numerical results tend to overpredict the experimental findings. This is mainly caused by an overprediction of the maximum adiabatic film cooling effectiveness—$\eta_{aw}$ reaches unity over an extended region on the trailing edge surface whereas it stayed always below that level in the experiment.

Furthermore, strong temperature gradients between the hot and cold regions in lateral direction on the trailing edge cutback indicate that the turbulent mixing process is underpredicted by CFD.

**Flow Field Downstream of the Ejection Slot.** In the following section, the view is focused on the mechanisms of the coolant jet interaction. **Figure 11** shows the relative velocity magnitude as well as the $y$-component of the velocity on a plane, parallel to the trailing edge cutback along the centerlines of the coolant jets ($y=H/2$) for $M=0.80$.

The plot of the relative velocity magnitude clearly shows the characteristic jet attachment. The relative $y$-component indicates that interaction is caused by the constriction of the coolant jets as hot gas from above locally expands into the wake region of every second rib and displaces the jets (note that due to the inclination

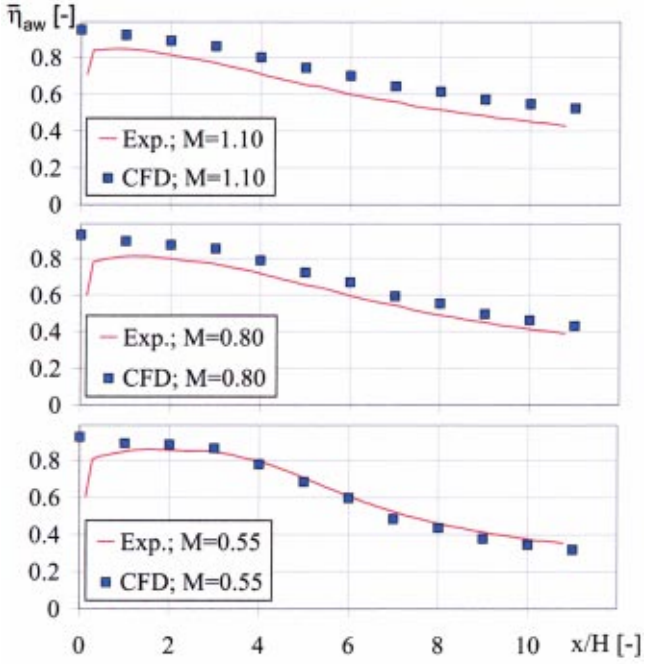


**Fig. 10 Comparison of measured and predicted laterally averaged adiabatic film cooling effectiveness for different blowing ratios $M$**

of the trailing edge cutback even a flow parallel to that wall has a positive $y$-component). Due to the Coanda effect each two jets stay attached so that a stable state is developed. The resulting flow field is highly complex and consists of different vortex-systems and recirculation zones. **Figure 12** shows velocity vector plots downstream of the ejection slot at different planes ($x$-$z$ as well as $y$-$z$ planes).

It is evident that the flow simulation based on a model which considers just two coolant jets is only able to predict dual jet interaction (if any). Therefore additional (steady) simulations are performed utilizing the second model with six coolant jets. These computations should give an answer to the question whether the observed interaction of three jets is predicted by CFD, too. **Figure 13** shows the adiabatic wall temperature distribution on the trailing edge cutback for a blowing ratio of $M=0.8$. It indicates that even the interaction of three jets is correctly predicted by CFD.

The mechanisms for the interaction are just the same as described above. In the present simulation the hot gas randomly expands at two locations in the wake region of a rib which leads not only to an attachment of two jets but also to a group of three

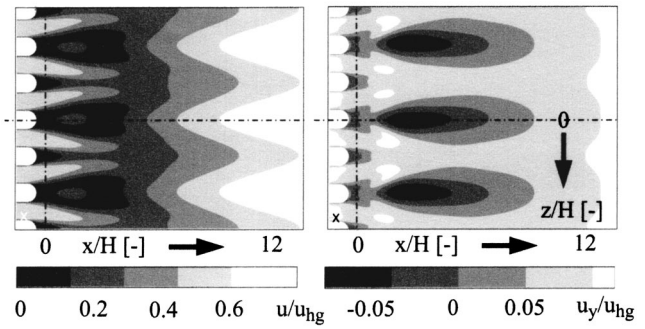


**Fig. 11 Velocity magnitude (left) and relative $y$-velocity component (right) in the plane of the jet centerlines ($y=H/2$) for a blowing ratio of $M=0.80$**

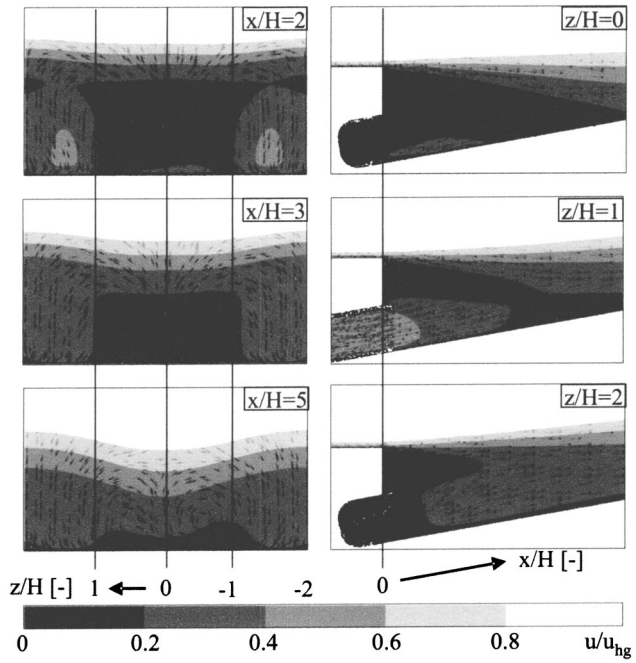


**Fig. 12 Flow field at different planes downstream of the ejection slot for $M=0.80$ (vectors not to scale)**

jets coalescing. Finally, there are some observations in the solution progress of additional CFD studies which are not considered here, indicating that also the observed process of regrouping can be captured by CFD.

## Conclusions

In this work, film cooling of a turbine blade trailing edge by means of circular coolant jets emerging from a ribbed passage is experimentally as well as numerically investigated. It is found that interaction between the coolant jets and the main flow leads to an attachment of up to three jets resulting in a characteristic temperature distribution on the trailing edge cutback. By means of numerical studies, the mechanisms of the observed interaction phenomenona are identified.

Finally, it must be emphasized that the investigated cooling configuration seems to be not desirable for film cooling of the trailing edge cutback as the attachment of coolant jets results in severe temperature gradients on the film cooled surface. Furthermore, the observed phenomenon of regrouping of attached coolant jets leads to an additional thermal fatigue of the film cooled trailing edge.

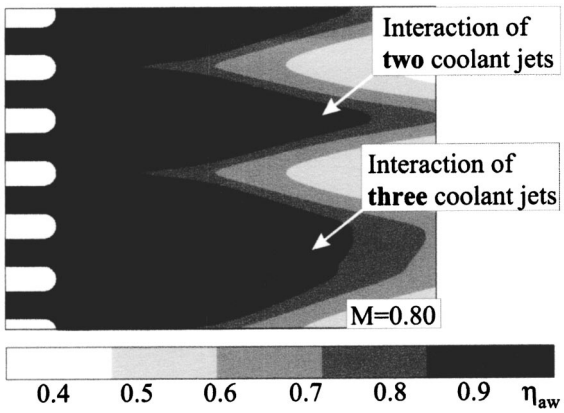


**Fig. 13 Predicted adiabatic film cooling effectiveness (j-6 model)**

## Acknowledgments

The reported work was performed within a research project that is part of the European project "Aerothermal Investigation of Turbine Endwalls and Blades" (AITEB, 5FP, G4RD-CT-1999-00055). The permission for the publication is gratefully acknowledged by the authors.

## Nomenclature

$A$ = ejection slot total area ($m^2$)
$b_r$ = rib width (mm)
$C_D$ = discharge coeff. ($C_D = m_{c,\text{real}}/m_{c,\text{ideal}}$)
$D$ = diameter of circular coolant passage (mm)
$H$ = slot height (mm)
$h$ = heat transfer coefficient ($W/(m^2K)$)
$L$ = char. length ($L = L0 + L1 + L2 + L3$) referring to **Fig. 3** (mm)
$M$ = blowing ratio ($M = (\rho_c u_c)/(\rho_{hg} u_{hg})$)
$m$ = mass flow rate (kg/s)
$p$ = pressure ($N/m^2$)
$q$ = heat flux ($W/m^2$)
$R$ = ideal gas constant (J/kg K)
Re = Reynolds number (based either on $D$ or $L$ as characteristic length)
$R_f$ = fillet radius (mm)
$s$ = rib pitch (mm)
$T$ = temperature (K)
$t$ = lip thickness (mm)
$u$ = velocity (m/s)
$x, y, z$ = coordinates (origin: ejection slot) (m)

### Greek

$\alpha$ = trailing edge wedge angle (deg)
$\delta$ = boundary layer thickness (mm)
$\delta_1$ = displacement thickness (mm)
$\eta_{aw}$ = adiabatic film cooling effectiveness ($\eta_{aw} = (T_{hg} - T_{aw})/(T_{hg} - T_c)$)
$\kappa$ = ratio of specific heats
$\lambda$ = thermal conductivity (W/(mK))
$\mu$ = dynamic viscosity (Pas)
$\pi$ = pressure ratio
$\rho$ = density ($kg/m^3$)

### Subscripts

$aw$ = adiabatic wall
$c$ = coolant
cond = conductive
$f$ = iso-energetic
$hg$ = hot gas
rad = radiative
$r_i$ = rib index
tot = total
$w$ = wall

## References

[1] Seban, R. A., and Back, L. H., 1962, "Effectiveness and Heat Transfer for a Turbulent Boundary Layer with Tangential Injection and Variable Free-Stream Velocity," ASME J. Heat Transfer, **84**, pp. 235–244.
[2] Samuel, A. E., and Joubert, P. N., 1965, "Film Cooling of an Adiabatic Plate in Zero Pressure Gradient in the Presence of a Hot Mainstream and Cold Tangential Secondary Injection," ASME J. Heat Transfer, **87**, pp. 409–417.
[3] Kacker, S. C., and Whitelaw, J. H., 1968, "The Effect of Slot Height and Slot Turbulence Intensity on the Effectiveness on the Uniform Density, Two-Dimensional Wall Jet," ASME J. Heat Transfer, **90**, pp. 469–475.
[4] Sivasegaram, S., and Whitelaw, J. H., 1969, "Film Cooling Slots: The Impor-

tance of Lip Thickness and Injection Angle,'' J. Mech. Eng. Sci., **11**(1), pp. 22–27.
[5] Goldstein, R. J., 1971, ''Film Cooling,'' Adv. Heat Transfer, **7**, pp. 321–379.
[6] Ballal, D. R., and Lefebvre, A. H., 1973, ''Film-Cooling Effectiveness in the Near Slot Region,'' ASME J. Heat Transfer, **95**, pp. 265–266.
[7] Mukherjee, D. K., 1976, ''Film Cooling With Injection Trough Slots,'' ASME J. Eng., **98**, pp. 556–559.
[8] Bittlinger, G., Schulz, A., and Wittig, S., 1994, ''Film Cooling Effectiveness and Heat Transfer Coefficients for Slot Injection at High Blowing Ratios,'' ASME Paper 94-GT-182.
[9] Taslim, M. E., Spring, S. D., and Mehlman, B. P., 1990, ''An Experimental Investigation of Film Cooling Effectiveness for Slots of Various Exit Geometries,'' Paper No. AIAA-90-2266.
[10] Holloway, D. S., Leylek, J. H., and Scott, F. A., 2002, ''Pressure Side Bleed Film Cooling: Part 1—Steady Framework for Experimental and Computational Results,'' ASME Paper GT-2002-30471.
[11] Holloway, D. S., Leylek, J. H., and Scott, F. A., 2002, ''Pressure Side Bleed Film Cooling: Part 2—Unsteady Framework for Experimental and Computational Results,'' ASME Paper GT-2002-30472.
[12] Sturgess, G. J., 1985, ''Design of Combustor Cooling Slots for High Film Effectiveness: Part 1—Film General Development,'' ASME Paper 85-GT-35.
[13] Sturgess, G. J., and Pfeiffer, G. D., 1985, ''Design of Combustor Cooling Slots for High Film Effectiveness: Part 2—Film Initial Development,'' ASME Paper 85-GT-36.
[14] Rastogi, A. K., and Whitelaw, J. H., 1973, ''The Effectiveness of Three Dimensional Film-Cooling Slots—1. Measurements,'' Int. J. Heat Mass Transfer, **16**, pp. 1665–1681.
[15] Nina, M. N. R., and Whitelaw, J. H., 1971, ''The Effectiveness of Film Cooling With Three Dimensional Slot Geometries,'' ASME Paper 71-GT-11.
[16] Martini, P., Schulz, A., Whitney, C. F., and Lutum, E., 2003, ''Experimental and Numerical Investigation of Trailing Edge Film Cooling Downstream of a Slot with Internal Rib Arrays,'' 5th European Conference on Gas Turbines, to be published.
[17] Roach, P. E., 1987, ''The Generation of Nearly Isotropic Turbulence by Means of Grids,'' Heat and Fluid Flow, **8**(2), pp. 83–92.
[18] Gritsch, M., Baldauf, S., Martiny, M., Schulz, A., and Wittig, S., 1999, ''The Superposition Approach to Local Heat Transfer Coefficients in High Density Ratio Film Cooling Flows,'' ASME Paper 99-GT-168.
[19] Bittlinger, G., 1995, ''Filmkühlung mit tangentialer Spaltausblasung: Experimentelle und numerische Ansätze zur Optimierung des Brennkammer-Kühlluftbedarfes,'' Ph.D. thesis, Institut für Thermische Strömungsmaschinen (ITS), Universität Karlsruhe.

# Interaction of Film Cooling Rows: Effects of Hole Geometry and Row Spacing on the Cooling Performance Downstream of the Second Row of Holes

**Christian Saumweber**
e-mail:
Christian.Saumweber@its.uni-karlsruhe.de

**Achmed Schulz**

Lehrstuhl und Institut für Thermische
Strömungsmaschinen,
Universitat Karlsruhe (T.H.),
Kaiserstr. 12,
Karlsruhe 76128, Germany

*A comprehensive set of generic experiments is conducted to investigate the interaction of film cooling rows. Five different film cooling configurations are considered on a large-scale basis each consisting of two rows of film cooling holes in staggered arrangement. The hole pitch to diameter ratio within each row is kept constant at $P/D=4$. The spacing between the rows is either $x/D=10$, 20, or 30. Fan-shaped holes or simple cylindrical holes with an inclination angle of 30 deg and a hole length of 6-hole diameters are used. With a hot gas Mach number of $Ma_m=0.3$, an engine like density ratio of $\rho_c/\rho_m=1.75$, and a freestream turbulence intensity of $Tu=5.1\%$ are established. Operating conditions are varied in terms of blowing ratio for the upstream and, independently, the downstream row in the range $0.5<M<2.0$. The results illustrate the importance of considering ejection into an already film-cooled boundary layer. Adiabatic film cooling effectiveness and heat transfer coefficients are significantly increased. The decay of effectiveness with streamwise distance is much less pronounced downstream of the second row primarily due to pre-cooling of the boundary layer by the first row of holes. Additionally, a comparison of measured effectiveness data with predictions according to the widely used superposition model of Sellers is given for two rows of fanshaped holes.*
[DOI: 10.1115/1.1731395]

## Introduction

Todays gas turbines are heading towards higher pressure ratios and higher turbine inlet temperatures to increase cycle efficiency, and primarily in aeroengine applications towards less turbine stages. Consequently, the thermal and mechanical loads of components exposed to the hot gas are increased as well, which necessitates extremely efficient cooling configurations in order to guarantee acceptable lifetimes. State-of-the-art film cooling schemes with shaped holes of various geometry are employed in advanced high-pressure turbines. To achieve maximum benefit from the expended cooling air, film cooling configurations have to be very accurately adjusted to the local thermal and aerodynamic conditions, i.e., the local heat load.

Downstream of a single row of film cooling holes the coolant mixes with the hot gas resulting in decreasing cooling effectiveness. Particularly in high-pressure turbine cooling applications it is, therefore, necessary to regenerate the cooling film. This is achieved by ejecting coolant from a second row of holes which is placed downstream of the first row at a certain streamwise distance. The coolant jets from the second row interact with the coolant from the upstream row, that partially has mixed with hot gas. In the past, a limited number of studies has been conducted that aim on characterizing the major phenomena of this interaction and on highlighting the resulting effects on film cooling effectiveness and heat transfer. A common trend in the results of those investigations is an increase of both heat transfer coefficient, [1], and adiabatic film cooling effectiveness downstream of the second ejection location (e.g., [2,3]). The latter finding is usually substantiated by the fact that the coolant ejected by the upstream row of holes effectively lowers the temperature at the ejection location of the second row of holes. Another reason is given by Sinha et al. [4], who report that the coolant ejected by the upstream row of holes significantly thickens the boundary layer. For conditions with velocity ratios of coolant-to-hot gas smaller than unity, i.e., blowing ratios smaller than the density ratio, the thicker boundary layer will reduce the velocity gradients in the shear layer between the coolant from the second row and the external flow. This will, according to the authors, result in lower turbulence levels and consequently in reduced mixing of coolant and hot gas.

For film cooling schemes consisting of two or more rows of holes, the row arrangement (''in line'' or ''staggered'') and the distance between the rows are important geometric parameters. As can be expected, larger row to row spacing is detrimental in terms of film cooling effectiveness downstream of the second row of holes, [5]. In general, a staggered arrangement shows superior performance as compared to an in line configuration, [6,7]. For a large row to row spacing, however, the impact of the row arrangement, staggered or in line, is small since with increasing distance the coolant film from the upstream row becomes more uniform and two-dimensional, [8]. In order to improve the lateral distribution of the coolant, holes with compound angle orientation are sometimes used for one or both rows of holes. In general, this leads to higher laterally averaged film cooling effectiveness, at least close to the ejection location, [5,9]. On the other hand, there might be a detrimental effect in terms of heat transfer augmentation, [10], and possibly aerodynamic losses, [5].

From the studies mentioned so far it can be concluded, that the performance of two or more rows of holes significantly depends on the geometric set up. Since most film cooling data is available for single rows of holes only, designers need to use a superposition law to predict film cooling effectiveness downstream of multiple ejection locations. Most widely used is the approach of Sellers [11], which was derived for multiple slot film cooling. The

Contributed by the International Gas Turbine Institute and presented at the International Gas Turbine and Aeroengine Congress and Exhibition, Atlanta, GA, June 16–19, 2003. Manuscript received by the IGTI December 2002; final revision March 2003. Paper No. 2003-GT-38195. Review Chair: H. R. Simmons.

  

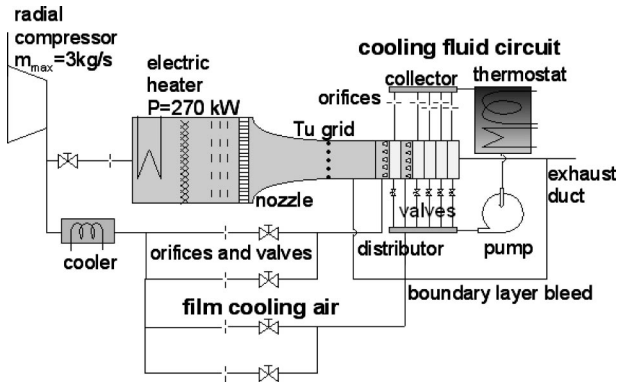


**Fig. 1 Schematic of the experimental facility**

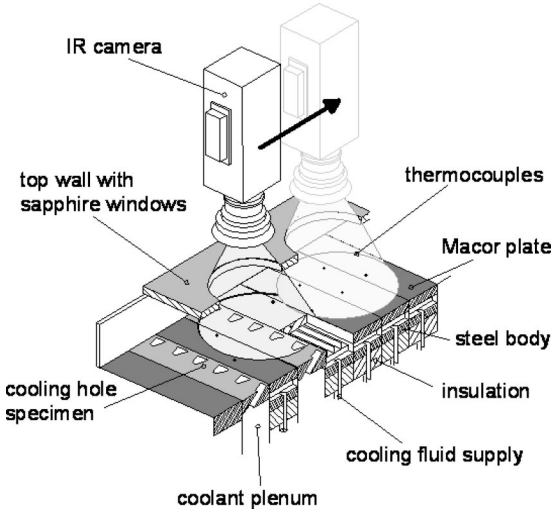


**Fig. 2 Film-cooling test section (modules for heat transfer tests)**

adiabatic wall temperature downstream of a second row of holes is predicted by substituting the adiabatic wall temperature due to upstream coolant ejection for the hot gas temperature in the expression of film cooling effectiveness. By assuming equal coolant temperatures at both ejection locations it can be shown that this leads to

$$\eta_{aw} = \eta_1 + \eta_2(1 - \eta_1) \tag{1}$$

with $\eta_1$ the film cooling effectiveness for only the upstream row present and $\eta_2$ the film cooling effectiveness of only the downstream row present. It is obvious that Eq. (1) can be extended to calculate film cooling effectiveness downstream of an arbitrary number of ejection locations. For film cooling with cylindrical holes, the agreement between predictions according to Eq. (1) and measured data was found to be good not only for flat plate tests but also on airfoils, [2]. However, in case of higher blowing rates and smaller row to row spacing significant discrepancies have been detected, [12–14]. No validations are available in the literature for rows of shaped film-cooling holes.

All studies mentioned so far have been conducted using different combinations of rows with cylindrical holes. The ejection configuration was varied with respect to compound or simple angle holes, inline or staggered arrangement of the rows, inclination angle, and pitch to diameter ratio. However, to the authors knowledge, up to now no investigation on the interaction of film cooling rows with shaped holes is available in the open literature. Furthermore, only a very limited number of studies has been conducted, that aim to investigate the impact of varying streamwise distances between the two rows. Finally, in terms of ejection parameters, there is only one investigation that focuses on the impacts of various combinations of blowing ratios, which necessitates, that the ejected mass flow rates from the two rows can be varied independently. The present study addresses these three issues and contains a comprehensive set of measurements on the interaction of film cooling rows, that allows extensive validation of correlations and CFD tools.

## Experimental Facility and Test Conditions

The present investigation is carried out in an open loop hot wind tunnel at the Institut für Thermische Strömungsmaschinen (ITS), University of Karlsruhe, (**Fig. 1**). Air is delivered to the test section by a radial compressor with a pressure ratio of 1.5 and a maximum mass flow rate of 3 kg/s. After passing a control valve, the air enters an electrical heater consisting of 18 heating cartridges with a maximum total power of 270 kW. A static mixer, several screens, a flow straightener, and a contraction nozzle generate a homogenous temperature and velocity field at the wind tunnel inlet. A boundary layer bleed allows to control the boundary layer thickness at the location of coolant film ejection. In front of the boundary layer bleed, 90-hole diameters upstream of the ejection holes, turbulence grids of various geometry can be installed. Just downstream of the boundary layer bleed, the boundary layer is tripped to be turbulent.

The test section (**Fig. 2**) consists of a channel with rectangular cross section and measures 220 mm in width and 48 mm in height. On the top, several sapphire windows enable excellent optical access for nonintrusive diagnostics. One sidewall is equipped with a traversing mechanism for combined total-pressure–total-temperature probes, that can be placed at several streamwise positions. The bottom of the test section is given by a modular segmented test plate, that carries the film-cooling hole specimen which are connected to the coolant plenum. The segmentation of the test plate allows for a straightforward modification of the spacing between the two film cooling rows. Cooling air is supplied to the plenum as part of the air delivered by the radial compressor, which is split into main (hot gas) and secondary (coolant) flow upstream of the hot gas control valve (see **Fig. 1**). The coolant mass flow rate is controlled by two valves upstream of the coolant plenum. The temperature of the cooling air is controlled by a water cooled heat exchanger. The coolant plenum is equipped with a screen to ensure a uniform distribution of cooling air.

All tests are carried out using ejection modules with seven film-cooling holes in a row. Two types of holes are investigated: a simple cylindrical hole and a fan-shaped hole. Their baseline geometry is shown in **Fig. 3**. The diameter of the cylindrical hole and the diameter of the cylindrical inlet portion of the fanshaped hole is $D=5$ mm. Downstream of a cylindrical inlet section with a length of $2 \cdot D$, the fan-shaped holes are expanded in lateral direction with an angle of 14 deg resulting in an exit-to-entry-area ratio of 3. For both holes, the inclination angle with respect to the

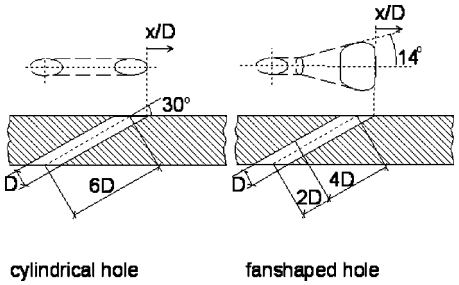


**Fig. 3 Film-cooling hole geometry**

**Table 1 Operating conditions**

| | | |
|---|---|---|
| Mach number | $Ma_m$ | 0.3 |
| Reynolds number 1st row | $Re_{x,m,1}$ | $1.53\ 10^6$ |
| Reynolds number 2nd row | $Re_{x,m,2}$ | $\leqslant 2.04\ 10^6$ |
| Hole diameter | $D$ | 5 mm |
| Distance upstream 1st row | $\xi$ | $85D$ |
| Pitch to diameter ratio | $P/D$ | 4 |
| Turbulence intensity | $Tu$ | 5.1% |
| Integral length scale | $\Lambda$ | $2.1 \cdot D$ |
| Hot gas temperature | $T_{tm}$ | 515 K |
| Coolant temperature | $T_{tc}$ | 290 K |
| Density ratio | $\rho_c/\rho_m$ | 1.75 |
| Blowing ratio upstream (1st) row | $M_1$ | cylindrical holes: 0.5, 1.0, 1.5 fan-shaped holes: 0.5, 1.0, 2.0 |
| Blowing ratio downstream (2nd) row | $M_2$ | cylindrical holes 0.5, 0.75, 1.0, 1.25, 1.5 fan-shaped holes 0.5, 0.75, 1.0, 1.5, 2.0 |
| Cooling Configurations (1st row, 2nd row, streamwise spacing, Cy=cylindrical holes Fs=fanshaped holes) | - | 1) Cy, Cy, $x/D=20$ 2) Cy, Fs, $x/D=20$ 3) Fs, Fs, $x/D=20$ 4) Fs, Fs, $x/D=10$ 5) Fs, Fs, $x/D=30$ |

hot gas surface is 30 deg, the length-to-diameter ratio $L/D$ is 6, the pitch-to-diameter ratio is kept constant at 4. Entry and exit of the holes are sharp edged. The interior surfaces are aerodynamically smooth. Five cooling configurations are tested, each consisting of two rows of film cooling holes in staggered arrangement with different hole geometry and varying streamwise spacing between the two rows. For each cooling configuration a series of steady-state experiments is conducted at exactly the same hot gas flow conditions. During all the tests, the static temperature ratio $T_c/T_m$ is kept constant at 0.57, leading to an engine-like density ratio of $\rho_c/\rho_m=1.75$. Each cooling configuration is tested with 15 different combinations of blowing ratios at the upstream and downstream row. The calculation of the blowing ratio $M$ is based on the cross-sectional area at the hole inlet. A complete set of the operating conditions is given in **Table 1**.

The first quantity of interest is the adiabatic film-cooling effectiveness which is defined by

$$\eta_{aw}=\frac{T_{\mathrm{rec},m}-T_{aw}}{T_{\mathrm{rec},m}-T_{tc}}. \tag{2}$$

To measure adiabatic film-cooling effectiveness it is required to establish thermal boundary conditions as close as possible to adiabatic. The segmented test plate used for these experiments consists of 6 modules, each $10D$ long in streamwise direction, which are machined out of the high temperature thermoplastic material Tecapeek©. Tecapeek© has a low thermal conductivity of 0.3 W/(mK) and a maximum operating temperature of about 570 K. The superposition approach of film cooling, [15–19], is used in order to determine the local adiabatic film cooling effectiveness as well as the local heat transfer coefficient with film cooling, $h_f$, which is the second quantity of interest in the present study:

$$h(\theta)=h_f\cdot(1-\eta_{aw}\theta) \tag{3}$$

with

$$\theta=\frac{T_{tc}-T_{\mathrm{rec},m}}{T_w-T_{\mathrm{rec},m}}. \tag{4}$$

In general, to acquire the linear relation between $h$ and $\theta$ of Eq. (3), two measurements of $h$ at two different $\theta$ have to be performed. The first data set is given by the measurements with the low thermal conductivity test plate. For a given flow field data points close to $h=0$ and $\theta=\theta_{aw}=1/\eta$ are generated. The second data set has to be acquired with a dimensionless temperature different from $1/\eta$ but at the same flow conditions as for the "close-to-adiabatic" tests, particularly the same temperature ratio. For that reason $\theta$ is varied by varying the wall temperature only. The segmented test plate used for this second set of experiments again consists of 6 modules, that are made of the glass-ceramic material Macor© which has a thermal conductivity of 2 W/(mK). To enhance the heat flux through the test plate and, therefore, to decrease $\theta$, internal cooling with a temperature controlled silicon oil circuit is applied (see **Fig. 1**).

For both, "close-to-adiabatic" and heat transfer tests, surface temperature mappings on the test plates are acquired by an infrared (IR) camera system (AGEMA 900), that has proven its accuracy and reliabilty in previous studies, [20,21]. The IR camera provides a two-dimensional distribution of temperatures that is digitized into an array of 272 times 136 pixels. According to the optical setup used in the experiments this results in a spatial resolution of 0.8 mm times 0.8 mm per pixel. The hot gas surface of each test plate is covered by a black paint with a well-known emissivity of 0.95. Two 0.25 mm NiCr-Ni-thermocouples are embedded flush with the surface of each module for an in-situ calibration of the infrared camera readings, [22]. The temperatures on the back surface of each module are monitored by two further 0.25 NiCr-Ni thermocouples in case of the Macor© modules and one 0.25 NiCr-Ni thermocouple in case of the Tecapeek© modules. For each test, IR images and thermocouple temperatures are recorded simultaneously. The measured temperatures are interpolated onto a finite element (FE) mesh of the respective test plate. The FE model is restricted to a representative slice of the test plate and extends half a pitch to either side of the symmetry plane of the center hole. By this approach and due to the large width of the test section, sidewall effects can be neglected. A steady-state thermal analysis is performed in order to calculate the three-dimensional heat flux distribution of the test plate. The FE analysis allows to account for conduction effects in lateral and streamwise direction and to derive the correct wall normal heat flux. The measured surface temperatures of the two data sets together with the respective wall normal heat flux distribution from the FE analysis allow to calculate two pairs of $h$ and $\theta$. From these, finally, the adiabatic film cooling effectiveness and the heat transfer coefficients with film cooling $h_f$ can be determined by means of an extrapolation according to Eq. (3).

## Experimental Uncertainties

Uncertainties are estimated according to the procedure proposed by Kline and McClintock [23]. Mach number is kept constant within $\pm 1.6\%$. Uncertainty in setting the blowing ratio is $\pm 2\%$. Density ratio uncertainty is $\pm 1.7\%$. The uncertainty in laterally averaged adiabatic effectiveness amounts to $\Delta\eta=0.004 \div 0.036$. The lower value of the range corresponds to locations with poor cooling performance, the upper value to regions with excellent cooling performance. Based on the above $\Delta\eta$ a maximum relative error in laterally averaged adiabatic effectiveness of $\pm 4\%$ is calculated. For the laterally averaged dimensionless heat transfer coefficient with film cooling $h_f/h_0$ a maximum uncertainty of $\pm 15\%$ is estimated.

## Results

In the following only a limited part of the complete data base is presented and discussed. It is intended to extract the more relevant features in order to focus on the key issues of the interaction of film cooling rows with shaped holes.

In order to benchmark and validate the experimental procedure, adiabatic film-cooling effectiveness data downstream of a single row of holes is compared to results of previous investigations, see **Fig. 4**. Because no other study is available with a hole pitch of $4D$, centerline effectiveness data is used instead of laterally averaged data in case of the cylindrical holes (open symbols and dash-dotted line, respectively). Since for fan-shaped holes (filled symbols and solid line, respectively) centerline data are rarely found in the literature, comparison is made on basis of laterally averaged

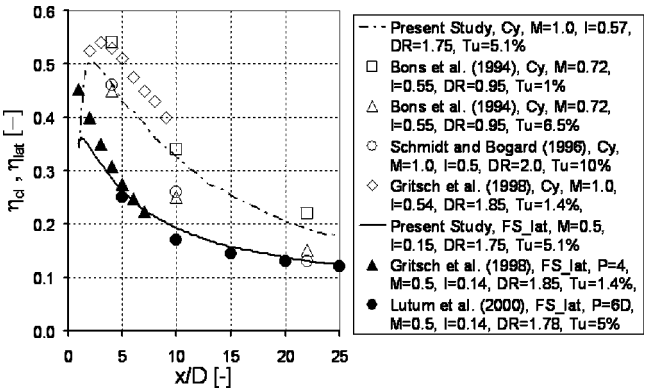


**Fig. 4 Comparison of film cooling effectiveness with data of other studies**

values in spite of different pitches. Operating conditions have been selected such to establish similarity in terms of momentum flux ratio rather than in terms of blowing ratio because the various investigations have been conducted with very different density ratios (DR, indicated in the caption). For the cylindrical holes, the film cooling effectiveness is smaller as compared to the data of Gritsch et al. [20] at $Tu=1.4\%$ and the data of Bons et al. [24] at $Tu=1\%$, since the turbulence level in the present study is increased to 5.1%. On the other hand, film-cooling effectiveness is larger in comparison to the studies of Schmidt and Bogard [25] at $Tu=10\%$ and Bons et al. [24] at $Tu=6.5\%$, which again is attributed to the different turbulence levels. The fact, that the data of Bons et al. [24] is very close to the data of Schmidt and Bogard [25] despite the lower freestream turbulence intensity can be explained by the steeper inclination angle employed in Ref. [24]. The film-cooling effectiveness of the fanshaped holes is compared to the data of Lutum et al. [26], which used a very similar hole geometry. Although the pitch is larger in Ref. [26], laterally averaged effectiveness levels are very similar. This finding is a result of the convex surface curvature employed by Lutum et al. [26], which—at blowing ratios lower than approximately $M=1$—increases film cooling effectiveness and, therefore, partially compensates for the larger pitch. The single hole data of Gritsch et al. [20] could be converted to a ''virtual pitch'' of $4D$ (in [20] it is given for $P=5.5D$ only) since the local values are available at ITS. Close to the ejection location effectiveness levels are larger in comparison to those of the present study primarily because of the lower turbulence level in [20]. Since Gritsch et al. [20] used a single hole (as opposed to a row of holes in the current paper) film cooling effectiveness decays more rapidly resulting in similar effectiveness levels for both data sets at $x/D=7$. Comprising the results presented in **Fig. 4** it can be stated that the data agree quite well with results of previous studies although only a reasonable match of the experimental conditions can be obtained.

For a rather qualitative first impression local distributions of adiabatic film cooling effectiveness downstream of the second row of holes are presented in **Fig. 5** for varying row to row spacing and different hole shapes. The blowing ratio of the first (upstream) row is $M_1=1.0$ whereas the blowing ratio of the second (downstream) row is kept constant at $M_2=0.5$. Additionally, comparison is made to coolant ejection from single rows of cylindrical and fan-shaped holes, for which the respective effectiveness pattern is shown on the bottom of **Fig. 5**. For each of the seven different cooling configurations the shape of the second row of holes is indicated schematically in the figure. At a first glance, the beneficial effect of the upstream row coolant ejection becomes apparent despite the fact, that the general characteristics are dominated by the second row of holes and are similar to coolant ejection from a single row. If the second row consists of cylindrical holes, the coolant is concentrated in the area downstream of the hole centerline, leading to pronounced temperature gradients in lateral direction. By the first row coolant ejection, these temperature gradients are extenuated in comparison to single row ejection. In case of a second row of fan-shaped holes, the coolant distribution is more uniform in lateral direction with a double-peak pattern close to the hole exit as typical for this kind of holes. Based on CFD studies for single fan-shaped holes it can be stated that the two outer peaks close to the ejection location are a result of a separation bubble forming inside the diffuser on the downstream wall close to the centerline. The bubble forces more coolant towards the sidewalls of the diffuser thereby improving the lateral coolant distribution and generating the double peak pattern. For both, cylindrical and fanshaped holes, the upstream coolant ejection increases the local values of adiabatic effectiveness by up to 50% or even more. This is caused by a pre-cooling of the boundary layer by the upstream row and the presence of additional coolant in the mid-pitch area of the downstream row. Another plausible explanation for the beneficial effect of the upstream row might be the following. For the staggered arrangement considered in the present study the jets of the downstream row of holes are ejected in the midpitch area of the upstream row. In this region, the kidney vortices of the upstream row generate a secondary flow which is oriented towards the wall. By that, the jets of the downstream row are pushed towards the surface which results in a reduced tendency to detach from the wall. Since the strength of this secondary flow is highly dependent on blowing ratio, hole shape, and row spacing, more work is required to prove this hypothesis. Finally, it is obvious that an upstream row of fanshaped holes results in much better surface protection also downstream the second row of holes in comparison to an upstream row of cylindrical holes. The distance between two rows of fan-shaped holes on the other hand appears to only moderately affect the effectiveness levels with advantages at smaller row to row spacing, as could be expected.

For the designer it might be important to know which combination of upstream and downstream row blowing ratios lead to maximum film cooling performance. Large blowing ratios can extend the intensively cooled area downstream the second row of holes and have been recommended to be used rather for the upstream row by other authors previously, [8]. On the other hand, a large blowing ratio used for the upstream row of holes might drastically reduce film-cooling performance in the area between the two rows due to jet detachment. In the following, results for different combinations of upstream and downstream row blowing ratios are presented in order to highlight their impact on film cooling performance. Laterally and spatially averaged values of adiabatic film-cooling effectiveness are used whereas lateral averaging has been performed over a width of one pitch ($=4D$) and spatial averages have been calculated over an area of one pitch in width and 20-hole diameters in streamwise length, starting $1.5D$ downstream of the ejection location.

**Figure 6** shows laterally averaged values of adiabatic film cooling effectiveness plotted versus the distance from the second ejection location for two rows of cylindrical holes with a spacing of 20-hole diameters. Data from single-row ejection is shown additionally for a blowing ratio of $M=0.5$. It can be recognized that due to the upstream coolant ejection laterally averaged effectiveness is increased by the order of 40–50% in comparison to single-row ejection. Again, the results indicate, that the cooling performance is dominated by the downstream row of holes, whereas the upstream row blowing ratio is less important. In all cases, however, an upstream blowing ratio of $M_1=1.0$ leads to higher film cooling effectiveness than a blowing ratio of $M_1=0.5$ or $M_1=1.5$ for constant downstream blowing ratio $M_2$.

The predominance of the second row of holes is most pronounced for the combination of an upstream row of cylindrical holes with a downstream row of fanshaped holes, see **Fig. 7**. Particularly for the largest second row blowing ratio of $M_2=2.0$ a variation of the mass flow rate ejected by the upstream row in the

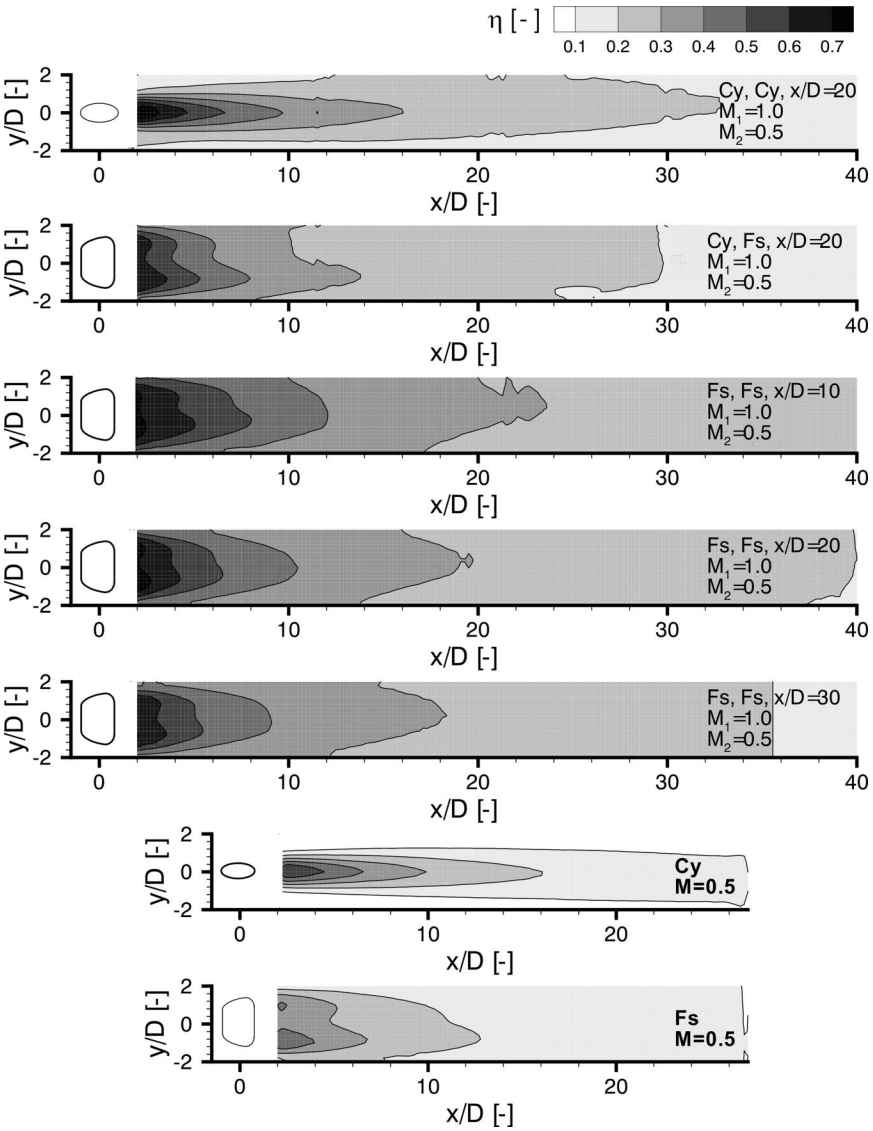


**Fig. 5 Local distributions of film-cooling effectiveness**

range $0.5 < M_1 < 1.5$ is almost ineffective for the adiabatic film-cooling effectiveness. This finding indicates, that for this particular film cooling configuration the blowing ratio of the upstream row should be such that the area upstream of the second row is sufficiently cooled.

A completely different characteristic is observed when two rows of fanshaped holes are used, see **Fig. 8**. For the operating conditions established in the current study, no jet detachment or separation from the sidewalls of the diffusor could be detected for the fanshaped holes. Consequently lateral distribution of coolant is excellent and a continuous augmentation of film cooling effectiveness with increasing ejected mass flow rate is found. For that reason, not only the downstream but also the upstream row blowing ratio significantly affects film cooling effectiveness for this configuration.

Spatially averaged values of adiabatic film-cooling effectiveness can be used in order to give a survey on the performance of the three film-cooling configurations discussed just previously, see **Fig. 9**. For two rows of cylindrical holes with a spacing of 20*D* optimum performance based on spatially averaged effectiveness is achieved with an upstream blowing ratio of rather $M_1 = 1.0$ than 0.5 or 1.5. The downstream row blowing ratio should be in the range of $M_2 = 0.75$. More interesting in this figure is the fact, that

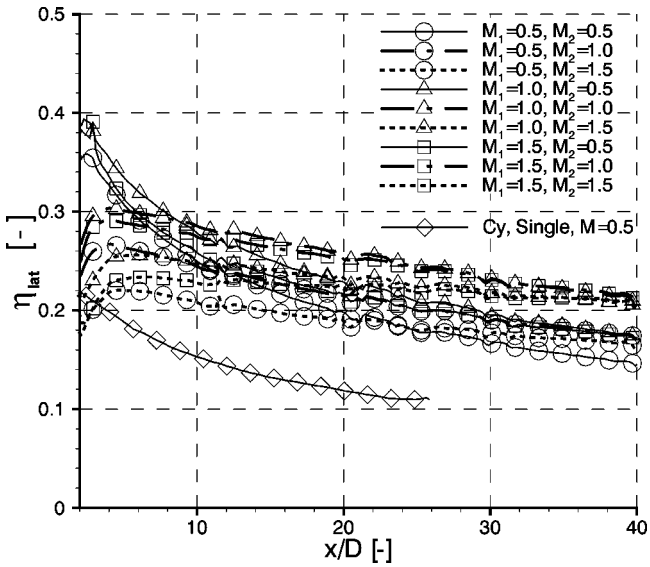


**Fig. 6 Laterally averaged adiabatic effectiveness; first row: cylindrical; second row: cylindrical; spacing: 20*D***

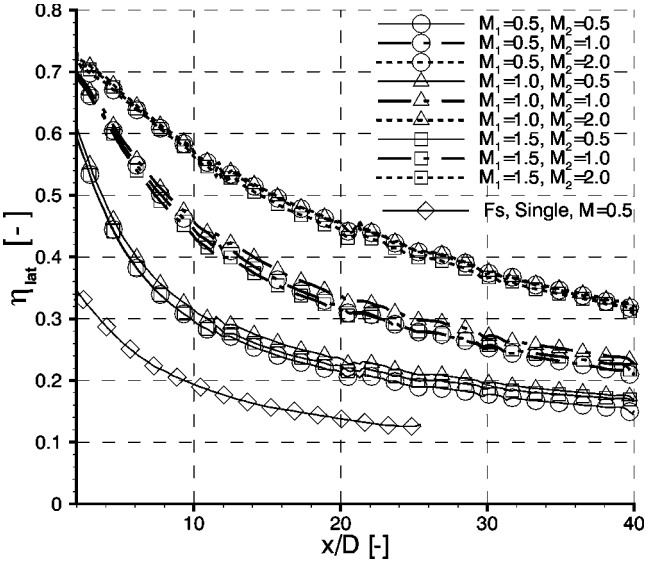


**Fig. 7 Laterally averaged adiabatic effectiveness; first row: cylindrical; second row: fan-shaped; spacing: 20*D***

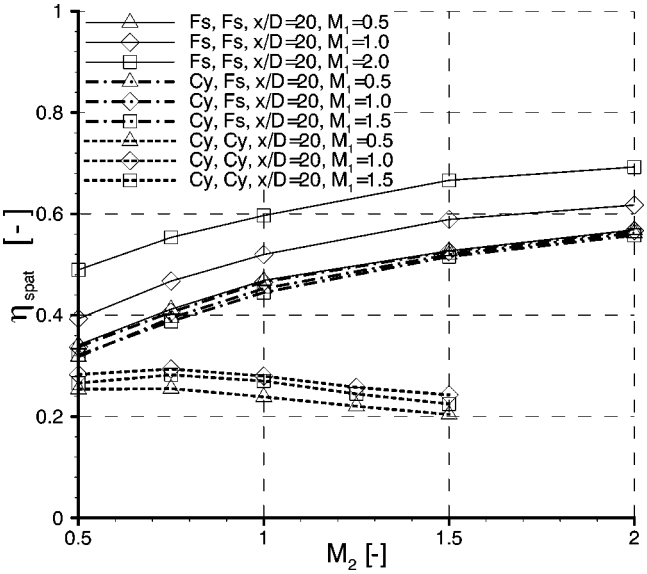


**Fig. 9 Spatially averaged adiabatic film-cooling effectiveness versus downstream row blowing ratio**

downstream of two rows of cylindrical holes a deviation from the optimum blowing ratios does not lead to significant penalties. This is in contrast to the observations made for single row ejection (e.g., [27]), for which usually a pronounced decline of spatially averaged effectiveness due to jet detachment is detected when the blowing ratio is increased beyond the optimum. This finding confirms the previous statement, that larger blowing ratios can be used more effectively with the second row of holes. The fact, that the influence of the first row blowing ratio significantly depends on the geometry of the upstream row of holes is again impressively substantiated by **Fig. 9**. For a combination of an upstream row of cylindrical holes and a downstream row of fanshaped holes, the spatially averaged effectiveness is basically a function of the downstream row blowing ratio. If the first row consists of fan-shaped holes too, the upstream row blowing ratio is an additional important parameter for the film cooling performance downstream of the second ejection location.

The spacing between two rows of cylindrical film-cooling holes has been identified a crucial quantity in previous investigations. In the current study, for the first time, data sets on adiabatic film-cooling effectiveness are presented with varying distances between two rows of fan-shaped holes at otherwise constant conditions, see **Fig. 10**. It can be seen that for a given combination of upstream and downstream row blowing ratio the impact of the spacing is quite significant. By reducing the distance between the two rows of fanshaped holes from 30*D* to 10*D*, an increase of laterally averaged effectiveness of up to 20% is observed. Additionally, when performance downstream of both rows is considered for different combinations of upstream and downstream row blowing ratio, the figure again indicates, that higher coolant mass flow rates are used more effectively with the downstream row of holes.

As already mentioned in the introduction, the widely used superposition approach of Sellers [11] to predict film cooling effec-

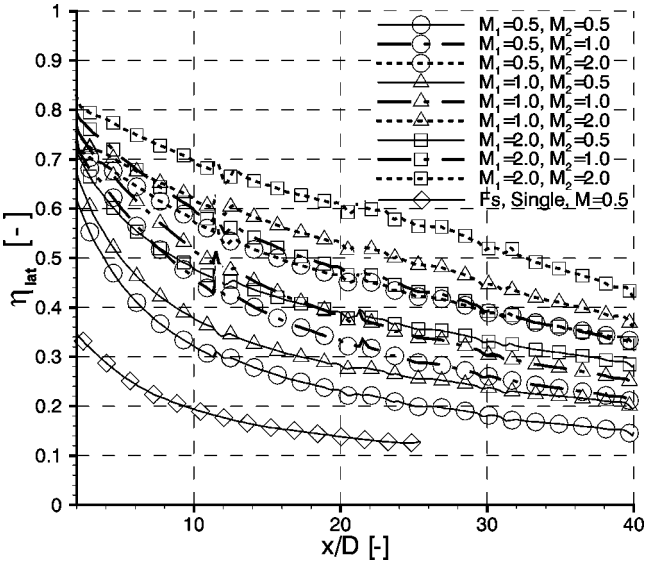


**Fig. 8 Laterally averaged adiabatic effectiveness; first row: fan-shaped; 2nd row: fan-shaped; spacing: 20*D***

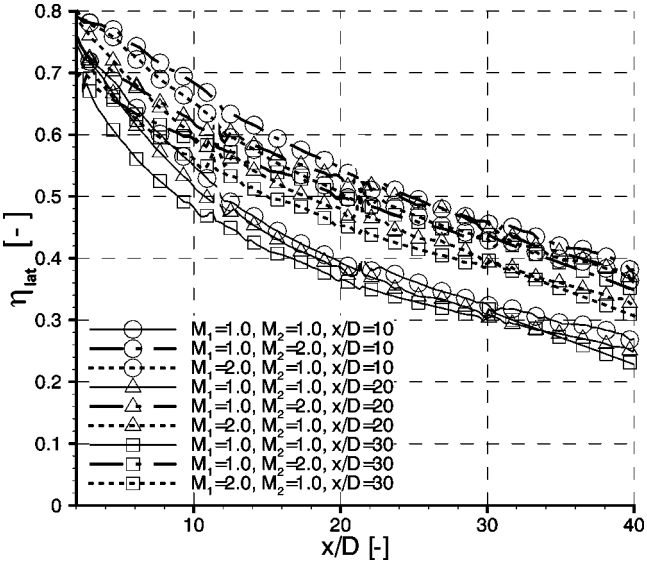


**Fig. 10 Laterally averaged adiabatic effectiveness; first row: fan-shaped; second row: fan-shaped; effect of row spacing**

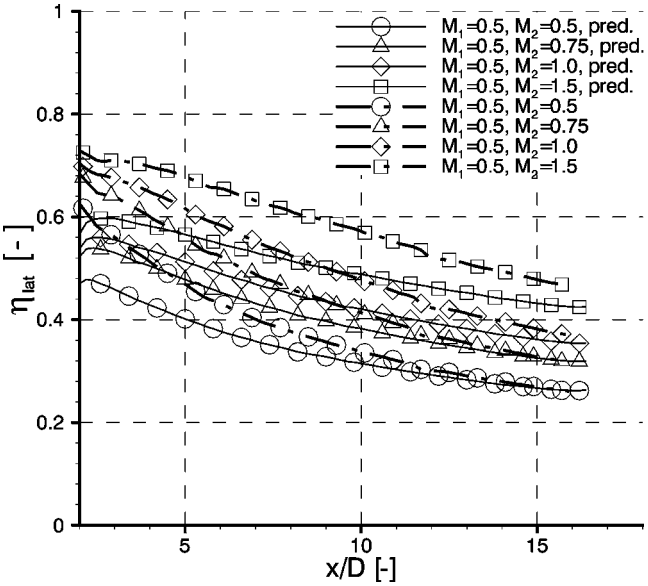


**Fig. 11 Comparison of measured and predicted data; first row: fan-shaped; second row: fan-shaped; spacing: 10*D*, $M_1 = 0.5$**

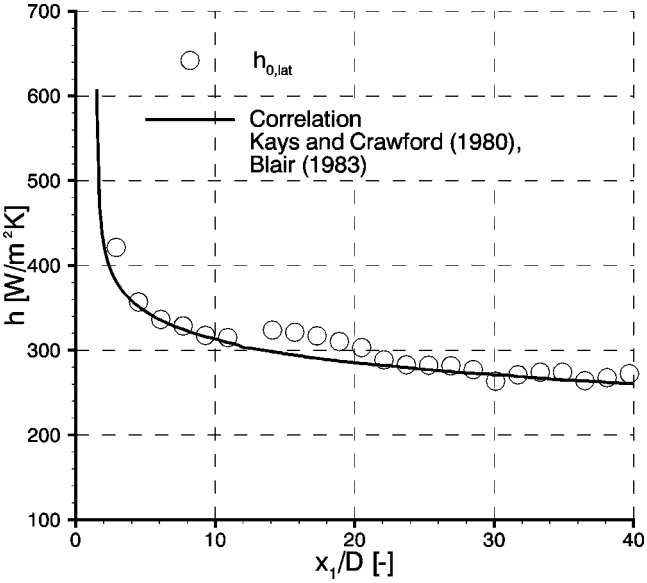


**Fig. 13 Comparison of measured reference heat transfer coefficient $h_0$ with a correlation according to [28,29]**

tiveness downstream of multiple ejection stations has been validated for cylindrical holes and slot film cooling so far. No comparison of measured and predicted data is available in the open literature for several rows of shaped film-cooling holes. An attempt was made to bridge that gap, compare **Figs. 11 and 12**. Since it was expected, that small distances between the two rows are most challenging for the model, the configuration with two rows of fan-shaped holes and a spacing of 10*D* was selected for this purpose. Furthermore, since the region immediately downstream of the second ejection location is most critical, the test of the approach is restricted to this area. As can be seen from **Figs. 11 and 12**, the agreement of predicted and measured data is quite satisfying for small second row blowing ratios and distances more than 10-hole diameters downstream of the second ejection location. Close to the second row, however, differences of up to 25% are detected. Furthermore, it can be stated that the absolute differences increase with increasing second row blowing ratio. The comparison also shows that the model consistently underpredicts the cooling performance. The latter finding implies, that the approach of Sellers might be used with some confidence as long as it can be afforded that the potential of the coolant is not used completely.

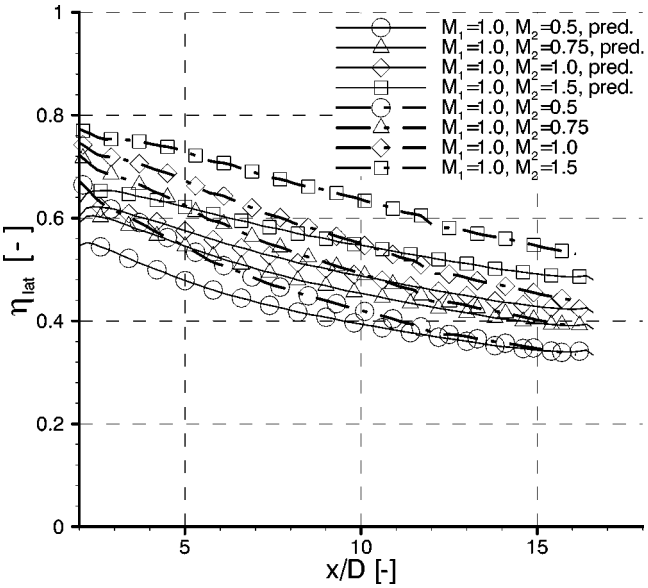


**Fig. 12 Comparison of measured and predicted data; first row: fan-shaped; second row: fan-shaped; spacing: 10*D*, $M_1 = 1.0$**

The results of the heat transfer measurements are presented in terms of laterally averaged heat transfer coefficients with film cooling, $h_f$, normalized with a laterally averaged baseline heat transfer coefficient for the flat plate, $h_0$. The laterally averaged baseline heat transfer coefficients $h_0$ are derived from additional measurements without film cooling. A dummy insert without holes instead of the film-cooling hole specimen is used for these tests in order to avoid disturbances caused by the holes, that can significantly affect the near-wall aerodynamics. In order to validate the experimental approach, the baseline heat transfer coefficients are compared to a correlation for a flat plate with a turbulent boundary layer and unheated starting length given by Kays and Crawford [28], which corresponds to the experimental set up of the current study. To account for the enhanced freestream turbulence level of 5.1% a correction according to Blair [29] is employed. Good agreement of correlation and measured data with maximum deviations of about 10% was found, see **Fig. 13**.

In **Fig. 14** laterally averaged heat transfer coefficient ratios are presented for two rows of cylindrical holes with a spacing of 20-hole diameters. In general, the heat transfer coefficient ratio is enhanced with increasing ejected mass flow rate. Though not shown in the figure, it was found that this is also true when the blowing ratio of the upstream row is increased. However, the impact of the first row blowing ratio is much weaker. Highest values of heat transfer coefficients are detected close to the ejection location. The decline with streamwise distance is not very pronounced, which is in accordance to the results of Ligrani et al. [9]. The latter finding implies, that coolant ejection from a double row of holes affects the boundary layer for quite a long distance from the ejection location. By comparing the data of **Fig. 14** to laterally averaged heat transfer coefficient ratios from single-row ejection (e.g., from Ref. [30]), it becomes apparent, that downstream of two rows of holes higher heat transfer coefficients can be expected. This might be explained by the fact, that due to the staggered arrangement of the rows a larger part of the hot gas flow along the surface is modified and disturbed by the coolant down-

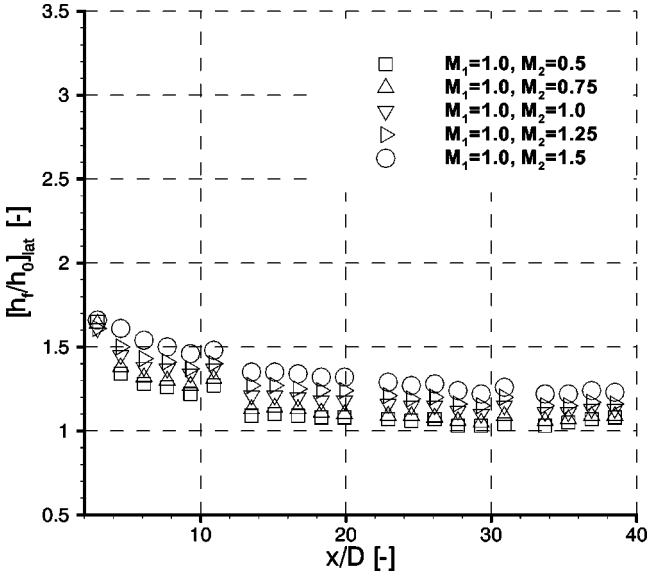


**Fig. 14 Laterally averaged heat transfer coefficient ratios: first row: cylindrical; second row: cylindrical; spacing: 20*D***

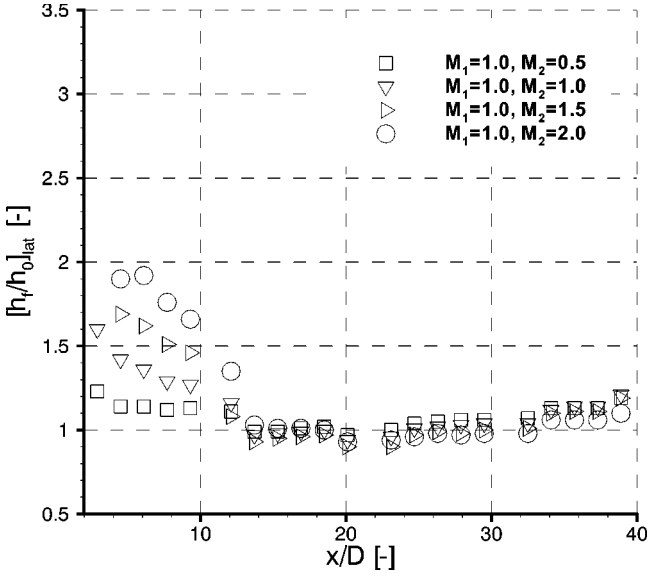


**Fig. 16 Laterally averaged heat transfer coefficient ratios; first row: fan-shaped; second row: fan-shaped; spacing: 20*D***

stream of both rows due to the presence of additional cold air in the midpitch area of the second row. Furthermore, as explained previously, kidney vortices, which result from the upstream row of holes, might generate a secondary flow, that is oriented towards the wall in the region of the downstream coolant ejection. By that, the jets of the second row are eventually pushed onto the surface which results in an intensified contact of coolant and hot gas and higher heat transfer coefficients.

In **Fig. 15** the laterally averaged heat transfer coefficient ratio for an upstream row of cylindrical holes and a downstream row of fan-shaped holes is presented. The spacing between the two rows is likewise 20-hole diameters. Close to the hole exit the heat transfer coefficients are again enhanced with increased ejected mass flow. In comparison to the configuration of **Fig. 14** with two rows of cylindrical holes, higher values for the extrapolated heat transfer coefficient $h_f$ are found close to the hole exit for the same combination of blowing ratios. According to flow field measurements from Thole et al. [31], larger turbulence levels prevail at the exit of a fan-shaped hole in comparison to a cylindrical hole, which might explain the higher heat transfer coefficients in the near-hole region. The cause for the enhanced turbulence intensities at the hole exit is the separation bubble forming inside the diffuser, as discussed in context with **Fig. 5**. Further downstream, however, the heat transfer coefficient ratios decline rapidly, which implies, that the variation of heat transfer coefficient with streamwise distance is much more pronounced as compared to the previous configuration. Additionally, the dependence of heat transfer coefficient ratio on the ejected mass flow rate becomes very small at downstream distances beyond about 15-hole diameters. Though not shown in **Fig. 15**—based on additional measurements—it can be stated that the impact of the upstream row blowing ratio is again much weaker.

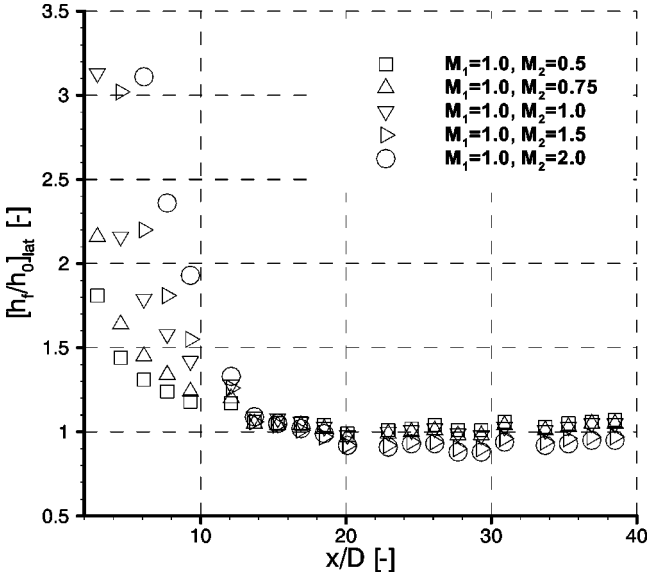


**Fig. 15 Laterally averaged heat transfer coefficient ratios: first row; cylindrical; second row: fan-shaped; spacing: 20*D***

Similar results are found for a combination of two rows of fanshaped holes with a spacing of 20-hole diameters, compare **Fig. 16**. Again, there is a large variation of heat transfer coefficients with the ejected mass flow rate and the distance from the ejection location in the near hole region. Further downstream, however, heat transfer coefficients vary only slightly with streamwise distance and are almost independent of the ejected mass flow rate. In comparison to the configuration of **Fig. 15**, the heat transfer coefficients are smaller, which appears to be surprising from a first glance. In order to better understand this experimental result, supplementary CFD calculations are performed using Fluent 6© by Fluent© Inc.. The computational domain starts 8.5 $D$ upstream of the first ejection location and extends 21 $D$ downstream of the second row of holes. The central pitch of the second row is modeled. With the exception of the integral length scale, the boundary conditions are consistent to the experiments, see **Table 1**. Turbulence modeling is achieved using a realizeable $k$-$\varepsilon$ model with two layer wall treatment. The near wall region is very accurately resolved with $y^+$ values of unity, leading to an overall grid size of 1.6 million hexahedral cells. Parallel computations are run on four machines with together eight CPUs and 8 GB RAM. The velocity vectors presented in **Fig. 17** are used to explain the experimental observations. By comparing the size and location of the kidney vortices downstream of the coolant ejection ($x=2D$) it is evident, that they are more stretched out in lateral direction in case of an upstream row of cylindrical holes. Furthermore, the vertical velocities in the center ($y=0$) are smaller for the configuration with an upstream row of cylindrical holes. Both findings imply, that the

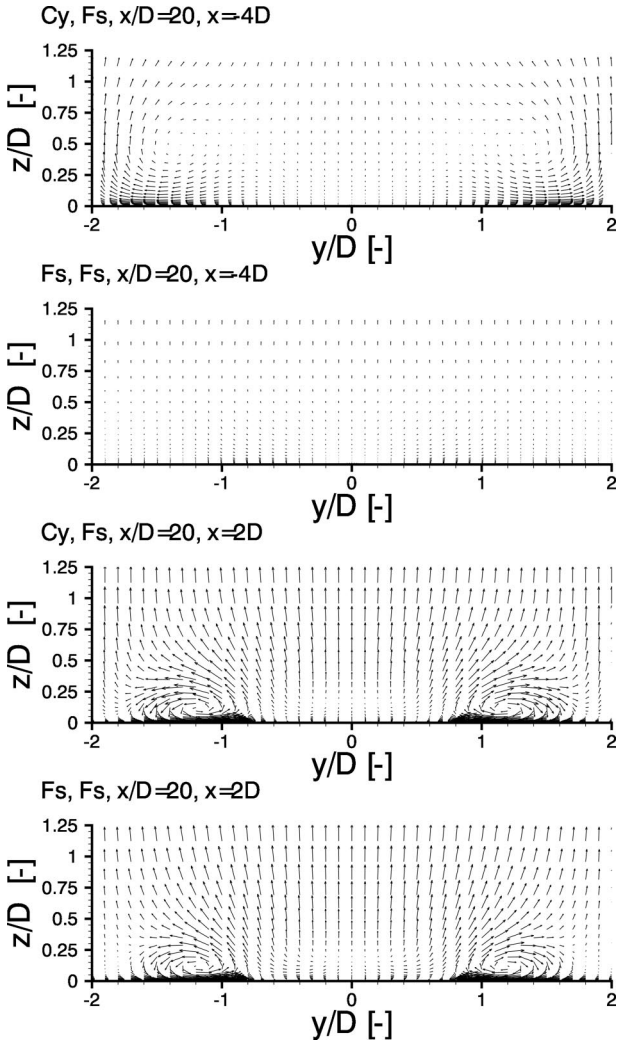


**Fig. 17 Velocity vectors in a lateral-normal place 4*D* upstream and 2*D* downstream of the second row for $M_1=1.0$ and $M_2=0.5$**

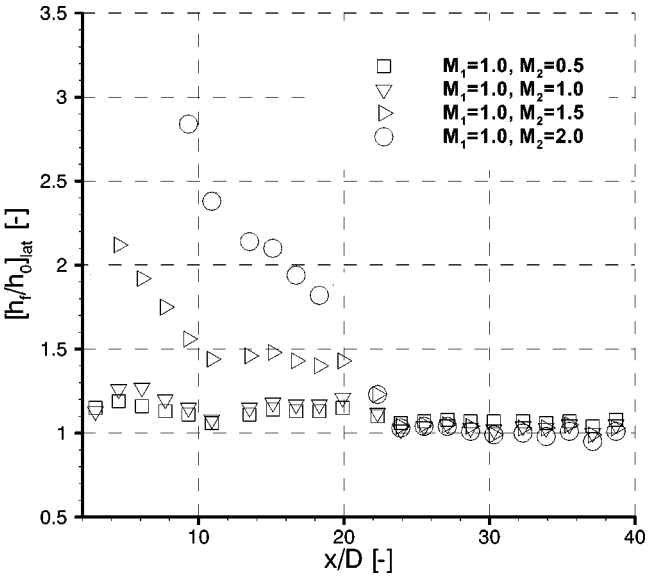


**Fig. 18 Laterally averaged heat transfer coefficient ratios; first row: fan-shaped; second row: fan-shaped; spacing: 10*D***

strength of the vortex motion upstream of the second ejection location and the resulting secondary flow towards the wall is more intense in case of an upstream row of cylindrical holes, which is confirmed by the corresponding vector plots in a plane just upstream the coolant ejection ($x=-4D$). This, however, leads to an intensified contact of second row coolant with the wall, resulting in higher heat transfer coefficients. Furthermore, though not shown in **Fig. 17**, it is observed that the CFD prediction indicates higher near-wall velocities and higher velocity gradients in case of an upstream row of cylindrical holes. This again substantiates and partially explains the higher heat transfer coefficients found in the experiments for this configuration.

From the results of **Figs. 14–16** it can be concluded that similar to the corresponding film cooling effectiveness results, the heat transfer coefficients seem to be dominated by the geometry and the blowing ratio of the downstream row of holes. Reducing the spacing between two rows of fan-shaped holes increases the area downstream of the second ejection location where higher heat transfer coefficients prevail, see **Fig. 18**. Additionally, the level of the heat transfer coefficient ratio is increased at moderate to high blowing ratios. It can be expected that this detrimental effect at least partially compensates the increased effectiveness levels due to a reduced spacing, which have been presented in **Fig. 10**.

## Conclusions

An experimental study has been performed to investigate the interaction of film cooling rows. Fan-shaped holes or simple cylindrical holes with an inclination angle of 30 deg and a hole length of 6-hole diameters have been used. Operating conditions have been varied in terms of blowing ratio for the upstream and—independently—the downstream row in the range $0.5<M<2.0$. The key findings of this study can be summarized as follows:

- Film-cooling performance downstream of two rows of holes is dominated by the second row hole shape and blowing ratio.
- Due to the coolant ejection by an upstream row film cooling effectiveness is significantly increased downstream of the second ejection location.
- For two rows of cylindrical holes a second row blowing ratio in the range of $M_2=0.75$ leads to optimum performance. In contrast to single-row ejection, deviations from this optimum have only moderate impacts on film-cooling performance in the near hole region. For that reason, higher blowing ratios can be used with the downstream row more effectively. The latter statement is also valid, if the downstream and/or upstream row consists of fan-shaped holes. The advantage of higher second row blowing ratios is, that the area of adequate cooling can be extended further in streamwise direction.
- If the downstream row consists of fan-shaped holes no distinct optimum for the second row blowing ratio is found within the range investigated ($M<=2.0$). Film cooling effectiveness is continuously improved with increasing downstream row blowing ratio.
- The effect of decreasing the spacing between two rows of fanshaped holes on film cooling performance will be small, since both film cooling effectiveness and heat transfer coefficient ratios are increased simultaneously.
- The superposition approach of Sellers [11] leads to satisfying agreement between measured and predicted data for two rows of fan-shaped holes for low blowing ratios in regions more than 10*D* downstream of the second ejection location. Close to the second row of holes the model consistently underpredicts the measured film-cooling effectiveness by up to 25%.

## Acknowledgements

This study was partly funded by the European Union through grant by the BRITE EURAM program ''Turbine Aero-Thermal External Flows'' under Contract No. BRPR-CT97-0519.

## Nomenclature

$D$ = film-cooling hole diameter
$h(\theta)$ = heat transfer coefficient according to Eq. (3)
$h_f$ = heat transfer coefficient with film cooling
$h_0$ = heat transfer coefficient without film cooling
$L$ = film-cooling hole length measured along the centerline
$M$ = blowing ratio: $(\rho_c u_c)/(\rho_m u_m)$
Ma = Mach number
$\dot{m}_c$ = mass flow rate through film-cooling hole
$P$ = pitch
$p_m$ = static pressure hot gas
$p_{tc}$ = total pressure coolant
$T_{aw}$ = adiabatic wall temperature
$T_{\mathrm{rec},m}$ = recovery temperature hot gas
$T_{tc}$ = total temperature coolant
$Tu$ = turbulence intensity
$x$ = streamwise distance from 2nd ejection location
$x_1$ = streamwise distance from end of uncooled starting length
$y$ = lateral coordinate
$\theta$ = dimensionless temperature ratio (Eq. (4))
$\rho_c$ = coolant density
$\rho_m$ = hot gas density
$\eta_{aw}$ = adiabatic film cooling effectiveness
$\eta_{\mathrm{lat}}$ = laterally averaged adiabatic film cooling effectiveness
$\eta_{\mathrm{spat}}$ = spatially averaged adiabatic film cooling effectiveness

## References

[1] Ames, F. E., 1998, ''Aspects of Vane Film Cooling With High Turbulence—Part I: Heat Transfer,'' ASME J. Turbomach., **120**, pp. 768–776.
[2] Muska, J. F., Fish, R. W., and Suo, M., 1976, ''The Additive Nature of Film Cooling From Rows of Holes,'' ASME J. Eng. Gas Turbines Power, **98**, pp. 457–463.
[3] Jabbari, M. Y., and Goldstein, R. J., 1978, ''Adiabatic Wall Temperature and Heat Transfer Downstream of Injection Through Two Rows of Holes,'' ASME J. Eng. Gas Turbines Power, **100**, pp. 303–307.
[4] Sinha, A. K., Bogard, D. G., and Crawford, M. E., 1991, ''Gas Turbine Film Cooling: Flowfield due to a Second Row of Holes,'' ASME J. Turbomach., **113**, pp. 450–456.
[5] Jubran, B. A., and Brown, A., 1985, ''Film Cooling From Two Rows of Holes Inclined in the Streamwise and Spanwise Directions,'' ASME J. Turbomach., **107**, pp. 84–91.
[6] Jubran, B. A., and Maiteh, B. Y., 1999, ''Film Cooling and Heat Transfer from a Combination of Two Rows of Simple and/or Compound Angle Holes in Inline and/or Staggered Configuration,'' Heat and Mass Transfer, **34**, pp. 495–502.
[7] Afejuku, W. O., Hay, N., and Lampard, D., 1983, ''Measured Coolant Distributions Downstream of Single and Double Rows of Film Cooling Holes,'' ASME J. Eng. Gas Turbines Power, **105**, pp. 172–177.
[8] Afejuku, W. O., Hay, N., and Lampard, D., 1980, ''The Film Cooling Effectiveness of Double Rows of Holes,'' ASME J. Eng. Gas Turbines Power, **102**, pp. 601–606.
[9] Ligrani, P. M., Ciriello, S., and Bishop, D. T., 1992, ''Heat Transfer, Adiabatic Effectiveness, and Injectant Distributions Downstream of a Single Row and Two Staggered Rows of Compound Angle Film-Cooling Holes,'' ASME J. Turbomach., **114**, pp. 687–700.
[10] Ligrani, P. M., and Ramsey, A. E., 1995, ''Film Cooling From Spanwise Oriented Holes in Two Staggered Rows,'' ASME Paper No. 95-GT-39.
[11] Sellers, J. P., 1963, ''Gaseous Film Cooling With Multiple Injection Stations,'' AIAA J., **1**(9), pp. 2154–2156.
[12] Mayle, R. E., and Camarata, F. J., 1975, ''Multihole Cooling Film Effectiveness and Heat Transfer,'' ASME J. Heat Transfer, **97**, pp. 534–538.
[13] Sasaki, M., Takahara, K., Kumagai, T., and Hamano, M., 1979, ''Film Cooling Effectiveness for Injection for Multirow Holes,'' ASME J. Eng. Gas Turbines Power, **101**, pp. 101–108.
[14] Harrington, M. K., McWaters, M. A., Bogard, D., Lemmon, C. A., and Thole, K. A., 2001, ''Full-Coverage Film Cooling With Short Normal Injection Holes,'' ASME Paper No. 2001-GT-0130.
[15] Metzger, D. E., and Fletcher, D. D., 1971, ''Evaluation of Heat Transfer for Film-Cooled Turbine Components,'' J. Aircr., **8**, pp. 33–38.
[16] Choe, H., Kays, W. M., and Moffat, R. J., 1974, ''The Superposition Approach to Film Cooling,'' ASME Paper No. 74-WA/HT-27.
[17] Eckert, E. R. G., 1984, ''Analysis of Film Cooling and Full-Coverage Film Cooling of Gas Turbine Blades,'' ASME J. Eng. Gas Turbines Power, **106**, pp. 207–213.
[18] Forth, C. J. P., Loftus, P. J., and Jones, T. V., 1985, ''The Effect of Density Ratio on the Film Cooling of a Flat Plate,'' *Heat Transfer and Cooling in Gas Turbines*, AGARD-CP-390, Paper 10.
[19] Teekaram, A. J. H., Forth, C. J. P., and Jones, T. V., 1989, ''The Use of Foreign Gas to Simulate the Effects of Density Ratios in Film Cooling,'' ASME J. Turbomach., **111**, pp. 57–62.
[20] Gritsch, M., Schulz, A., and Wittig, S., 1998, ''Adiabatic Wall Effectiveness Measurements of Film-Cooling Holes With Expanded Exits,'' ASME J. Turbomach., **120**, pp. 568–574.
[21] Baldauf, S., Schulz, A., and Wittig, S., 2001, ''High Resolution Measurements of Local Effectiveness by Discrete Hole Film Cooling,'' ASME J. Turbomach., **123**, pp. 758–765.
[22] Martiny, M., Schiele, R., Gritsch, M., Schulz, A., and Wittig, S., 1996, ''In Situ Calibration for Quantitative Infrared Thermography,'' QIRT '96 Eurotherm Seminar No. 50, Stuttgart, Germany, Sept. 2–5.
[23] Kline, S. J., and McClintock, F. A., 1953, ''Describing Uncertainties in Single Sample Experiments,'' Mech. Eng. (Am. Soc. Mech. Eng.), **75**, pp. 3–8.
[24] Bons, J. P., MacArthur, C. D., and Rivir, R. B., 1996, ''The Effect of High Free-Stream Turbulence on Film Cooling Effectiveness,'' ASME J. Turbomach., **118**, pp. 814–825.
[25] Schmidt, D. L., and Bogard, D. G., 1996, ''Effects of Free-Stream Turbulence and Surface Roughness on Film Cooling,'' ASME Paper No. 96-GT-462.
[26] Lutum, E., von Wolfersdorf, J., Weigand, B., and Semmler, K., 2000, ''Film Cooling on a Convex Surface With Zero Pressure Gradient Flow,'' Int. J. Heat Mass Transfer, **43**, pp. 2973–2987.
[27] Saumweber, C., Schulz, A., and Wittig, S., 2003, ''Free-Stream Turbulence Effects on Film Cooling With Shaped Holes,'' ASME J. Turbomach., **125**, pp. 65–73.
[28] Kays, W. M., and Crawford, M. E., 1980, *Convective Heat and Mass Transfer*, McGraw-Hill, New York.
[29] Blair, M. F., 1983, ''Influence of Free-Stream Turbulence on Turbulent Boundary Layer Heat Transfer, Part I and II,'' ASME J. Heat Transfer, **105**, pp. 33–47.
[30] Baldauf, S., Scheurlen, M., Schulz, A., and Wittig, S., 2002, ''Heat Flux Reduction From Film Cooling and Correlation of Heat Transfer Coefficients From Thermographic Measurements at Engine Like Conditions,'' ASME J. Turbomach., **124**, pp. 699–709.
[31] Thole, K., Gritsch, M., Schulz, A., and Wittig, S., 1998, ''Flow Field Measurements for Film Cooling Holes With Expanded Exits,'' ASME J. Turbomach., **120**, pp. 327–336.

# A Technique for Processing Transient Heat Transfer, Liquid Crystal Experiments in the Presence of Lateral Conduction

**John P. C. W. Ling**
e-mail: john.ling@eng.ox.ac.uk

**Peter T. Ireland**

Department of Engineering Science,
University of Oxford,
Parks Road,
Oxford, OX1 3PJ, UK

**Lynne Turner**
Rolls-Royce plc.,
P.O. Box 3, Filton,
Bristol, BS34 7QE, UK
e-mail: lynne.turner@rolls-royce.com

*New techniques for processing transient liquid crystal heat transfer experiment have been developed. The methods are able to measure detailed local heat transfer coefficient and adiabatic wall temperature in a three temperature system from a single transient test using the full intensity history recorded. Transient liquid crystal processing methods invariably assume that lateral conduction is negligible and so the heat conduction process can be considered one-dimensional into the substrate. However, in regions with high temperature variation such as immediately downstream of a film-cooling hole, it is found that lateral conduction can become significant. For this reason, a procedure which allows for conduction in three dimensions was developed by the authors. The paper is the first report of a means of correcting data from the transient heat transfer liquid crystal experiments for the effects of significant lateral conduction. The technique was applied to a film cooling system as an example and a detailed uncertainty analysis performed.*
[DOI: 10.1115/1.1740777]

## Introduction

Thermochromic liquid crystals (TLC) have been widely used in experimental heat transfer studies because of their ability to obtain full-surface temperature measurement accurately. Liquid crystal techniques are also more economical than multiple surface thermocouples measurements and (unlike IR imaging) can be used on the inside surfaces of wind tunnels without expensive IR thermal images or special windows. Liquid crystals are used in both steady-state and transient heat transfer measurement techniques. Steady-state heat transfer techniques have been developed by numerous researchers such as Den Ouden and Hoogendoorn [1], Cooper et al. [2], Baughn et al. [3], Lucas et al. [4], Sargison et al. [5], etc.

Transient tests offer full coverage data from a single test and can produce high resolution data faster than alternative methods. Transient techniques also make experiments with narrow band liquid crystals easier to process. It is more desirable to use several narrow band liquid crystals to obtain multiple temperature signals by the means of color intensity rather than the hue signals of the wide band crystals because of problems in viewing angle, lighting, and internal reflection. Ireland et al. [6,7] have described the basic transient liquid technique in detail. In such heat transfer experiments, a test piece is exposed to a sudden rise or drop in the freestream temperature. The normal assumptions are that the test piece is a semi-infinite solid and that the transient temperature response is governed by the heat conducting one-dimensionally into the model. An experiment is classified as a two temperature system when the thermal boundary conditions are set by a single gas temperature and the wall temperature. A liquid crystal coating is applied to the surface exposed to the flow. A video camera records the color play while the model temperature starts to change. The color play data yields the temperature history of the model surface and hence the local heat transfer coefficient distribution. Much effort (Wang et al. [8,9], Lucas et al. [10], van Treuren et al. [11], Son et al. [12], etc.) has been expended in the advancement of transient liquid crystal methods. Recent developments have included changes in the form of the variation of the gas temperature throughout the experiment to include a series of steps (Baughn et al. [13]).

Transient liquid crystal techniques are also widely used in three-temperature systems (e.g., where boundary conditions are set by the freestream temperature, wall temperature, and injection temperature), such as film-cooling heat transfer experiments. Because the heat transfer coefficient and the film-cooling effectiveness in film cooling tests are both unknown at every measurement location, two equations need to be solved for the two parameters. This can be implemented by either carrying out a multiple test strategy or by applying a mixture of two or more carefully chosen liquid crystals to the model surface (Ireland and Jones [14]) while keeping the problem well conditioned. Vedula and Metzger [15] proposed a two-test strategy for film-cooling configurations in which two experimental tests were performed with different local fluid temperatures, to determine both the film-cooling and heat transfer distributions by altering the fixed mainstream and injection flow temperature. Chambers et al. [16] further developed the idea to a three-test strategy for experiments with a significant range of heat transfer coefficient. Earlier, Wang et al. [9] had developed the ''temperature history matching technique'' to find both parameters from one single test. This applied a regression method to select heat transfer and adiabatic wall temperature values to minimize the sum of the squared differences between the measured surface temperature and a semi-infinite transient conduction model.

All the transient techniques mentioned above assume that heat conduction can be considered one-dimensional. However, in regions where large temperature variations occur or when the test duration is long, lateral conduction becomes significant and the one-dimensional heat equation is not applicable. A few workers have presented methods of overcoming problems of lateral conduction in associated methods. Walker et al. [17–19] gave an overview of the existing estimation methods and proposed a two-dimensional inverse heat conduction method to evaluate high unsteady heat fluxes in supersonic flow. They corrected the results from multiple heat flux gauges by iteratively refining a guessed $h$ distribution. Lin and Wang [20] suggested that under some condi-

Contributed by the International Gas Turbine Institute and presented at the International Gas Turbine and Aeroengine Congress and Exhibition, Atlanta, GA, June 16–19, 2003. Manuscript received by the IGTI Dec. 2002; final revision Mar. 2003. Paper No. 2003-GT-38446. Review Chair: H. R. Simmons.

  

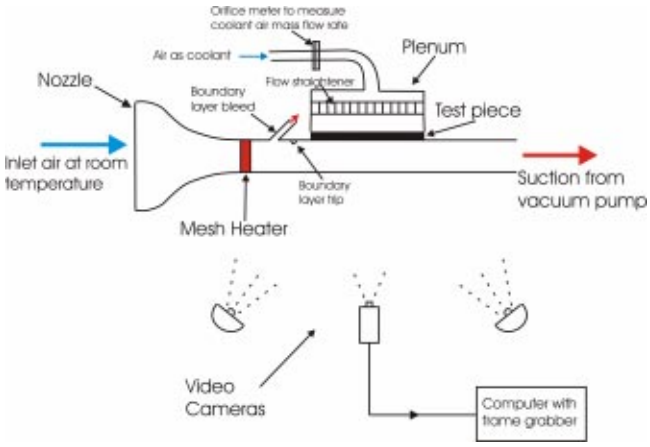


**Fig. 1 Film cooling experimental setup**

tions results using the one-dimensional analysis were 15–20% higher than using the three-dimensional conduction technique. They presented a hue-angle transient liquid crystal technique using electrical heater and a three-dimensional inverse transient conduction scheme. However, these methods were only developed to measure heat transfer in two temperature systems and are not of direct application to the conventional transient liquid crystal method. Saumweber et al. [21] used full-surface temperature data from an IR camera as a boundary condition in a finite element model of the surface but for a steady-state experiment.

The present paper details the authors' development of a transient narrow-band liquid crystal technique to overcome problems in using wideband liquid crystals and the lack of robustness in three temperature system measurements. The new technique also corrects errors cause by lateral conduction in a computationally efficient way. The first part of this paper described a technique to measure both the heat transfer coefficient and adiabatic wall temperature of a three-temperature system from a single test in the absence of lateral conduction. The second part reports a three-dimensional direct numerical method to measure these parameters when effect of lateral conduction becomes significant. A simple film-cooling experiment was employed to demonstrate the technique on a three-temperature system and an uncertainty analysis was reported.

## Description of the Experimental Facility and the Procedure

A series of film cooling experiments was performed in a test rig section built into one side of a suction type wind tunnel shown in **Fig. 1**. The engine flow fields were characterized by low Mach number and the investigation was performed using air as freestream and coolant at low speed.

Air is drawn through the test section at nominal velocity of 16 m/s. The test section was manufactured from perspex plate which has a rectangular shape of 160 mm by 57 mm. The air was guided into the test section by the inlet contraction. The mesh heater (Gillespie [22]) was electrically powered and provided a near step change increase in the freestream temperature of up to 70°C. A boundary layer bleed followed by a boundary layer trip were placed after the heater mesh and before the test piece to produce repeatable, known test conditions of a turbulent boundary layer. The test piece consisted of one single film-cooling hole. The hole has a diameter of 3 mm and was inclined at 20° to the surface of the test plate, as shown in **Fig. 2**. The test plate was 16 mm thick, and hence with a test duration time of no more than 45 s, a semi-infinite wall analysis could be used.

The coolant flow (air) to the film cooling holes was supplied via a British Standard orifice meter to a plenum and through a flow

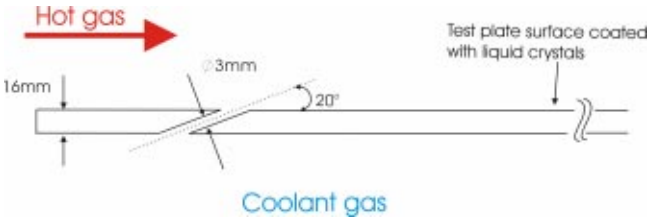


**Fig. 2 Section of the test plate**

straightener. The coolant is at room temperature and therefore the coolant to freestream flow density ratio is about 1.17.

The test plates were first coated with a layer of black ink on top of the perspex to eliminate transmitted light. A layer comprising a mixture of three liquid crystals was applied on top. The mixture contains liquid crystal materials BM/R25C1W/S40, BM/R30C1W/S40 and BM/R33C1W/S40 supplied by Hallcrest Limited. A foil type-T thermocouple was glued to the surface before the ink and the liquid crystal were applied. This was used to measure the starting temperature of the test plate for each test and to calibrate the liquid crystal coating. A video camera was positioned to record the liquid crystal color change during the test. After the experiment, a frame grabber was used to capture the image signals at a rate of 25 frames per second and to convert the VHS format tapes to digital BMP format. The captured frames were next converted to raw red, blue and green signals using software written in MATLAB.

Each transient test began when the heater mesh was switched on. Simultaneously, the video camera captured the liquid crystal color change. A data logger was used to record the transient temperature history of freestream gas and coolant injection flow measured using fast response thermocouples.

## Theory and Processing Technique

Film cooling is a conventional three temperature system where the thermal boundary conditions are set by the freestream gas temperature $T_{gas}$, the wall surface temperature, $T_w$, and the coolant temperature, $T_c$, as illustrated in **Fig. 3**.

In a transient heat transfer experiment, if we assume that the heat conduction process is one-dimensional into a semi-infinite substance, the heat conduction model can be mathematically described by the Fourier equation

$$\frac{\partial^2 T}{\partial z^2} = \frac{1}{\alpha}\frac{\partial T}{\partial t}. \tag{1}$$

With initial conditions

$$T = T_o \quad \text{when} \quad t = 0.$$

The boundary conditions are

$$-k\frac{\partial T}{\partial z} = h(T_{aw} - T_w) \quad \text{when} \quad z = 0; \tag{2}$$

and

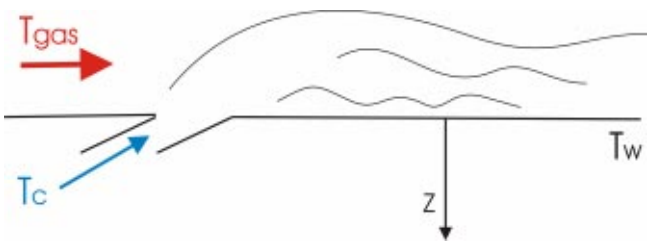


**Fig. 3 Film cooling**

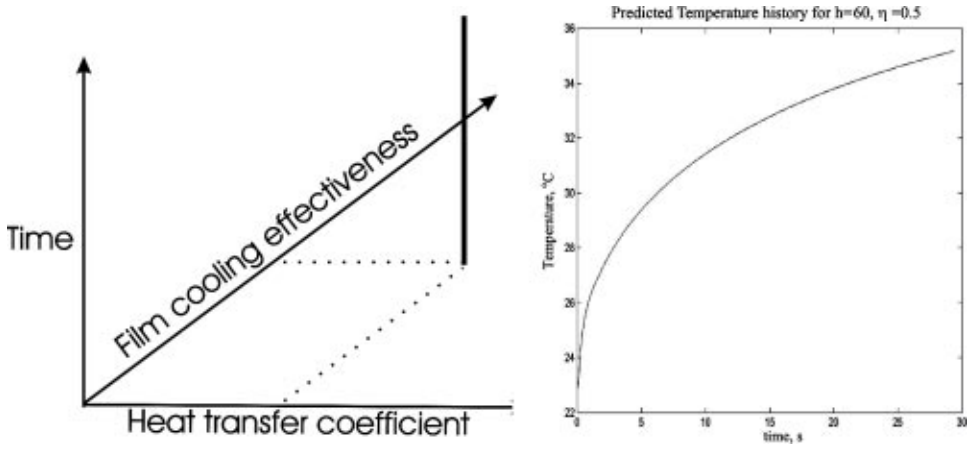


**Fig. 4 Three-dimensional surface temperature lookup table**

$$T = T_o \quad \text{when} \quad z \to \infty.$$

$T_{aw}$ is the adiabatic wall temperature and $T_o$ is the initial wall temperature. With a step change in fluid temperature, the surface temperature, $T_w$, is given by

$$\frac{T_w - T_o}{T_{aw} - T_o} = 1 - \exp(\beta^2)\operatorname{erfc}(\beta) \tag{3}$$

where

$$\beta = \frac{h\sqrt{t}}{\sqrt{\rho c k}}. \tag{4}$$

If we define the dimensionless adiabatic wall temperature (or film cooling effectiveness) as

$$\eta = \frac{T_{aw} - T_{\text{gas}}}{T_c - T_{\text{gas}}}, \tag{5}$$

by substituting for $T_{aw}$ using Eq. (5) into Eq. (3)

$$\frac{T_w(t) - T_o}{\eta(T_c - T_{\text{gas}}) + T_{\text{gas}} - T_o} = 1 - \exp(\beta^2)\operatorname{erfc}(\beta). \tag{6}$$

As the values of $T_o$, $T_c$, $T_{\text{gas}}$ and $\sqrt{\rho c k}$ are known for any experiment the surface temperature history $(T_w(t))$ can be calculated given specific values of $h$ and $\eta$ using Eq. (6). This allows a search routine to select $h$ and $\eta$ to minimize the sum of the squared differences between the measured green signal and a predicted signal as described below. The image processing software first calculates all such surface temperature variations for permutations of $h$ and $\eta$. **Figure 4** illustrates the process. In practice $h$ was divided into 70 logarithmically incremented steps and $\eta$ into 20 equally divided steps. Location on the lower heat transfer coefficient, film-cooling effectiveness plane is determined by the guessed values of $h$ and $\eta$. The surface temperature then varies along the vertical bold line with time as shown in the plot on the right.

The search routine adopted, which considers a set of permutations, was found to be faster than alternative routines and the results more easily interpreted as the method developed.

In fact, as the batteries used to supply power to the heater mesh aged, the gas temperature change began to deviate from a simple step. The differential equation for temperature was solved under conditions of a ramp change in gas temperature. **Figure 5** describes the method of ramps graphically. The gas temperature change was represented as a single step combined with a series of summed and delayed ramps. The equation for surface temperature can be rewritten as

$$T_w = T_o + T_{\text{step}} + \sum_{i=1}^{n} m_i U(t - t_i) \tag{7}$$

where

$$T_{\text{step}} = (T_{\text{gas}_o} - T_o)[1 - e^{\beta^2}\operatorname{erfc}(\beta)] \quad \text{with} \quad \beta = \frac{h\sqrt{t}}{\sqrt{\rho c k}}. \tag{8}$$

$m_i$ is the gradient of each ramp in the series, and

$$U(t - t_i) = (t - t_i)\left[1 - \frac{2}{\beta'\sqrt{\pi}} + \frac{1 - e^{\beta'^2}\operatorname{erfc}(\beta')}{\beta'^2}\right] \tag{9}$$

with

$$\beta' = \frac{h\sqrt{t - t_i}}{\sqrt{\rho c k}}.$$

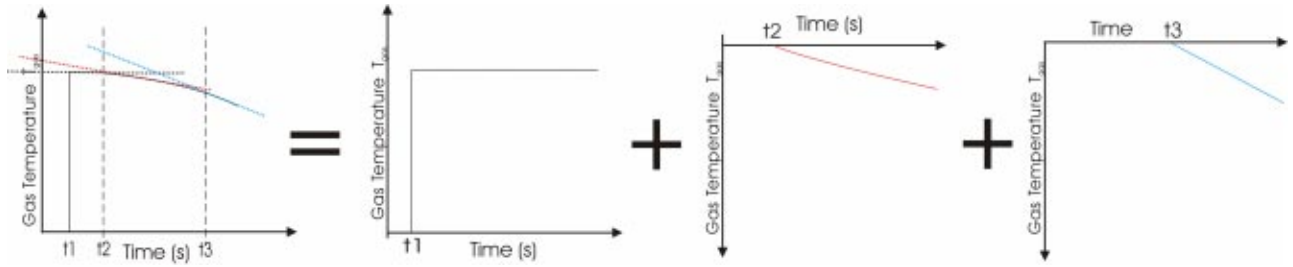


**Fig. 5 Method of ramps**

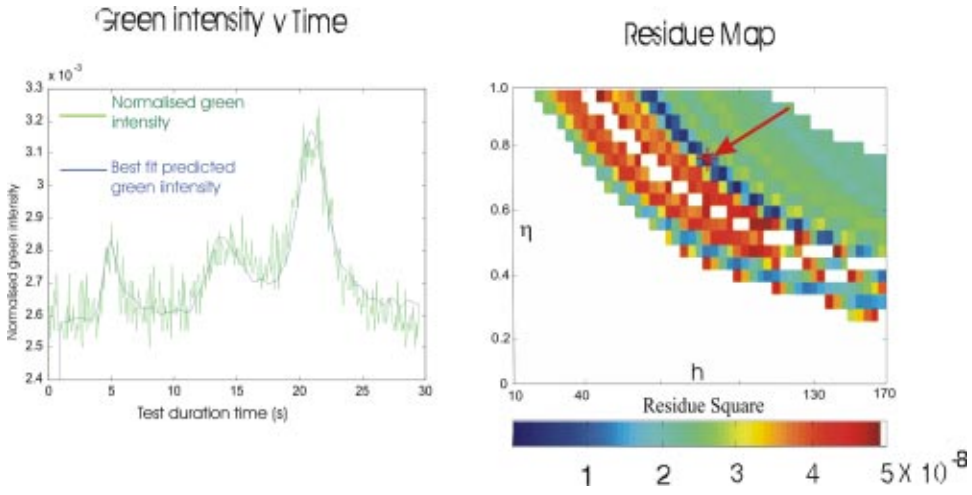


**Fig. 6 The least-squares regression technique**

Both the measured gas temperature and measured coolant temperature were represented by synchronized superposed and delayed ramps.

A predicted surface temperature history for any particular value of $h$ and $\eta$ can be extracted from the three-dimensional matrix, as indicated by the diagram on the right of **Fig. 4**. For simplicity, this three-dimensional surface temperature history matrix will be called $T_{predict}$. $T_{predict}$ is used in the regression analysis explained below.

## Liquid Crystal Color Signal Analysis

After the calibration was determined, all the predicted temperature histories in $T_{predict}$ were combined with the liquid crystal calibration to create a three-dimensional predicted green intensity lookup table. Each theoretical green intensity history in this three-dimensional lookup table was normalized by dividing the sum of the theoretical green signals for each samples for the duration of the analysis. In other words, each element in the block shown in **Fig. 4** is divided by the sum of all the elements in the vertical column (meaning same $h$ and $\eta$) that includes the element. The normalized signals are stored in the new three-dimensional array denoted **S**. Exactly the same process of normalization was carried out for the measured green signals for every pixel. This experimental normalized green intensity level was stored in a three-dimensional matrix with the same size as **S**, and the former is referred to as **G**. After normalization, the normalized green intensity signal should rise from the same base level and reach the same intensity peak level for all the pixels reaching the same temperature, and hence least regression can be applied directly between **S** and **G** to determine the most like combination of $h$ and $\eta$. The least square regression is used to select the two parameters ($h$ and $\eta$) that minimize the sum of the square differences between the measured normalized green intensity in **G** and the predicted normalized signals in **S**. The right pair of $h$ and $\eta$ generates a predicted surface temperature history that best fits the experimental temperature data for every pixel. The least-square regression gives the

$$\text{Minimum}[\text{sum}((\mathbf{G}-\mathbf{S})^2)]. \tag{10}$$

An example of best fit is illustrated in **Fig. 6**. The plot on the left shows the best fit predicted normalized green intensity matching on the experimental signal for a particular pixel. The diagram on the right represents a residue map for all combination of $h$ and $\eta$, where residue is the sum of $(\mathbf{G}-\mathbf{S})^2$. The left plot in **Fig. 6** indicates some advantages of the regression method over the multiple peak detection method used in other heat transfer experiments. The noise on the signal would make it difficult to detect the location of peaks for the green signal shown above. With the new regression method, the fitting process is strongly influenced by the location of the large slopes of the normalized green signal rather than the peak positions. This image processing method uses the full time history of the liquid crystal data and does not rely on identification of discrete features such as intensity peaks. The method allows analysis of noisy data, such as the above, because of the wide range of data points that are compared in the regression sum as opposed to analysis of just three peaks.

The diagram on the right of **Fig. 6** represents the residue levels for all combination of $h$ (along the horizontal axis) and $\eta$ (vertical axis). All residue values above a limit (i.e., particularly poor fits) were rejected and appear as white in the final $h$ and $\eta$ contours. The red cross indicates the position of the smallest residue and hence the best fit.

## Three-Dimensional Conduction Technique Development

When analyzing in detail the surface immediately downstream of the film cooling hole, the authors found that heat conducted in the $x$ (aligned with a hole axis and in same direction as the freestream) and $y$ (across the hole and perpendicular to the freestream) directions could not be neglected. The coordinate system is shown in **Fig. 7**.

Consider the three-dimensional transient conduction equation

$$\frac{\partial^2 T}{\partial x^2}+\frac{\partial^2 T}{\partial y^2}+\frac{\partial^2 T}{\partial z^2}=\frac{1}{\alpha}\frac{\partial T}{\partial t}. \tag{11}$$

Heat conduction can only be assumed to be one-dimensional ($\partial^2 T/\partial z^2 = 1/\alpha \partial T/\partial t$) when

$$\frac{\partial^2 T}{\partial x^2} \ll \frac{1}{\alpha}\frac{\partial T}{\partial t} \quad \text{and} \quad \frac{\partial^2 T}{\partial y^2} \ll \frac{1}{\alpha}\frac{\partial T}{\partial t}. \tag{12}$$

Under the related thermal boundary condition of a step change in heat flux, it can be shown that this condition is satisfied when

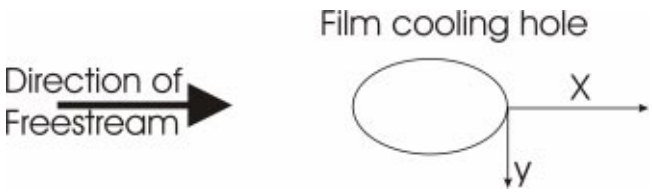


**Fig. 7 Direction of freestream and axis of a film cooling hole**

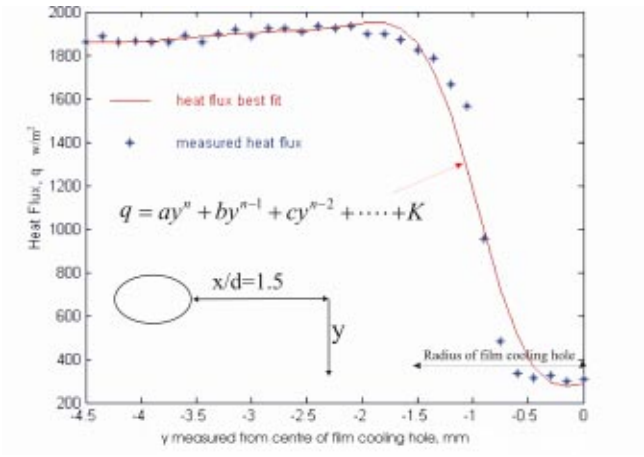


**Fig. 8 Polynomial approximation of the measured heat flux along the *y*-axis**

$$\frac{\partial^2 q}{\partial x^2} \ll \frac{q}{2\alpha t} \quad \text{and} \quad \frac{\partial^2 q}{\partial y^2} \ll \frac{q}{2\alpha t}. \tag{13}$$

This is the necessary condition that lateral conduction has no significant effect on the analysis for the perspex temperature change and the complete differential equation can be approximated by the one-dimensional version.

In order to determine whether lateral conduction was significant in the film cooling experiments, the heat flux at different times during the test was calculated from the measured surface temperature history from liquid crystal images at position $x/d=1.5$ downstream of a film cooling hole. These heat flux levels can be approximated by an *n*th-order polynomial and so heat flux can be expressed as a function of distance along the *y* axis. This is illustrated in **Fig. 8** for a typical test 30 secs from the start. This diagram shows the measured heat flux levels along the *y* axis and the polynomial best fit (*q*). Note that the heat flux levels are almost uniform away from the film cooling hole, but decrease sharply in regions downstream of the film cooling hole.

After the surface heat flux and *q* are found, $q/2\alpha t$ and $\partial^2 q/\partial y^2$ for different test durations can be determined. **Figure 9** and **Fig. 10** present the $q/2\alpha t$ and $\partial^2 q/\partial y^2$ variations for a test duration of 1 second and 5 seconds, respectively. It can be observed from both

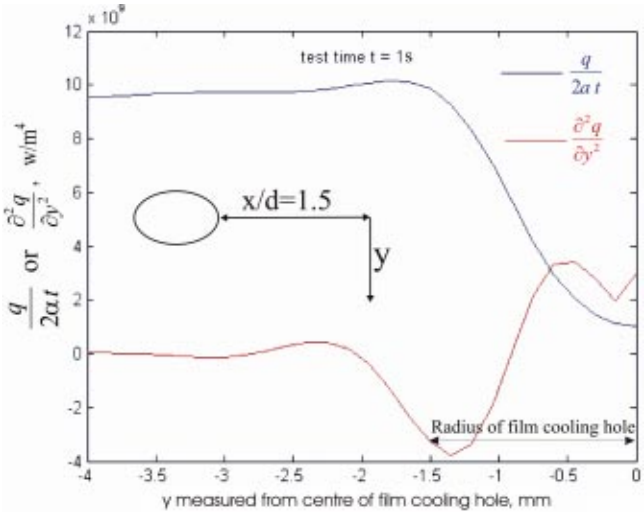


**Fig. 9 Assessment of $\delta^2 q/\delta y^2$ and $q/2\alpha t$ downstream of a film cooling hold, test time $t=1$ s**

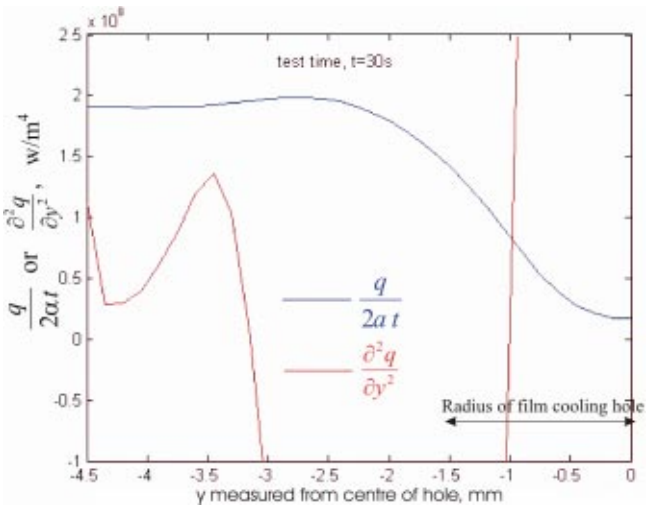


**Fig. 10 Assessment of $\delta^2 q/\delta y^2$ and $q/2\alpha t$ downstream of a film cooling hold, test time $t=5$ s**

figures that levels in $\partial^2 q/\partial y^2$ is much smaller than $q/2\alpha t$ outside the film cooling regions, the criterion $\partial^2 q/\partial y^2 \ll q/2\alpha t$ is satisfied and hence lateral conduction is not significant in these areas. However, in regions downstream of the film cooling hole, $\partial^2 q/\partial y^2$ rises above $q/2\alpha t$ as the test duration increases from 1 to 5 seconds. The criterion $\partial^2 q/\partial y^2 \ll q/2\alpha t$ is not satisfied in these regions. Hence without considering heat flow in the *x* direction, we can conclude that lateral conduction is significant as we require both criteria of Eq. (13) to be satisfied. This also suggested that lateral conduction is more likely to occur with longer test duration. It became apparent that a three-dimensional model of the conduction process was required.

## Direct Methods of Solving the Three-Dimensional Conduction Equation

In order to process the lateral conduction affected data, a direct method was developed to calculate the three-dimensional temperature solution in the perspex substrate using the measured transient surface temperature from the liquid crystal images as the boundary condition. The heat flux distribution at the surface was then calculated using Fourier's law from the calculated temperature distribution. Walker et al. [16] stated that, although direct methods are straightforward to implement, assumptions about temperature distribution have to be made between sensors and the differentiation of discretised data tends to cause unstable behavior and inaccurate results. However, the liquid crystal technique provides much higher resolution data across the test surface than conventional sensors. The pixel separation for the film cooling experiments corresponds to a distance on the test surface of 0.165 mm. Because of the small distance between pixels, errors caused by distribution assumptions above were minimized. These direct methods have not been applied to the transient liquid crystal technique before and therefore the authors gave a detailed description in this work.

In one dimension, the heat flux is calculated as follows in a conduction equation:

$$q = -k\Delta T = -k\frac{\partial T}{\partial z}. \tag{14}$$

Equation (1) shows the one-dimensional Fourier equation. The parabolic partial differential (Eq. (1)) can be solved by one of three numerical methods, which are known as (1) the explicit method, (2) the Crank-Nicolson method or (3) the implicit method. The Crank-Nicolson and implicit methods are frequently

used for one-dimensional problems because they are unconditionally stable, and have the ability to converge with larger time steps than the explicit method as shown in Gerald [23]. However, these methods are not very efficient for solving the three-dimensional Fourier equation. Therefore, new techniques have been developed and described in the next section.

**Three-Dimensional Analysis—Explicit Method.** The transient heat conduction equation in three dimensions is given by Eq. (11). We can use finite difference approximations to transform the equation into the following algebraic equation. If we set $\Delta x = \Delta y = \Delta z = \Delta$, and let $r = k\Delta t / c\rho\Delta^2$, Eq. (11) becomes

$$T^{n+1}_{i,j,k} = r(T^n_{i+1,j,k} + T^n_{i-1,j,k} + T^n_{i,j+1,k} + T^n_{i,j-1,k} + T^n_{i,j,k+1} + T^n_{i,j,k-1}) + (1-6r)T^n_{i,j,k} \tag{15}$$

where $x_i = i\Delta x$, $y_j = j\Delta y$, $z_k = k\Delta z$, $t_n = n\Delta t$ for all the discretised equations in this work.

Note that a forward difference approximation was used for the time derivative and central differences used for the spatial derivatives.

Once the video is recorded, the temperature data are sampled at the image pixel resolution and $\Delta$ is fixed if $\Delta x$, $\Delta y$, and $\Delta z$ are all equal. Thus value of $r$ is governed by the time steps. In this case, $r$ has a maximum value of 1/6 for convergence and stability, [23]. However, although each pixel is square in shape ($\Delta x = \Delta y$), $\Delta z$ (step size into the semi-infinite substance) can be changed to a smaller value than $\Delta x$ and $\Delta y$ to improve accuracy. Gerald [23] showed that, if $\Delta x = \Delta y \neq \Delta z$, the stability criterion becomes

$$\frac{k\Delta t}{c\rho[(\Delta x)^2 + (\Delta y)^2 + (\Delta z)^2]} \leqslant \frac{1}{12}. \tag{16}$$

Equation (16) shows that the maximum value of $\Delta t$ is restricted by the size of element. Decreasing the values of $\Delta x$, $\Delta y$, and $\Delta z$ can increase the spatial resolution but $\Delta t$ must decrease for the solution to remain stable. Each solution thus requires more time steps and increased processing time. Gerald [23] also showed that methods such as the implicit method have a higher accuracy, when using the same $\Delta t$, than the explicit method. The explicit method has a stability limit on $\Delta t$ and in practice each solution requires a large number of time steps. For this reason, the implicit method is often used as it permits a larger $\Delta t$ without loss of stability.

**Three-Dimensional Analysis—Alternating Direction Implicit Method (ADI).** For simplicity, at this point we consider just the two-dimensional case rather than three-dimensional. Gerald [23] showed that by rewriting the two-dimensional heat equation using the implicit method, we obtain Eq. (17);

$$T^{n+1}_{i,j} - T^n_{i,j} = r(T^{n+1}_{i+1,j} - 2T^{n+1}_{i,j} + T^{n+1}_{i-1,j} + T^{n+1}_{i,j+1} - 2T^{n+1}_{i,j} + T^{n+1}_{i,j-1}). \tag{17}$$

Note that the central differences for the spatial derivatives used in the explicit method and implicit method are different. In the explicit method, a central difference approximation is used for $\partial^2 T/\partial x^2$ and $\partial^2 T/\partial y^2$ at time $t^n$ so $T^{n+1}_{i,j}$ is solved in terms of temperature at time step $n$. In the implicit method, a central difference approximation is applied at time $t^{n+1}$. Therefore, the new temperature $T^{n+1}_{i,j}$ is a function of unknown temperatures at adjacent positions, but not given directly in terms of known temperature at time step $n$ as for the explicit method. For the Crank-Nicolson method, $\partial^2 T/\partial x^2$ and $\partial^2 T/\partial y^2$ are replaced by central difference approximations at both $t^{n+1}$ and $t^n$. The new temperature $T^{n+1}_{i,j}$ for the Crank-Nicolson method is thus both a function of known temperature at $t^n$ and adjacent unknown temperatures at $t^{n+1}$. Both the implicit method and Crank-Nicolson method are unconditionally stable for any size of $\Delta t$, although small time steps are more accurate.

However, this method requires solution of a large set, ($M$) times ($N$), of simultaneous equations at each time step, where $M$ is the number of unknown values in the $x$-direction and $N$ in the $y$-direction. A large amount of memory space is needed to store the elements of the coefficient matrix in this implicit method, and the solution to each set of equations is slower. Therefore, to solve the two or three-dimensional Fourier equation using the implicit method, a great deal of memory is required and the processing speed would be slow.

Peaceman and Rachford [24] were the first to propose a method now called the alternating direction implicit method (ADI). In one-dimensional and two-dimensional analyses, this method, like the implicit method, was proven to be stable for any time step, and to give rapid convergence. But the main advantage of this ADI scheme over the implicit method is that the coefficient matrix is now tri-diagonal, allowing rapid solution to each time step and a significant saving in memory required. However, it should be note that in the three-dimensional case, not all fixed values of $r$ and hence $\Delta t$ are stable using this method.

Douglas [25] presented a modified alternating direction method which retained the stability advantage for the three-dimensional transient heat conduction equation. The method is unconditionally stable for all values of $r$ and $\Delta t$. Researchers such as Kellogg [26], Fairweather and Mitchell [27], and Stone [28] also introduced other modifications of the ADI method. Douglas' scheme, however, is well established and relatively easy to implement in computer program and was chosen to analyze the transient liquid crystal data.

Following Douglas [25], we can write the three-dimensional heat conduction equation using the Crank-Nicolson approximation as

$$\frac{1}{2}(\Delta_x^2 + \Delta_y^2 + \Delta_z^2)(T^{n+1}_{i,j,k} + T^n_{i,j,k}) = \frac{T^{n+1}_{i,j,k} - T^n_{i,j,k}}{\Delta t} \tag{18}$$

where

$$\Delta_x^2 T^n_{i,j,k} = \frac{(T^n_{i+1,j,k} - 2T^n_{i,j,k} + T^n_{i-1,j,k})}{(\Delta x)^2}, \quad \text{etc.} \tag{19}$$

Note that the scheme uses central differences for approximations to both spatial and a temporal derivatives.

The next step is to obtain an estimate of the temperature solution at a time $t^{n+1}$ by using a central difference approximation for the second derivative with respect to $x$ and forward difference for $y$ and $z$ second derivates:

$$\frac{1}{2}\Delta_x^2(T^{*n+1} + T^n) + \Delta_y^2 T^n + \Delta_z^2 T^n = \frac{T^{*n+1} - T^n}{\Delta t}. \tag{20a}$$

Central difference approximation can also be used for the $y$ direction 2nd derivative, Eq. (20$b$) and the $z$ direction 2nd derivative, Eq. (20$c$)

$$\frac{1}{2}\Delta_x^2(T^{*n+1} + T^n) + \frac{1}{2}\Delta_y^2(T^{**n+1} + T^n) + \Delta_z^2 T^n = \frac{T^{**n+1} - T^n}{\Delta t} \tag{20b}$$

$$\frac{1}{2}\Delta_x^2(T^{*n+1} + T^n) + \frac{1}{2}\Delta_y^2(T^{**n+1} + T^n) + \frac{1}{2}\Delta_z^2(T^{n+1} + T^n) = \frac{T^{**n+1} - T^n}{\Delta t}. \tag{20c}$$

$T^{*n+1}$ and $T^{**n+1}$ are the initial approximations of $T^{n+1}$ from Eqs. (20$a$) and (20$b$). After some rearrangement, Eqs. (20) become

$$\left(\Delta_x^2 - \frac{2}{\Delta t}\right)T^{*n+1} = -\left(\Delta_x^2 + 2\Delta_y^2 + 2\Delta_z^2 + \frac{2}{\Delta t}\right)T^n \tag{21a}$$

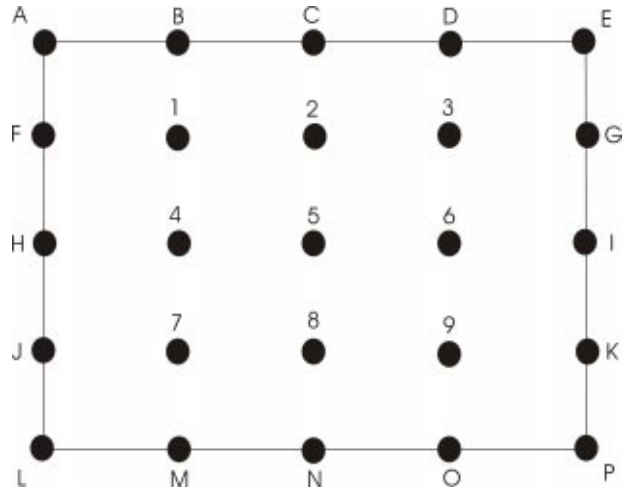


**Fig. 11 Node system for the three-dimensional conduction analysis**

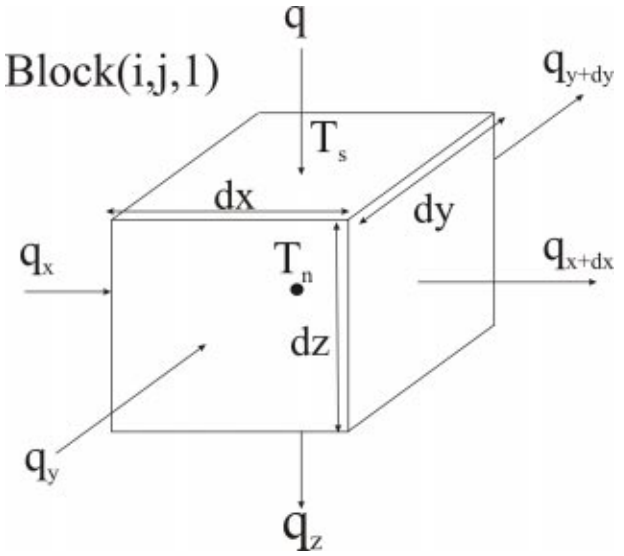


**Fig. 12 Heat flow within an element of the test section**

$$\left(\Delta_y^2 - \frac{2}{\Delta t}\right) T^{**n+1} = \Delta_y^2 T^n - \frac{2}{\Delta t} T^{*n+1} \tag{21b}$$

$$\left(\Delta_z^2 - \frac{2}{\Delta t}\right) T^{n+1} = \Delta_z^2 T^n - \frac{2}{\Delta t} T^{**n+1}. \tag{21c}$$

Note that each Eq. (21) is derived from the forward difference approximations in two dimensions and uses a central difference for one dimension at a time, i.e., $x$ in ($a$), $y$ in ($b$) and $z$ in ($c$). The left hand side of each equation gives a tri-diagonal matrix that can be readily solved using a compact solution procedure since the right-hand side is comprised of terms that can be evaluated from the previous time step. To approximate the temperature $T^{n+1}$, $T^n$ at time $t^n$ was first used in Eq. (21$a$) to calculate first the temporary temperature $T^{*n+1}$, which was used with $T^n$ again in Eq. (21$b$) to evaluate the next temporary temperature $T^{**n+1}$. $T^{**n+1}$ and $T^n$ were finally used in Eq. (21$c$) to calculate $T^{n+1}$. Therefore, for each time step, the temperature $T^n$ and the subsequent temporary temperature approximations have to alternate through Eq. (21$a$), Eq. (21$b$), and finally Eq. (21$c$) for the approximation of temperature $T^{n+1}$.

With a cubic or a rectangular parallelepiped region, Douglas also proved that this method is stable for all values of $\Delta x$, $\Delta y$, $\Delta z$, and $\Delta t$. The tri-diagonal matrix only needs three coefficients with a dramatic reduction in memory space, relative to the implicit or the Crank-Nicolson method with the non-triadiagonal ($M$) and ($N$) matrix.

**Figure 11** shows schematically the node system used to analyze the conduction problems. Each node is at an individual located pixel from a processed video. The nodes from number 1 to 9 represent the area with nonuniform heat flux while nodes A to P have uniform heat flux. The least square regression method of processing the normalized green signal above is used to determine the surface temperature variation for each pixel during an experiment. These surface temperature histories are then used as boundary condition for each node. Note that the procedure employs a one-dimensional solution of the transient conduction equation to regress on parameters $h$ and $\eta$. As stated earlier, lateral conduction was found to influence the temperature transient in regions downstream of the film-cooling holes. The values of $h$ and $\eta$ recovered in this fitting procedure are not used subsequently. The process is merely a method of establishing a best estimate of the surface temperature variation over thirty to forty five seconds at each pixel from the multicrystal image data. The excellent agreement achieved between the measured normalized green signals and these best fit extracted from the **S** matrix was evidence (as shown in **Fig. 6**) of the success of this approach.

The temperature distribution for each pixel is calculated by cycling through (21$a$), (21$b$), and (21$c$). The boundary condition at each node corresponds to the measured surface temperature history. Note that each Eq. (21) can be written in the form of

$$\mathbf{A} \cdot \vec{b} = \vec{c}$$

where **A** is a tridiagonal coefficient matrix and $\vec{b}$ is the temperature vector to be determined in the form

$$\begin{pmatrix} T_{1,1,1} \\ T_{2,1,1} \\ \vdots \\ T_{i,j,k} \\ \vdots \end{pmatrix}.$$

As matrix **A** is tridiagonal, the equations can be solved easily with a minimal memory requirement using LU decomposition.

In the present procedure, $\Delta x$ and $\Delta y$ are taken to be the pixel size and the accuracy can be improved by decreasing $\Delta z$ and $\Delta t$. Note that increased accuracy is at the expense of prolonged processing time.

Once the ADI method has been used to determine the three-dimensional temperature field variation with time, the temperature gradient at the surface is calculated to find the heat flux variation with time. **Figure 12** shows an element of the test section at the top surface. The element has a top surface area corresponding to the size of a pixel ($\Delta x \times \Delta y$) and depth $\Delta z$. Heat flows into the element through the top surface and flows into neighboring elemental blocks through conduction in $x$, $y$, and $z$-directions. Once the temperature distribution is evaluated by the ADI method, $q_x$, $q_y$, and $q_z$ can be estimated. The heat flux on the surface area can then be calculated from

$$\frac{q - q_z}{dz} = \rho c \frac{\partial T}{\partial t} + \frac{\partial q_x}{\partial x} + \frac{\partial q_y}{\partial y}. \tag{22}$$

The calculated surface heat flux can then be used to determine the adiabatic wall temperature (hence the film cooling effectiveness) and the heat transfer coefficient a procedure which can be explained using the plot shown in **Fig. 13**. The surface heat flux for each pixel can be plotted against the surface temperature rise. If the mainstream temperature rise is a step change, the heat trans-

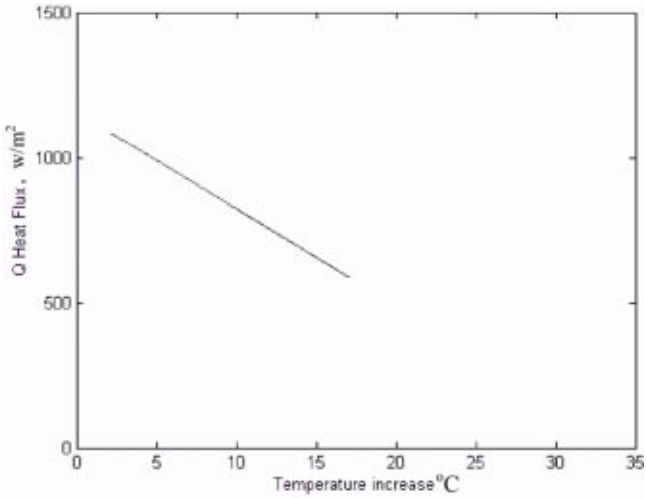


**Fig. 13 Calculated heat flux against surface temperature rise**

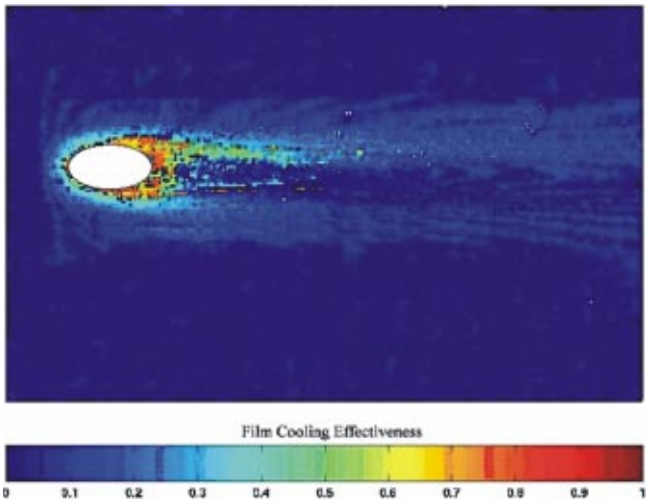


**Fig. 15 Local film-cooling effectiveness data using one-dimensional transient model**

fer coefficient can be determined by the gradient of the plot and the adiabatic wall temperature can be found by the interception between the plot and the temperature rise axis. When the mainstream gas temperature is not a step change, surface heat flux variation $q$ can first be predicted with different combinations of $h$ and $\eta$ to generate a lookup table. A regression method can be used to compare the predicted $q$ and the calculated surface heat flux history from Eq. (22) to find the right $h/\eta$ pair.

Variations were evident between the different three-dimensional conduction analysis techniques. **Figure 14** shows a comparison of heat flux variation against surface temperature rise calculated by the three-dimensional ADI and explicit methods for different time steps. The heat flux from a pixel was calculated by both three-dimensional techniques using time steps of 0.005, 0.01, and 0.03s. As shown in the diagram, the heat flux calculated by the ADI method approaches the ''true'' response much quicker by decreasing $\Delta t$ than the explicit method. We can consider the heat flux line calculated by the ADI method with $\Delta t = 0.005$ s as the ''true'' response, using the explicit method with the same time step yields an error of 3.5% in heat flux, 22% in $\eta$ and 5.3% in $h$. For a $\Delta t$ of 0.03s in the ADI method gives an error of 2% in heat flux, 15% in $\eta$ and 0.86% in $h$, with a $\Delta t = 0.01$ s by the same method yields an error of less than 1% in both parameters. This demonstrates the advantages of ADI technique over the explicit method as processing time can be decreased by more than six times and yet, a better accuracy is achieved.

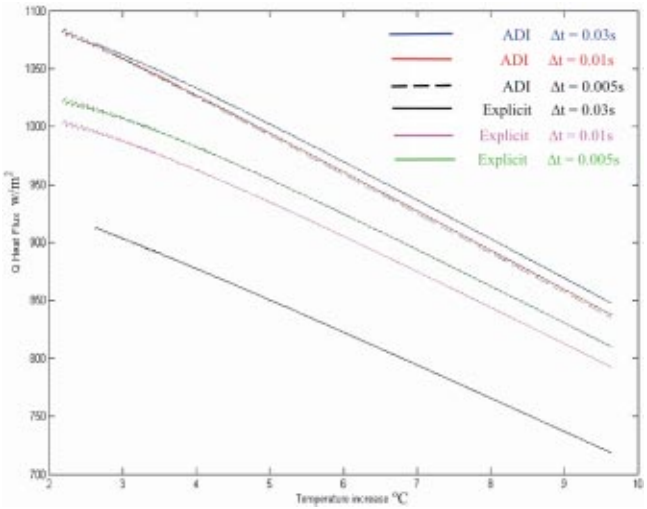


**Fig. 14 Comparison of the ADI and the explicit method**

## Results and Discussions

Film-cooling experiments were carried out on a single 3 mm diameter hole test plate. The analysis employed the methods developed above to obtain both film cooling effectiveness and heat transfer coefficient. The experiments were carried out with a freestream velocity of 16m/s, a blowing ratio (BR) of 0.5 using air as coolant and hole inclination at 20°. The experiments were performed with heated freestream (~60°C) and unheated coolant. The zone immediately downstream of the hole is highly cooled and lateral conduction in this region helps cause the surface to heat up and the liquid crystal to change color. **Figure 15** presents the local film-cooling effectiveness data analyzed by the one-dimensional transient method. With a blowing ratio of 0.5, a high film cooling effectiveness distribution is expected immediately downstream of the film cooling hole. However, the figure shows very low effectiveness values in this region. This indicates that the one-dimensional model wrongly measures the effectiveness in region downstream of the film-cooling hole, where high temperature variation is expected, as explained in **Fig. 8** previously. The analysis also suggests that the one-dimensional transient model can only be used in regions away from the film cooling hole, where the temperature gradient is significantly lower, and is again shown in **Fig. 15**. **Figure 16** shows the detailed local film cooling effectiveness data of the same test analyzed by the three-dimensional conduction method. The three-dimensional model gives a more accurate analysis in the region experiencing lateral conduction. The three-dimensional technique yields a region of high effectiveness downstream of the film-cooling hole as expected. In regions outside the film coverage, effectiveness values measured by either the one-dimensional or three-dimensional model are similar. Note that the three-dimensional conduction correction is only applied from the trailing edge of the hole.

**Figure 17** presents the film-cooling effectiveness values along the centreline downstream of the film-cooling hole. Comparison was made to data from Burd and Simon [29] with air as coolant and an injection angle of 35°. The plot shows that the effectiveness levels immediately downstream of the film cooling hole are higher for the 20° injection angle hole than the 35°. The shallower injection angle and the higher density ratio allow the cooling film to stay attached to the surface better initially, and the effectiveness values drop to similar level as the 35° injection angle from a distance $x \sim 2d$.

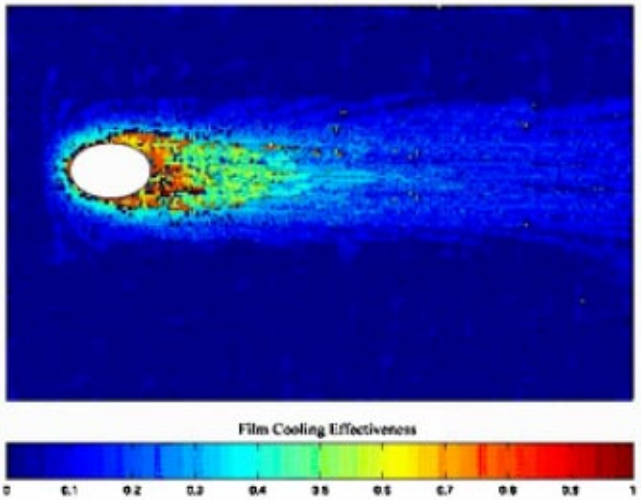


**Fig. 16 Local film-cooling effectiveness data using three-dimensional model**

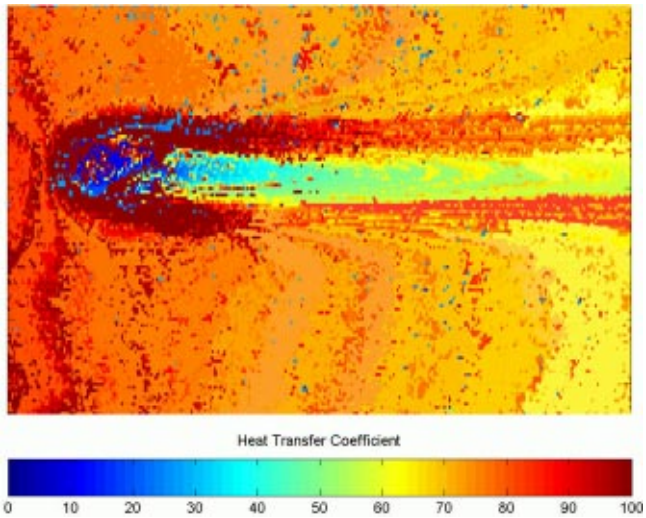


**Fig. 18 Local heat transfer coefficient measured by three-dimensional model**

**Figure 18** shows the detailed local heat transfer distribution of the same film cooling experiment, analyzed by the three-dimensional conduction technique. The heat transfer levels are significantly lower in the region downstream of the film cooling hole than the ''flat plate'' region outside. With a mainstream velocity of 16 m/s and a blowing ratio at 0.5, the Re through the hole is about 1300. As the Re is low, the film coolant through the hole is likely to be in a laminar state, hence the coolant flow would be more steady and limits the amount of mixing with the freestream. Note that the heat transfer coefficient for fully developed pipe flow would be $(4.36k/d)$. The shallow angle of injection also helps the film to remain well attached to the surface to reduce mixing in this region, causing the heat transfer coefficient level to be lower than it would be in on a flat plate. However, heat transfer enhancement is found around the front of film-cooling hole where a horseshoe vortex is probably present. Heat transfer coefficient along the edge of the film is most likely caused by turbulent mixing.

**Figure 19** shows the heat transfer coefficient in the region immediately downstream of the film-cooling hole. As mentioned before, the $h/h_\infty$ ratio along the centreline is significantly less than 1 initially, but rises gradually to unity downstream. The blue line shows the $h/h_\infty$ levels averaged in the spanwise direction downstream of the film cooling hole over a strip $1.5d$ wide. The latter shows the expected enhancement in $h/h_\infty$.

## Estimation of Experimental Uncertainty

Experimental uncertainty estimates were made for both the one-dimensional and three-dimensional processing techniques at various conditions. Using the method of small perturbations described by Moffat [30], estimates of the experimental error associated with the one-dimensional transient technique and the three-dimensional conduction method under a uniform heat flux are shown in **Table 1**. The experimental parameters were set to test conditions typical of those found in the film cooling tests and the contribution of uncertainty in each measured variable presented in

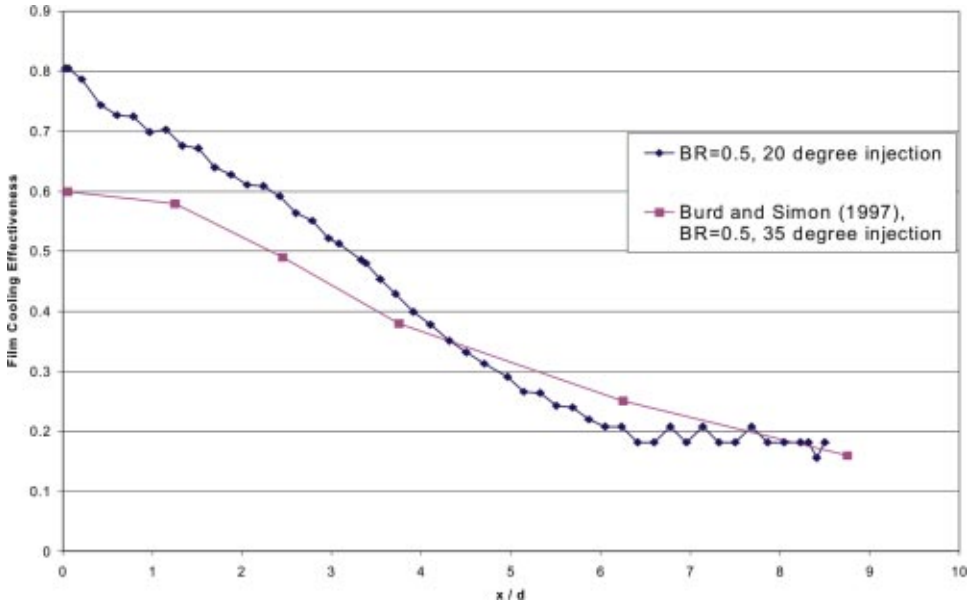


**Fig. 17 Centerline film-cooling effectiveness distribution downstream of hold**

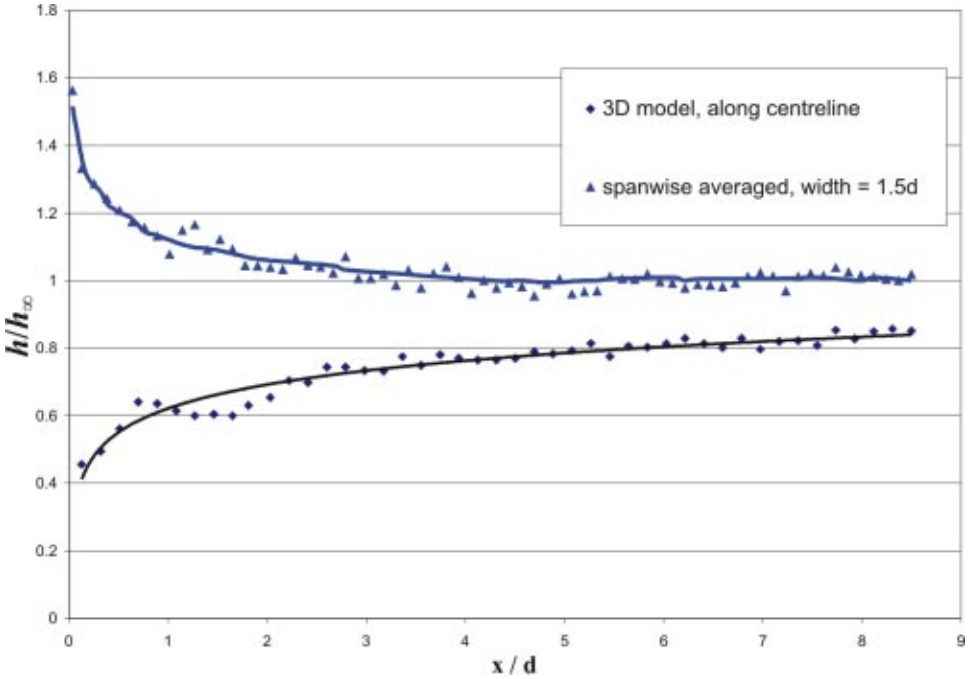


**Fig. 19 Heat transfer coefficient variation downstream of the hold. The values averaged over 1.5*d* wide strips shows the familiar enhancement downstream of the hold.**

**Table 1**. The most likely uncertainty is presented as the RMS sum of the component errors and the worst error is the sum of the component errors. In these analyses $h$ was equal to 100 $Wm^{-2}K^{-1}$ and $\eta=0.5$ over a rectangular surface area of $5\times8$ pixels. Typical levels of h and $\eta$ for the series of experiments are chosen and not all the data are reported here. For the three-dimensional technique $\Delta t$ was 0.01. The table shows that in a uniform heat flux region, RMS errors in heat transfer coefficient and film cooling effectiveness for both one-dimensional and three-dimensional techniques are very similar. Note that the errors in film-cooling effectiveness for both techniques are significantly less than the error in $h$. This feature was observed by Wang et al. [31] for a one-dimensional analysis.

In a region where heat flux is not uniform, if the thermal boundary conditions do not satisfy the criterion of Eq. (13), lateral conduction becomes significant in this region and the one-dimensional transient model no longer provides accurate heat transfer and effectiveness measurement. **Figure 20** and **Fig. 21** present the averaged $\eta$ and $h$ values measured by the one-dimensional transient method and the three-dimensional conduction technique for boundary conditions for which lateral conduction is significant. Both $h$ and $\eta$ are averaged for the $5\times8$ pixel zone. The thermal boundary condition was deliberately set to ensure that lateral conduction was important and it is not surprising that the one-dimensional model gives an incorrect $\eta$ and $h$.

**Table 2** shows the contributions to uncertainties in heat transfer coefficient and effectiveness for thermal boundary conditions with significant lateral conduction as used in **Fig. 20** and **Fig. 21**. The three-dimensional conduction technique is valid for both the uniform heat flux distribution and the non-uniform heat flux with significant lateral conduction condition. The RMS errors for both heat transfer coefficient and film cooling effectiveness, summarized in **Table 2**, are well within an acceptable range.

## Summary and Conclusions

Two techniques have been developed to measure the heat transfer coefficient and film cooling effectiveness for a three-temperature system using multiple narrow band liquid crystals. The one-dimensional transient technique can be applied in regions not affected by lateral conduction, to determine both $h$ and $\eta$ in a single test with acceptable accuracy. The technique employs a regression method that uses a multiple crystal coating over an extended range of temperature which increases the amount of data for analysis from more common peak intensity spotting methods. The new method has been found to be robust to noisy data. For

**Table 1 Contributions to uncertainties in heat transfer coefficient and effectiveness for a uniform heat flux boundary condition**

| | | | 1D Transient Technique | | 3D Conduction Technique | |
|---|---|---|---|---|---|---|
| Test Condition | Exp. Condition | Typical Error | htc Error | Effectiveness Error | htc Error | Effectiveness Error |
| Gas temperature $T_{gas}$, °C | 53.5 | 0.5 | 0.05% | 1.46% | 0.075% | 1.24% |
| Start temperature $T_o$, °C | 19.4 | 0.2 | 6.81% | 2.76% | 6.77% | 3.02% |
| Coolant temperature $T_c$, °C | 19.8 | 0.5 | 0.05% | 1.5% | 0.075% | 1.28% |
| Crystal temperature $T_{crystal}$, °C | 25,30,33 | 0.3 | 10.05% | 1.64% | 10.16% | 1.46% |
| Perspex properties ($\sqrt{\rho ck}$) | 569 | 29 | 5.10% | 1% | 4.92% | 0.22% |
| RMS error | | | 13.17% | 3.96% | 13.16% | 3.80% |
| Maximum error | | | 22.06% | 8.36% | 17.23% | 7.22% |

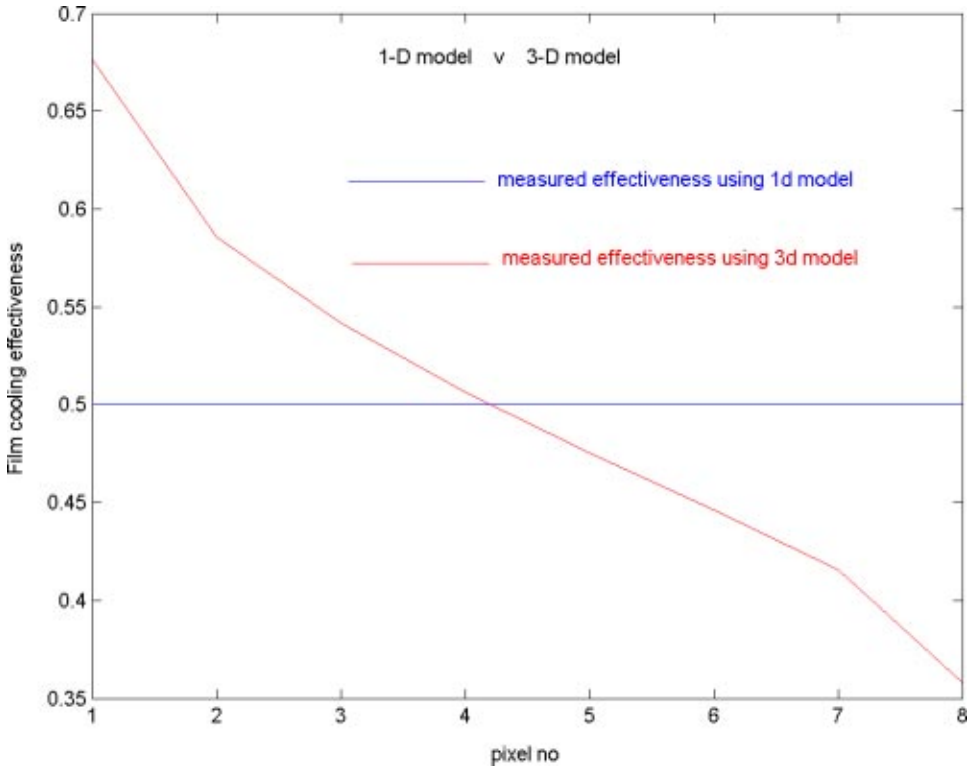


**Fig. 20 Comparison of film cooling effectiveness values measured by one-dimensional and three-dimensional models**

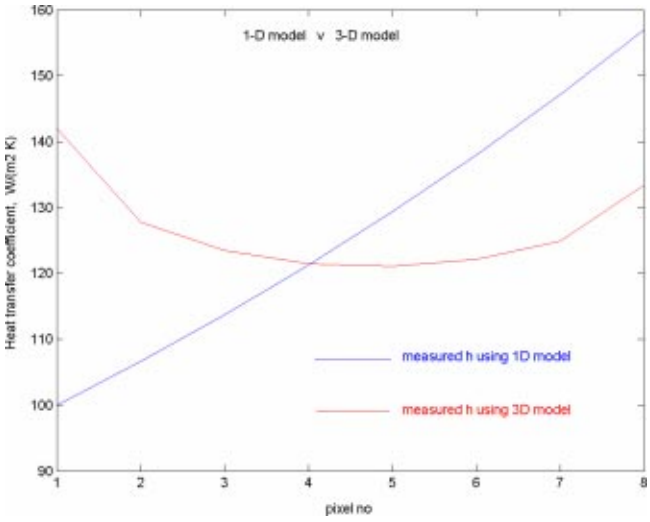


**Fig. 21 Comparison of heat transfer coefficient levels calculated by one-dimensional and three-dimensional techniques**

regions of high temperature variation, the one-dimensional method is first used to estimate the surface temperature measurements, followed by a three-dimensional conduction analysis which evaluates the heat flux and hence the heat transfer coefficient and film cooling effectiveness distributions. The three-dimensional technique has been shown to produce high quality and accurate data where is not possible to use the one-dimensional technique. The authors have also compared several numerical methods for solving the three-dimensional conduction problem, with the ADI method showing obvious advantages over the others such as unconditionally stable, faster convergence, less processing time and reduced computing power. It is thought that the methods described in this report will be of use in many other heat transfer experiments.

## Acknowledgment

The authors greatly appreciate support from Rolls-Royce plc towards this work.

**Table 2 Contributions to uncertainties in heat transfer coefficient and effectiveness for thermal boundary condition with significant lateral conduction as used for Fig. 20 and Fig. 21**

| | | | 3D Conduction Technique | |
|---|---|---|---|---|
| Test Condition | Exp. Condition | Typical Error | htc Error | Effectiveness Error |
| Gas temperature $T_{gas}$, °C | 53.5 | 0.5 | 3.5% | 2.3% |
| Start temperature $T_o$, °C | 19.4 | 0.2 | 4.4% | 3.8% |
| Coolant temperature $T_c$, °C | 19.8 | 0.5 | 4.5% | 2.1% |
| Crystal temperature $T_{crystal}$, °C | 25,30,33 | 0.3 | 5.1% | 3.9% |
| Perspex properties ($\sqrt{\rho ck}$) | 569 | 29 | 5.2% | 0.19% |
| RMS error | | | 10.2% | 6.28% |
| Maximum error | | | 22.7% | 12.29% |

## Nomenclature

BR = blowing ratio, $\rho_c V_c / (\rho_{gas} V_{gas})$
$c$ = specific heat capacity, J/(kg K)
$d$ = hole diameter, m
$G$ = measured normalized green intensity block
$h$, $htc$ = heat transfer coefficient, W/(m$^2$ K)
$k$ = thermal conductivity of air, W/(m K)
$m$ = temperature gradient at time step $n$
$q$ = heat flux, W/m$^2$
Re = Reynolds number, $\rho V d / \mu$
$S$ = predicted normalized green intensity block
$T$ = temperature, °C
$t$ = time, s
$V$ = velocity, m/s
$x$ = distance in mainstream wise direction, measured from the hole, m
$y$ = distance perpendicular to flow direction, measured from hole axis, m
$z$ = distance into the test plate, measured from the top surface, m

### Greek

$\alpha$ = thermal diffusivity=k/($\rho$c), m$^2$/s
$\Delta t$ = time step, s
$\eta$ = film cooling effectiveness
$\rho$ = mass density, kg/m$^3$
$\mu$ = dynamic viscosity of freestream, kg/(m s)

### Subscripts

$aw$ = adiabatic wall
$o$ = starting condition
$c$ = coolant
gas = freestream
$n$ = time step
$w$ = wall
$\infty$ = remote from film-cooling hole

## References


[1] den Ouden, C., and Hoogendoorn, C. J., 1974, ''Local Convective Heat Transfer Coefficients for Jets Impinging on a Plate: Experiments Using a Liquid Crystal Technique,'' *Proceedings of the 5th International Heat Transfer Conference*, Taylor and Francis, London, **5**, pp. 293–295.

[2] Copper, T. E., Field, R. J., and Meyer, J. F., 1975, ''Liquid Crystal Thermograph and Its Applications of the Study of Convective Heat Transfer,'' ASME J. Heat Transfer, **97**, pp. 442–450.

[3] Baughn, J. W., Hechanova, A. E., and Yan, X., 1991, ''An Experimental Study of Entrainment Effects on the Heat Transfer From a Flat Surface to a Heated Circular Impingement Jet,'' ASME J. Heat Transfer, **113**, pp. 1023–1025.

[4] Lucas, M. G., Ireland, P. T., Wang, Z., Jones, T. V., and Pearce, W. J., 1992, ''Fundamental Studies of Impingement Cooling Thermal Boundary Conditions,'' AGARD, Turkey, Paper 14.

[5] Sargison, J., E., Guo, S., M., Oldfield M., L., G., Lock, G., D., and, Rawlinson, A., J., 2001, ''A Converging Slot-Hole Film-Cooling Geometry Part 1: Low-Speed Flat-Plate Heat Transfer and Loss,'' ASME Paper 2001-GT-0126.

[6] Ireland, P. T., and Jones, T. V., 1986, ''Detailed Measurements of Heat Transfer on and Around a Pedestal in Fully-Developed Channel Flow,'' *Proc. 8th Int. Heat Trans. Conf.*, San Francisco, Taylor and Francis, London, pp. 975–986.

[7] Ireland, P. T., Wang, Z., and Jones, T. V., 1995, ''Liquid Crystal Heat Transfer Measurements,'' Measurement Techniques Lecture Series 1995-01, von Karman Institute for Fluid Dynamics.

[8] Wang, Z., Ireland, P. T., and Jones, T. V., 1993, ''An Advanced Method of Processing Liquid Crystal Video Signals From Transient Heat Transfer Experiments,'' ASME J. Turbomach., **117**, pp. 184–189.

[9] Wang, Z., Ireland, P. T., and Jones, T. V., 1994, ''A Color Image Processing System for Transient Liquid Crystal Heat Transfer Experiments,'' ASME J. Turbomach., **118**, pp. 421–427.

[10] Lucas, M. G., Ireland, P. T., Wang, Z., and Jones, T. V., 1993, ''Fundamental Studies of Impingement Cooling Thermal Boundary Conditions,'' AGARD CP-527, Paper No. 14.

[11] Van Treuren, K. W., Wang, Z., Ireland, P. T., and Jones, T. V., 1994, ''Detailed Measurements of Local Heat Transfer Coefficient and Adiabatic Wall Temperature Beneath an Array of Impinging Jets,'' ASME J. Turbomach., **116**, pp. 369–374.

[12] Son, C., Gillespie, D. R. H., Ireland, P. T., and Dailey, G. M., 2001, ''Heat Transfer and Flow Characteristics of an Engine Representative Impingement Cooling System,'' ASME J. Turbomach., **123**, pp. 154–160.

[13] Baughn, J. W., Mayhew, J. E., Anderson, M. R., and Butler, R. J., 1998, ''A Periodic Transient Method Using Liquid Crystals for the Measurement of Local Heat Transfer Coefficients,'' ASME J. Heat Transfer, **120**, pp. 772–775.

[14] Ireland, P. T., and Jones, T. V., 1987, ''Note on the Double Crystal Method of Measuring Heat Transfer Coefficient,'' OUEL Report 1710/87.

[15] Vedula, R. J., and Metzger, D. E., 1991, ''A Method for Simultaneous Determination of Local Effectiveness and Heat Transfer Distributions in Three-Temperature Convection Situations,'' ASME Paper 91-GT-345.

[16] Chambers, A. C., Gillespie, D. R. H., and Ireland, P. T., 2003, ''A Novel Transient Liquid Crystal Technique to Determine Heat Transfer Coefficient Distributions and Adiabatic Wall Temperature in a Three Temperature Problem,'' ASME J. Turbomach., **125**, pp. 538–546.

[17] Walker, D. G., and Scott, E. P., 1998, ''The Effects of Lateral Conduction on Heat Flux Estimation From Surface Temperature Measurements,'' *AIAA/ASME Joint Thermophysics and Heat Transfer Conference*, ASME, New York, **3**, pp. 245–252.

[18] Walker, D. G., and Scott, E. P., 1998b, ''Evaluation of Estimation Methods for High Unsteady Heat Fluxes From Surface Measurements,'' J. Thermophys. Heat Transfer, **12**(4), pp. 543–551.

[19] Walker, D. G., Scott, E. P., and Nowak, R. J., 2000, ''Estimation Methods for Two-Dimensional Conduction Effects of Shock-Shock Heat Fluxes,'' J. Thermophys. Heat Transfer, **14**(4), pp. 533–539.

[20] Lin, M., and Wang, T., 2002, ''A Transient Liquid Crystal Method Using a 3-D Inverse Transient Conduction Scheme,'' Int. J. Heat Mass Transfer, **45**, pp. 3491–3501.

[21] Saumweber, C., Schulz, A., and Wittig., S., 2002, ''Free-Stream Turbulence Effects on Film Cooling With Shaped Holes,'' ASME Paper GT-2002-30170.

[22] Gillespie, D. R. H., 1996, ''Intricate Internal Cooling Systems for Gas Turbine Blading,'' D. Phil thesis, Department of Engineering Science, Oxford University, Oxford, UK.

[23] Gerald, C. F., and Wheatley, P. O., 1994, *Applied Numerical Analysis*, 5th Ed., Addison-Wesley, New York.

[24] Peaceman, D. W., and Rachford, Jr., H. H., 1955, ''The Numerical Solution of Parabolic and Elliptic Differential Equations,'' J. Soc. Ind. Appl. Math., **3**(1), pp. 28–41.

[25] Douglas, Jr., Jim, 1962, ''Alternating Direction Methods for Three Space Variables,'' Numer. Math., **4**, pp. 41–63.

[26] Kellogg, R. B., 1963, ''Another Alternating Direction Implicit Method,'' J. Soc. Ind. Appl. Math., **11**(4), pp. 976–979.

[27] Fairweather, G., and Mitchell, A. R., 1965, ''A New Alternating Direction Method for Parabolic Equations in Three Space Variables,'' J. Soc. Ind. Appl. Math., **13**(4), pp. 957–965.

[28] Stone, H. L., 1968, ''Iterative Solution of Implicit Approximations of Multidimensional Partial Differential Equations,'' SIAM (Soc. Ind. Appl. Math.) J. Numer. Anal., **5**(3), pp. 530–558.

[29] Burd, S. W., and Simon., T. W., 1997, ''The Influence of Coolant Supply Geometry on Film Coolant Exit Flow and Surface Adiabatic Effectiveness,'' ASME Paper 97-GT-25.

[30] Moffat, R. J., 1982, ''Contributions to the Theory of Single Sample Uncertainty Analysis,'' ASME J. Fluids Eng., **104**, p. 250.

[31] Wang, Z., Ireland, P. T., Kohler, S. T., and Chew, J. W., 1996, ''Heat Transfer Measurements to a Gas Turbine Cooling Passage With Inclined Ribs,'' ASME J. Turbomach., **120**, pp. 63–69.

# Predicting Skin Friction and Heat Transfer for Turbulent Flow Over Real Gas Turbine Surface Roughness Using the Discrete Element Method

**Stephen T. McClain**
Assistant Professor,
Department of Mechanical Engineering,
The University of Alabama at Birmingham,
1530 3rd Avenue South, BEC 358B,
Birmingham, AL 35294-4461
e-mail: smcclain@uab.edu

**B. Keith Hodge**
Professor,
Department of Mechanical Engineering,
Mississippi State University,
P.O. Box ME,
Mississippi State, MS 39762
e-mail: hodge@me.msstate.edu

**Jeffrey P. Bons**
Associate Professor,
Department of Mechanical Engineering,
Brigham Young University,
435 CTB, P.O. Box 24201
Provo, UT 84602-4201
e-mail: jbons@byu.edu

*The discrete element method considers the total aerodynamic drag on a rough surface to be the sum of shear drag on the flat part of the surface and the form drag on the individual roughness elements. The total heat transfer from a rough surface is the sum of convection through the fluid on the flat part of the surface and the convection from each of the roughness elements. The discrete element method has been widely used and validated for predicting heat transfer and skin friction for rough surfaces composed of sparse, ordered, and deterministic elements. Real gas turbine surface roughness is different from surfaces with sparse, ordered, and deterministic roughness elements. Modifications made to the discrete element roughness method to extend the validation to real gas turbine surface roughness are detailed. Two rough surfaces found on high-hour gas turbine blades were characterized using a Taylor-Hobson Form Talysurf Series 2 profilometer. Two rough surfaces and two elliptical-analog surfaces were generated for wind tunnel testing using a three-dimensional printer. The printed surfaces were scaled to maintain similar boundary layer thickness to roughness height ratio in the wind tunnel as found in gas turbine operation. The results of the wind tunnel skin friction and Stanton number measurements and the discrete element method predictions for each of the four surfaces are presented and discussed. The discrete element predictions made considering the gas turbine roughness modifications are within 7% of the experimentally measured skin friction coefficients and are within 16% of the experimentally measured Stanton numbers.* [DOI: 10.1115/1.1740779]

## Introduction

The deleterious effects of blade surface roughness on gas turbine performance are well known. Roughness bleeds energy through increased skin friction on the blades. Surface roughness also increases the heat transfer rates from the combustion products to the blades. Consequently, turbine blade surface roughness has a twofold effect in decreasing the efficiency of gas turbines.

To make sound economic decisions, gas turbine manufacturers and operators need predictions for the effects of surface roughness on gas turbine performance over the life of the gas turbine. Historically, the two dominant methods for evaluating the effects of surface roughness on drag and heat transfer have been the equivalent sand-grain roughness model and the discrete element model. The equivalent sand-grain roughness model, first proposed by Schlichting [1], is an empirical model in which rough surfaces with various features are compared to data from Nikuradse [2] concerning flow in pipes with varying sizes of sieved sand glued to the wetted surface. Rough surfaces are assigned a value of equivalent sand-grain roughness height based on comparisons with Nikuradse's data. Recent literature on the equivalent sand-grain roughness method has involved determining correlations for equivalent roughness height based on the actual roughness height, the roughness shape, and the roughness density. Dvorak [3], Simpson [4], Dirling [5], Sigal and Danberg [6], and Bons [7] have all proposed functions to predict the effective sand-grain roughness height based on parameters involving the roughness height, spacing, and shape.

Several disadvantages of the equivalent sand-grain method have been noted. A detailed discussion of these disadvantages is presented by Taylor [8]. While a parameter presented by Sigal-Danberg [6] has demonstrated the most promise for correlating the available equivalent roughness height data, the best correlation based on the parameter is still limited in its range of surface conditions. Bons [7] has also shown that the Sigal-Danberg parameter is difficult to define for roughness elements with random spacings, shapes, and heights, that wind tunnel measurements of equivalent sand-grain roughness heights for randomly rough surfaces can vary as much as 40% from predicted heights using logarithmic data curve-fits based on the parameter, and that different curve-fits are required for randomly rough surfaces and for three-dimensional uniform roughness, such as cone roughness, generated to simulate random roughness.

Attempts to use one value of equivalent sand-grain roughness height to predict both skin friction and heat transfer have been unsuccessful, [7]. In fact, there is no reason that two surfaces with the same skin friction coefficients, which implies that they would have the same equivalent sand-grain roughness value from a friction standpoint, should have the same Stanton numbers, [8].

The discrete element model is an alternative model to the equivalent sand-grain model. While the equivalent sand-grain model is based completely on empirical correlations, the discrete element model evaluates the effects of roughness by considering the physical characteristics of the roughness elements in the solution of the boundary layer equations. The discrete element model

Contributed by the International Gas Turbine Institute and presented at the International Gas Turbine and Aeroengine Congress and Exhibition, Atlanta, GA, June 16–19, 2003. Manuscript received by the IGTI Dec. 2002; final revision Mar. 2003. Paper No. 2003-GT-38813. Review Chair: H. R. Simmons.

  

is semi-empirical in the sense that the closure relationships used to determine the drag and heat transfer from the individual roughness elements are based on empirical data.

The basis for the discrete element model was also described by Schlichting in his 1937 paper. In attempting to explain the effect of roughness element density on the effective sand-grain height, Schlichting suggested that the total drag on a rough surface is the sum of skin friction on the flat part of the surface and the form drag on the individual roughness elements. Methods to solve the boundary layer equations for flow over rough surfaces, such as Finson [9], Adams and Hodge [10], and Lin and Bywater [11], incorporated momentum sink terms into the boundary layer equations based on Schlichting's suggestion. The form of the discrete element roughness model presented in this work originated in the work of Finson [9] and was rigorously derived by Taylor [8].

## The Discrete Element Model

The discrete element model is formulated for roughness elements with three-dimensional shapes for which the element cross section can be defined at every height, $y$. The differential equations including roughness effects are derived by applying the basic conservation statements for mass, momentum, and energy to a control volume such as that shown in **Fig. 1**. Basic to this approach is the idea that the two-dimensional, time-averaged turbulent boundary layer equations can be applied in the flow region below the crests of the roughness elements. The flow variables are spatially averaged over the transverse ($z$) direction and the streamwise ($x$) direction. The physical effects of the roughness elements on the fluid in the control volume are modeled by considering the flow blockage, the local element heat transfer, and the local element form drag. The openage factors, $\beta$, are defined as the fraction of the area open to flow. For nonuniform roughness, the form drag force on the control volume is due to the roughness elements penetrating the control volume and is expressed using a local drag coefficient as

$$F_D=\frac{1}{2}\rho u^2\delta y\sum_{i=1}^{N_r} C_{D,i}d_i(y). \tag{1}$$

Likewise, the rate of heat transfer between the elements penetrating the control volume and the fluid is expressed using a local Nusselt number as

$$Q=\pi k_f(T_R-T)\,\delta y\sum_{i=1}^{N_r} \mathrm{Nu}_{d,i}\,. \tag{2}$$

Using the above ideas, the continuity, momentum, and energy equations for a steady, Reynolds-averaged two-dimensional turbulent boundary layer with nonuniform roughness become

$$\frac{\partial}{\partial x}(\rho\beta_x u)+\frac{\partial}{\partial y}(\rho\beta_y v)=0 \tag{3}$$

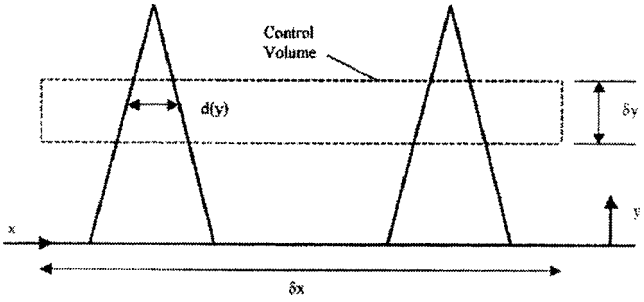


**Fig. 1 The discrete element roughness model control volume schematic for conical roughness elements**

$$\beta_x\rho u\frac{\partial u}{\partial x}+\beta_y\rho v\frac{\partial u}{\partial y}=-\frac{\partial}{\partial x}(\beta_x P)+\frac{\partial}{\partial y}\left[\beta_y\left(\mu\frac{\partial u}{\partial y}-\overline{\rho u'v'}\right)\right]-\frac{1}{2}\rho\frac{u^2}{L_pL_t}\sum_{i=1}^{N_r} C_{D,i}d_i \tag{4}$$

and

$$\beta_x\rho u\frac{\partial H}{\partial x}+\beta_y\rho v\frac{\partial H}{\partial y}=\frac{\partial}{\partial y}\left[\beta_y\left(\frac{k_f}{c_p}\frac{\partial H}{\partial y}-\overline{\rho v'h'}\right)\right]+u\frac{\partial}{\partial x}(\beta_x P)+\beta_y\frac{\partial u}{\partial y}\left(\mu\frac{\partial u}{\partial y}-\overline{\rho u'v'}\right)+\frac{1}{2}\rho\frac{u^3}{L_pL_t}\sum_{i=1}^{N_r} C_{D,i}d_i+\frac{\pi k_f}{L_pL_t}(T_R-T)\sum_{i=1}^{N_r}\mathrm{Nu}_{d,i} \tag{5}$$

where $\beta$ is the fraction of area open to flow, which is $(1-\alpha)$ where $\alpha$ is the blockage fraction, and $L_p$ and $L_t$ are the parallel and transverse spacing parameters for uniform roughness or the parallel length or transverse width of the control volume for nonuniform roughness. The above equations are rigorously derived in Taylor [8]. The boundary conditions for Eqs. (3), (4), and (5) are

$$\begin{aligned} &y=0: u=v=0, \quad H=H_w \\ &y\to\infty: u=U_e, \quad H=H_e\,. \end{aligned} \tag{6}$$

The turbulence model is not modified to include roughness effects since the physical effects of the roughness on the flow are explicitly included in the differential equations. The Prandtl mixing length with van Driest damping is used for turbulence closure. Hence

$$-\overline{\rho u'v'}=\rho l_m^2\left(\frac{\partial U}{\partial y}\right)\left|\frac{\partial U}{\partial y}\right| \tag{7}$$

where

$$l_m=\begin{cases} 0.41y[1-\exp(-y^+/26)] & \text{for } l_m\leqslant 0.09\delta \\ 0.09\delta & \text{otherwise.}\end{cases} \tag{8}$$

Closure in the energy equation is achieved using a turbulent Prandtl number, $\mathrm{Pr}_t$, of 0.9.

In addition to the usual turbulence modeling closure requirements for $-\overline{\rho u'v'}$, $\overline{u'^2}$, and $-\overline{\rho v'h'}$, the roughness model has closure requirements for $C_D$ and $\mathrm{Nu}_d$. $C_D$ and $\mathrm{Nu}_d$ are formulated as functions of the local roughness element Reynolds number

$$\mathrm{Re}_d=\frac{\rho u(y)d(y)}{\mu} \tag{9}$$

thus directly including information on the roughness element size and shape. The functional forms for $C_D$ and $\mathrm{Nu}_d$ used in this study for circular roughness elements are

$$C_D=\begin{cases}\left(\dfrac{\mathrm{Re}_d}{1000}\right)^{-0.125} & \mathrm{Re}_d<60{,}000 \\ 0.6 & \mathrm{Re}_d>60{,}000\end{cases} \tag{10}$$

and

$$\mathrm{Nu}_d=\begin{cases}1.7\,\mathrm{Re}_d^{0.49}\mathrm{Pr}^{0.4} & \text{for } \mathrm{Re}_d\leqslant 13{,}776 \\ 0.0605\,\mathrm{Re}_d^{0.84}\mathrm{Pr}^{0.4} & \text{for } \mathrm{Re}_d>13{,}776\end{cases}. \tag{11}$$

The functional form for $C_D$ was determined by extensive calibrations using a number of deterministic surface roughness data sets, [8,12]. This functional form yields good skin friction predictions with a wide range of uniform surface roughness shapes and

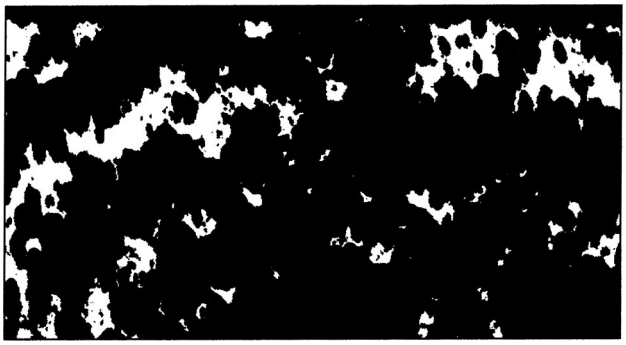

**Fig. 2 Randomly rough surface blockage at 25% elevation**

distributions from a number of data sets, [8,12]. The functional form for $\mathrm{Nu}_d$ was chosen for use in this study because of its accuracy for roughness-element Reynolds numbers less than 1000, [12].

Once the boundary layer equations have been solved, the skin friction coefficient is evaluated as

$$C_f = \frac{(1-\alpha)\mu \left.\frac{du}{dy}\right|_{y=0} + \frac{1}{2}\frac{1}{L_t L_p}\int_0^\infty (\rho u^2 \Sigma_{i=1}^{N_r} C_{D,i} d_i) dy}{\frac{1}{2}\rho U_e^2} \quad (12)$$

and the Stanton number is determined using the expression

$$\mathrm{St} = \frac{-(1-\alpha)k_f \left.\frac{dT}{dy}\right|_{y=0} + \frac{1}{L_t L_p}\int_0^\infty \pi k_f (T_R - T)\Sigma_{i=1}^{N_r} \mathrm{Nu}_{d,i} dy}{\rho U_e c_p (T_w - T_e)}. \quad (13)$$

Equations (12) and (13) demonstrate that the skin friction on a rough surface is the sum of the shear force on the flat part of the surface and the drag on the individual roughness elements and that the heat transfer between a flow and a rough surface is evaluated as the sum of the convection through the fluid in contact with the flat surface and the heat transferred between the fluid and the individual roughness elements.

**Randomly Rough Surface Adaptations.** The discrete element roughness model was validated for a series of sparse cones, spheres, or hemispheres placed on a flat surface. For these deterministic type surfaces, the computational field began at the flat surface and extended into the freestream. A randomly rough surface does not have an obvious reference surface. A reference or datum is needed for the application of the boundary conditions in solving the boundary layer equations. A reference surface at the minimum elevation makes sense for the blockage-fraction evaluation, but the roughness model needs both blockage-fraction and blockage-diameter distributions. For random roughness with closely spaced roughness features below the mean elevation, the concept of a blockage diameter is not appropriate. Because all of the blockage elements are connected, the effective diameter of the blockages becomes the length of the profilometer trace. In fact, below the mean elevation, most of the flow is blocked, and an ''openage'' diameter is more appropriate.

**Figure 2** shows the blockage of a randomly rough surface at an elevation of 25% of the minimum valley-to-maximum peak. Areas blocked from flow are shown in black, while areas open to flow are shown in white. **Figure 2** demonstrates that although a blockage fraction can be calculated (84.1%), determining a blockage diameter is not appropriate. The discrete element model assumes that the fluid flows around the blockages, but from **Fig. 2**, the only way that fluid can get from one open region to another is to flow over the blockages. That motion results in secondary-flow phenomena not considered in the discrete element model.

**Randomly Rough Datum or Reference.** Schlichting suggested an alternative for a reference surface. Schlichting used wall-variable plots to determine equivalent sand-grain roughness values as compared to Nikuradse's earlier experiments, [1,2]. To evaluate the sand-grain roughness values, the correct reference height had to be used. Schlichting found that the most meaningful results were obtained if what Taylor [8] called the ''melt down'' surface was used as the reference height. The ''melt down'' surface is the resulting surface if all of the material were melted down and allowed to solidify with a constant height in the same area. The ''melt down'' surface is equivalent to a surface placed at the mean height of a rectangular surface, as evaluated using Eq. (14).

$$h_m = \frac{\int_0^{L_p}\int_0^{L_t} y(x,z)\,dz\,dx}{L_p L_t} \quad (14)$$

This reference surface worked well, but Schlichting did not present a justification of this choice.

Taylor [8] ran the discrete element model for a series of closely packed hemispheres with differing reference heights and compared the results to the experimental results. Taylor found that the discrete element predictions agreed best when the ''melt down'' height of the closely packed hemispheres was used as the reference surface. Taylor did not speculate on a physical justification for this choice of reference height.

The best argument for using the height of the mean elevation relates to the nature of the discrete element model, a spatially averaged method for evaluating the effects of surface roughness. The mean elevation is the average height of the ''no-slip'' location along the surface. Consequently, the mean elevation acts as the reference height for spatially averaged analysis of flow over a rough surface.

**Effect of Flow Area Below the Mean Elevation.** Below the mean elevation, there is flow which contributes to friction drag as well as to heat transfer, but in this model, solving the boundary layer equations requires the application of the ''no-slip'' condition at the mean elevation. Equation (12) is the expression used to evaluate the skin friction coefficient for a flow over a rough surface. In Eq. (12), $y=0$ is the ''no-slip'' location. The two terms in the numerator of Eq. (12) represent the contributions of skin friction on the smooth part of the wall and roughness-element drag. The method used for this study treats any point below the mean elevation as a flat surface at the mean elevation and adds the skin friction associated with the flat surface of the mean elevation. The blockage fraction, $\alpha$, at the mean elevation is used in Eq. (12) to calculate the drag associated with the skin friction. This maintains consistency with the spatially averaged model and the boundary layer equations. The Stanton number is also evaluated for randomly rough surfaces by adding the heat convected from the roughness elements and the heat convected from the flat surface area on the mean elevation.

With the above changes, the boundary conditions for the discrete element model for randomly rough surfaces are

$$\begin{aligned} y = y_{me} &: u = v = 0, \quad H = H_w \\ y \to \infty &: u = U_e, \quad H = H_e. \end{aligned} \quad (15)$$

The expressions for the skin friction coefficient and Stanton number are

$$C_f = \frac{(1-\alpha)\mu \left.\frac{du}{dy}\right|_{y=y_{me}} + \frac{1}{2}\frac{1}{L_t L_p}\int_{y_{me}}^\infty (\rho u^2 \Sigma_{i=1}^{N_r} C_{D,i} d_i) dy}{\frac{1}{2}\rho U_e^2} \quad (16)$$

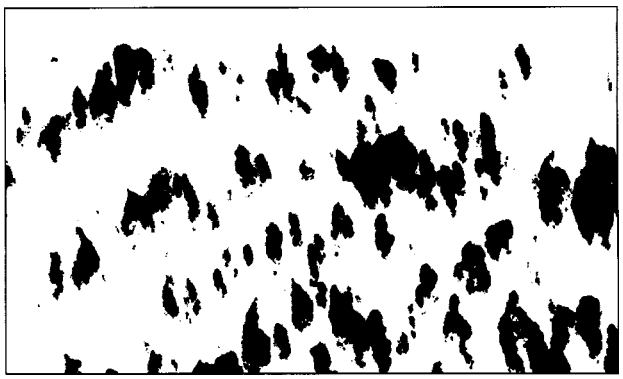

**Fig. 3 Randomly rough surface blockage at 60% elevation**

and

$$\mathrm{St}=\frac{-(1-\alpha)k_f\left.\frac{dT}{dy}\right|_{y=y_{me}}+\frac{1}{L_tL_p}\int_{y_{me}}^{\infty}\pi k_f(T_R-T)\Sigma_{i=1}^{N_r}\mathrm{Nu}_{d,i}dy}{\rho U_e c_p(T_w-T_e)} \tag{17}$$

where $y_{me}$ is the height of the mean elevation of the randomly rough surface.

**Noncircular Roughness Element Corrections.** **Figure 3** shows the roughness elements for the same randomly rough surface presented in **Fig. 2** at an elevation of 60% of the minimum valley to the maximum surface height. For the surface in **Fig. 3**, the direction of flow is from top to bottom. **Figure 3** demonstrates that the random roughness elements for this surface are not circular in general. While the surface represented in **Fig. 3** is anisotropic, the roughness element cross-sections of isotropic surface roughness are likely to be noncircular.

The local drag coefficient and Nusselt numbers must be calculated for each roughness element at a given height. Observing Eqs. (10) and (11), the local drag coefficient and Nusselt number are determined as a function of the local Reynolds number. For circular roughness elements, the characteristic length used to calculate the local Reynolds number is the diameter. For random roughness elements that are not circular, a physically meaningful characteristic length to calculate local Reynolds numbers is the maximum width of the roughness element in the direction transverse to the flow. The local element drag coefficients and Nusselt numbers may be determined using Eqs. (9), (10), and (11) using the maximum width of the random roughness element. This option for determining local drag and heat transfer is called the circular discrete element model.

**Elliptical Discrete Element Model.** Revisiting **Fig. 3**, the roughness elements for that surface appear elongated in the direction of the flow. This elongation provides some relieving effect on the drag. To account for this, an elliptical discrete element drag model was developed. **Figure 4** shows an ellipsoidal blockage aligned with the major axis parallel to the flow direction. The eccentricity, $\varepsilon$, of the blockage is defined as the ratio of the maximum width perpendicular to the flow direction to the maximum length of the blockage parallel to the flow direction.

$$\varepsilon=\frac{2a}{2b}=\frac{a}{b} \tag{18}$$

Using the elliptical discrete element model, the maximum width of the roughness element and the eccentricity are used to calculate the local drag and heat transfer. A representation of an actual roughness element and its elliptical model are presented in **Figs. 5**(***a***) and **5**(***c***). **Figure 5**(***b***) presents a circular model of the

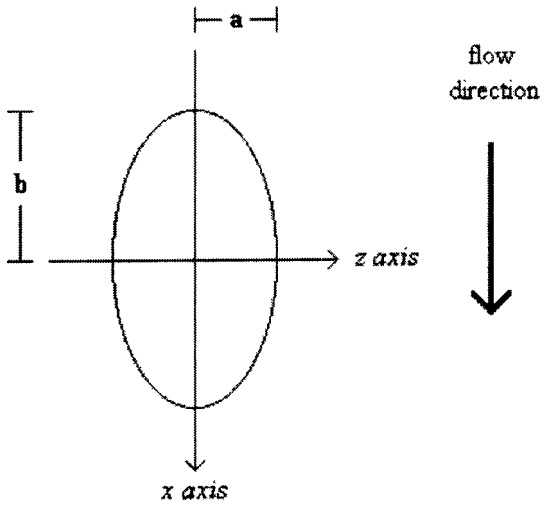


**Fig. 4 An elliptical roughness element**

random roughness element. **Figure 5** visually demonstrates the differences in an actual roughness element and the circular and elliptical discrete element models.

To determine a local drag coefficient function for elliptical blockages, drag coefficient data from Lindsey [13] and Delany and Sorensen [14] for elliptical cylinders of varying eccentricities with transverse thickness Reynolds numbers around $1\times10^5$ are plotted in **Fig. 6**. A function of eccentricity which best represented these data was found by determining the log-log regression curve of the form shown below.

$$C_{D,\mathrm{Re}=10^5}=c\varepsilon^g \tag{19}$$

The constants $c$ and $g$ were found to be 0.97379 and 0.73456, respectively. Since the constant $c$ is close to unity and since the eccentricity function should equal unity when the blockage element is circular, the constant $c$ was set to unity. The eccentricity function with $c$ set to unity is not a true regression curve, but the eccentricity function represents the trend of the data. The resulting eccentricity function, $\varepsilon^{0.73456}$, is also shown in **Fig. 6.**

The circular blockage element drag function, Eq. (10), was then multiplied by the eccentricity function to yield an ellipsoidal blockage element drag function, as shown in Eq. (20).

$$C_D=\begin{cases}\left(\dfrac{\mathrm{Re}_d}{1000}\right)^{-0.125}\varepsilon^{0.73456} & \mathrm{Re}_d<60{,}000\\ 0.6\varepsilon^{0.73456} & \mathrm{Re}_d>60{,}000\end{cases} \tag{20}$$

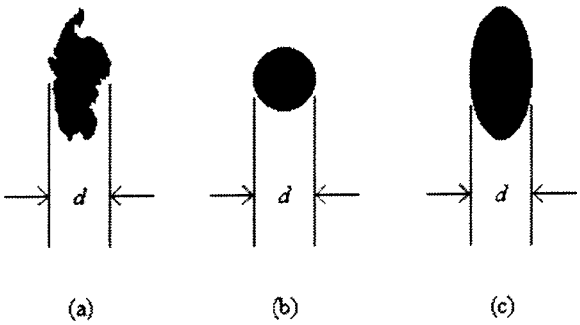


**Fig. 5 Example roughness element representation: (*a*) actual roughness element, (*b*) circular roughness element with same transverse width, (*c*) elliptical element with same transverse width and eccentricity**

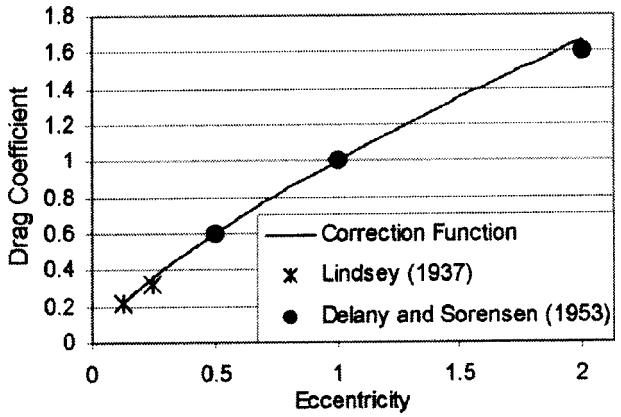


**Fig. 6 Drag coefficients of elliptical cylinders with varying eccentricities, [13,14]**

Roughness element eccentricity has a two-fold effect on the local heat transfer from the roughness elements as compared to circular roughness elements. Eccentricity changes the average convection coefficient around elliptical roughness elements, and eccentric roughness elements have different ''wetted'' surface areas than circular roughness elements with equivalent transverse widths.

An attempt was made to evaluate an eccentricity factor to multiply the circular element Nusselt relationships as was performed for the local drag coefficient relationship in Eq. (20) based on measurements made by Reiher [15] as presented by Jacob [16]. Jacob [16] presented Hilpert constants for the Nusselt numbers of two elliptical cylinders with lower Reynolds number limits of 1400. Because of the lack of experimental data on Nusselt numbers of elliptical cylinders in crossflow at Reynolds numbers below 1000, which is important for the rough-wall boundary layers of this study, the circular Nusselt number relationship, Eq. (11), is used in the elliptical discrete element model.

While sufficient data do not exist to correct for elliptical element Nusselt numbers, the increased surface area of elliptical roughness elements as compared to circular roughness elements is evaluated in the elliptical discrete element model. From the *Machinery's Handbook* [17], a good approximation of the perimeter of the ellipse shown in **Fig. 5** is

$$P_{re}=\pi\left[2(a^2+b^2)-\frac{(a-b)^2}{2.2}\right]^{1/2}. \tag{21}$$

With the changes in the perimeter of the elliptical elements the boundary layer energy equation, Eq. (5), becomes

$$\begin{aligned}\beta_x\rho u\frac{\partial H}{\partial x}+\beta_y\rho v\frac{\partial H}{\partial y}=&\frac{\partial}{\partial y}\left[\beta_y\left(\frac{k_f}{c_p}\frac{\partial H}{\partial y}-\overline{\rho v' h'}\right)\right]+u\frac{\partial}{\partial x}(\beta_x P)\\&+\beta_y\frac{\partial u}{\partial y}\left(\mu\frac{\partial u}{\partial y}-\overline{\rho u' v'}\right)\\&+\frac{1}{2}\rho\frac{u^3}{L_p L_t}\sum_{i=1}^{N_r}C_{D,i}d_i\\&+\frac{\pi k_f}{L_p L_t}(T_R-T)\sum_{i=1}^{N_r}K_{\varepsilon,i}\mathrm{Nu}_{d,i}\end{aligned} \tag{22}$$

where

$$K_\varepsilon=\left[\frac{1}{2}\left(1+\frac{1}{\varepsilon^2}\right)-\frac{1}{8.8}\left(1-\frac{1}{\varepsilon}\right)^2\right]^{1/2}. \tag{23}$$

While random roughness elements are neither circular nor elliptical, the increased surface area associated with the elliptical roughness model will provide more accurate heat transfer predictions.

## Experimental Methodology

Two real randomly rough surfaces found on actual gas turbine blades were studied. The two surfaces were chosen because they reflected different manifestations of random roughness found on gas turbines blades. One surface studied exhibited large anisotropic roughness elements created by fuel deposits solidifying on the blade. The second surface exhibited smaller isotropic roughness elements created by erosion.

The surface-roughness measurements were made using a Taylor-Hobson, Form Talysurf Series 2 profilometer, hence referred to as a Talysurf 2. The Talysurf 2 used in the study employed an inductive measurement system with a 1-mm range in the vertical measurement direction, a 90 deg conisphere diamond stylus with 2-$\mu$m nominal radius tip, and a vertical resolution of 16 nm. A Stratasys Genisys Xs three-dimensional printer was used to create scaled plastic replicas, coupons, of the rough surfaces. The geometrical scaling factors for each surface are listed in Bons [7]. The Genisys Xs printer generates three-dimensional models with a resolution of 0.33 mm using a durable polyester. The printed surfaces were placed in a wind tunnel for testing.

The wind tunnel used in this study is housed at the Air Force Research Laboratory (AFRL) at Wright-Patterson Air Force Base in Dayton, OH. The skin friction coefficients were determined by suspending the roughness panels in the wind tunnel using wires attached to the wind-tunnel framing and measuring the downstream movement of the panels during a test. Bons [7] reports a systematic uncertainty (bias) of 0.00022 in the measured skin friction coefficients with a 2.8% random uncertainty (repeatability).

A transient method was used to determine the convective heat transfer coefficient from the rough surfaces. The method used to evaluate the convection coefficient is based on the method of Schultz and Jones [18]. Using the temperature responses of both the fluid and the roughness panel as heated air is blown over the panels, the average convection coefficient was calculated. Bons [7] reports a systematic uncertainty of 0.00008 in the measured Stanton numbers with a 3% random uncertainty. Detailed information on the wind tunnel, the average skin friction coefficient determination technique, and the average convection coefficient determination method can be found in Bons [7]. Detailed information on the simulations and their comparisons to the experimental data can be found in McClain [19].

To compare to the discrete element predictions for the surface, a Stanton number was calculated based on the convection coefficient using Eq. (24). The Stanton number is defined as the heat flux divided by the dynamic energy difference between the wall and the freestream.

$$\mathrm{St}=\frac{q''}{\rho_e U_e c_{p,e}(T_e-T_w)}=\frac{\overline{h}}{\rho_e U_e c_{p,e}} \tag{24}$$

## Surface Descriptions

Two randomly rough surfaces, the deposit surface and the erosion-2 surface, were used in the modeling study. The deposit surface contains relatively large, anisotropic roughness elements aligned in the direction of the flow. The deposit surface has a centerline average roughness, $Ra$, of 1.183 mm, where

$$Ra=\frac{1}{N}\sum_{i=1}^{N}|y_i| \tag{25}$$

The average eccentricity of the roughness elements of the deposit surface is 0.8. A bitmap image of a section of the deposit surface is shown in **Fig. 7**. The ''as-printed'' dimensions of the surface depicted in **Fig. 7** is 240 mm by 130 mm. The height difference from minimum valley (black) to maximum peak

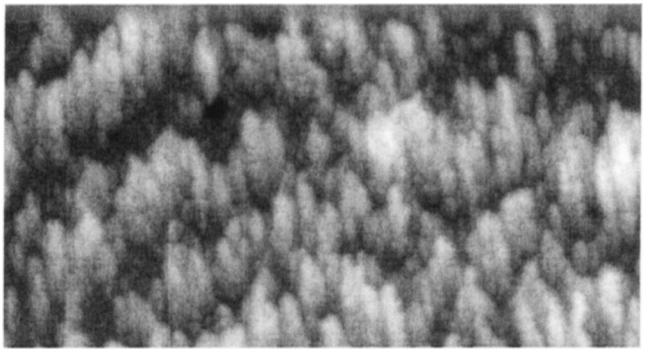

**Fig. 7 Bitmap image of the deposit surface (flow direction is top to bottom)**

(white) is 8.11 mm. The erosion-2 surface contains smaller roughness elements elongated in the direction transverse to the flow direction. The erosion-2 surface has a centerline average roughness of 0.504 mm. The average eccentricity of the roughness elements of the erosion-2 surface is 1.5. A bitmap image of a section of the erosion-2 surface is shown in **Fig. 8**. The ''as-printed'' dimensions of the surface depicted in **Fig. 8** is 140 mm by 60 mm. The height difference from minimum valley to maximum peak is 4.23 mm.

Along with the randomly rough surfaces, two layered-analog surfaces were studied. The surfaces were derived from the deposit surface and the erosion-2 surface. The spacings and heights of the roughness elements are random as measured from the original randomly rough surface, but the roughness elements were generated by placing ellipsoidal blockages of equivalent area and eccentricity at the height of the original random blockage element. Because the blockage elements were created at distinct heights between the mean elevation and the maximum elevation of the surface, the surfaces have a ''layered'' appearance. The layered representation of the deposit surface, the deposit-layered surface,

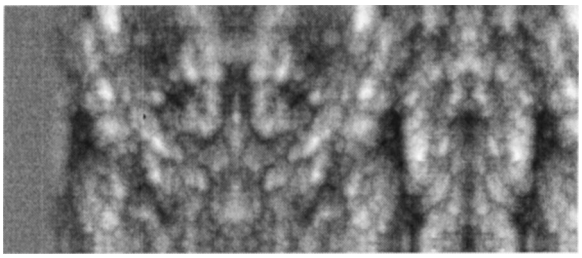

**Fig. 8 Bitmap image of the erosion-2 surface (flow direction is left to right)**

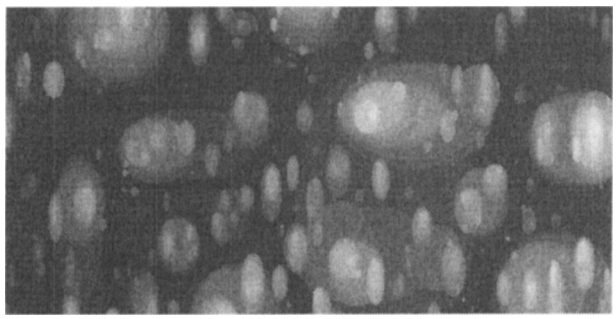

**Fig. 9 Bitmap image of the deposit-layered surface (flow direction is top to bottom)**

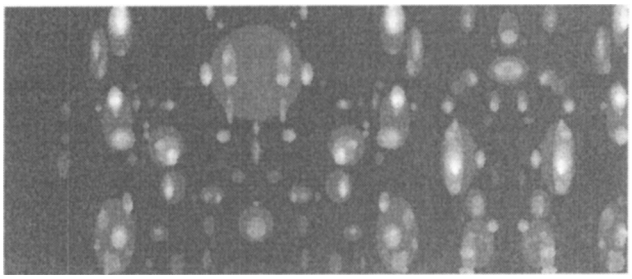

**Fig. 10 Bitmap image of the erosion-2-layered surface (flow direction is left to right)**

is shown in **Fig. 9**. The layered representation of the erosion-2 surface, the erosion-2-layered surface, is shown in **Fig. 10**.

## Results and Discussion

All of the discrete element skin friction coefficient and Stanton number predictions for the random or layered surfaces were referenced to the mean elevations of the respective surfaces with the roughness element temperature equal to the temperature at the mean elevation. The skin friction coefficient predictions were made using the following options for each surface:

1. the eccentricities of all of the roughness elements set to unity in the prediction (representing the circular discrete element results)
2. the average eccentricity for each surface used in the prediction ($\varepsilon=0.8$ for the deposit and deposit-layered surfaces, and $\varepsilon=1.5$ for the erosion-2 and the erosion-2-layered surfaces)
3. the measured eccentricity of each roughness element used in the prediction

The circular discrete element skin friction coefficient predictions, $C_{f,\mathrm{cir}}$, the elliptical discrete element predictions using an average eccentricity, $C_{f,\varepsilon\mathrm{ave}}$, the elliptical discrete element predictions using each measured roughness element eccentricity, $C_{f,\varepsilon}$, and the experimentally measured skin friction coefficients, $C_{f,\mathrm{meas}}$, are presented in **Table 1** for the high Reynolds numbers and in **Table 2** for the low Reynolds numbers.

It should be noted that the Reynolds numbers' designation as ''high'' or ''low'' are compared only to the Reynolds numbers used in this study. A typical turbine blade chord Re is 500,000 to 2,000,000. The finite range used in this study is in the low to midrange of typical gas turbine chord Reynolds numbers.

**Tables 1 and 2** show that the circular discrete element model overestimated the skin friction for the deposit and deposit-layered surfaces ($\varepsilon_{\mathrm{ave}}\approx 0.8$) for both the high and low Reynolds number cases. **Tables 1 and 2** also indicate that the circular discrete element model underestimated the skin friction for the erosion-2 and the erosion-2-layered surfaces ($\varepsilon_{\mathrm{ave}}\approx 1.5$). The facts that the circular discrete element model overestimates the skin friction for the deposit and deposit-layered surfaces and that it underestimates

**Table 1 Comparison of the random and layered surface skin friction coefficient results and discrete element predictions at high Reynolds numbers**

| Surface | $\mathrm{Re}_{\bar{x}}$ | $C_{f,\mathrm{meas}}$ | $C_{f,\mathrm{cir}}$ (% diff) | $C_{f,\varepsilon\mathrm{ave}}$ (% diff) | $C_{f,\varepsilon}$ (% diff) |
|---|---|---|---|---|---|
| Deposit | 924800 | 0.00937 | 0.00988 (5.4) | 0.00921 (−1.7) | 0.00891 (−4.9) |
| Deposit layered | 927500 | 0.00674 | 0.00726 (7.7) | 0.00676 (0.3) | 0.00667 (−1.1) |
| Erosion 2 | 925700 | 0.01030 | 0.00945 (−8.2) | 0.01047 (1.6) | 0.01053 (2.2) |
| Erosion 2 layered | 921900 | 0.00838 | 0.00736 (−12.2) | 0.00819 (−2.3) | 0.00850 (1.5) |

**Table 2 Comparison of the random and layered surface skin friction coefficient results and discrete element predictions at low Reynolds numbers**

| Surface | $Re_{\bar{x}}$ | $C_{f,\text{meas}}$ | $C_{f,\text{cir}}$ (% diff) | $C_{f,\varepsilon\text{ave}}$ (% diff) | $C_{f,\varepsilon}$ (% diff) |
|---|---|---|---|---|---|
| Deposit | 517300 | 0.00928 | 0.00959 (3.3) | 0.00894 (−3.7) | 0.00863 (−7.0) |
| Deposit layered | 517700 | 0.00688 | 0.00702 (2.1) | 0.00656 (4.6) | 0.00645 (−6.3) |
| Erosion 2 | 518300 | 0.00980 | 0.00879 (−10.3) | 0.00974 (−0.6) | 0.00979 (−0.1) |
| Erosion 2 layered | 516200 | 0.00797 | 0.00685 (−14.1) | 0.00757 (−5.0) | 0.00783 (−1.7) |

**Table 3 Comparison of the random and layered surface Stanton number results and discrete element predictions at high Reynolds numbers**

| Surface | $Re_{\bar{x}}$ | $St_{\text{meas}}$ | $St_{\text{cir}}$ (% diff) | $St_{\varepsilon\text{ave}}$ (% diff) | $St_{\varepsilon}$ (% diff) |
|---|---|---|---|---|---|
| Deposit | 905500 | 0.00308 | 0.00303 (−1.7) | 0.00321 (4.1) | 0.00349 (13.2) |
| Deposit Layered | 874000 | 0.00274 | 0.00242 (−11.8) | 0.00248 (−9.4) | 0.00265 (−3.5) |
| Erosion 2 | 901900 | 0.00308 | 0.00349 (13.4) | 0.00324 (5.2) | 0.00334 (8.6) |
| Erosion 2 Layered | 871000 | 0.00313 | 0.00295 (−5.8) | 0.00285 (−9.0) | 0.00286 (−8.7) |

the skin friction for the erosion-2 and erosion-2-layered surfaces emphasize and reinforce the importance of considering roughness anisotropy or roughness element eccentricity in the discrete element model.

**Tables 1 and 2** show that agreement between the measured skin friction coefficients and the elliptical discrete element predictions using the average eccentricity for each surface is excellent. At the high Reynolds number, the maximum percentage difference is 2.3%. At the low Reynolds number, the maximum percentage difference is 5.0%. Agreement between $C_{f,\text{meas}}$ and $C_{f,\varepsilon\text{ave}}$ is excellent with the maximum percentage difference of 5%.

Very good agreement is also reported in **Tables 1 and 2** between the experimentally measured skin friction coefficients and the elliptical discrete element predictions generated using the measured eccentricities for each individual roughness element. For the high Reynolds number cases, the maximum percentage difference between the predictions and the experimental friction coefficients is 4.9%. For the low Reynolds number cases, the maximum percentage difference is 7.0%.

Agreement between the elliptical discrete element predictions and the measured skin friction coefficients is better for the erosion-2 and erosion-2-layered surfaces than for the deposit and deposit-layered surfaces. **Tables 1 and 2** show that the maximum percentage difference for the erosion-2 or the erosion-2-layered surfaces is 2.2% when using each measured roughness-element eccentricity. The maximum percentage difference for the deposit and deposit-layered surfaces is 7.0%. The skin friction coefficient predictions for the deposit and deposit-layered surfaces have higher percentage differences from the measured values for the low Reynolds number cases. This suggests that the eccentricity function developed for the elemental drag function in Eq. (3.4) may underestimate drag at low Reynolds numbers for roughness elements with eccentricities less than unity. While the elemental drag relationships may need slight calibration for low Reynolds numbers and roughness elements elongated in the direction of the flow, agreement within 10% of the measured skin friction coefficients is considered very good.

The close agreement of the elliptical discrete element predictions also confirms the validity of referencing the discrete element analysis to the mean elevation of the rough surfaces and including shear drag on the area of reference surface not blocked by roughness elements. One of Nikuradse's [2] important findings was that for laminar flow, friction factors in rough pipes were the same as for smooth pipes. Bons [7] reports that the values of $k^+$ for the deposit and erosion-2 surfaces are much greater than the limit set for completely rough flow. The validity of referencing the analysis to the mean elevation and including shear drag on the "open" area at the mean elevation suggests that while the laminar sublayer region is usually considered destroyed in completely rough flow, there may still be a viscous-dominated region below the mean elevation which tends to attenuate the effects of the surface features below the mean elevation.

The Stanton number predictions were made using the same three options for handling the element eccentricity as were used for the skin friction coefficient predictions. The circular discrete element Stanton number predictions, $St_{\text{cir}}$, the elliptical discrete element predictions using an average eccentricity, $St_{\varepsilon\text{ave}}$, the elliptical discrete element predictions using each measured roughness element eccentricity, $St_{\varepsilon}$, and the experimentally measured Stanton numbers, $St_{\text{meas}}$, are presented in **Table 3** for the high Reynolds numbers and in **Table 4** for the low Reynolds numbers

**Tables 3 and 4** show that agreement between the experimental measurements and the discrete element predictions is good for all three discrete element model variations for handling the roughness element eccentricity. None of the three options for handling the roughness element eccentricities is clearly better than the other two.

The most interesting observation from **Tables 3 and 4** is that, in general, all three variations of handling the eccentric roughness elements overestimate the Stanton numbers for the randomly rough surfaces and underestimate the Stanton numbers for the layered surfaces. One possible reason the discrete element model overestimates the measured Stanton numbers for the randomly rough surfaces is the surface area for heat transfer calculated using either the circular or elliptical discrete element model is not appropriate for random-roughness elements. **Figure 4** shows a random roughness element with its circular and elliptical discrete element equivalent determined using the maximum width of the random-roughness element and its eccentricity. Neither of the equivalent roughness elements has the same "wetted" area as the random roughness element. Along these same lines, the circular Nusselt number correlation, Eq. (11), was used in each discrete element prediction. The circular Nusselt correlation may be underestimating the local Nusselt numbers for the elliptical roughness elements of the layered surfaces and overestimating the local Nusselt numbers for the random-roughness elements.

Several phenomena not considered in the discrete element predictions are affecting the heat transfer predictions. Even without considering these phenomena, the predictions are in good agree-

**Table 4 Comparison of the random and layered surface Stanton number results and discrete element predictions at low Reynolds numbers**

| Surface | $Re_{\bar{x}}$ | $St_{\text{meas}}$ | $St_{\text{cir}}$ (% diff) | $St_{\varepsilon\text{ave}}$ (% diff) | $St_{\varepsilon}$ (% diff) |
|---|---|---|---|---|---|
| Deposit | 514950 | 0.00341 | 0.00345 (1.1) | 0.00364 (6.7) | 0.00395 (15.8) |
| Deposit Layered | 546100 | 0.00296 | 0.00266 (−10.1) | 0.00273 (−7.9) | 0.00290 (−1.9) |
| Erosion 2 | 519350 | 0.00329 | 0.00375 (14.0) | 0.00353 (7.2) | 0.00363 (10.3) |
| Erosion 2 Layered | 551400 | 0.00331 | 0.00313 (−5.5) | 0.00305 (−7.8) | 0.00307 (−7.4) |

ment with the measured Stanton numbers. The maximum percentage difference between any of the discrete element predictions and the measured Stanton numbers was 15.8%.

## Conclusions

Randomly rough surfaces differ considerably from the ordered-rough surfaces that Taylor used to derive and validate the discrete element model. The discrete element model was adapted for use with randomly rough surfaces. For randomly rough surfaces, there is no ''flat surface.'' Random roughness elements have varying height and frontal area shapes. The plan-form sizes and shapes of the random roughness elements also vary.

This study focused on characterizing a randomly rough surface using three-dimensional profilometery for the discrete element model, on evaluating an appropriate reference elevation for randomly rough surfaces, and on evaluating the effects of varying plan-form roughness-element shapes.

The mean elevation or mean height of the randomly rough surfaces was used as the reference elevation. For a randomly rough surface, the ''no-slip'' condition is applied at the mean elevation. The total drag on a randomly rough surface is then the sum of the drag on the roughness elements and the shear force acting on the plan-form area at the mean elevation that is not blocked by roughness elements.

The element eccentricity was incorporated in the discrete element model to account for random roughness-element plan-form shapes and roughness anisotropy. A term was added to account for the roughness element eccentricity in the local element drag coefficient relationship. While the local element Nusselt number correlation was not changed, the change in wetted surface area associated with noncircular shapes was included in the local element heat transfer calculations.

Using the model adaptations, skin friction coefficient predictions were made for each of the surfaces and flow situations observed in the wind tunnel. The skin friction predictions for the randomly rough surfaces and the layered-roughness surfaces was excellent when referenced to the mean elevation and including the element eccentricity in the local drag correlation. The maximum percentage difference between the measured skin friction coefficient and the discrete element prediction using the eccentric drag correlations was 7.0%. The maximum percentage difference occurred for the low Reynolds number cases on the deposit surface. The maximum percentage difference for the erosion-roughness surfaces was 2.2%. The roughness elements on the deposit and deposit-layered surfaces had average eccentricities around 0.8, and the roughness elements on the erosion-2 and erosion-2-layered surfaces exhibited average eccentricities around 1.5. Because of the excellent agreement for the erosion surfaces and the differences between the predictions and measured skin friction coefficients for the fuel-deposit surfaces at low Reynolds numbers, the eccentric-element drag correlations may need more calibration for eccentricities less than 1.0 at low Reynolds numbers. The excellent agreement between the measured skin friction coefficients and the discrete element predictions using the elliptical-element drag correlations demonstrates the relevance of using the mean elevation as the reference elevation when analyzing the flow over randomly rough surfaces. Using the circular-element drag correlation, the discrete element model overestimated the drag associated with the deposit and deposit-layered surfaces and underestimated the drag associated with the erosion-2 and erosion-2-layered surfaces. This demonstrated that element eccentricity must be considered in the discrete element model skin friction analysis.

Stanton number predictions were also made for each of the surfaces and flow situations observed in the wind tunnel. The Stanton number predictions for the random and layered surfaces made by referencing the discrete element model to the mean elevation were within 16% of the experimentally measured values. In the randomly rough Stanton number predictions, considering the element eccentricity in the wetted area calculations of local element heat transfer did not show a marked improvement. The discrete element Stanton number predictions using the elliptical-element wetted area calculations and the predictions using the circular element wetted area calculations were scattered around the experimentally measured Stanton numbers within the maximum percentage difference of 16%. Since the actual random-roughness-element wetted area and elliptical-element Nusselt correlations were not used in the predictions, agreement within 16% of the experimentally measured Stanton numbers is surprising and acceptable.


## Acknowledgments

This work was performed under sponsorship from the U.S. Department of Energy, the National Energy Technology Laboratory, and the South Carolina Institute for Energy Studies through the Advanced Land-Based Gas Turbine Systems Research Consortium (AGTSR). The authors also gratefully acknowledge the assistance of Dr. Robert Taylor and the assistance of Dr. Richard Rivir in the wind tunnel measurements.


## Nomenclature

$A$ = blockage area
$a$ = maximum width of elliptical element in transverse direction
$b$ = maximum length of elliptical element in streamwise direction
$C_D$ = local element drag coefficient
$C_f$ = skin friction coefficient
$d(y)$ = maximum transverse width of roughness element as function of distance from wall
$\underline{h}$ = specific enthalpy
$h$ = convection heat transfer coefficient
$h_m$ = mean surface height
$H$ = enthalpy
$k^+$ = $y^+$ evaluated at the point on the roughness element farthest from the wall
$k_f$ = fluid thermal conductivity
$K_\varepsilon$ = elliptical element area correction factor
$l_m$ = mixing length
$L_p$ = element spacing parameter in direction of flow
$L_t$ = element spacing parameter transverse to the flow direction
$N_r$ = number of roughness elements
$\mathrm{Nu}_d$ = local element Nusselt number
$P$ = pressure
$P_{re}$ = roughness element perimeter
$Q$ = local element heat transfer
$Ra$ = centerline-averaged roughness height
Re = Reynolds Number
St = Stanton number
$T$ = temperature
$t$ = time
$U_e$ = freestream velocity
$u$ = local streamwise velocity
$v$ = local velocity normal to wall
$\underline{x}$ = streamwise flow direction
$\overline{x}$ = distance from knife edge to center of roughness panel
$y$ = direction normal to wall
$y^+$ = nondimensional $y$; $y/\nu\sqrt{\tau_w/\rho}$
$z$ = transverse flow direction

**Greek**

$\alpha$ = blockage fraction
$\beta$ = openage fraction, $1-\alpha$
$\varepsilon$ = ellipse eccentricity
$\delta$ = boundary layer thickness
$\kappa$ = von Karman constant

$\mu$ = dynamic viscosity
$\nu$ = kinematic viscosity
$\rho$ = density
$\sigma$ = spatial variance
$\tau$ = shear
$\tau_w$ = shear at the no-slip surface

**Superscripts**

$'$ = turbulent fluctuating values

**Subscripts**

$R$ = roughness element
$e$ = edge of boundary layer or freestream value
$w$ = wall value

## References


[1] Schlichting, H., 1936, ''Experimental Investigation of the Problem of Surface Roughness,'' Ing.-Arch. **7**(1); NACA TM 823 (1937).
[2] Nikuradse, J., 1933, ''Laws for Flows in Rough Pipes,'' VDI-Forchung. 361, Series B, **4**; NACA TM 1292 (1950).
[3] Dvorak, F. A., 1969, ''Calculation of Turbulent Boundary Layers on Rough Surfaces in Pressure Gradients,'' AIAA J., **7**, pp. 1752–1759.
[4] Simpson, R. L., 1973, ''A Generalized Correlation of Roughness Density Effects on the Turbulent Boundary Layer,'' AIAA J., **11**, pp. 242–244.
[5] Dirling, R. B., 1973, ''A Method for Computing Rough Wall Heat Transfer Rates on Reentry Nose Tips,'' AIAA Paper No. 73–763.
[6] Sigal, A., and Danberg, J. E., 1990, ''New Correlation of Roughness Density Effect on the Turbulent Boundary Layer,'' AIAA J., **28**(3), pp. 554–556.
[7] Bons, J. P., 2002, ''St and $C_f$ Augmentation for Real Turbine Roughness with Elevated Freestream Turbulence,'' ASME J. Appl. Mech., **124**, pp. 632–644.
[8] Taylor, R. P., 1983, ''A Discrete Element Prediction Approach for Turbulent Flow Over Rough Surfaces,'' Ph.D. dissertation, Department of Mechanical and Nuclear Engineering, Mississippi State University.
[9] Finson, M. L., 1982, ''A Model for Rough Wall Turbulent Heating and Skin Friction,'' AIAA Paper 82-0199.
[10] Adams, J. C., and Hodge, B. K., 1977, ''The Calculation of Compressible Transitional Turbulent and Relaminarizational Boundary Layers Over Smooth and Rough Surfaces Using an Extended Mixing-Length Hypothesis,'' AIAA Paper 77-682.
[11] Lin, T. C., and Bywater, R. J., 1980, ''The Evaluation of Selected Turbulence Models for High-Speed Rough-Wall Boundary Layer Calculations,'' AIAA Paper 80-0132.
[12] Taylor, R. P., and Hodge, B. K., 1993, ''A Validated Procedure for the Prediction of Fully-Developed Nusselt Numbers and Friction Factors in Pipes With 3-Dimensional Roughness,'' J. of Enhanced Heat Transfer, **1**, pp. 23–35.
[13] Lindsey, W. F., 1938, ''Drag of Cylinders of Simple Shapes,'' NACA TR 619.
[14] Delany, N. K., and Sorensen, N. E., 1953, ''Low-Speed Drag of Cylinders of Various Shapes,'' NACA TN 3038.
[15] Reiher, H., 1925, ''Forschungsarb. a. d. Geb. d. Ingenieurwes,'' Forsch. Geb. Ingenieurwes., **269**.
[16] Jacob, M., 1949, *Heat Transfer*, John Wiley and Sons, New York.
[17] *Machinery's Handbook*, 1996, 25th Ed., Industrial Press, New York.
[18] Schultz, D. L., and Jones, T. V., 1973, ''Heat-Transfer Measurements in Short-Duration Hypersonic Facilities,'' Advisory Group for Aerospace Research and Development (165). NATO.
[19] McClain, S. T., 2002, ''A Discrete Element Model for Turbulent Flow Over Randomly Rough Surfaces,'' Ph.D. dissertation, Department of Mechanical Engineering, Mississippi State University.

**Paolo Boncinelli**
e-mail: Paolo.Boncinelli@icad.de.unifi.it

**Filippo Rubechini**

**Andrea Arnone**

"Sergio Stecco" Department of Energy Engineering,
University of Florence,
Via S. Marta, 3,
Florence 50139, Italy

**Massimiliano Cecconi**

**Carlo Cortese**
e-mail: Carlo.Cortese@np.ge.com

GE Oil & Gas Nuovo Pignone,
Via Felice Matteucci, 2,
Florence 50127, Italy

# Real Gas Effects in Turbomachinery Flows: A Computational Fluid Dynamics Model for Fast Computations

*A numerical model was included in a three-dimensional viscous solver to account for real gas effects in the compressible Reynolds averaged Navier-Stokes (RANS) equations. The behavior of real gases is reproduced by using gas property tables. The method consists of a local fitting of gas data to provide the thermodynamic property required by the solver in each solution step. This approach presents several characteristics which make it attractive as a design tool for industrial applications. First of all, the implementation of the method in the solver is simple and straightforward, since it does not require relevant changes in the solver structure. Moreover, it is based on a low-computational-cost algorithm, which prevents a considerable increase in the overall computational time. Finally, the approach is completely general, since it allows one to handle any type of gas, gas mixture or steam over a wide operative range. In this work a detailed description of the model is provided. In addition, some examples are presented in which the model is applied to the thermo-fluid-dynamic analysis of industrial turbomachines.*
[DOI: 10.1115/1.1738121]

## Introduction

In recent years, turbomachinery industry has continued to take more and more advantage of the capabilities of computational fluid dynamic (CFD) techniques in everyday activities. The aerodynamic analysis of components by means of three-dimensional viscous single-row/multistage, steady/unsteady computations has become a basic tool for the industrial design of turbomachines. The accuracy of the most modern numerical techniques allows one to predict both the main performance characteristics (specific work, efficiency) and the aerodynamic behavior, both at design conditions and in off-design, providing the designer with many useful details about the flow structure.

While reliable and robust numerical methodologies have been assessed for the spatial and temporal integration of the Reynolds averaged Navier-Stokes (RANS) equations, further efforts are made now to improve the analysis of some specific aspects of the flow: turbulence and transition modeling, heat transfer and thermophysical properties of the working fluid. In this work, attention is focused on the last topic.

In the design of industrial turbines and compressors, different evolving fluids are encountered, working over a wide range of thermodynamic operating conditions. In most cases, the perfect gas model is accurate enough to describe the physical characteristics of the fluid. However, there is a number of applications for which such an approach is not satisfactory. In steam turbine LP stages, thermodynamic transformations occur near or above the saturation curve of steam, where a biphasic fluid is present. Also some centrifugal cryogenic compressors make use of complex mixtures of gases, whose behavior at operating conditions is far from ideal.

In practical applications, it is quite common to carry out a CFD analysis of these machines using the perfect gas model with modified ''ad hoc'' values of the gas constant and the isentropic coefficient. However, the assumption that the thermodynamic properties of the fluid do not affect aerodynamic performance too much can be misleading in predicting some basic design parameters. Poor evaluation of total pressure and temperature values leads to bad predictions of losses, specific work and heat exchange. Errors in evaluating density affect computation of momentum components, and consequently the predicted flow structure. For these reasons, an accurate and reliable analysis for design purposes cannot leave flow property modeling out of consideration.

A good numerical model to account for real gas effects should satisfy some basic requirements: accuracy in predicting thermodynamic properties of the fluid; capability of dealing with a wide range of state parameters; effective and time-efficient implementation for CFD computations. A number of models have been developed, which are divided into two main categories: models which use analytical equations of state, and models based on numerical fitting of gas tables.

The use of an analytical equation of state makes it possible to have a reasonably accurate and consistent description of gas properties throughout a large range of temperature, pressure, and density for many substances. Many equations have been proposed for a variety of fluids and different applications. The model from Young [1] provides a simple equation of state for superheated and two-phase steam in virial form, formulated for turbomachinery calculations. The Benedict-Webb-Rubin (BWR) equation of state (Benedict et al. [2]), and its modified version (MBWR—first proposed by Jacobsen and Stewart [3]), are widely used to represent properties of hydrocarbons, cryogenic fluids and refrigerants. A more detailed review of the state of the art is reported by Cravero and Satta [4].

In most analytical formulations, pressure, temperature, and density are used as input parameters. However, since these equations can be considerably more complex than those ones used in a perfect gas analysis, evaluating properties during a solution can lead to significant computing overhead. Actually, as practical applications requires one to predict values of different variables, such as enthalpy, internal energy or entropy, time-consuming iterative calculations are needed. In a typical single-row steady turbomachinery computation, using a computational grid with $5 \cdot 10^5$ cells and requiring 500 multigrid iterations to reach convergence, it is esti-

Contributed by the International Gas Turbine Institute and presented at the International Gas Turbine and Aeroengine Congress and Exhibition, Atlanta, GA, June 16–19, 2003. Manuscript received by the IGTI Dec. 2002; final revision Mar. 2003. Paper No. 2003-GT-38101. Review Chair: H. R. Simmons.

  

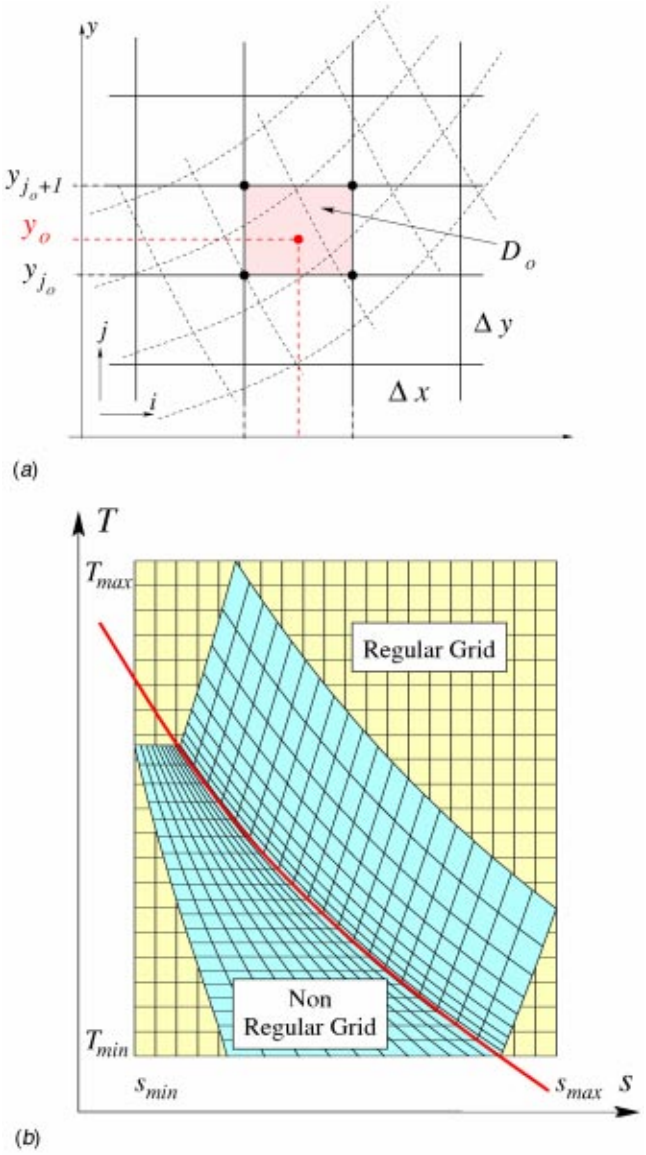


**Fig. 1 Grids representing gas property tables; (*a*) search scheme, (*b*) regular and nonregular grids**

mated that $10^{13}$ thermodynamic evaluations are performed. Consequently, an increase in the computational time needed for each evaluation impacts dramatically on the solver efficiency. Moreover, since analytical equations are tuned to specific categories of fluids, each model is not easily extendable to different kinds of substances.

Models for the fitting of gas tables have been developed for the most common fluids of industrial interest (air and steam). Pátek [5] gives an overview of different thermodynamic relationships and pairs of independent variables considered by several authors, which are most frequently used in steam computations. He also proposes a polynomial form for fitting functions to approximate thermodynamic properties of superheated steam, which is applicable to any gas in an adequate region of state parameters. Other formulations consist of surface fitting of scattered data using splines (Dierckx [6]), even in presence of discontinuities, such as for steam tables at the saturation curve. However, this procedure involves considerable trial and error to obtain an acceptable description of the surface for any thermodynamic relationship, and its implementation into a CFD code is not straightforward.

The model presented in this paper was developed according to these criteria: ease of implementation in an existing CFD solver; speed and accuracy suitable for everyday industrial design; capability of dealing with any kind of gases to be applied to different problems. The behavior of real gases, gas mixtures, or steam is reproduced by replacing analytic relationships from the perfect gas model with the use of gas property tables. Using two-variable formulations, a number of thermodynamic functions and different couples of independent variables are identified. A local interpolation of gas data is performed to provide the thermodynamic property required by the solver in each solution step. This method is generally applicable to any working fluid, and extends property evaluations into saturated and superheated regions. One main restriction is given by the assumption that only one working fluid exists in the solution domain.

To reduce computational costs, a number of regular gas tables are generated off-line to be used during CFD solution. Accessing these tables proved to be much faster than evaluating thermodynamic properties directly by means of a real-gas equation of state. The gas database resides external to the flow solver. Either commercial or in-house developed databases can be exploited, such as a commercial refrigerant or steam package. Applications presented here use the NIST/ASME steam properties database (IAPWS [7], Harvey et al. [8], and Wagner et al. [9]) to determine steam properties. Gas tables for the HFC-134a refrigerant are provided by a proprietary software developed by GE-Nuovo Pignone (GE-NP), which computes the thermodynamic characteristics of gas mixtures at fixed chemical composition through a number of equations of state and correlations (Benedict et al. [2], Benzler and Koch [10], Schultz [11], Cooper and Goldfrank [12], Lee and Kesler [13], and Lin and Chao [14]).

## Numerical Procedure

**Perfect Gas Solver.** The numerical model for real gas effects is implemented into the TRAF solver (Arnone et al. [15]). TRAF is a fully viscous, multigrid, multirow code developed at the University of Florence, capable of solving three-dimensional cascade flows in coupled, fixed and rotating blade passages using nonperiodic H-type or C-type grids. Governing equations are the three-dimensional unsteady compressible Reynolds-averaged Navier-Stokes equations (RANS). The equation of state for a perfect gas is used to link fluid-dynamic and thermodynamic quantities, and close the RANS system. The eddy-viscosity hypothesis is used to account for the effect of turbulence. To compute the eddy viscosity, both algebraic (Baldwin and Lomax [16] and Arnone and Pacciani [17]) and multiequations (Spalart and Allmaras [18] and Menter [19]) models of turbulence are implemented. A detailed description of the numerical procedure is not reported here for conciseness, and can be found in Arnone [20] and Arnone and Pacciani [17].

**Gas Tables.** In the TRAF code, five couples of independent thermodynamic variables $(x,y)$ and thirteen functions $z(x,y)$ were identified to be used in computations:

$$T(p,\rho) \tag{1}$$

$$a(p,\rho) \tag{2}$$

$$\mu(p,\rho) \tag{3}$$

$$\kappa(p,\rho) \tag{4}$$

$$h(p,\rho) \tag{5}$$

$$s(p,\rho) \tag{6}$$

$$e(p,\rho) \tag{7}$$

$$p(h,s) \tag{8}$$

$$\rho(h,s) \tag{9}$$

$$T(h,s) \tag{10}$$

$$p(e,\rho) \tag{11}$$

$$\rho(T,p) \tag{12}$$

$$p(T,\rho) \tag{13}$$

Nine different thermodynamic variables are used: $T$, $p$, $\rho$, $h$, $s$, $e$, $a$, $\mu$, $\kappa$. Their values must be provided by gas tables over a range of thermodynamic states which is set by the user, depending on the physical problem to be investigated.

In each $x$-$y$ plane, tables are represented by a structured grid of points identified by two grid indices $i$ and $j(1\leqslant i\leqslant nx; 1\leqslant j\leqslant ny)$. Values of function $z(x,y)$ are known on grid nodes. Given a thermodynamic state of the system $(x_o, y_o)$, the thermodynamic quantity of interest $z_o = z(x_o, y_o)$ is computed by a local interpolation on the grid cell $D_o$ which contains the point $(x_o, y_o)$ (**Fig. 1(*a*)**). If the grid is regular, orthogonal to $x$ and $y$-axes, and equally spaced, $D_o$ can be found by

$$x_{i_o} \leqslant x_o < x_{i_o+1}; \quad y_{j_o} \leqslant y_o < y_{j_o+1}.$$

If $x_{\min}$, $x_{\max}$, $y_{\min}$, $y_{\max}$ are minimum and maximum values of variables $x$ and $y$ in the table, $i_o$ and $j_o$ indices are given by

$$\begin{aligned} i_o &= \text{int}[(x_o - x_{\min})/(x_{\max} - x_{\min})] + 1; \\ j_o &= \text{int}[(y_o - y_{\min})/(y_{\max} - y_{\min})] + 1. \end{aligned} \tag{14}$$

As a result, the computational cost of $D_o$ search has order $O(1)$, regardless of the number of grid points.

If thermodynamic points are provided on a nonregular curvilinear grid, searching for cell $D_o$ has a computational cost of order $O(nx \times ny)$. This impacts strongly on the solver efficiency, so a regularization of the grid is suggested. In **Fig. 1**(***b***) two grids are reported in the $T-s$ plane for steam, as an example. Regular grids can be built using specific equations of state or interpolating algorithms, apart from CFD computations. Nonregular shapes of physical domains may require one to produce grids which are much larger than needed, to cover the whole $(x_{\min}, x_{\max}) \times (y_{\min}, y_{\max})$ range, including many points far from the physical region of interest. However, using the search algorithm (14), grid dimensions do not affect computational efficiency.

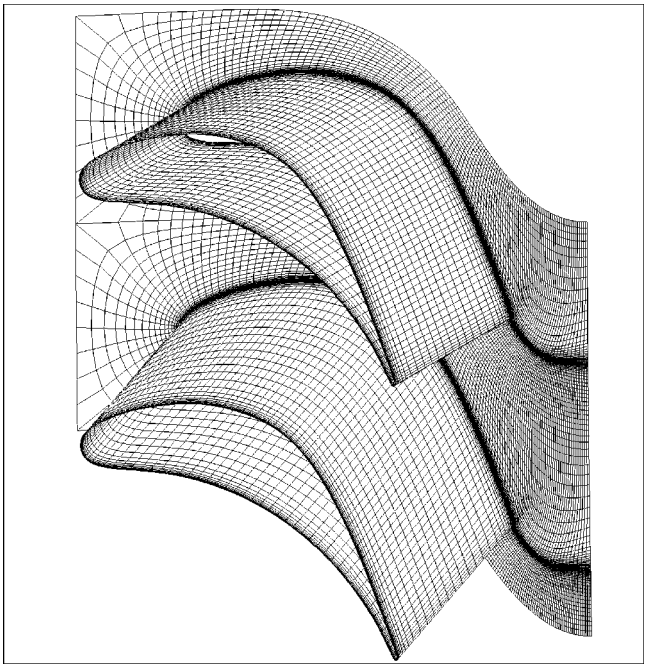

**Fig. 2 Computational mesh for the LP steam turbine first stator**

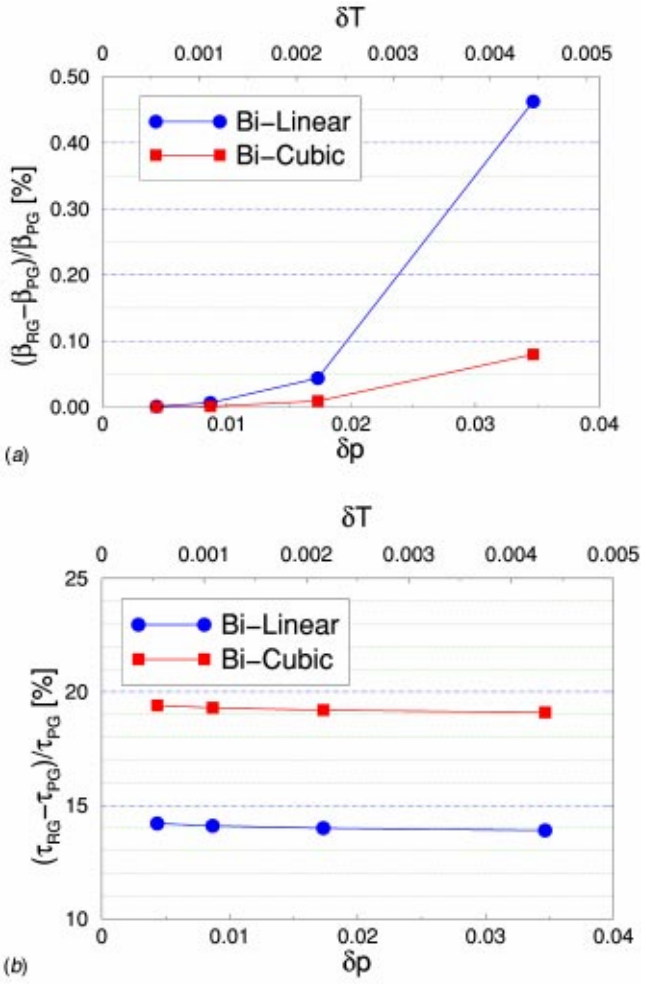


**Fig. 3 Accuracy and computational time increase for different gas tables and interpolating algorithms; (*a*) error on total pressure ratio, (*b*) computational time increase**

**Interpolation of Thermodynamic Functions.** To perform interpolations, a couple of local variables $(\xi, \eta)$ are defined on cell $D_o$:

$$\xi(x) \equiv (x - x_{i_o})/\Delta x; \quad \eta(y) \equiv (y - y_{j_o})/\Delta y$$

with $0 \leqslant \xi \leqslant 1$, $0 \leqslant \eta \leqslant 1$.

Let $\xi_o \equiv \xi(x_o)$, $\eta_o \equiv \eta(y_o)$; introducing the local surface and its derivative:

$$r(\xi,\eta) \equiv z(x(\xi), y(\eta)); \quad r_\xi \equiv \frac{\partial r}{\partial \xi}; \quad r_\eta \equiv \frac{\partial r}{\partial \eta}; \quad r_{\xi\eta} \equiv \frac{\partial^2 r}{\partial \xi \partial \eta}.$$

Two different interpolating algorithms are implemented to compute the wanted value $r_o = r(\xi_o, \eta_o)$ (Rogers and Adams [21]):

*Bi-linear interpolation*:

$$r_o = ((1-\xi_o)\xi_o) \begin{pmatrix} r(0,0) & r(0,1) \\ r(1,0) & r(1,1) \end{pmatrix} \begin{pmatrix} (1-\eta_o) \\ \eta_o \end{pmatrix}; \tag{15}$$

*Bi-cubic interpolation*:

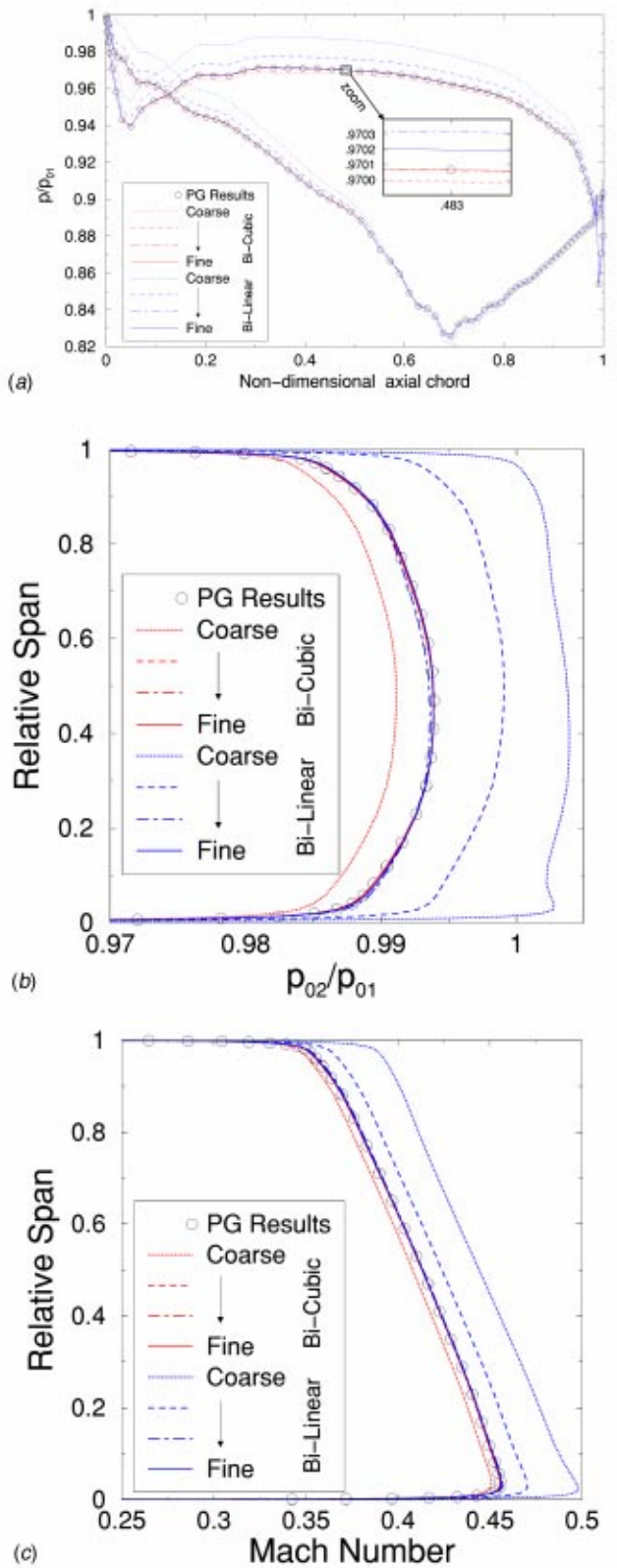


**Fig. 4 Blade and spanwise distributions for different gas tables and interpolating algorithms; (*a*) blade pressure at mid-span, (*b*) outlet total pressure, (*c*) outlet Mach number**

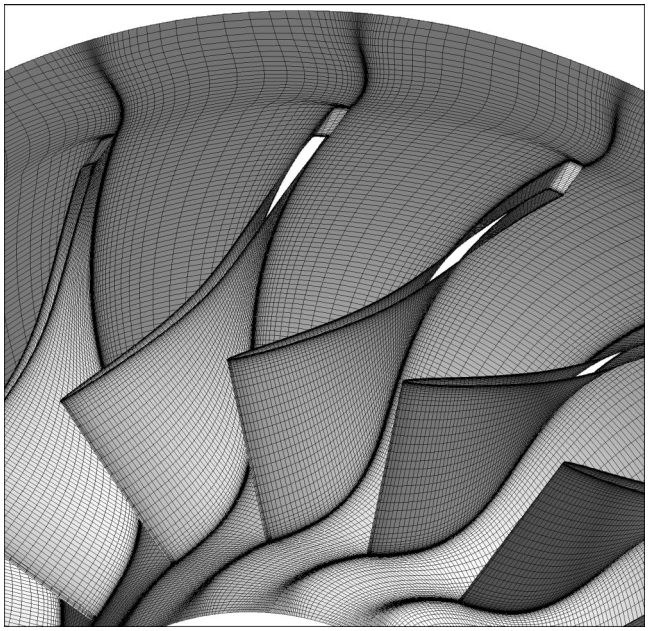

**Fig. 5 Three-dimensional view of the transonic centrifugal impeller**

$$r_o=(f_1(\xi_o)f_2(\xi_o)g_1(\xi_o)g_2(\xi_o))S\begin{pmatrix} f_1(\eta_o)\\ f_2(\eta_o)\\ g_1(\eta_o)\\ g_2(\eta_o)\end{pmatrix} \tag{16}$$

where

$$f_1(\zeta)\equiv 2\zeta^3-3\zeta^2+1;\quad f_2(\zeta)\equiv -2\zeta^3+3\zeta^2$$

$$g_1(\zeta)\equiv \zeta^3-2\zeta^2+\zeta;\quad g_2(\zeta)\equiv \zeta^3-\zeta^2$$

$$S\equiv\begin{pmatrix} r(0,0) & r(0,1) & r_\eta(0,0) & r_\eta(0,1)\\ r(1,0) & r(1,1) & r_\eta(1,0) & r_\eta(1,1)\\ r_\xi(0,0) & r_\xi(0,1) & r_{\xi\eta}(0,0) & r_{\xi\eta}(0,1)\\ r_\xi(1,0) & r_\xi(1,1) & r_{\xi\eta}(1,0) & r_{\xi\eta}(1,1)\end{pmatrix}$$

and derivatives are computed using a central difference scheme; for example,

$$r_\xi(0,0)=z_x(x_{i_o},y_{j_o})\cdot\Delta x=(z(x_{i_o+1},y_{j_o})-z(x_{i_o-1},y_{j_o}))/2.$$

Both algorithms can be used separately: interpolation (15) is faster, while interpolation (16) provides a higher accuracy and guarantees continuity of functions and their first derivatives. When using the bi-cubic interpolation, cells at grid boundaries are treated with the bi-linear one as well.

**Total Quantities and Boundary Conditions.** Total pressure $p_0$, temperature $T_0$ and density $\rho_0$ are computed from static values $p$, $T$ and $\rho$ by performing an isentropic transformation of the real gas. Knowing $p$ and $\rho$, functions (5) and (6) are used to obtain specific static enthalpy $h$ and entropy $s$. Then, the kinetic term $c^2/2$ is computed from the velocity components, and the corresponding value of specific total enthalpy is evaluated as $h_0=h+c^2/2$. Finally, $p_0$, $\rho_0$ and $T_0$ are obtained through functions (8) to (10), using $h_0$ while keeping $s$ fixed. The same procedure is followed when static quantities are computed from total ones.

In multiblock, multistage turbomachinery computations there are mainly five different types of boundary conditions. The way they are handled by the real gas solver is briefly described here:

*Inlet*: Spanwise distributions of flow angles, total pressure $p_0$, and total temperature $T_0$ are given. Total density $\rho_0$ is computed

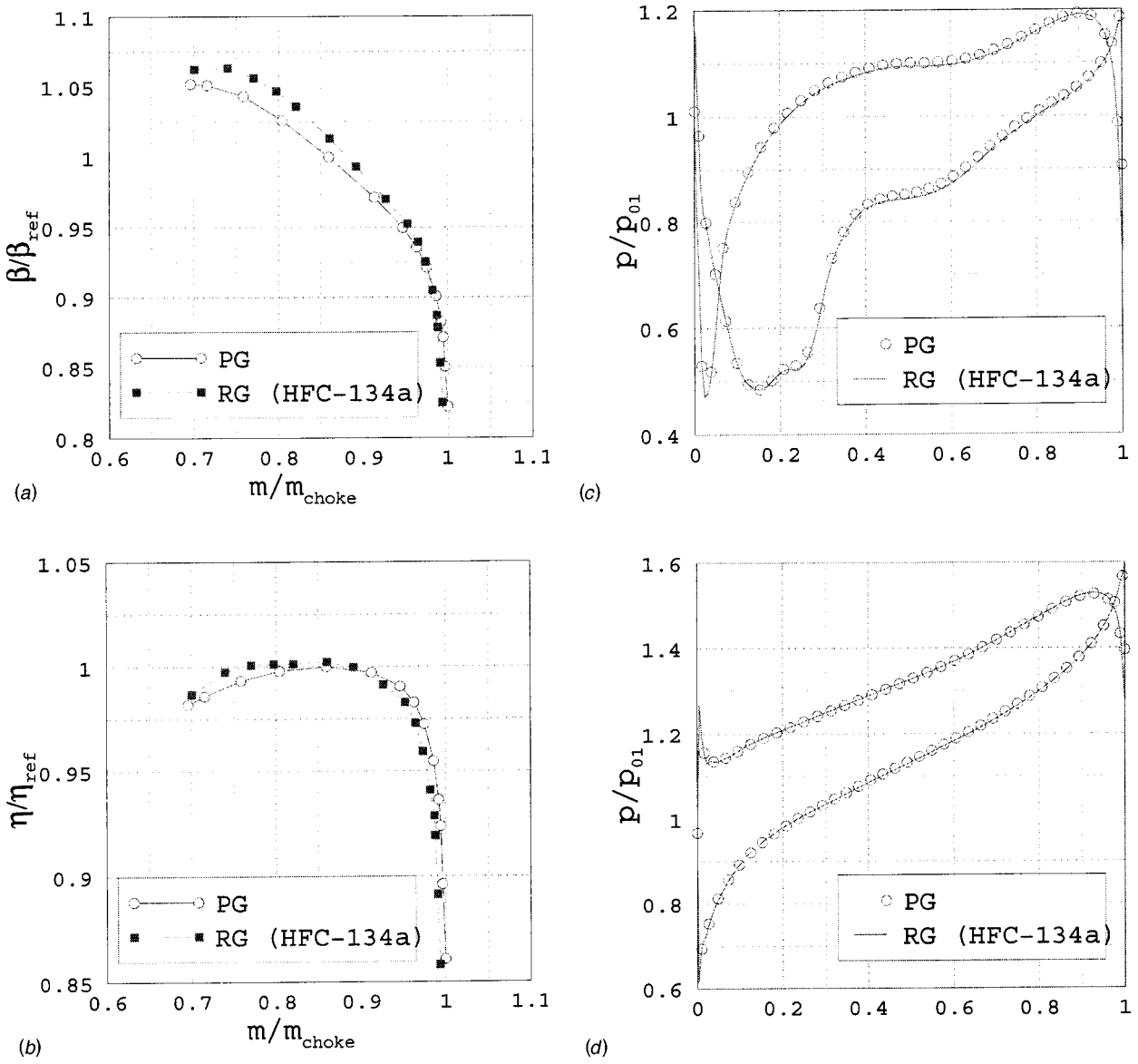


**Fig. 6 Comparison between the perfect and real gas model results for the transonic centrifugal impeller; (*a*) total pressure ratio, (*b*) isentropic efficiency, (*c*) blade pressure at midspan near choke, (*d*) blade pressure at midspan near stall**

using function (12). For a subsonic inlet, the axial component of the velocity is extrapolated from the interior of the domain. The other velocity components are computed by means of flow angles, and static quantities are obtained by following the procedure previously described. Specific total energy is computed as $e_0 = h_0 - p/\rho$.

*Outlet*: Spanwise distribution of static pressure is assigned. Density and velocity components are extrapolated from the interior. Specific internal energy $e$ is computed through function (7), and total energy calculated as $e_0 = e + c^2/2$.

*Solid walls*: No-slip conditions are imposed on the velocity components. Either the wall temperature or the adiabatic wall condition are assigned, as well. Pressure is extrapolated from the interior, and density computed using function (12). In the case of a biphasic fluid, such as steam in the saturation region, density is extrapolated, and pressure at wall is obtained through function (13). Total energy is computed by means of function (7), adding the kinetic term $c^2/2$.

*Periodic boundaries*: The same treatment is done as for the perfect gas solver. Pressure is obtained from independent variables $e$ and $\rho$ through function (11).

*Interface planes*: The same approach as in the perfect gas solver is used, both for steady multirow analysis (mixing planes) and unsteady time-accurate computations (pitchwise linear interpolation of dependent variables). Pressure is computed from $e$ and $\rho$ using function (11).

**Table Dependence Analysis.** A number of tests were carried out to investigate the effectiveness of the numerical method, and assess the dependence of the results on gas table density. As an example of turbomachinery configuration, the first stator of a GE-NP three-stage LP package was used, whose geometry is illustrated in **Fig. 2**. A perfect gas was considered as evolving fluid. Real gas computations were performed using perfect gas tables, and results were compared to those obtained with the perfect gas model, taken as a reference.

Gas tables were built using the standard analytical relationships between thermodynamic quantities. Four different tables were selected, with an increasing number of grid points within the same thermodynamic range. A measure of table density is given here in terms of the ratio between grid spacings and the average values of variables $(x,y)$ on the table range, that is

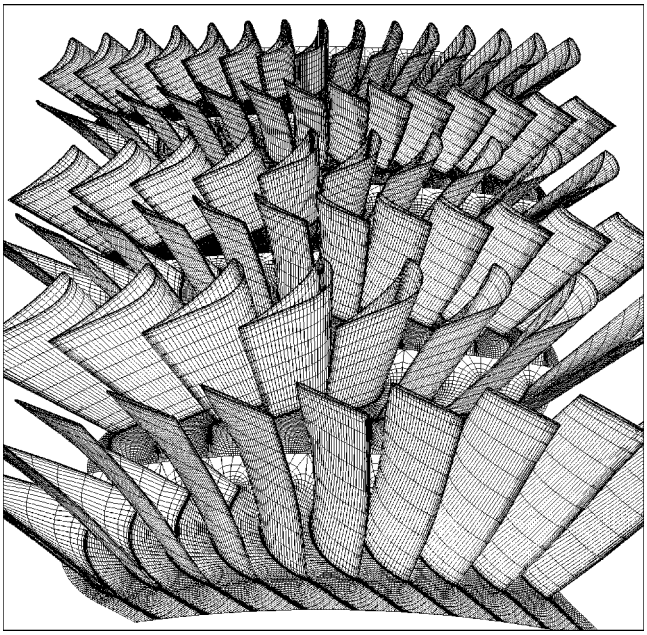

**Fig. 7 Computational mesh for the three-stage LP turbine**

$$\delta x \equiv \Delta x / x_{av}\,; \quad \delta y \equiv \Delta y / y_{av}\,.$$

Both bi-linear and bi-cubic interpolations were used.

In **Fig. 3**(***a***), the relative error on total pressure ratio $\beta$ is reported as a function of $\delta p$ and $\delta T$, for both bi-linear and bi-cubic interpolations. As expected, using the same table, the bi-cubic interpolation is more accurate than the bi-linear one. For both of them, error decreases asymptotically to zero when increasing grid resolution.

The numerical algorithm was required to be fast, in order to be an effective tool for practical applications. Actually, the observed increase in computational times is low with respect to the perfect gas solver: about 14% and 19% for the bi-linear and bi-cubic interpolations, respectively (**Fig. 3**(***b***)). As a major result, the proposed search algorithm (14) makes times independent of table dimensions. When a higher resolution is required by the problem under investigation, the only increase in computational costs is due to data storage.

Comparisons were made between blade pressure distributions at midspan (**Fig. 4**(***a***)), and spanwise distributions of pitch-averaged total pressure (**Fig. 4**(***b***)) and Mach number (**Fig. 4**(***c***)) at outlet. The agreement with the reference solution improves using finer and finer tables. As a general criterion, differences below 0.05% are compatible with accuracy required in CFD computations. Using bi-cubic interpolation, this criterion is satisfied from the second table on ($\delta p \simeq 0.02$, $\delta T \simeq 0.002$), while at least the third one ($\delta p \simeq 0.009$, $\delta T \simeq 0.001$) is needed by bi-linear interpolation.

## Applications

The model for real gas effects was thought to be used as an industrial tool for turbomachinery design. Two applications of industrial interest are presented here: the analysis of a transonic centrifugal impeller and of a three-stage LP steam turbine.

**Analysis of a Transonic Centrifugal Impeller.** **Figure 5** shows the geometry of a transonic centrifugal impeller for heavy-duty applications, designed by GE-NP, which is representative of a class of industrial impellers of the latest generation. Such impellers are critical for the high values of the relative Mach number of the flow, especially in the axial inducer. Therefore, great attention must be paid in order to obtain satisfactory performance

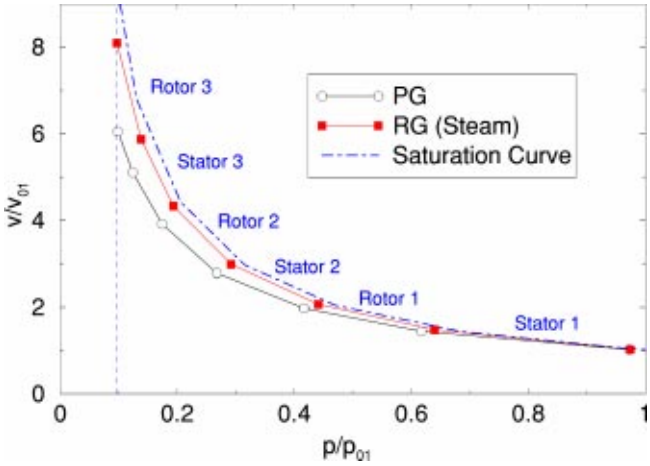


**Fig. 8 Steam expansion in the *p*–*v* plane for the LP turbine**

curves in terms of both operative range extension and peak efficiency. They are mainly employed either in refrigerating compressors for ''natural gas liquefaction'' (LNG) applications or in ethylene synthesis compressors. Evolving fluids consist of complex mixtures of hydrocarbons, cryogenic gases and refrigerants, whose behavior at operating conditions is far from ideal. Then, the capability to account for thermodynamic properties of such mixtures is of primary importance to obtain reliable numerical predictions.

In the design process, CFD computations are used to assess the impeller performance both at design point and in off-design conditions. In the application presented here, a numerical analysis was carried out over the impeller's operative range. A grid of about $5 \cdot 10^5$ cells was used in computations (**Fig. 5**). HFC-134a was considered as working fluid, which is a well-known refrigerant, widely used in test rigs to reproduce some of the main thermodynamic features of natural gases encountered in petrochemical applications. Boundary and operating conditions reproduce those one of a test rig, set up for experimental measurements on a scaled geometrical model.

Two series of computations were performed: the first one using the perfect gas model, the other one exploiting gas tables. In the perfect gas equation, an equivalent gas constant $R_{PG}$ and isentropic exponent $\gamma_{PG}$ were used, defined as follows:

$$R_{PG} \equiv \frac{p_{01}}{\rho_{01} T_{01}} = 79.86 \ \text{J/kg K} \qquad \gamma_{PG} = 1.1.$$

Gas tables were generated using the proprietary routines of GE-NP, according to the general criterion for accuracy discussed above, with $\delta p = 0.005$ and $\delta T = 0.001$. Bi-cubic interpolation was used.

Results are compared in **Fig. 6**. In **Figs. 6**(***a***)–**6**(***b***) the total pressure ratio $\beta/\beta_{\text{ref}}$ and the isentropic efficiency $\eta/\eta_{\text{ref}}$ are reported as a function of nondimensional mass flow rate $\dot{m}/\dot{m}_{\text{choke}}$. The prediction of the impeller operative range is slightly affected by the gas model, since both models provide similar choke and stall inception limits. Higher values of $\beta$, up to 2%, are predicted by the real gas model, with a steeper slope of the characteristic curve. Looking at the efficiency curves, a similar behavior is observed, with real gas efficiency up to 0.7% higher. Moreover, the real gas curve shows a plateau where the perfect gas one is narrower around its maximum.

The impeller's aerodynamics seems not to be influenced by the thermodynamic model adopted. Comparisons between blade pressure distributions at midspan near choke (**Fig. 6**(***c***)) and near stall (**Fig. 6**(***d***)) show that the same blade loading is predicted by both models. This result can be explained by referring to the reduced variables $p/p_c$ and $T/T_c$, $p_c$ and $T_c$ being the critical pressure and

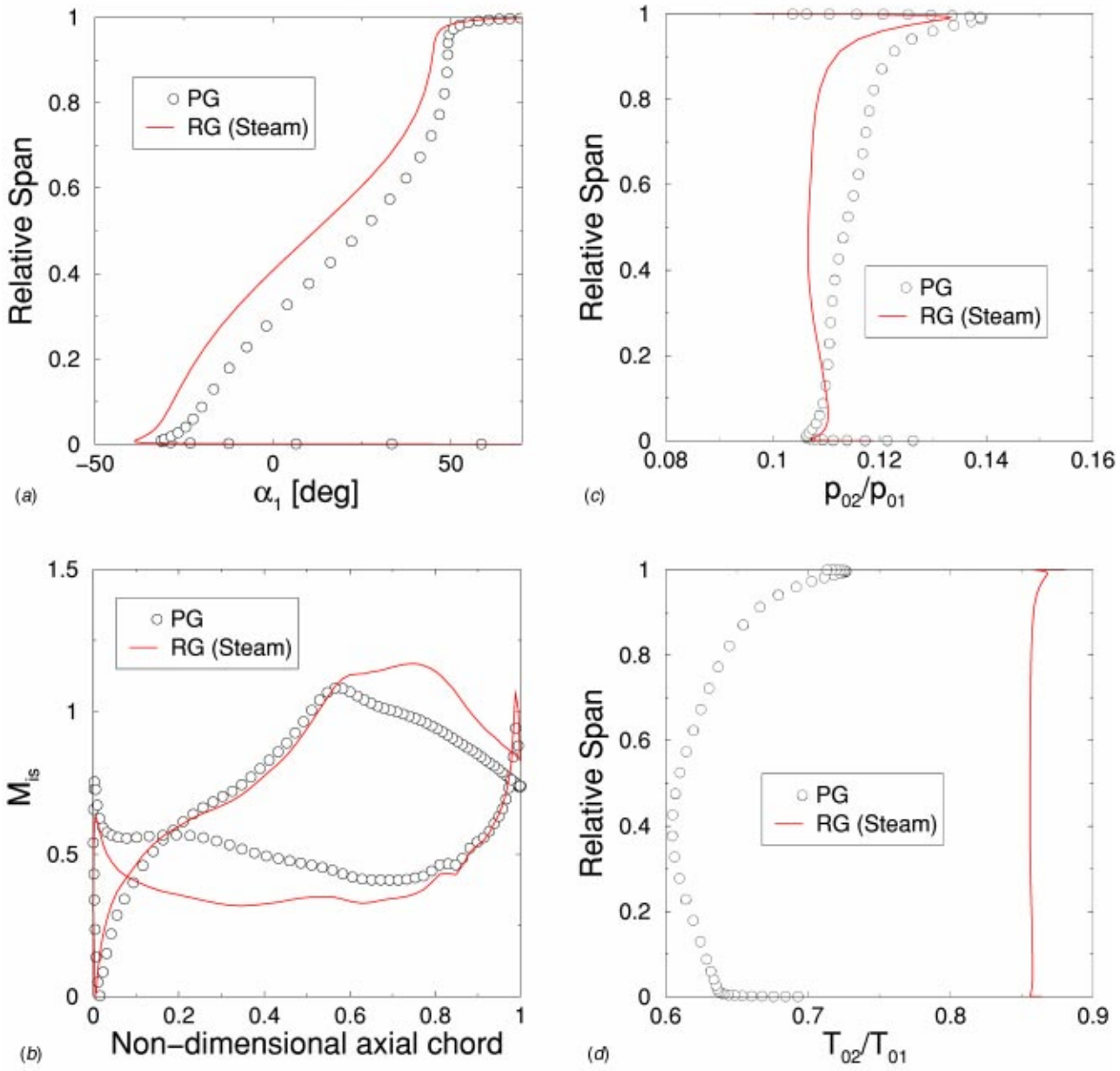


**Fig. 9 Comparison between the perfect and real gas model results for the LP turbine third rotor; (*a*) inlet blade-to-blade flow angle, (*b*) blade isentropic Mach number at midspan, (*c*) outlet total pressure, (*d*) outlet total temperature**

temperature of HFC-134a. In the present configuration, the reduced variables, evaluated using inlet total quantities, are $T_{01}/T_c = 0.80$ and $p_{01}/p_c = 0.025$. Since pressure is well below its critical value, compression occurs within a thermodynamic range where small deviations from ideal behavior are expected. In such conditions, the aerodynamic design can be carried out on the basis of a perfect gas. Nevertheless, the nonideal nature of the fluid comes out in the evaluation of the main industrial performance characteristics: specific work input and efficiency.

**Analysis of a Three-Stage LP Steam Turblne.** The three-stage LP package of a GE-NP steam turbine was selected as a representative case of a common industrial problem in which the impact of the working fluid modelization cannot be neglected.

In HP and IP turbines, superheated steam is accurately described by the perfect gas model up to $p \simeq 100$ bar, while in LP stages this is not true any more, due to the occurrence of the liquid phase. Therefore, the modelization of the working fluid is expected to affect predictions of the turbine performance significantly.

Two different numerical computations were performed imposing the same boundary conditions. The computational mesh is shown in **Fig. 7**. It consists of six C-type grids, and its total size is about $2 \cdot 10^6$ cells. In the figure, one half of the grid lines have been omitted for sake of clarity. A first computation was carried out using the perfect gas model. The steam equation of state was approximated assuming an equivalent gas constant $R_{PG} = 454$ J/kg K and isentropic exponent $\gamma_{PG} = 1.33$. The real gas model was adopted for the second computation. Gas tables were generated via the NIST/ASME routines over the estimated extent

of the expansion process. Their relative density is given by $\delta p = 0.005$; $\delta v = 0.005$; $\delta h = 0.001$; $\delta e = 0.002$; $\delta T = 0.001$; $\delta s = 0.001$. Bi-cubic interpolation was used.

In **Fig. 8** two transformations are compared in the $p-v$ plane which correspond to the expansion undergone by the fluid through the LP turbine, computed by the perfect gas and the real gas models. Both expansions completely occur in the two-phase region. At the first stator inlet, the same inlet conditions are imposed for both models. As the expansion goes on, the perfect gas model progressively underestimates values of the specific volume. At the third rotor outlet, where back pressure is imposed, the deviation from the real gas model is about 35%. This leads to an overall underestimation of the specific work output.

These discrepancies impact not only on the prediction of the thermodynamic quantities, but also on the aerodynamic performance of the turbine components. Attention is focused here on the third rotor, for which maximum differences are expected.

The spanwise distributions of the inlet blade-to-blade flow angle are compared in **Fig. 9**(***a***). Significant differences are observed throughout blade span. At midspan, the perfect gas model predicts a negative incidence about 9° higher than the real gas one. As a consequence, blade operating conditions are different in the two cases. This effect is highlighted by the comparison between the blade isentropic Mach numbers, reported in **Fig. 9**(***b***). Due to the negative incidence, the blade loading predicted by the perfect gas model is much lower on the pressure side near leading edge. Discrepancies are also observed on the suction side near the trailing edge, suggesting a different shock structure in the transonic region. Outlet spanwise distributions of total pressure and temperature (**Figs. 9**(***c***)–**9**(***d***)) also show a substantial difference in loss prediction and emphasize the inconsistency of the perfect gas model in the two-phase region.

In **Figs. 10**(***a***)–**10**(***b***) flow stream lines in the blade-to-blade surface at midspan, obtained by means of particle traces, are reported for both models. A stronger recirculation is observed on the pressure side of the blade in the perfect gas case, according to the higher negative incidence found. This result highlights the influence of the gas model on the flow structure.

## Conclusions

In this work a numerical model was presented to account for real gas effects in CFD computations. The method is based on the use of gas property tables, and exploits a local fitting of gas data to compute thermodynamic properties required in each solution step. Gas tables reside external to the flow solver, and can be provided using either commercial databases or in-house developed ones.

The model was implemented in an existing three-dimensional solver for the RANS equations, originally based on the perfect gas state equation. The effectiveness of the method was assessed by performing real gas computations using perfect gas tables, and comparing results to those obtained with the perfect gas solver.

Two applications were discussed: the analysis of a transonic centrifugal impeller and of a three-stage LP steam turbine. They were selected as representative cases of common industrial problems in which the working fluid modelization affects performance prediction. The impeller aerodynamics was well described by the perfect gas model in the examined operating conditions, while real gas effects came out in the evaluation of specific work input and efficiency. In the LP steam turbine, significant departures from the ideal behavior were observed in the thermodynamic expansion, which completely occurs in the two-phase region. The impact was found to be strong on both thermodynamic performance and flow structure.

The proposed model proved to be an efficient and reliable design tool for industrial applications. Its characteristics also make it attractive as a research tool to investigate specific aspects of the flow, such as the impact of gas constant variation with temperature in perfect gas analyses.

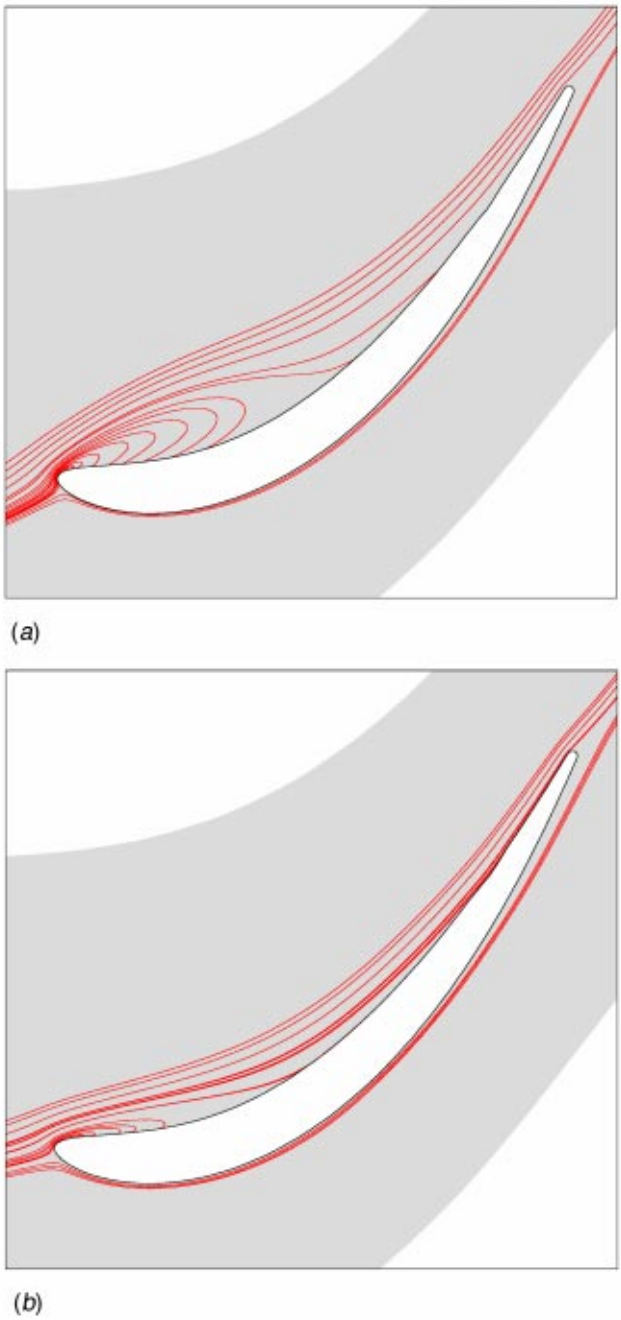


**Fig. 10 Comparison between particle traces in blade-to-blade plane at midspan for the LP turbine third rotor; (*a*) perfect gas model, (*b*) real gas model**

## Acknowledgments

The authors would like to express their gratitude to Prof. Ennio Carnevale of the University of Florence, for encouraging and promoting this joint research activity; to Dr. Leonardo Baldassarre, Dr. Giovanni Saccardi, and Dr. Gabriele Giovani of GE-Nuovo Pignone, for providing the centrifugal impeller configuration and gas property data for HFC-134a.

## Nomenclature

$T$ = temperature
$p$ = pressure
$\rho$ = density
$v$ = specific volume

$h$ = specific enthalpy
$s$ = specific entropy
$e$ = specific internal energy
$a$ = speed of sound
$\mu$ = molecular viscosity
$\kappa$ = thermal conductivity
$c$ = absolute velocity modulus
$R$ = gas constant
$\gamma$ = specific heat ratio
$x, y$ = independent thermodynamic variables
$z$ = dependent thermodynamic variable
$nx, ny$ = gas table dimensions
$\Delta x, \Delta y$ = gas table spacings
$\beta \equiv p_{02}/p_{01}$ = total pressure ratio
$\tau$ = computational time
$\eta$ = isentropic efficiency
$\dot{m}$ = mass flow rate
$\alpha$ = blade-to-blade flow angle
$M_{is}$ = isentropic Mach number

**Subscripts**

$PG$ = perfect gas model
$RG$ = real gas model
choke = choke conditions ($PG$)
ref = reference conditions (peak efficiency, $PG$)
min, max, av = minimum, maximum, average values
$o$ = current thermodynamic state
0 = stagnation condition
1, 2 = inlet conditions, outlet conditions
$c$ = critical conditions

## References


[1] Young, J. B., 1988, ''An Equation of State for Steam for Turbomachinery and Other Flow Computations,'' ASME J. Fluids Eng., **110**, pp. 1–7.
[2] Benedict, M., Webb, G. B., and Rubin, L. C., 1951, ''An Empirical Equation for Thermodynamic Properties of Light Hydrocarbons and Their Mixtures,'' Chem. Eng. Prog., **47**(8), p. 419.
[3] Jacobsen, R. T., and Stewart, R. B., 1973, ''Thermodynamic Properties of Nitrogen Including Liquid and Vapor Phases From 63 K to 2000 K With Pressures to 10,000 Bar,'' J. Phys. Chem. Ref. Data, **2**, pp. 757–922.
[4] Cravero, C., and Satta, A., 2000, ''A CFD Model for Real Gas Flows,'' ASME Paper 2000-GT-518.
[5] Pátek, J., 1996, ''Functional Forms to Describe Thermodynamic Properties of Gases for Fast Calculations,'' ASME Journal of Engineering for Gas Turbine and Power, **118**, pp. 210–213.
[6] Dierckx, P., 1993, *Curve and Surface Fitting With Splines*, Oxford University Press, New York.
[7] IAPWS, 1997, ''IAPWS Industrial Formulation 1997 for the Thermodynamic Properties of Water and Steam,'' IAPWS Release, IAPWS Secretariat, Technical Report.
[8] Harvey, A. H., Peskin, A. P., and Klein, S. A., 2000, ''NIST/ASME Steam Properties,'' NIST Standard Reference Database 10, Version 2.2, Standard Reference Data Program, National Institute of Standards and Technology, Gaithersburg, MD.
[9] Wagner, W., Cooper, J. R., Dittmann, A., Kijima, J., Kretzschmar, H.-J., Kruse, A., Mareš, R., Oguchi, K., Sato, H., Stöcker, I., Šifner, O., Takaishi, Y., Tanishita, I., Trübenbach, J., and Willkommen, T., 2000, ''The IAPWS Industrial Formulation 1997 for the Thermodynamic Properties of Water and Steam,'' ASME J. Eng. Gas Turbines Power, **122**, pp. 150–182.
[10] Benzler, H., and Koch, A. V., 1955, ''Ein Zustandsdiagram für Athylen bis zu 10,000 Ata Druck,'' Chem.-Ing.-Tech., **27**(2), p. 71.
[11] Schultz, J. M., 1962, ''The Polytropic Analysis of Centrifugal Compressors,'' ASME J. Eng. Gas Turbines Power, **69**.
[12] Cooper, H. W., and Goldfrank, J. C., 1967, ''B-W-R Constants and New Correlations,'' Hydrocarbon Process., **46**(12), p. 141.
[13] Lee, B. I., and Kesler, M. G., 1975, ''A Generalized Thermodynamic Correlation Based on Three-Parameter Corresponding States,'' AIChE J., **21**(3).
[14] Lin, H., and Chao, K., 1984, ''Correlation of Critical Properties and Acentric Factor of Hydrocarbons and Derivatives,'' AIChE J., **30**(6).
[15] Arnone, A., Liou, M. S., and Povinelli, L. A., 1993, ''Multigrid Calculation of Three-Dimensional Viscous Cascade Flows,'' J. Propul. Power, **9**(4), pp. 605–614.
[16] Baldwin, B. S., and Lomax, H., 1978, ''Thin Layer Approximation and Algebraic Model for Separated Turbulent Flows,'' AIAA paper, **78**, p. 257.
[17] Arnone, A., and Pacciani, R., 1998, ''IGV-Rotor Interaction Analysis in a Transonic Compressor Using the Navier-Stokes Equations,'' ASME J. Turbomach., **120**(1), pp. 143–155.
[18] Spalart, P., and Allmaras, S., 1992, ''A One-Equation Turbulence Model for Aerodynamic Flows,'' AIAA Paper 92-0439.
[19] Menter, F. R., 1993, ''Zonal Two-Equations $k-\omega$ Turbulence Models for Aerodynamic Flows,'' AIAA Paper 93-2906.
[20] Arnone, A., 1994, ''Viscous Analysis of Three-Dimensional Rotor Flow Using a Multigrid Method,'' ASME J. Turbomach., **116**, pp. 435–445.
[21] Rogers, D. F., and Adams, J. A., 1990, *Mathematical Elements for Computer Graphics*, WBC/McGraw-Hill, New York.

# The Influence of Leading-Edge Geometry on Secondary Losses in a Turbine Cascade at the Design Incidence

**M. W. Benner**[1]
e-mail: michael.benner@nrc-cnrc.gc.ca

**S. A. Sjolander**

Department of Mechanical and Aerospace Engineering,
Carleton University,
Ottawa, ON, Canada

**S. H. Moustapha**
Pratt and Whitney Canada, Inc.,
Longueuil, PQ, Canada

*The paper presents detailed experimental results of the secondary flows from two large-scale, low-speed linear turbine cascades. The aerofoils for the two cascades were designed for the same inlet and outlet conditions and differ mainly in their leading-edge geometries. Detailed flow field measurements were made upstream and downstream of the cascades using three and seven-hole pressure probes and static pressure distributions were measured on the aerofoil surfaces. All measurements were made exclusively at the design incidence. The results from this experiment suggest that the strength of the passage vortex plays an important role in the downstream flow field and loss behavior. It was concluded that the aerofoil loading distribution has a significant influence on the strength of this vortex. In contrast, the leading-edge geometry appears to have only a minor influence on the secondary flow field, at least for the design incidence.*
[DOI: 10.1115/1.1645533]

## Introduction

A turbine aerofoil is usually designed to produce minimum losses at its design operating point. Additional losses then occur when the operating conditions vary from the design point. In aircraft engines, operation at idle, take-off, and cruise all result in changes in the operating conditions for the turbines, particularly the low-pressure stages. These changes can take a number of different forms, including deviations in Reynolds number and Mach number from their design values. Perhaps the most significant effect on losses occurs when the incidence differs from its design value. The present study is part of an on-going project concerned with the effects of off-design incidence on profile and secondary losses.

Empirical loss correlations and meanline analysis continue to play an important role in the early stages of the design process. As progress is made in understanding the flow physics, it is necessary to review and improve these correlations. The ultimate objective of this project is to improve the off-design correlations for profile and secondary losses. However, a sound understanding of the flow physics is a precondition for improving loss correlations, and therefore, a large part of the project is aimed at improving the current understanding of the flow and loss behavior. Work related to profile losses has largely been completed, [1]. A previous investigation has focused on the physical insights into the relationship between the behavior of secondary flows and incidence, [2]. The present paper continues the examination of secondary flows and looks in more detail at the losses.

Secondary flows in turbine cascades have been the subject of extensive experimental research in the past decades. Several excellent reviews have appeared. Research from the 1950s to the mid 1980s was summarized by Sieverding [3]. Gregory-Smith [4] and Langston [5] have reviewed the more recent research on secondary flows. Based on these reviews, it is clear that there is still a requirement for an improved understanding of a number of aspects of the physics, including in particular the influence of the inlet boundary layer separation process (i.e., the horseshoe vortex formation) on the flow and loss behavior in the endwall region.

The flow at the junction of a cylindrical body and flat plate, and the resulting horseshoe vortex formation, has been studied in great detail (e.g., Baker [6], Eckerle and Langston [7], Pierce and Tree [8], and Devenport and Simpson [9]). The flow and geometric parameters that affect the structure and dimensions of the horseshoe vortices are therefore reasonably well understood, [10]. However, for these flows the pressure field imposed on the incoming boundary layer is a function of the size of the obstacle only. In the case of the turbomachinery-aerofoil-endwall junction, the upstream pressure field becomes a function of the magnitude and distribution of the loading of the aerofoil itself. The effect of this is likely to be particularly strong in turbine aerofoil rows because of their high aerofoil loadings. To the authors' knowledge, only one investigation has focused on the development of the horseshoe vortex in turbine cascades, [11], and therefore, the physics of this flow are not as well understood. The geometric and flow parameters that affect the characteristics of the vortex have yet to be fully identified.

The present paper describes an experimental study of secondary flows in a large-scale, low-speed, cascade wind tunnel. Two aerofoil designs, which differ mainly in their leading-edge geometries, have been investigated. The paper concentrates on providing insight into the effect of leading-edge geometry on the endwall flow field and loss behavior at the design incidence. A subsequent paper will address the effects of off-design incidence. Detailed flow field measurements were made upstream and downstream of the cascade and static pressure distributions were measured on the aerofoil surfaces. The data were supplemented by extensive surface oil flow visualization.

## Experimental Apparatus and Procedures

**Test Section and Test Cascades.** All measurements were made in the linear cascade test section shown schematically in **Fig. 1.** Two cascades, designated as LS2 and LS3, were examined. The sets of five aerofoils are mounted on a turntable that allows the cascades to be tested over a wide range of inlet flow angles. The test section has been used extensively in the past, primarily for the study of the effects of off-design incidence on profile

Contributed by the International Gas Turbine Institute and presented at the International Gas Turbine and Aeroengine Congress and Exhibition, Atlanta, GA, June 16–19, 2003. Manuscript received by the IGTI December 2002; final revision March 2003. Paper No. 2003-GT-38107. Review Chair: H. R. Simmons.

[1]Current address: Institute for Aerospace Research, Propulsion Laboratory, National Research Council of Canada, Ottawa, ON, Canada. To whom correspondence should be addressed.

  

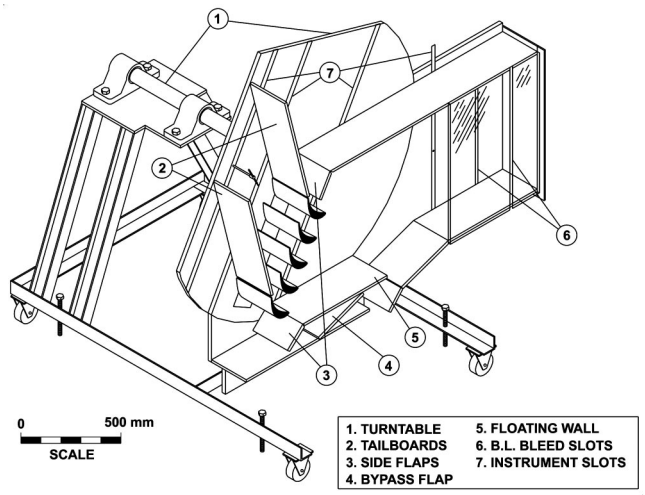


**Fig. 1 Schematic of variable-incidence cascade test section**

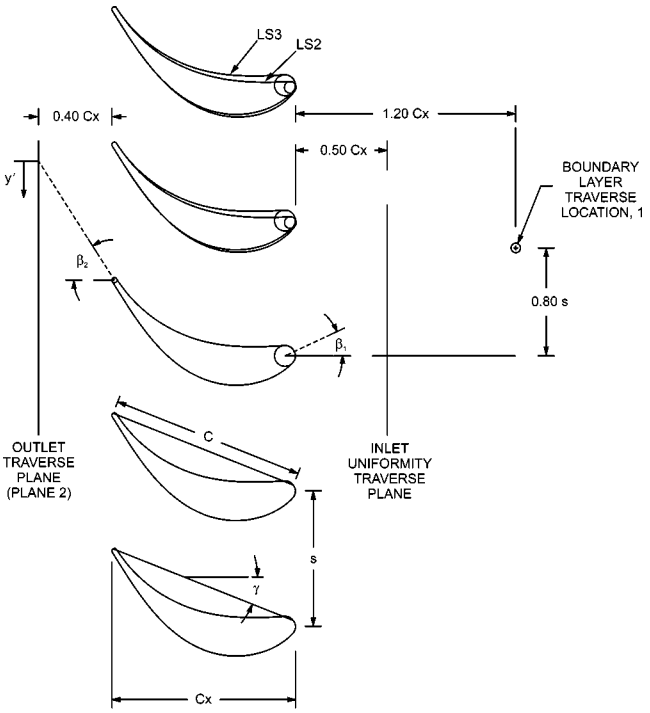


| Parameters | LS2 | LS3 |
|---|---|---|
| Blade span, h [mm] | 203.7 | 203.7 |
| Blade spacing, s [mm] | 110.7 | 110.7 |
| True chord, C [mm] | 162.8 | 162.3 |
| Axial chord, Cx [mm] | 150.0 | 149.4 |
| Stagger angle, $\gamma$ [deg] | 23.1 | 21.6 |
| $t_{max}/c$ [%] | 18.0 | 19.6 |
| Inlet metal angle, $\beta_1$ [deg] | 29.3 | 25.5 |
| Outlet metal angle, $\beta_2$ [deg] | 57.5 | 57.5 |
| Design inlet flow angle, $\alpha_1$ [deg] | 28.4 | 28.4 |
| Design outlet flow angle, $\alpha_2$ [deg] | 57.7 | 57.7 |
| Incidence, i [deg] | -0.9 | 2.9 |
| Leading-edge diameter, d [mm] | 9.4 | 16.7 |
| Leading-edge wedge angle, We [deg] | 52.4 | 43.0 |
| Trailing-edge thickness, tet [mm] | 4.2 | 4.2 |

**Fig. 2 Cascade geometry and measurement locations**

losses (e.g., Benner et al. [1], Goobie et al. [12], Tremblay et al. [13], and Rodger et al. [14]). The side flaps, bypass flap, and tailboards are adjusted to obtain good inlet flow uniformity and outlet flow periodicity. For the present work, all the measurements were made at the design incidence.

The geometries of the two cascades are summarized in **Fig. 2**. LS2 represents the midspan section of a power turbine blade of fairly recent design. After the development of the Moustapha et al. [15] correlation, cascade LS3 was fabricated to examine further the effect of leading-edge geometry on the off-design profile losses. The two aerofoils were designed for the same inlet and outlet conditions and lifing requirements, using the same turbine-profile design system.

As shown in **Fig. 2**, LS3 has a leading-edge diameter roughly twice that of LS2. To maintain similar lifing requirements, which required the cross-sectional metal areas to be essentially the same, the leading-edge wedge angle for LS3 was reduced to 43.0 deg from the value of 52.4 deg used for LS2. In addition, the stagger angle was reduced from the value of 23.1 deg for LS2 to 21.6 deg for LS3. Korakianitis and Papagiannidis [16] have noted an influence of stagger angle on the loading distribution, and as a result, the present measurements include the effects of more than the leading-edge geometry.

**Figure 2** also shows the locations of the flow field measurements. Detailed measurements of the inlet boundary layer were made at 1.2 axial chord lengths upstream of the leading edge. The reference upstream dynamic and total pressures were obtained on the centerline at this location. Traverses were made at 0.5 axial chord lengths upstream of the leading edge to verify the inlet flow uniformity. All downstream measurements were made at 0.4 axial chord lengths downstream of the trailing edge, unless otherwise noted.

**Instrumentation and Data Acquisition.** All flow field measurements were obtained in the present study and were made with pressure probes. The upstream measurements and downstream midspan measurements were made with a three-hole probe used in the non-nulling mode. The probe tip has a width of 2.0 mm and a thickness of 0.64 mm. The probe has been calibrated in 0.5 deg steps over a range of $\pm 10$ deg of flow misalignment in the yaw direction. The uncertainty in the measured yaw angles is estimated to be $\pm 0.5$ deg and the uncertainty in the measured dynamic and total pressures is estimated to be $\pm 0.6\%$ and $\pm 0.3\%$ of the reference dynamic pressure. Two seven-hole probes were used for the detailed downstream measurements, and like the three-hole probe, they were used in the non-nulling mode. Both seven-hole probes have a diameter of 2.4 mm and a conical tip with an apex angle of 60 deg. The probe used for the LS3 measurements was calibrated in 5 deg steps for all combinations of pitch and yaw up to 50 deg of flow misalignment relative to the probe axis. For the range of flow misalignment angles encountered during the testing (approximately 25 deg), the estimated uncertainty for measured flow angles is $\pm 0.6$ deg, and for measured dynamic pressure and total pressure is $\pm 1.4\%$ and $\pm 0.7\%$ of the reference dynamic pressure, respectively. The probe used for the LS2 measurements was calibrated in 2 deg steps over a range of 40 deg of flow misalignment in both pitch and yaw. The estimated uncertainties are slightly smaller than those reported above: $\pm 0.5$ deg; for measured dynamic pressure and total pressure is $\pm 1.2\%$ and $\pm 0.3\%$ of the reference dynamic pressure, respectively. The inlet boundary layer was traversed using a pitot-tube with inner and outer diameters of 0.33 and 0.64 mm, respectively. The uncertainty in the mass-averaged inlet total-pressure deficit, as obtained from the pitot-tube traverses, is estimated to be $\pm 0.5\%$ of the reference dynamic pressure.

The measurements with the seven-hole pressure probes were made on a plane that extends 1.287 blade spacings in the pitchwise direction (142.5 mm) and 0.700 blade heights in the spanwise direction (142.5 mm). For the traverses performed at 0.4 axial chord lengths downstream of the trailing edge, the spacing between measurement points was 7.5 mm in both the pitchwise and spanwise directions, for a total of 400 grid points. At the traverse plane located 0.1 axial chord lengths downstream of the trailing edge, the spacing was 3.75 mm in both directions, for a

total of 1521 grid points. The total-pressure loss coefficients ($Y$) obtained by mass-averaging the grid data are estimated to be accurate to $\pm 0.0035$.

To measure aerofoil surface static pressures, one of the aerofoils is instrumented over half of its span with 12 chordwise rows of 43 static taps. Each row consists of 25 suction surface taps, 17 pressure surface taps and one base pressure tap.

Two pressure acquisition systems were used during the course of this experimental work. For the earlier LS3 measurements, the pressures were measured with capacitive-type differential transducers. A new, faster pressure-scanning module, which uses piezoresistive differential transducers, was employed for the LS2 measurements. In both systems, the analog pressure signals were converted to digital form with 12-bit resolution. All quoted uncertainty intervals apply to both data acquisition systems.

**Data Reduction.** The loss data presented here is expressed mainly in terms of the total-pressure loss coefficient, $Y$. This coefficient is obtained using the mass-averaged total-pressure coefficient, $Cp_0''$, where the reference total and dynamic pressures are the values on the centerline upstream of the cascade.

The mass-averaged values of $Cp_0$ are calculated from

$$Cp_0''=\frac{\int\int Cp_0(y',z)\rho u dy' dz}{m_{\text{ref}}} \tag{1}$$

where $m_{\text{ref}}$ is the reference mass flow rate over one blade pitch and 50% of the span at the inlet to the cascade. As a means of verifying the data quality, the outlet mass flow measured over an equal area downstream of the cascade was compared to the reference mass flow. For the cases presented in this paper, the inlet and outlet mass flow rates differed by no more than 2.5%.

The total-pressure loss coefficient is defined as

$$Y=(Cp_{0,1}''-Cp_{0,2}'')\left(\frac{q_{CL}}{q_2}\right)'' \tag{2}$$

where $Cp_0$ is obtained from Eq. (1).

A knowledge of the streamwise vorticity and secondary kinetic energy distributions is useful for studying the three-dimensional structures downstream of the aerofoil row.

The axial and tangential components of vorticity were calculated from the grid data at the downstream traverse plane using

$$\omega_x=\frac{\partial w}{\partial y}-\frac{\partial v}{\partial z} \tag{3}$$

and

$$\omega_y=\frac{1}{u}\left(v\omega_x+\frac{1}{\rho}\frac{\partial P_0}{\partial z}\right). \tag{4}$$

Equation (4) is derived from the incompressible Euler equations (Gregory-Smith et al., [17]) and a discussion of its validity in viscous flows is given by Yaras and Sjolander [18]. The streamwise component of vorticity is then calculated from

$$\omega_s=\omega_x\cos\alpha_2''+\omega_y\sin\alpha_2''. \tag{5}$$

Secondary kinetic energy is defined as the kinetic energy associated with the velocity components in a plane perpendicular to the mass-averaged exit flow angle, $\alpha_2''$. Mathematically, this may be expressed as

$$\text{SKE}=\frac{1}{2}\rho(v_{\text{sec}}^2+w_{\text{sec}}^2) \tag{6}$$

where

$$v_{\text{sec}}=-u\sin\alpha_2''+v\cos\alpha_2'' \quad \text{and} \quad w_{\text{sec}}=w. \tag{7}$$

**Table 1 Summary of experimental results**

| LOCATION | FLOW QUANTITY | CASCADE LS2 | CASCADE LS3z |
|---|---|---|---|
| INLET | $\delta^*$ (mm) | 2.6 | 2.2 |
| | $\theta$ (mm) | 1.9 | 1.5 |
| | $H$ | 1.39 | 1.41 |
| | $Cp''_{0\ \text{inlet}}$ | −0.033 | −0.027 |
| OUTLET (Traverse plane: 40%$Cx$ downstream of trailing edge) | $Cp''_{0\ \text{total}}$ | −0.090 | −0.083 |
| | $Cp'_{0\ \text{profile}}$ | −0.047 | −0.052 |
| | $Cp''_{0\ \text{secondary}}$ | −0.043 | −0.031 |
| | $Y_{\text{total}}$ | 0.043 | 0.041 |
| | $Y_{\text{profile}}$ | 0.021 | 0.025 |
| | $Y_{\text{secondary}}$ | 0.022 | 0.016 |
| | $C_{\Gamma+}$ | 0.196 | 0.159 |
| | $C_{\Gamma-}$ | −0.110 | −0.086 |
| | $C''_{\text{SKE}}$ | 0.013 | 0.008 |
| | $\alpha_2''$ (deg) | −53.6 | −52.6 |
| | $q_2/q''_{CL}$ | 2.09 | 2.02 |
| | $\alpha'_{\text{midspan}}$ (deg) | −54.1 | −52.9 |
| | $q_2/q'_{CL\ \text{midspan}}$ | 2.18 | 2.09 |
| | AVR | 0.98 | 0.99 |
| | Quality factor, $Q$ | 5.06 | 4.50 |
| MIXED-OUT | $Cp''_{0\ \text{total}}$ | −0.108 | −0.096 |
| | $Cp'_{0\ \text{profile}}$ | −0.048 | −0.054 |
| | $Cp''_{0\ \text{secondary}}$ | −0.060 | −0.042 |
| | $Y_{\text{total}}$ | 0.053 | 0.048 |
| | $Y_{\text{profile}}$ | 0.022 | 0.026 |
| | $Y_{\text{secondary}}$ | 0.031 | 0.023 |
| | $q_2/q''_{CL}$ | 2.04 | 1.98 |
| | $q_2/q'_{CL\ \text{midspan}}$ | 2.18 | 2.08 |

## Experimental Results

**Operating Conditions.** All measurements were made at a Reynolds number of $3.0\pm0.03\times10^5$ based on inlet velocity and aerofoil chord. The inlet velocity was approximately 30 m/s so that the conditions were essentially incompressible. The turbulence intensity at the cascade inlet was about 0.3%. It is noteworthy that Gregory-Smith and Cleak [19] examined the influence of inlet turbulence intensity on the secondary flows and found it had very little effect on the flow field and loss behavior.

The inlet endwall boundary layer parameters are given in **Table 1**, and as can be seen, the thickness of the layer for LS2 is slightly larger than for LS3. This arises from a small difference in the endwall boundary layer bleed flows upstream of the two cascades. The location of the bleed slots is shown in **Fig. 1**.

**Blade Static Pressure Distributions.** The strength of secondary flows downstream of a turbine have been shown to depend strongly on the overall aerofoil loading (e.g., [20–23]) and the loading distribution (e.g., [2,23]). To provide background for the subsequent discussions, the blade pressure distributions are presented first.

**Figure 3** shows the measured variations in the midspan blade pressure for LS2 and LS3. The aerofoil loading data for LS2 were obtained from a study of the effects of axial velocity ratio (AVR) on the midspan aerodynamic behavior of a turbine cascade, [14]. In their study, an arrangement of endplates was used for controlling the flow convergence or divergence. With the use of endplates, the effective aspect ratio of the cascade was reduced to approximately 1.0 (from 1.25), and the thickness of the inlet endwall boundary layer was substantially decreased. The loading measurements for LS3 were obtained in the present study and therefore correspond to somewhat higher values of endwall boundary layer thickness.

**Figure 3** shows that LS2 is also slightly more forward loaded than LS3. This is consistent with the fact that LS2 has a higher

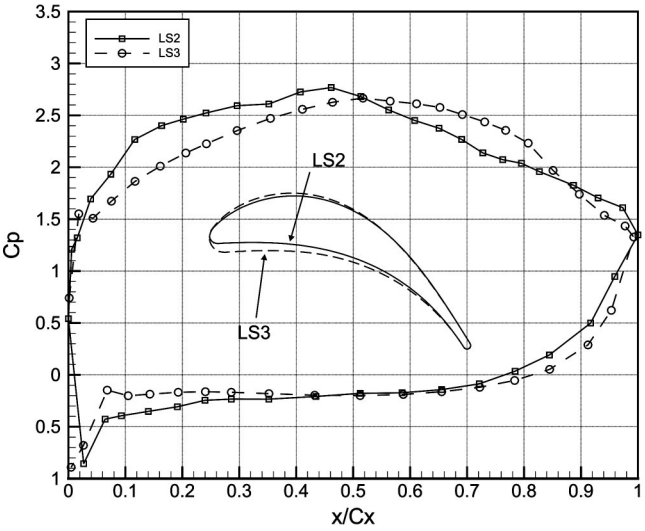


**Fig. 3 Measured midspan surface pressure distributions for LS2 and LS3 at design incidence**

stagger angle than LS3 (23.1 deg versus 21.6 deg, as shown in **Fig. 2**). As seen from the figure, LS2 experiences significantly higher acceleration in the first 10% *Cx*. Also, the magnitude of the suction peak has increased and the peak has moved forward from about 55% *Cx* for LS3 to 45% *Cx* for LS2. On the aft portion of the suction surface, the deceleration is quite uniform for LS2. In contrast, a change in the slope of the pressure distribution at about 80% *Cx* is observed for LS3 and appears to correspond to the reattachment point of a small laminar separation bubble which starts at about 60% *Cx*, [2].

### Physics of the Endwall Flow at the Design Incidence

*Introduction.* Extensive work has been performed since the 1940s on secondary flows and has provided a basis for a number of detailed descriptions of the endwall flow within the blade passage at the design incidence (e.g., [3,21,24]). Amongst these descriptions, there is fairly broad agreement about the details of the flow field. However, some questions still remain. To further advance the understanding of the endwall flow, Benner et al. [2] and Wang et al. [25] provided additional data in the form of oil and smoke flow visualization. Both groups of authors gave detailed interpretations of the flow physics inside the blade passage; a brief summary of the present authors' interpretation is presented below as background for the subsequent discussions of the effect of leading-edge geometry. As well, the interpretation of the flow structures has evolved slightly from that given in Benner et al. [2]. It is now believed to be more consistent with both the present downstream measurements and the smoke flow visualization of Wang et al. [25] and Sonoda [26]. Some of the downstream flow field measurements are included in this section to help explain the difference between the current and previous interpretation (i.e., [2]).

*Interpretation of the Flow Field.* **Figures 4(*a*)** and **4(*b*)** summarize the interpretation of the flow near the endwall and suction surfaces, respectively. This interpretation is based mainly on the surface oil flow visualization presented in Benner et al. [2]. Downstream flow field measurements made in this work were also used to interpret the inside-passage flow physics. These figures will be discussed below.

**Figure 4(*a*)** shows the near-endwall flow behavior. In the leading-edge region, there were two major separation lines, designated as $S_1$ and $S_2$. $S_1$ is commonly associated with the separation of the inlet endwall boundary layer, whereas $S_2$ is regarded as the lift-off line of the horseshoe vortex. Also shown is the

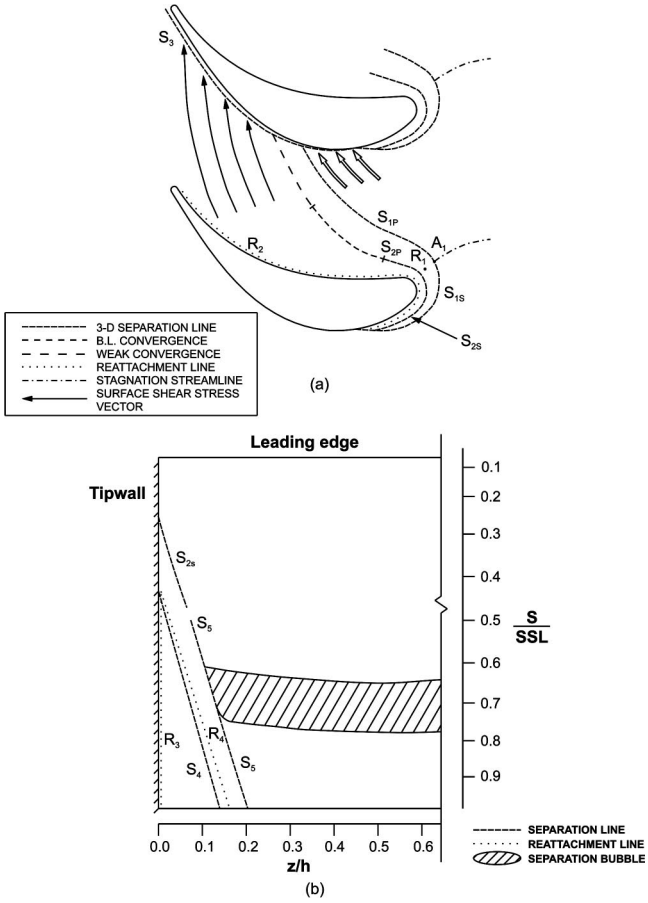


**Fig. 4 Interpretation of the (*a*) endwall, and (*b*) suction surface flow visualization at the design incidence (modified from [2])**

reattachment point $R_1$ and the separation saddle point $A_1$ (the intersection point between the stagnation streamline and the primary separation line). The portion of the inlet boundary layer fluid that takes part in the horseshoe vortex is divided along the stagnation streamline into the pressure and suction side branches, subscripted *p* and *s* in **Fig. 4**. The other major separation line is that of the endwall boundary layer in the suction corner, $S_3$: it seems to originate at the point of intersection of the suction-side leg of $S_1/S_2$ with the suction surface. The only reattachment line that was visible was near the corner at the blade pressure surface and is denoted as $R_2$.

As observed by a number of investigators (e.g., [2,21,24–27]) some of the inlet endwall boundary layer fluid can end up at the suction surface, at separation line $S_3$, without having taken part in the separations, $S_1$ or $S_2$. This region is indicated on **Fig. 4(*a*)** with double-lined arrows. As will be discussed below, this fluid seems to be associated with one of the dominant high-loss regions in the downstream flow field.

The interpretation of the flow structures near the suction surface is given in **Fig. 4(*b*)**. There appear to be two major separation lines on the suction surface in the endwall region: $S_5$, an apparent extension of $S_{2s}$, and $S_4$. $S_4$ is the most commonly observed separation line and it is associated with the passage vortex whereas $S_{2s}$ is the separation line for the suction-side leg of the horseshoe vortex. The flow visualization clearly showed a finite distance between the starting points for the $S_{2s}$ and $S_4$ separation lines. This supports the earlier interpretation that some of the inlet endwall boundary layer fluid was not involved in the inlet endwall boundary layer separation. Based on similar observations, Hodson and Dominy [21] and Denton [28] described this fluid as being ''funnelled'' between the passage vortex and suction-side leg of

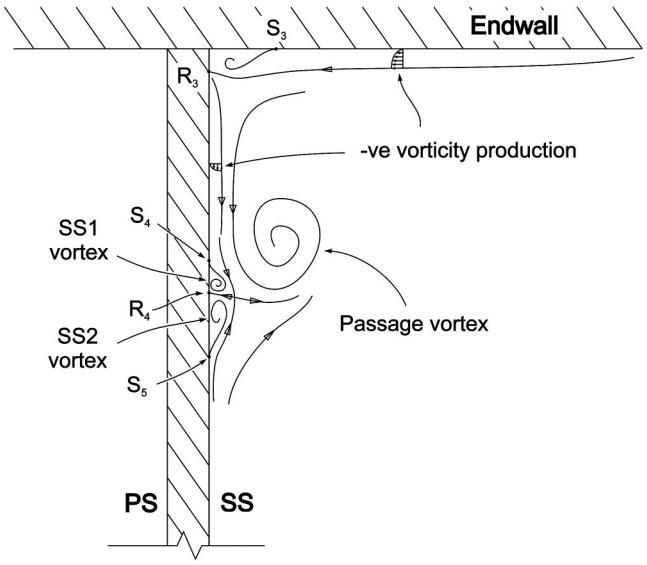


**Fig. 5 Interpretation of the flow structures in the endwall region**

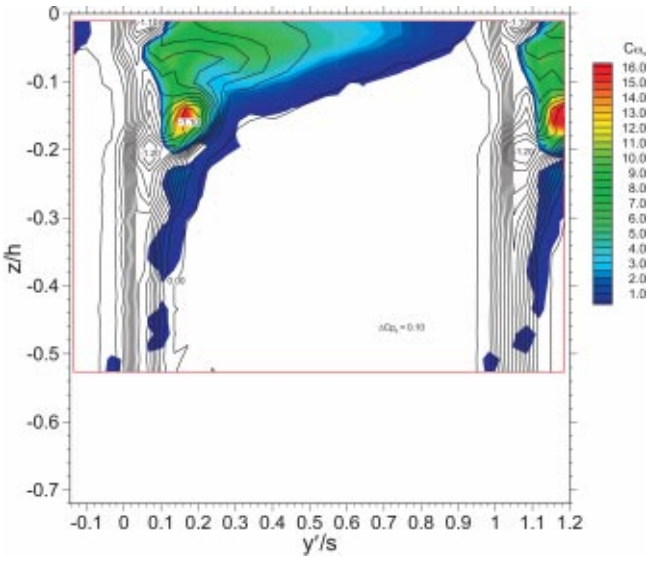


**Fig. 6 Line contours of total-pressure coefficient superimposed on flood contours of positive streamwise vorticity for LS3 ($x/Cx=1.10$)**

the horseshoe vortex. In the present flow, the suction-side leg of the horseshoe vortex does not appear to remain close to the suction surface with downstream distance, as the $S_{2s}$ separation line seemed to fade fairly quickly. The only plausible explanation for this seems to be that the passage vortex interacts with the suction side leg of the horseshoe vortex, thus forcing it off the suction surface. Presumably, the suction-side leg of the horseshoe vortex wraps itself around the passage vortex, as has been observed by many investigators (e.g., [24–26,29,30]). The separation line $S_5$ occurs where the suction-surface boundary layer meets the funnelled fluid. Finally, there are also two regions of attaching flow. Line $R_3$ represents the reattachment of the endwall fluid that separated along $S_3$. As in many experiments, it was possible to identify the resulting corner vortex in the present downstream measurements. The $R_4$ reattachment line is discussed further below.

The interpretation of the flow behavior within the region bounded by the $S_4$ and $S_5$ lines has evolved slightly from the one originally given in Benner et al. [2]. Because the region between $S_4$ and $S_5$ is so small, the details of the surface flow behavior are difficult to discern, particularly using surface oil flow visualization alone. Therefore, pressure probe measurements were made near the trailing edge.

**Figure 5** gives the resulting, tentative interpretation. The region between separation lines $S_4$ and $S_5$ is believed to be occupied, in part, by the funnelled endwall boundary layer fluid. The present authors also believe that some of the suction-surface fluid from beneath the passage vortex is convected into this region. Therefore, $R_4$ is the reattachment line that divides the funnelled boundary-layer flow from the suction-surface fluid that has been convected from beneath the passage vortex. In the region bounded by $R_4$ and $S_5$, the surface flow visualization showed very little evidence of either flow convergence on the $S_5$ separation line or flow divergence from the $R_4$ reattachment line. For this reason, it appears that the vortical structure, referred to as SS2, is quite weak. The vortex in the region bounded by $S_4$ and $R_4$, which is denoted as SS1, appears to be considerably smaller than SS2 but quite intense. This interpretation is based on measurements that are presented below and the smoke flow visualization results of Wang et al. [25].

**Figures 6** and **7** show contour plots of total-pressure deficit overlaid with color floods of positive and negative streamwise vorticity, respectively.

The measurements presented in these figures were taken for LS3 at 0.1 axial-chord lengths downstream of the trailing edge. These contour plots were found to be useful for identifying the location and characteristics (e.g., size, strength, and direction of rotation) of the vortical structures. Vorticity can be used to visualize the motion of the flow since it is convected with the fluid particles. It should be noted that for the selected coordinate system, the passage vortex contains positive streamwise vorticity.

From **Fig. 6**, it can be seen that the endwall region is occupied predominantly by fluid with positive streamwise vorticity. Within this region, there are two cores of high vorticity. The one closest to midspan is coincident with a region of high loss and is quite intense: it is typically identified as the passage vortex. The other vorticity core, which is closer to the endwall, is weaker and associated with relatively low-loss fluid. To the authors' knowledge, this flow feature has not been observed previously.

The negative vorticity region shows a number of distinctive features, including a small region of intense vorticity beneath the passage vortex, and partially overlapping this, a region of high-

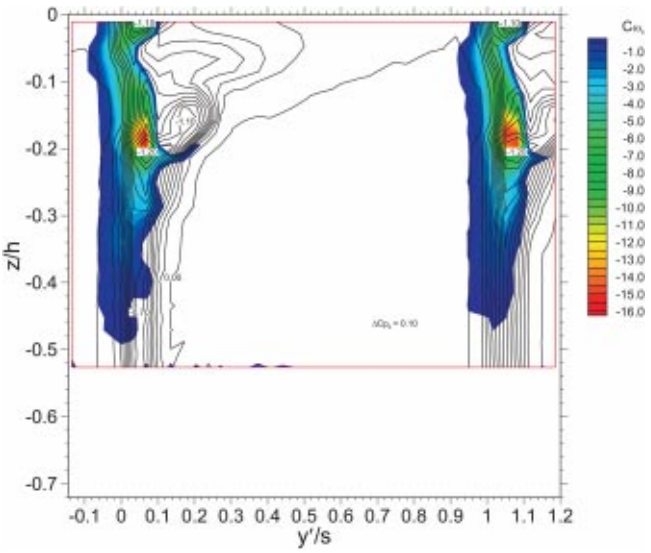


**Fig. 7 Line contours of total-pressure coefficient superimposed on flood contours of negative streamwise vorticity for LS3 ($x/Cx=1.10$)**

loss fluid. The present authors believe that this loss core is associated with the funnelled boundary layer fluid. We also believe that, as mentioned earlier, the SS1 vortex is composed mainly of suction surface fluid. This fluid originates in the endwall suction surface corner (at $R_3$) and is driven towards the $S_4$ separation line by the cross flows induced by the passage vortex. The interaction appears to be quite strong from the surface flow visualization. Evidently, the boundary layer that originates at $R_3$, is being strongly accelerated as it makes its way towards $S_4$, and as a result, the vorticity production is high (the resultant vorticity is negative in sign). The region of high negative vorticity beneath the passage vortex, which is observed in **Fig. 7**, is likely the roll-up of this vorticity sheet. It is worth noting that the present authors have considered the possibility that the vorticity core was composed of trailing-shed vorticity, as has been suggested by a number of investigators. However, the surface static pressure measurements presented in Benner et al. [2] indicated very little spanwise variation in the loading in this region. Also, pressure probe measurements made slightly upstream of the trailing edge showed evidence of a core of high negative vorticity being present already in the vicinity of the $S_4/S_5$ separation lines.

The final feature in the negative vorticity field is the vortex located at the endwall suction surface corner. As expected, this region is characterized by high losses and elevated levels of negative vorticity.

**Mass-Averaged and Mixed-Out Results.** The mass-averaged and mixed-out results for LS2 and LS3 are presented in **Table 1**.

As seen from the table, the overall total-pressure losses for LS2 and LS3 are very similar. The profile losses are taken as the losses measured at midspan where the influence of the secondary flow is small. The secondary loss coefficient is then taken as the difference between the overall loss coefficient and the profile loss coefficient. Thus, it is implicitly assumed that the profile losses generated near the endwall are the same as those at midspan. This is the conventional loss breakdown and it seems to give reasonable results at design incidence. However, it has been shown by Benner et al. [2] that the conventional loss breakdown can result in misleadingly low values of the secondary loss coefficient at off-design incidence.

From **Table 1** it can be seen that the measured profile loss for LS3 is approximately 20% larger than that for LS2. Although the absolute difference between the two loss coefficients is quite small, the measured values are consistent, within $\pm 0.002$, with those measured by previous investigators (e.g., for LS2, [12–14]; for LS3, [31,32]). Therefore, the difference in the midspan losses appears to be genuine. Denton [28] argued that the loss production in a boundary layer varies as the cube of the edge velocity. **Figure 3** shows that LS3 has a larger leading-edge overspeed than LS2 and this may account for the higher profile losses for LS3.

The mass-averaged results presented in **Table 1** show that the measured and mixed-out secondary losses are higher for LS2. Also shown in the table are the values of the ''quality factor,'' $Q$. This parameter was proposed by Marchal [33], as referred to in Sieverding [3], to allow designers to qualitatively assess the effects of aerofoil loading and loading distribution on secondary losses. Marchal argued that an increase in the cross-passage pressure gradient or a shift in the loading distribution toward the leading edge would produce higher secondary losses. The higher value of $Q$ for LS2 is mainly due to the aerofoil being more forward-loaded, as can be seen in **Fig. 3**. The increase in secondary loss for LS2 is thus consistent with the higher value of $Q$. Weiss and Fottner [23] investigated the effect of loading distribution on secondary losses and also found that a more forward-loaded aerofoil (higher $Q$) produced higher losses and overall stronger secondary flows. In their investigation, the two cascades had identical leading-edge geometries; the main geometric difference was the stagger angle—the front-loaded cascade having a larger stagger angle.

**Table 2 Energy audit from the measurement plane to the mixed-out plane**

| Description | LS2 | LS3 | LS3-LS2 |
|---|---|---|---|
| ''Diffusion'' loss** | −0.006 | −0.005 | 0.000 |
| +ΔSecondary KE | −0.013 | −0.008 | **0.005** |
| =Mixing loss | −0.018 | −0.013 | **0.005** |
| Mixing loss | −0.018 | −0.013 | 0.005 |
| +Measured loss | −0.090 | −0.083 | 0.007 |
| =Mixed-out loss | −0.108 | −0.096 | 0.012 |

**Diffusion loss=ΔPrimary KE+Static Pressure Recovery
NOTE: All quantities are nondimensionalized by the inlet centreline dynamic pressure

In addition to the higher losses, the overall strength of the secondary flow field was also larger for LS2. Three parameters indicate this: the mass-averaged secondary kinetic energy ($C''_{SKE}$) and the absolute values of the positive and negative secondary circulation ($C_{\Gamma+}$ and $C_{\Gamma-}$), all of which were larger for LS2. The secondary kinetic energy is significant since one of the dominant mechanisms for loss generation is mixing (Denton [28]). Through this process, secondary kinetic energy is eventually lost if it is not used in a downstream rotor for work extraction. Therefore, secondary kinetic energy may be regarded as a potential loss source and a cascade with stronger secondary flows will ultimately generate more loss, as is the case for LS2.

**Table 2** summarizes the results of an ''energy audit'' from the measurement plane to the mixed-out plane. All loss values are normalized on the inlet dynamic pressure. The mixing losses are divided into two components. The first is described as the ''diffusion'' loss and is the portion of the primary kinetic energy that is lost between the measurement and mixed-out planes. The remaining portion of the primary kinetic energy is recovered as static pressure. The second term is the dissipation of secondary kinetic energy. Two observations are worth making: first, the diffusion losses are nearly identical for the two cascades and second, the difference in the mixing losses can be mostly attributed to the difference in the measured secondary kinetic energies.

The remainder of the paper examines the downstream traverses in more detail and presents a comparison of the measured secondary losses with empirical predictions.

**Total Pressure Distributions.** **Figures 8(*a*)** and **(*b*)** show contour plots of the total-pressure deficits at the downstream measurement plane for LS2 and LS3, respectively. Darker shading indicates higher losses.

In broad terms, the total-pressure deficit distributions for LS2 and LS3 are very similar. However, there are some differences. Starting near the endwall with the corner vortex, both the pitchwise extent of the high loss region and the peak loss magnitude are larger for LS2. Moreover, for LS2, the size of the loss cores associated with the SS1 and passage vortices are larger and have penetrated further toward midspan. The size of the loss cores must, to some extent, be related to the strength of the vortices. Data presented below support this assertion.

**Positive Vorticity Field.** **Figures 9** and **10** show the contour lines from **Figs. 8(*a*)** and **8(*b*)** superimposed with color floods illustrating the regions of positive streamwise vorticity for LS2 and LS3, respectively. As mentioned, the passage vortex has positive vorticity.

As can be seen, both flows are largely dominated by regions of positive streamwise vorticity with nearly equal area. However, the vorticity levels in this region are comparatively higher for LS2; thus, the circulation, or overall strength of the positive vorticity field is greater.

We believe that most of the fluid of positive streamwise vortic-

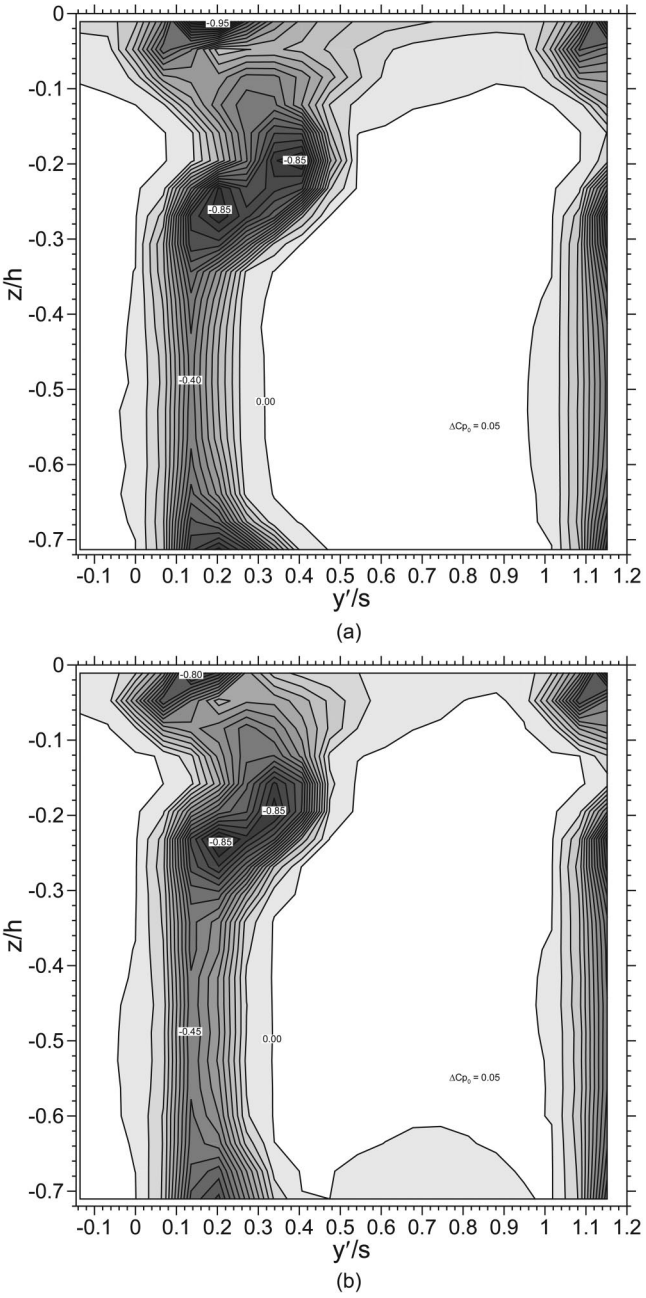


**Fig. 8 Line contours of total-pressure coefficient for (*a*) LS2 and (*b*) LS3 at design incidence (*x*/*Cx*=1.40)**

ity originates from the inlet endwall boundary layer. The other sources of vorticity mostly produce vorticity of the opposite sense. These sources include: the endwall region aft of separation line $S_{1P}$; the region of the suction surface between the endwall and the $S_4$ separation line; and the portion of the inlet endwall boundary layer that becomes the suction side leg of the horseshoe vortex. The negative vorticity produced by these sources will reduce, through mixing, the overall circulation associated with the fluid of positive vorticity. Thus, it is conceivable that the positive vorticity levels for LS3 are lower than those of LS2 because of stronger mixing with the endwall and suction surface boundary layer fluid. However, this does not seem likely since such mixing would also generate losses and the losses for LS3 are lower than those of LS2. A more plausible explanation is simply that LS2 produces a stronger positive streamwise vorticity field. Since the positive vorticity is believed to result from the separation of the inlet endwall

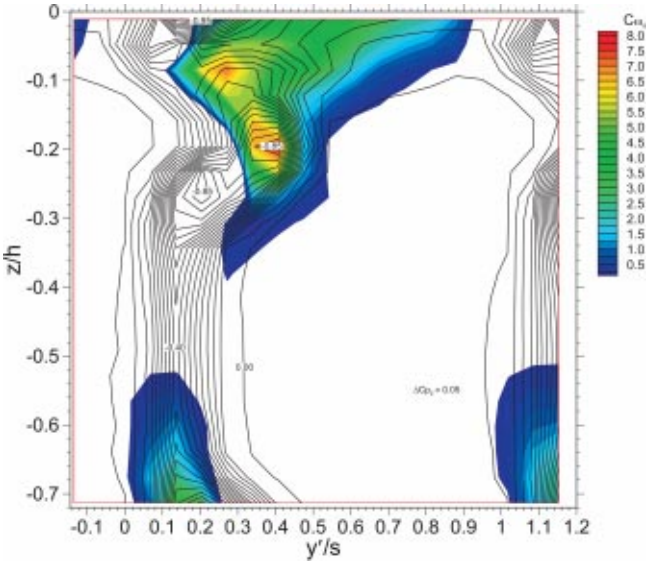


**Fig. 9 Line contours of total-pressure coefficient superimposed on flood contours of positive streamwise vorticity for LS2 (*x*/*Cx*=1.40)**

boundary, any factor that influences the extent of this separation should also affect the generation of positive vorticity. Another recent experiment, by Sauer et al. [34], also highlights the importance of the inlet endwall boundary layer separation. The authors found that the secondary loss in a cascade of high-turning turbine aerofoils could be significantly reduced by modifying the aerofoil shape over the first 20%$Cx$ in the aerofoil-endwall junction.

The process of horseshoe vortex formation in turbine cascades is not fully understood owing to the scarcity of detailed measurements in the leading-edge region. This contrasts with the flow at the junction of a cylindrical body and flat plate, which has been investigated extensively. A number of the studies have looked at the influence of leading-edge shape and size on the strength of the horseshoe vortex. For example, Mehta [35] and Kubendran et al. [36] showed experimentally that for the flow around the junction of a nonlifting body and a flat plate, simulating a wing/fuselage

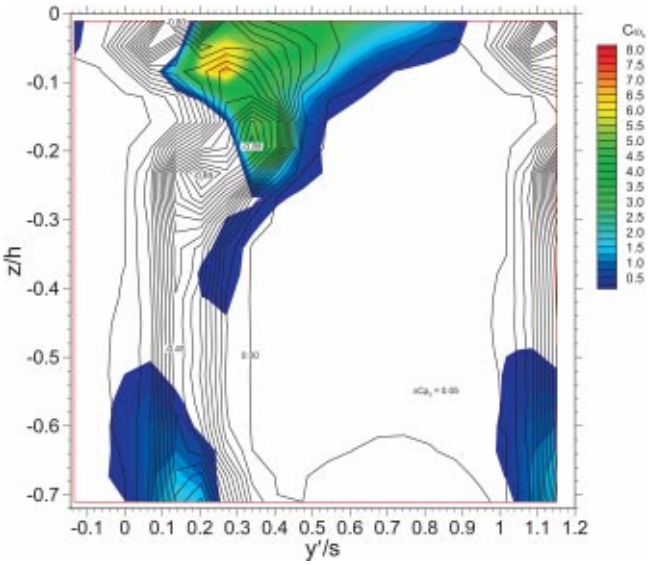


**Fig. 10 Line contours of total-pressure coefficient superimposed on flood contours of positive streamwise vorticity for LS3 (*x*/*Cx*=1.40)**

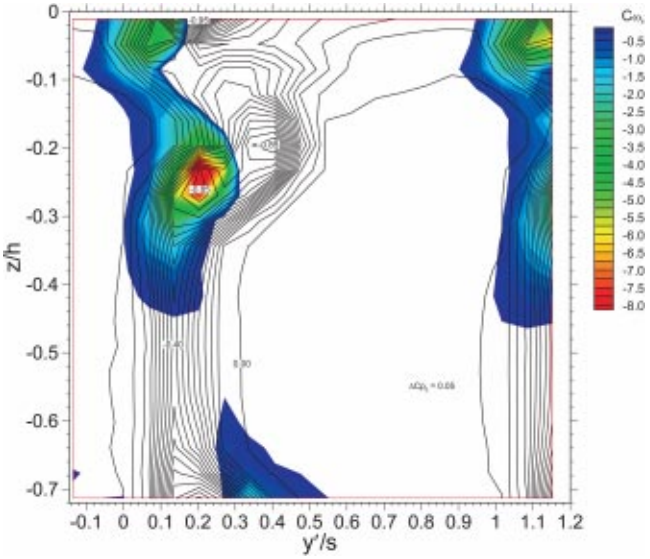


**Fig. 11 Line contours of total-pressure coefficient superimposed on flood contours of negative streamwise vorticity for LS2 ($x/Cx=1.40$)**

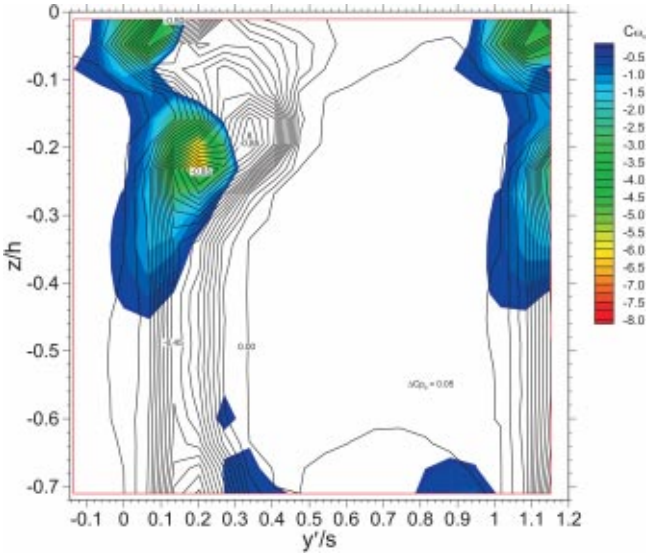


**Fig. 12 Line contours of total-pressure coefficient superimposed on flood contours of negative streamwise vorticity for LS3 ($x/Cx=1.40$)**

junction, the circulation associated with the horseshoe vortex was related to the shape of the leading edge. In both experiments, the strength increased significantly with nose (or leading-edge) bluntness. It appears that the strength of the vortex is closely related to the pressure disturbance produced by the obstacle: a larger pressure disturbance generates a stronger vortex.

For the simple junction flows, the pressure disturbance is solely a function of the leading-shape and size. However, the pressure disturbance produced by a lifting body, such as a turbine aerofoil, is more complex. The present authors believe that the pressure field on the endwall upstream of the leading edge is substantially influenced by the loading in the leading-edge region. This hypothesis is based on data from both Benner et al. [2] and Langston et al. [37] which show that the saddle point of separation moves towards midpitch as the blade loading distribution shifts forward. In both experiments, the loading in the leading-edge region was varied through changes in incidence. The important point is that the effective obstacle size seen by the oncoming endwall boundary layer seems to be strongly related to the loading on the forward part of the aerofoil, and only secondarily on the thickness of the leading edge. This argument provides a plausible explanation for why the more forward-loaded LS2 cascade generates a stronger positive vorticity field than LS3, despite the fact that LS2 has the smaller leading-edge diameter.

**Negative Vorticity Field.** **Figures 11** and **12** show the corresponding contours of negative streamwise vorticity for LS2 and LS3.

The most prominent feature is the core of negative vorticity associated with the SS1 vortex. This vortex and its neighboring passage vortex appear to be nearly identical in size and peak vorticity magnitude for the respective aerofoils. Therefore, like the passage vortices, the strength of the SS1 vortex for LS2 is significantly stronger than for LS3. The vortex is approximately the same size for both cases, but the peak vorticity level for LS2 is approximately 40% higher than for LS3.

As mentioned earlier, the SS1 vortex seems to be composed of fluid from the thin boundary layer on the suction surface between the corner vortex reattachment line, $R_3$, and the passage vortex separation line, $S_4$. The strong cross flows induced on the suction surface by the nearby passage vortex, together with the apparent thinness of the boundary layer, leads to high surface shear stress. Consequently, the production of negative streamwise vorticity on the surface will also be high. This vortical fluid is convected towards the $S_4$ separation line where it rolls up into the SS1 vortex. Since the vorticity in the SS1 vortex is largely generated by the action of the passage vortex, one would expect the strength of the two vortex structures to be related. In other words, a stronger passage vortex will lead to a stronger SS1 vortex, as is the case for LS2 as compared to LS3.

**Downstream Secondary Kinetic Energy Field.** **Figures 13** and **14** show contour lines of total-pressure deficit along with color floods of secondary kinetic energy for LS2 and LS3, respectively. As can be seen, there are two regions of fluid with relatively high secondary kinetic energy: one located immediately adjacent to the endwall, extending over approximately 30% of the pitch, and another located between the passage and the SS1 vortex. In both cases, there is comparatively little secondary kinetic energy associated with the vortex cores themselves.

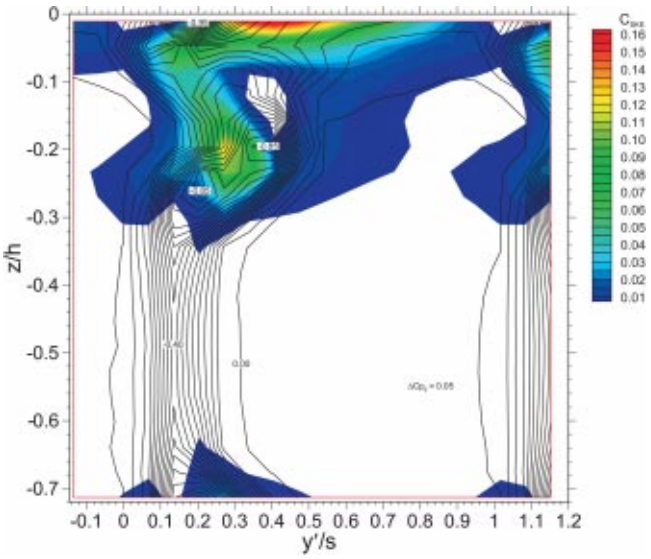


**Fig. 13 Line contours of total-pressure coefficient superimposed on flood contours of secondary kinetic energy for LS2 ($x/Cx=1.40$)**

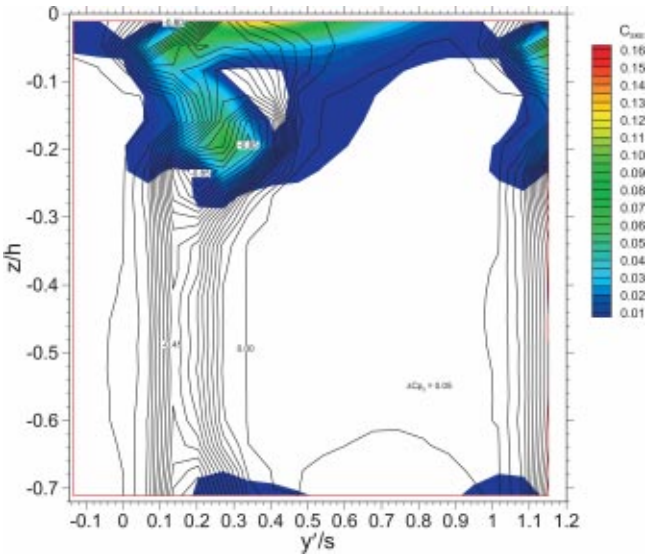


**Fig. 14 Line contours of total-pressure coefficient superimposed on flood contours of secondary kinetic energy for LS3 ($x/Cx=1.40$)**

The main difference between the two cases is that the peak levels of secondary kinetic energy are comparatively higher for LS2. Near the endwall, the peak level for LS2 is approximately 30% greater than for LS3, and for the region between the passage vortex and the SS1 vortex, the difference is even greater at approximately 60%. The most likely explanation for the latter difference lies with the strength of the vortical structures. The results presented earlier clearly showed that the two vortices for LS2 are much stronger than those for LS3, while there was no significant difference in their proximity. Therefore, the induced secondary velocities and corresponding secondary kinetic energies would be expected to be higher for LS2, as observed.

The stronger secondary kinetic energy near the endwall for LS2 is somewhat surprising since it was noted earlier that the cross-passage pressure difference is lower for LS2 on the rearward part of the aerofoil. The most probable explanation lies with the passage vortex. As shown in **Figs. 9** and **10**, the passage vortex for LS2 is comparatively stronger than the one for LS3. Because the downstream endwall region lies partly beneath the passage vortex, the higher secondary kinetic energy is likely induced by the stronger passage vortex. Therefore, in this part of the blade passage it is the passage vortex rather than the cross-passage pressure difference that seems to play the dominant role in determining the near-endwall secondary kinetic energy. The higher velocities near the endwall should also increase the entropy generation in the endwall boundary layer.

As noted earlier, the secondary kinetic energy is itself a potential source of losses, with the losses being generated through mixing as the flow proceeds downstream. As pointed out in connection with **Tables 1** and **2**, the increase in losses from the measurement plane to fully mixed-out conditions correlated well with the mass-averaged secondary kinetic energies obtained at the measurement plane and LS2 did indeed give the higher mixing losses.

## Comparison of Measured Secondary Losses With Empirical Predictions

Since empirical loss correlations continue to play an important role in the design process, there is an ongoing need to review and improve these correlations. This section compares the present results to a few of the most widely used correlations for secondary losses: Kacker and Okapuu [38], which is based on Ainley and Mathieson [39] and Dunham and Came [40]; Craig and Cox [41]; and Traupel [42]. The comparisons are given in **Table 3**.

**Table 3 Comparison of measured and predicted secondary losses**

| SOURCE | Secondary loss coefficient, $Y_{secondary}$ LS2 | LS3 |
|---|---|---|
| Measured (mixed-out) | 0.031 | 0.023 |
| Kacker and Okapuu [38] | 0.093 | 0.091 |
| Craig and Cox [41] | 0.071 | 0.072 |
| Measured (40%$Cx$ downstream of trailing edge) | 0.022 | 0.016 |
| Traupel [42]* | 0.062 | 0.063 |

*Loss coefficient is a function of downstream distance, and it has been assumed that the value of endwall skin friction coefficient is $C_f=0.003$.

The correlations are seen to predict significantly higher losses than those measured: In all cases the predicted losses are at least twice as large as the measured. Similar discrepancies between cascade results and the correlations have been noted before. As discussed by Sieverding [43], the loss correlations derived from cascade data are scaled or ''calibrated'' to reproduce stage efficiencies derived from rig or engine data. It appears that most of the differences between the correlation predictions and the present cascade results are due to this calibration process, since our measured secondary losses are comparable with those observed in similar turbine cascades. Given that these loss systems have been shown to predict turbine efficiency reasonably well, there are evidently additional and significant loss generating mechanisms in the engine environment that are not captured in cascade testing. Thus, cascade results such as the present ones should be used mainly to gain physical insights and to establish trends due to variations in particular aerodynamic or geometric parameters.

As shown in **Table 3**, the correlations predict no significant differences in the losses for LS2 and LS3. This is to be expected since the correlations do not account for differences in loading distributions, which are thought to be the main source of the differences in the measured losses.

## Conclusions

Detailed measurements have been made of the secondary flows for two turbine cascades with aerofoils that differ mainly in their leading-edge geometries. The baseline aerofoil represents the midspan section of a power turbine blade of fairly recent design. The modified aerofoil was designed with a larger leading-edge diameter to investigate the effect of leading-edge geometry on the profile and secondary losses. The modified aerofoil also has a slightly smaller stagger angle; therefore, it was more aft loaded than the baseline aerofoil.

The measured and mixed-out secondary losses were found to be higher for the baseline aerofoil. The detailed flow field measurements showed that the streamwise vorticity and secondary kinetic energy fields were also stronger for this aerofoil. It is argued that the higher loss generation for the baseline aerofoil is mainly the result of a stronger passage vortex. The increased strength of this vortex combined with its close proximity to the suction surface and endwall would be expected to produce thinner boundary layers and larger boundary-layer edge velocities, which in turn should increase the loss production near the walls. In addition, the stronger passage vortex seemed to induce a stronger separation vortex on the suction side of the aerofoil. The higher secondary velocities in the region where these two vortices interacted resulted in higher downstream mixing losses for the baseline aerofoil.

The greater size and strength of the passage vortex for the baseline aerofoil is attributed to this aerofoil's front-loaded pressure distribution and the resulting stronger upstream pressure field seen

by the endwall boundary layer approaching the leading edge. This effect seemed to dominate over any influence of the leading-edge diameter, which was smaller for the baseline aerofoil. It is tentatively concluded that in turbine blade rows the leading-edge geometry has at best a minor influence on the secondary flow field, and the corresponding secondary losses, at least for the design incidence and for conventional leading-edge geometries. On the other hand, the loading on the forward part of the aerofoil appears to be of primary importance.

## Acknowledgments

Financial support for this study provided by the Natural Sciences and Engineering Research Council of Canada and by Pratt & Whitney Canada, Inc., is gratefully acknowledged.

## Nomenclature

AVR = $\int_0^s (u_2)_{MS} dy' / (u_1)_{MS} dy'$ = axial velocity ratio
$C$ = aerofoil chord length
$Cx$ = aerofoil axial chord length
$Cp$ = $P - P_{CL}/1/2\rho V_{CL}^2$ = static-pressure coefficient
$Cp_0$ = $P_0 - P_{0,CL}/1/2\rho V_{CL}^2$ = total-pressure coefficient
$Cp_{0\,(\text{total})}$ = $P_{0,2} - P''_{0,1}/1/2\rho V_{CL}^2$ = total-pressure loss coefficient
$C_{\text{SKE}}$ = $\text{SKE}/1/2\rho V_{CL}^2$ = nondimensional secondary kinetic energy
$C_\Gamma$ = $\Gamma/V_{CL}C$ = nondimensional secondary circulation
$C\omega_s$ = $\omega_s C/V_{CL}$ = nondimensional streamwise vorticity
$h$ = span
$H$ = $\delta^*/\theta$ = shape factor
$i$ = $\alpha_1 - \beta_1$ = incidence, in degrees
$m_{\text{ref}}$ = reference mass flow rate
$P$ = static pressure
$P_0$ = total pressure
$q$ = $1/2\rho V^2$ = dynamic pressure
$Q$ = $(\Delta Cp_{\max} q_{CL}/q_{\text{mean}} Cx/s^*)^{1.25}(1 - x_{\min}/Cx)$ = quality factor
Re = $\rho V_{CL} C/\mu$ = Reynolds number
$s$ = blade pitch or spacing
$s^*$ = cross-passage distance (measured in tangential direction) at axial location of $\Delta Cp_{\max}$
$S$ = suction-surface coordinate
SKE = $1/2\rho(v_{\text{sec}}^2 + w_{\text{sec}}^2)$ = secondary kinetic energy
SSL = suction-surface length
$u,v,w$ = velocity components in axial, pitchwise and spanwise directions, respectively
$v_{\text{sec}}, w_{\text{sec}}$ = components of secondary velocity vector
$V$ = velocity
We = leading-edge wedge angle, in degrees
$x$ = axial coordinate measured from the leading-edge plane
$x_{\min}$ = axial distance from leading-edge plane to minimum suction-side pressure
$y', z$ = local pitchwise and spanwise coordinates
$Y$ = $P_{0,1} - P_{0,2}/1/2\rho V_2^2$ = mass-averaged total-pressure loss coefficient
$\alpha$ = flow angle measured from the axial direction, in degrees
$\beta$ = aerofoil metal angle measured from the axial direction, in degrees
$\delta^*$ = $\int_0^\delta (1 - V/V_e) dz$ = boundary layer displacement thickness
$\Delta Cp_{\max}$ = maximum nondimensional cross-passage pressure difference
$\gamma$ = stagger angle measured from the axial direction, in degrees
$\Gamma$ = $\int_0^{h/2} \int_0^s \omega_s \cos \alpha_2'' dy' dz$ = secondary circulation
$\mu$ = dynamic viscosity
$\theta$ = $\int_0^\delta (1 - V/V_e)\, V/V_e dz$ = boundary layer momentum thickness
$\rho$ = density
$\omega$ = vorticity

### Subscripts

$CL$ = centerline value at the inlet boundary layer traverse plane
$e$ = boundary layer edge value
mean = based on vector mean velocity
$MS$ = midspan
$x,y,z,s$ = components in axial, pitchwise, spanwise, and streamwise directions
1, 2 = cascade inlet and outlet
+, − = associated with positive and negative streamwise vorticity, respectively

### Superscripts

′ = pitchwise mass-averaged value
″ = mass-averaged value

## References

[1] Benner, M. W., Sjolander, S. A., and Moustapha, S. H., 1997, "Influence of Leading-Edge Geometry on Profile Losses in Turbines at Off-Design Incidence: Experimental Results and an Improved Correlation," ASME J. Turbomach., **119**, pp. 193–200.
[2] Benner, M. W., Sjolander, S. A., and Moustapha, S. H., 1997, "Measurements of Secondary Flows in a Turbine Cascade at Off-Design Incidence," ASME Paper 97-GT-382.
[3] Sieverding, C. H., 1985, "Recent Progress in the Understanding of Basic Aspects of Secondary Flows in Turbine Blade Passages," ASME J. Turbomach., **107**, pp. 249–257.
[4] Gregory-Smith, D. G., 1997, "Secondary and Tip-Clearance Flows in Axial Turbines," VKI LS 1997-01, Von Karman Institute for Fluid Dynamics, Rhode St. Genese, Belgium.
[5] Langston, L. S., 2001, "Secondary Flows in Axial Turbines—A Review," Ann. N.Y. Acad. Sci. **934**, pp. 11–26.
[6] Baker, C. J., 1980, "The Turbulent Horeshoe Vortex," J. Wind. Eng. Ind. Aerodyn., **6**, pp. 9–23.
[7] Eckerle, W. A., and Langston, L. S., 1987, "Horseshoe Vortex Formation Around a Cylinder," ASME J. Turbomach., **109**, pp. 278–285.
[8] Pierce, F. J., and Tree, I. K., 1990, "The Mean Flow Structure on the Symmetry Plane of a Turbulent Junction Vortex," ASME J. Fluids Eng., **112**, pp. 16–22.
[9] Devenport, W. J., and Simpson, R. L., 1990, "Time-Dependent and Time-Averaged Turbulence Structure Near the Nose of a Wing-Body Junction," J. Fluid Mech., **210**, pp. 23–55.
[10] Ballio, F., Bettoni, C., and Franzetti, S., 1998, "A Survey of Time-Averaged Characteristics of Laminar and Turbulent Horseshoe Vortices," ASME J. Fluids Eng., **120**, pp. 233–242.
[11] Moore, J., and Ransmayr, A., 1984, "Flow in a Turbine Cascade—Part 1: Losses and Leading-Edge Effects," ASME J. Eng. Gas Turbines Power, **106**, pp. 400–408.
[12] Goobie, S. M., Moustapha, S. H., and Sjolander, S. A., 1989, "An Experimental Investigation of the Effect of Incidence on the Two-Dimensional Performance of an Axial Turbine Cascade," *Proceedings, Ninth International Symposium on Air Breathing Engines*, pp. 197–204.
[13] Tremblay, B., Sjolander, S. A., and Moustapha, S. H., 1990, "Off-Design Performance of a Linear Cascade of Turbine Blades," ASME Paper 90-GT-314.
[14] Rodger, P., Sjolander, S. A., and Moustapha, S. H., 1992, "Establishing Two-Dimensional Flow in a Large-Scale Planar Turbine Cascade," AIAA Paper 92-3066.
[15] Moustapha, S. H., Kacker, S. C., and Tremblay, B., 1990, "An Improved Incidence Losses Prediction Method for Turbine Airfoils," ASME J. Turbomach., **112**, pp. 267–276.
[16] Korakianitis, T., and Papagiannidis, P., 1993, "Surface-Curvature-Distribution Effects on Turbine Cascade Performance," ASME J. Turbomach., **115**, pp. 334–341.
[17] Gregory-Smith, D. G., Graves, C. P., and Walsh, J. A., 1988, "Growth of Secondary Losses and Vorticity in an Axial Turbine Cascade," ASME J. Turbomach., **110**, pp. 1–8.
[18] Yaras, M. I., and Sjolander, S. A., 1990, "Development of the Tip-Leakage Flow Downstream of a Planar Cascade of Turbine Blades: Vorticity Field," ASME J. Turbomach., **112**, pp. 609–617.
[19] Gregory-Smith, D. G., and Cleak, J. G. E., 1992, "Secondary Flow Measurements in a Turbine Cascade With High Inlet Turbulence," ASME J. Turbomach., **114**, pp. 173–183.
[20] Marchal, P., and Sieverding, C. H., 1977, "Secondary Flows within Turboma-

chinery Bladings,'' *Secondary Flows in Turbomachines*, AGARD-CP-214, Paper 11, pp. 1–19.
[21] Hodson, H. P., and Dominy, R. G., 1987, ''Three-Dimensional Flow in a Low-Pressure Turbine Cascade at its Design Condition,'' ASME J. Turbomach., **109**, pp. 177–185.
[22] Perdichizzi, A., and Dossena, V., 1993, ''Incidence Angle and Pitch-Chord Effects on Secondary Flows Downstream of a Turbine Cascade,'' ASME J. Turbomach., **115**, pp. 383–391.
[23] Weiss, A. P., and Fottner, L., 1995, ''The Influence of Load Distribution on Secondary Flow in Turbine Cascades,'' ASME J. Turbomach., **117**, pp. 133–141.
[24] Sharma, O. P., and Butler, T. L., 1987, ''Predictions of Endwall Losses and Secondary Flows in Axial Turbine Cascades,'' ASME J. Turbomach., **109**, pp. 229–236.
[25] Wang, H. P., Olson, S. J., Goldstein, R. J., and Eckert, E. R. G., 1997, ''Flow Visualization in a Linear Turbine Cascade of High Performance Turbine Blades,'' ASME J. Turbomach., **119**, pp. 1–8.
[26] Sonoda, T., 1985, ''Experimental Investigation on Spatial Development of Streamwise Vortices in a Turbine Inlet Guide Vane Cascade,'' ASME Paper 85-GT-20.
[27] Jabbari, M. Y., Goldstein, R. J., Marston, K. C., and Eckert, E. R. G., 1992, ''Three-Dimensional Flow at the Junction between a Turbine Blade and End-Wall,'' Waerme- Stoffuebertrag., **27**, pp. 51–59.
[28] Denton, J. D., 1993, ''Loss Mechanisms in Turbomachinery,'' ASME J. Turbomach., **115**, pp. 621–656.
[29] Moore, J., and Smith, B. L., 1984, ''Flow in a Turbine Cascade: Part 2—Measurement of Flow Trajectories by Ethylene Detection,'' ASME J. Eng. Gas Turbines Power, **106**, pp. 409–413.
[30] Sieverding, C. H., and Van den Bosche, P., 1983, ''The Use of Coloured Smoke to Visualize Secondary Flows in a Turbine-Blade Cascade,'' J. Fluid Mech., **134**, pp. 85–89.
[31] Whitehouse, D. R., Moustapha, S. H., and Sjolander, S. A., 1993, ''The Effect of Axial Velocity Ratio, Turbulence Intensity, Incidence, and Leading Edge Geometry on the Midspan Performance of a Turbine Cascade,'' Can. Aeronautics Space J., **39**, pp. 150–156.
[32] Kind, R. J., Serjak, P. J., and Abbott, M. W. P., 1998, ''Measurements and Prediction of the Effects of Surface Roughness on Profile Losses and Deviation in a Turbine Cascade,'' ASME J. Turbomach., **120**, pp. 20–27.
[33] Marchal, P., 1980, ''Etude des ecoulements secondaires en grille d'aubes de detente,'' Ph.D. thesis, Universit Libre de Bruxelles, Brussels, Belgium.
[34] Sauer, H., Muller, R., and Vogeler, K., 2001, ''Reduction of Secondary Flow Losses in Turbine Cascades by Leading Edge Modifications at the Endwall,'' ASME J. Turbomach., **123**, pp. 207–213.
[35] Mehta, R. D., 1984, ''Effect of Wing Nose Shape on the Flow in a Wing/Body Junction,'' Aeronaut. J., **21**, pp. 499–522.
[36] Kubendran, L. R., McMahon, H. M., and Hubbartt, J. E., 1986, ''Turbulent Flow Around a Wing/Fuselage-Type Juncture,'' AIAA J., **24**, pp. 1447–1452.
[37] Langston, L. S., Nice, M. L., and Hooper, R. M., 1977, ''Three-Dimensional Flow Within a Turbine Cascade Passage,'' ASME J. Eng. Power, **99**, pp. 21–28.
[38] Kacker, S. C., and Okapuu, U., 1982, ''A Mean Line Prediction Method for Axial Flow Turbine Efficiency,'' ASME J. Turbomach., **104**, pp. 111–119.
[39] Ainley, D. G., and Mathieson, G. C. R., 1951, ''A Method of Performance Estimation for Axial Flow Turbines,'' British ARC, R&M 2974.
[40] Dunham, J., and Came, P. M., 1970, ''Improvements to the Ainley-Mathieson Method Turbine Performance Prediction Method,'' ASME J. Eng. Power, **88**, pp. 252–256.
[41] Craig, H. R. M., and Cox, H. J. A., 1971, ''Performance Estimation of Axial Flow Turbines,'' *Proc. Inst. Mech. Eng., 1970–1971*, ImechE, London, **185**, 32/71, pp. 407–424.
[42] Traupel, W., 1977, *Thermische Turbomaschinen*, Springer-Verlag, Berlin.
[43] Sieverding, C. H., 1985, ''Axial Turbine Performance Prediction Methods,'' *Thermodynamics and Fluid Mechanics of Turbomachinery* (Vol. **1** of NATO ASI, Series E), pp. 737–784.

# Influence of Loading Distribution on the Performance of Transonic High Pressure Turbine Blades

**D. Corriveau**[1]

**S. A. Sjolander**
Professor
e-mail: ssjoland@mae.carleton.ca

Department of Mechanical & Aerospace Engineering,
Carleton University,
Ottawa, ON K1S 5B6, Canada

*Midspan measurements were made in a transonic wind tunnel for three high pressure turbine blade cascades at design incidence. The baseline profile is the midspan section of a high pressure turbine blade of fairly recent design. It is considered mid-loaded. To gain a better understanding of blade loading limits and the influence of loading distributions, the profile of the baseline airfoil was modified to create two new airfoils having aft-loaded and front-loaded pressure distributions. Tests were performed for exit Mach numbers between 0.6 and 1.2. In addition, measurements were made for an extended range of Reynolds numbers for constant Mach numbers of 0.6, 0.85, 0.95, and 1.05. At the design exit Mach number of 1.05, the aft-loaded airfoil showed a reduction of almost 20% in the total pressure losses compared with the baseline airfoil. However, it was also found that for Mach numbers higher than the design value the performance of the aft-loaded blade deteriorated rapidly. The front-loaded airfoil showed generally inferior performance compared with the baseline airfoil.* [DOI: 10.1115/1.1645534]

## Introduction

Stiff competition in the gas turbine industry for market share combined with the ever more stringent requirements for clean, efficient engines as required by governments around the world has pushed gas turbine manufacturers to optimize every component of the engine. Gains can still be made in terms of reduction in losses as well as in weight of the engine in the high pressure (HP) turbine.

This can be achieved by carefully designing blade profiles such that minimum losses are generated within the passage while at the same time maximum loading is developed in order to reduce the number of airfoils required per stage. To succeed in designing such optimized blades, it is necessary to determine the maximum allowable amount of diffusion on the blade surface. The location of the diffusion region together with its extent must be considered. The diffusion limit is imposed by the need to avoid separation of the boundary layer on the blade surface which is associated with high losses, especially if the separated flow does not reattach. To create a successful blade design, one would like to delay the laminar-turbulent transition as far downstream of the leading edge as possible without incurring a complete boundary layer separation.

Designing highly loaded blades within the diffusion limits requires a knowledge of the effect of pressure gradient on boundary layer separation and transition under turbomachinery conditions. The importance of the pressure gradient on the boundary layer transition has been recognized for a long time. A good review of the field can be found in Mayle [1]. Abu-Ghannam and Shaw [2] presented a comprehensive set of measurements for natural transition on a flat plate for different pressure gradients and turbulence levels. Sharma et al. [3] investigated the influence of a simulated turbine blade pressure distribution on a transitional boundary layer. Gostelow [4], Gostelow and Blunden [5], and Gostelow et al. [6] have also developed a significant body of knowledge on boundary layer transition in adverse pressure gradient flows.

Some attempts have been made to apply the understanding of transition to the design of turbine blades. For example, Hourmouziadis [7] developed the concept of the CBL controlled boundary layer (CBL) for the design of low pressure (LP) turbine airfoils. Design guidelines were developed to ensure the presence of an attached boundary layer at the trailing edge.

A few experimental studies exist on the effect of loading distribution on the performance of actual turbine blades. However, the conclusions of these studies are often contradictory. Patterson and Hoeger [8] studied the effect of both the velocity distribution and Reynolds number on the performance of three LP turbine vanes. Their results were obtained mainly at low transonic Mach numbers. They concluded that the aft-loaded profile yielded the worst performance for the conditions investigated. The performance of the first and second stage stator vane of a LP turbine was tested for both front and aft-loaded profile by Hashimoto and Kimura [9]. It was found that the front-loaded designs yielded lower losses and a wider range of usable incidence for high subsonic Mach numbers. Hoheisel et al. [10] looked at the effect of freestream turbulence and blade pressure gradient on the losses for three turbine cascades. They studied a front-loaded profile together with two aft-loaded ones. The three designs had the same overall aerodynamic loading. Tests performed at low Mach numbers showed that lower losses can be obtained with an aft-loaded pressure distribution, provided that the rearward diffusion is carefully controlled. More recently, Howell et al. [11], presented results for high-lift and aft-loaded LP turbine profiles with unsteady incoming wakes. They showed that aft-loaded LP blades tend to have lower losses due to a reduction in the extent of turbulent boundary layer on the suction surface. It was concluded that the aft-loaded profile offered this advantage mainly in unsteady flow.

The present study examines experimentally the effect of loading distribution for HP turbine airfoils. Three profiles having different loading distributions were considered. The baseline airfoil is the midspan section of the HP rotor of a small gas turbine engine of recent design. Results for this cascade have been presented previously by Jouini et al. [12,13]. The three airfoils were designed for the same inlet and outlet velocity triangles and have the same Zweifel loading coefficients. The performance of the cascades was assessed based on loss, exit flow angle, and base pressure measurements. Loading measurements were also used to assist in the interpretation of the results. Measurements were made for a wide range of Reynolds numbers and transonic Mach numbers.

[1]Presently at Defense R&D Canada, Quebec City, PQ, Canada.

Contributed by the International Gas Turbine Institute and presented at the International Gas Turbine and Aeroengine Congress and Exhibition, Atlanta, GA, June 16–19, 2003. Manuscript received by the IGTI December 2002; final revision March 2003. Paper No. 2003-GT-38079. Review Chair: H. R. Simmons.

  

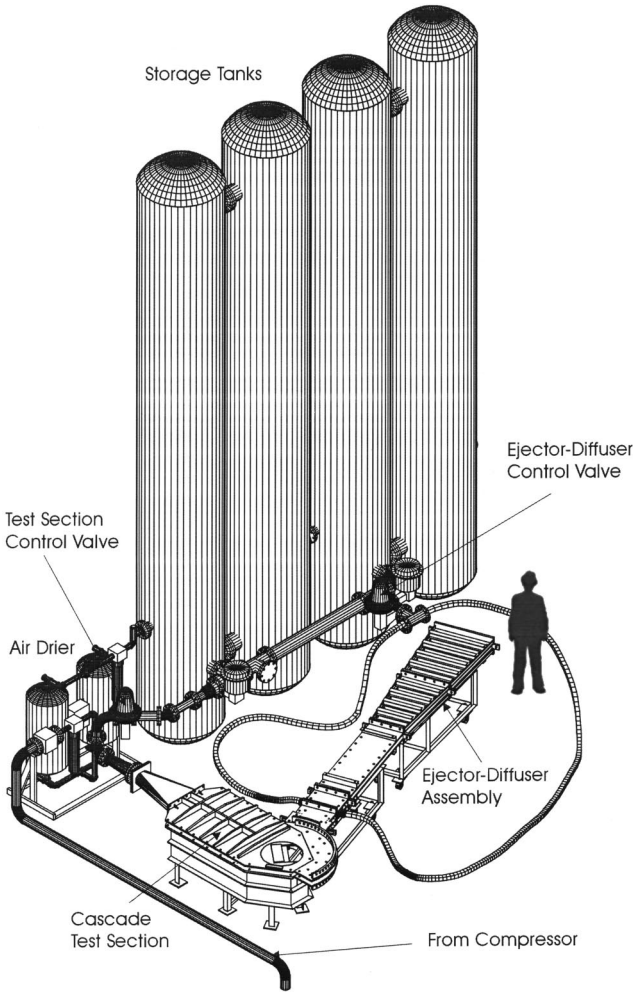


**Fig. 1 Pratt & Whitney Canada high-speed wind tunnel**

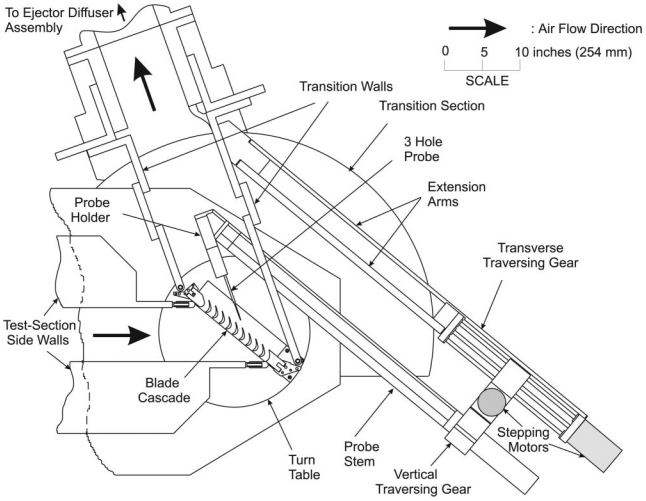


**Fig. 2 Plan view of the cascade test section (Jouini et al. [12])**

## Experimental Apparatus and Procedures

**High-Speed Wind Tunnel.** The measurements were obtained in the high-speed wind tunnel at Carleton University. A schematic of the wind tunnel is shown in **Fig. 1**. The wind tunnel is of the blow-down type. Prior to each run, the storage tanks are filled with air at a pressure of about 8 atmospheres. When the tanks are full, the control valve is opened and the air is discharged through the test section at constant blowing pressure. For typical transonic cascade testing, blowing pressures of the order of 2 to 3 bars are required. Run times of 30 to 60 seconds are achieved, depending on the blowing pressure and cascade outlet Mach number. The turbulence intensity in the test section is about 4%. The outlet of the cascade test section is fitted with an ejector-diffuser system. This system allows the static pressure downstream of the cascade to be controlled and thus permits the cascade outlet Mach number to be varied independently of the Reynolds number. The diffuser outlet exhausts to the laboratory at atmospheric conditions. A more detailed description of the wind tunnel is given by Jeffries [14].

**Cascade Test Section and Test Cascade.** The linear cascade test section used to make the measurements is shown in **Fig. 2**. The cascade is mounted on a turntable. By rotating the turntable, incidences between—10 deg and +15 deg can be obtained. Measurements are presented here for design incidence only. The procedure used to obtain good inlet flow uniformity and outlet flow periodicity is described in Corriveau and Sjolander [15]. The airfoil and cascades geometries are summarized in **Fig. 3**. **Figure 4** shows the three profiles superimposed and the corresponding loading distributions. The cascades were manufactured with a common axial chord of 37.3 mm.

The baseline blade (HS1A) is the midspan section of a high pressure turbine from a Pratt & Whitney Canada (PWC) engine and is considered to be a mid-loaded profile. Starting from the baseline profile, two other blades were designed by the authors using PWC design tools. The objective was to obtain front-loaded and aft-loaded profiles with the same Zweifel coefficients as the baseline. In addition, the metal areas were kept constant so that the new profiles would be structurally compatible with the existing engine airfoils.

The aft-loaded airfoil (HS1C) was obtained from HS1A by modifying several geometric parameters. The stagger angle was reduced from 25.1 deg to 22.5 deg and the uncovered turning angle was increased by 3.0 deg to 14.5 deg. The leading edge ellipse ratio and wedge angle were also modified to reduce the velocity overspeeds on both the pressure and suction surfaces in the vicinity of the leading edge. Finally, the suction-side curvature was modified to adjust the pressure distribution. The front-loaded airfoil (HS1D) was obtained mainly by increasing the stagger angle to 30.5 deg. Some minor modifications were also made to the suction-side curvature.

The three cascades consist of seven full blades and eight blade passages. Two of the blades at the center of the cascades were instrumented with static taps for loading measurements. One of the instrumented airfoils included a static tap at the center of the trailing edge to allow the base pressure to be measured. The base-pressure tap had a diameter of 20% of the trailing-edge thickness.

Experiments were performed for exit Mach numbers of 0.5 to 1.3. For these runs, the corresponding Reynolds numbers varied from about 500,000 to 1,000,000. For this range of Reynolds numbers the losses are essentially independent of Reynolds number. Additional measurements were made for Mach numbers of 0.6, 0.85, 0.95, and 1.05 to extend the Reynolds number to both higher and lower values. The Reynolds number was lowered by reducing the static pressure at the cascade exit using the ejector-diffuser assembly. The ejectors are driven using air from the main tanks and this has the effect of reducing the run times. The cascade outlet static pressure was raised by partially blocking the diffuser discharge. The AVDR was essentially equal to 1.0 for the conditions investigated.

**Instrumentation and Experimental Procedure.** The downstream flow field measurements were obtained with a three-hole pressure probe used in the non-nulling mode. The probe tip has a

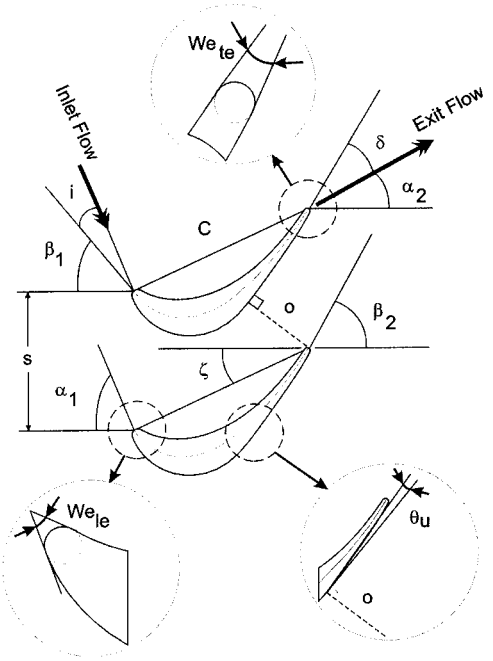


| Cascade Parameters | HS1A | HS1C | HS1D |
|---|---|---|---|
| Chord Length, C | 41.2mm | 40.4mm | 43.3mm |
| Blade Span, H | 61.0mm | 61.0mm | 61.0mm |
| Blade Pitch, s | 29.14mm | 29.14mm | 29.14mm |
| Leading Edge Ellipse Ratio, a/b | 1.0 | 2.1 | 1.0 |
| Leading Edge Ellipse Minor Axis, b | 1.02mm | 1.02mm | 1.02mm |
| Trailing Edge Thickness, t | 1.26mm | 1.26mm | 1.26mm |
| Aspect Ratio, H/C | 1.481 | 1.510 | 1.409 |
| Inlet Metal Angle, $\beta_1$ | 50.5° | 50.5° | 50.5° |
| Outlet Metal Angle, $\beta_2$ | 59.0° | 59.0° | 59.0° |
| Leading Edge Wedge Angle, $We_{le}$ | 38.0° | 15.0° | 38.0° |
| Trailing Edge Wedge angle, $We_{te}$ | 6.0° | 6.0° | 6.0° |
| Design Incidence, $i_{des}$ | -4.5° | -4.5° | -4.5° |
| Stagger Angle, $\xi$ | 25.1° | 22.5° | 30.5° |
| Throat Opening, o | 15.9mm | 15.9mm | 15.9mm |
| Unguided Turning, $\theta_u$ | 11.5° | 14.5° | 11.5° |

**Fig. 3 Summary of blade geometry and nomenclature**

width of 1.37 mm, which corresponds to 4.7% of the blade pitch, and a thickness of 0.46 mm. The probe was calibrated in 1-deg steps over a range of $+/-10$ deg of flow misalignment in yaw. Static-pressure probe measurements were also made downstream of the cascade. The cylindrical probe has a tip cone angle of 15 deg and a diameter of 1.02 mm. For the analysis of the results, the static-pressure measurements obtained with the static-pressure probe were combined with the flow angle and total pressure measurements from the three-hole probe. Fully mixed-out loss coefficients and other relevant quantities were calculated from the data using the procedures of Amecke and Safarik [16].

The pressure measurements were obtained using a 48-port Scanivalve system. A miniature fast-response Kulite transducer, model number XCQ-062-25A, was mounted in the Scanivalve. The full-scale range of the transducer is 0 to 25 psi absolute. The output from the transducer was recorded using a Hewlett-Packard high-speed data-acquisition system controlled by a microcomputer.

The locations of the upstream and downstream pressure measurement planes are shown in **Fig. 5**. For the downstream static and three-hole probe traverses, four runs are typically required to cover one blade pitch. For each run, ten measurements are made for a total of 40 measurements for one blade pitch. For cases where the ejector-diffuser system was used, a total of eight runs were required to traverse one blade pitch.

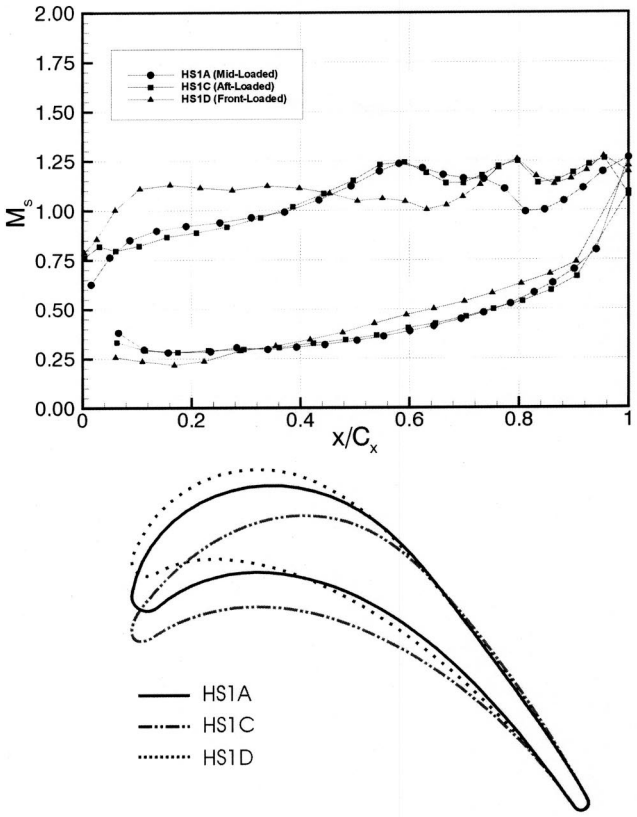


**Fig. 4 Cascade blade profiles and the corresponding loading distribution**

The measurement uncertainty for outlet angle flow angles is estimated to be $+/-1.0$ deg. The uncertainty for the static pressure measurements is $+/-2\%$ of the local dynamic pressure. The uncertainty in the cascade inlet Mach numbers is $+/-0.015$. The cascade exit Mach number uncertainty is about $+/-0.005$ for Mach numbers greater than 0.8. For lower Mach numbers the uncertainties in the Mach number increases due to drift in the blowing pressure. The uncertainty for the mixed-out total-pressure loss coefficients is estimated as $+/-0.006$ for Mach numbers between 0.85 and 1.1. For higher transonic Mach numbers the uncertainties are higher due to the formation of complex shock structures. The uncertainty values were estimated using the method of Moffat [17] for single-sample uncertainty analysis.

## Results and Discussion

**Profile Losses.** **Figure 6** shows the variation of the profile total-pressure-loss coefficient with outlet Mach number for the three cascades. All the results were obtained at Reynolds numbers of 500,000 or higher, for which results were found to be independent of Reynolds number.

For subsonic outlet Mach numbers ($M_2 < 1.0$), losses are essentially the same for the three blades. Losses start to increase for outlet Mach numbers above about 0.85. In the range of Mach numbers from 1.0 to approximately 1.15, which includes the design value of 1.05, the losses level off for both the mid-loaded and aft-loaded airfoils, HS1A and HS1C. However, the losses are noticeably lower, by roughly 20%, for the aft-loaded airfoil (HS1C) compared with the baseline. The reasons for this will be discussed in connection with the loading distributions and base pressures. Above a $M_2$ of about 1.15, the losses for HS1C begin to rise rapidly and its performance becomes significantly poorer than that

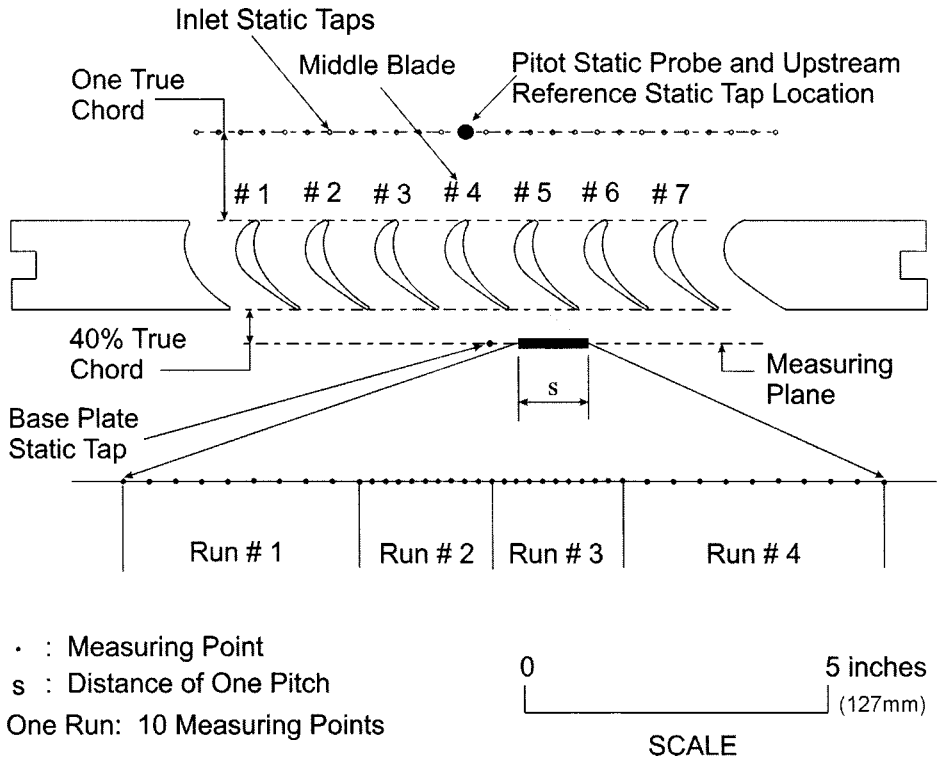


**Fig. 5 Cascade blade row measurement locations**

of the baseline airfoil. The loss performance of the forward-loaded airfoil, HS1D, is inferior to, or at best equal to, that of at least one of the two other airfoils at all operating conditions.

The effect of Reynolds number on the losses is shown in **Fig. 7** for the three airfoils. Measurements were made at Mach numbers of 0.60, 0.85, 0.95, and 1.05. As mentioned previously, the Reynolds number was lowered at the cascade exit by using the ejector-diffuser assembly and raised by partially blocking the diffuser outlet.

As seen from **Fig. 7**, the losses increase significantly at low Reynolds numbers for an exit Mach number of 0.60. For Mach numbers of 0.85 and 0.95 the losses are seen to increase slightly for the lowest Reynolds numbers achieved. For an outlet Mach number of 1.05, the Reynolds number could not be lowered enough to detect its effect on the losses. Interestingly, the aft-loaded airfoil (HS1C) showed the lowest sensitivity to reduced Reynolds numbers, in addition to its superior performance at high Reynolds numbers near the design Mach number.

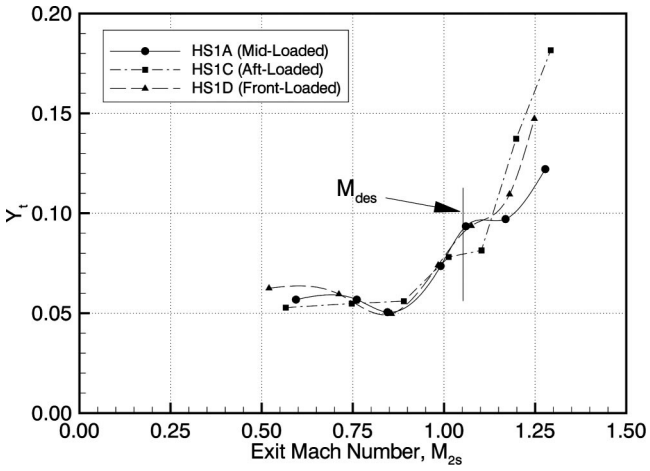


**Fig. 6 Effect of Mach number on losses (High Re)**

**Outlet Flow Angle.** Outlet flow angle measurements were obtained from the three-hole probe. **Figure 8** shows the variation of exit flow angle with Mach number for high Reynolds number values. The exit metal angle is indicated for reference. The trend in outlet flow angle with Mach number is very similar for the three cascades. That is, the outlet flow angle reaches a maximum at an exit Mach number close to 1.0. As expected, as the outlet flow becomes supersonic the flow direction must rotate towards the axial direction in order to increase the flow area and the flow turning is reduced. The forward-loaded airfoil, HS1D, is seen to give the lowest flow turning, particularly at supersonic outlet Mach numbers. This suggests the presence of a thicker suction-side boundary layer for this airfoil and perhaps even mild flow separation near the trailing edge, which would be consistent with the higher profile losses measured for HS1D.

**Figure 9** shows the variation of the outlet flow angle with the Reynolds number for the three cascades. As for the losses shown in **Fig. 7**, the Reynolds number effects are strongest at the lowest Mach number, namely 0.60. Both the lower flow turning and higher losses are presumably associated with the presence of a boundary layer separation on suction surface at lower Reynolds numbers.

**Blade Loading.** Blade loading measurements were made for several test cases. The results are presented as surface isentropic Mach numbers, as calculated from the blade-surface static pressures and the inlet total pressure. Repetitions of the loading measurements have shown that the uncertainty in the isentropic Mach numbers is about $+/-0.01$.

The loading measurements are shown in **Fig. 10**. At low Mach numbers, all three airfoils exhibit a region of near-constant pressure on the rear part of the suction surface. This might normally be seen as evidence of boundary layer separation at this location. However, the losses shown in **Fig. 6** and the outlet flow angle results shown in **Fig. 8** do not support this conclusion. As ob-

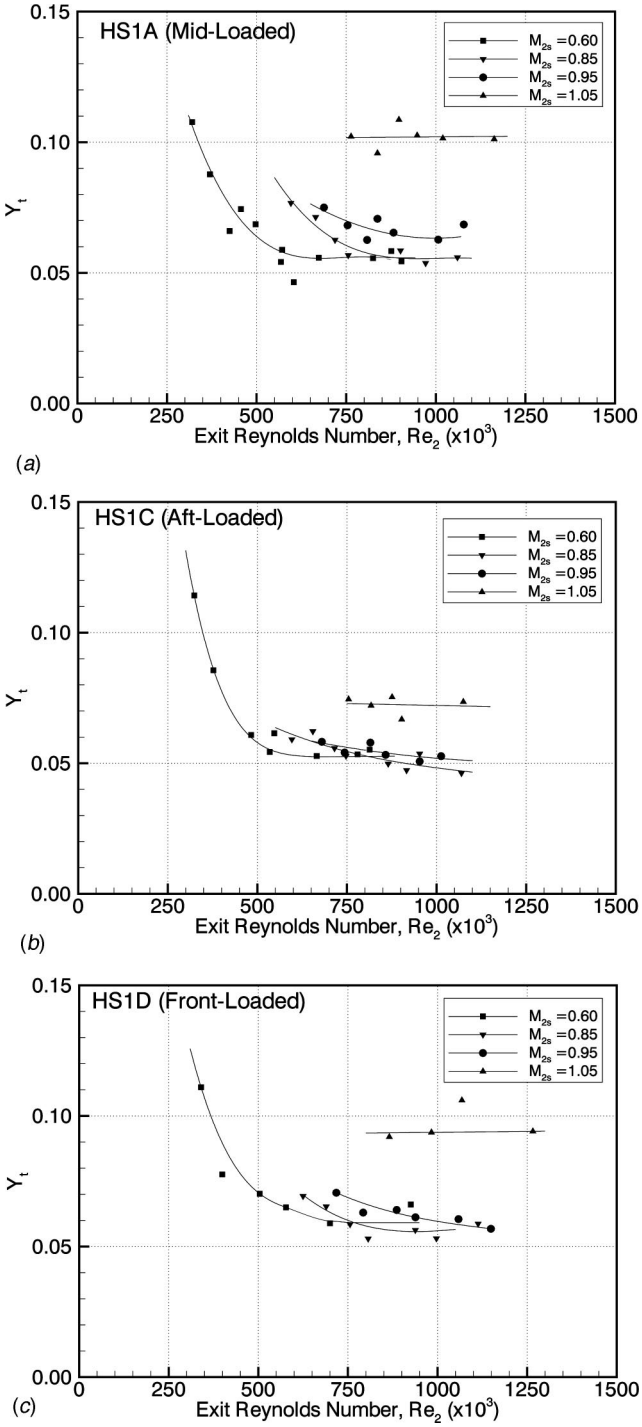


**Fig. 7 Reynolds number effect on losses for several Mach numbers. Subcaption: (*a*) HS1A (*b*) HS1C (*c*) HS1D.**

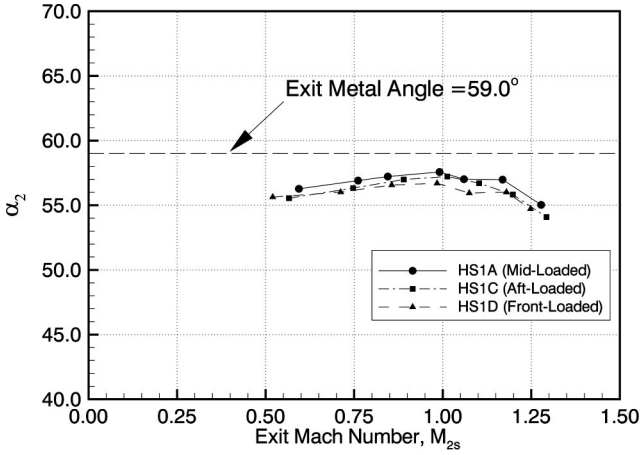


**Fig. 8 Effect of Mach number on exit flow angle (High Re)**

served, the losses at low Mach number are relatively low and the exit flow angles do not decrease significantly at lower exit Mach numbers. In fact, the unusual loading distributions are simply those resulting at low exit Mach numbers for airfoils designed for use at much higher Mach numbers.

For exit Mach numbers greater than about 1.0, the suction-side loading distributions remain constant from the leading edge up to an axial distance of about $x/C_x=0.75$ as the outlet exit Mach number increases (**Fig. 10**). This is due to the choking of the flow in the blade passage. At the highest outlet Mach numbers an oblique shock originating at the trailing edge of the adjacent airfoil impinges on the rear of the suction surface of all three airfoils. However, there are notable variations in the apparent strength of this shock, and the corresponding drop in Mach number, for the three cases. For HS1A at $M_2=1.07$ the pressure rise begins at about $0.75C_x$ and the decrease in Mach number is about 0.20. However, for HS1C the decrease in Mach number is only about 0.12 at a similar exit Mach number of 1.05. This indicates that near the design $M_2=1.05$ the impinging shock is weaker for the aft-loaded airfoil. This in turn will favorably affect the losses in two ways: through the lower direct total pressure losses through the shock wave and through its milder effect on the suction surface boundary layer. This is consistent with the 20% lower losses observed for HS1C compared with HS1A near design. However, these beneficial effects for HS1C seem to be confined to Mach numbers close to the design value. At $M_2$ of about 1.18, the rise in Mach number at the shock impingement is noticeably higher for HS1C than for HS1A. This probably explains the poorer loss performance of HS1C at higher Mach numbers.

**Figure 10(*c*)** shows that the strength of the impinging shock wave for the forward-loaded airfoil, HS1D, is similar to that for HS1C at most conditions. However, HS1D airfoil experiences the onset of mild deceleration on the suction surface at about $0.3C_x$ whereas it is delayed until about $0.6C_x$ for the other two airfoils. As a result the suction-side boundary layers will tend to be thicker for HS1D at all conditions and at the supersonic outlet conditions the layer will be more sensitive to the rise in pressure due the impinging shock wave. This is consistent with HS1D having loss performance inferior to that of at least one of the two other airfoils at all operating conditions.

**Base Pressure.** The base pressure is a measure of the static pressure at the center of the blade's trailing edge. The base pressure is known to have a strong influence on the profile losses. For example, Denton [18] has shown using a simplified control-volume analysis that the profile losses for incompressible flow can be related to the boundary layer parameters and base pressure coefficient as follows:

$$\zeta=-\frac{C_b t}{o}+\frac{2\theta}{o}+\left(\frac{\delta^*+t}{o}\right)^2 \tag{1}$$

where $C_b$ is the base pressure coefficient (see Nomenclature). The relative effect of $C_b$ is increased in compressible flow. The base pressure is known to be sensitive to both the thickness of the blade surface boundary layers at the trailing edge and the presence of trailing edge separation. Thus, base pressure measurements can be very helpful in understanding the sources of losses in cascade flows. As noted, all three cascades included one airfoil instrumented with a static tap at the trailing edge for measuring the base pressure.

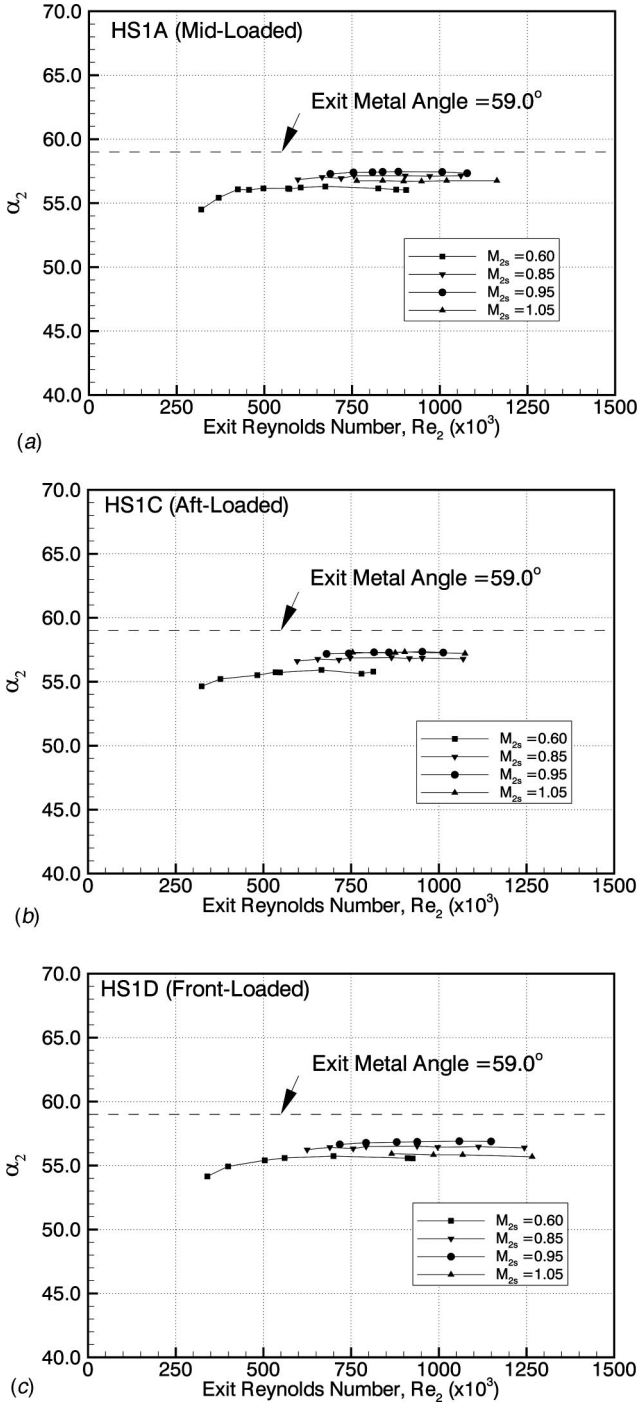


**Fig. 9 Reynolds number effect on exit flow angle for several Mach numbers. Subcaption: (*a*) HS1A (*b*) HS1C (*c*) HS1D.**

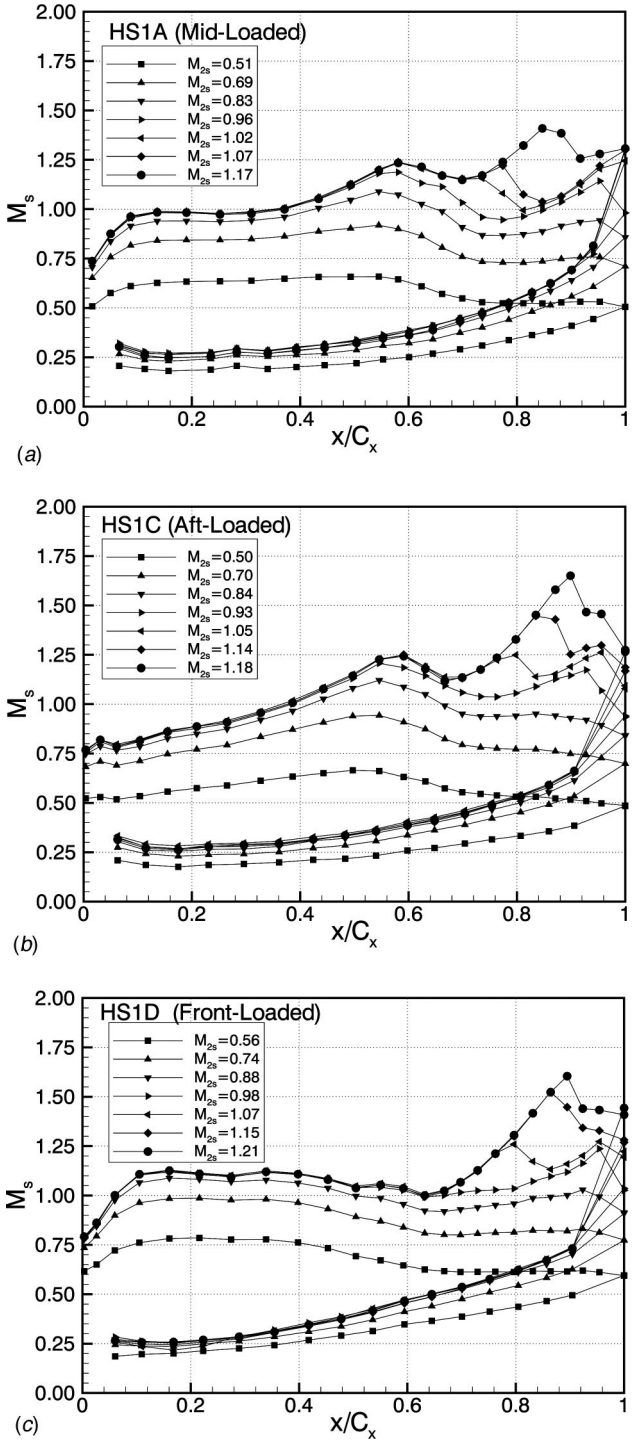


**Fig. 10 Effects of Mach number on blade loading for the three blade profiles. Subcaption: (*a*) HS1A (*b*) HS1C (*c*) HS1D.**

The variations of the base pressure coefficient with Mach number for the three cascades are shown in **Fig. 11**. The trends are significantly different for the three profiles.

Blade HS1A exhibits a sharp drop in the base pressure just before M=1.0 which corresponds to a significant rise in losses. A minimum $C_p$ is then reached at an exit Mach number close to 1.02. This trend in the variation of the base pressure is characteristic of blades having mild or no rear suction surface curvature. However, comparison of the base pressure measurements for blade HS1A with the Sieverding et al. [19] correlation shows that HS1A experiences slightly lower base pressures close to the design Mach number than what was observed for geometrically similar blades. The presence of a low base pressure at the trailing edge contributes to the creation of strong trailing edge shocks. This can be seen by comparing the loading distributions of blades HS1A and HS1D at M=1.07 and blade HS1C at M=1.05 in **Fig. 10**. For these conditions the shock impinging on the rear suction surface of blade HS1A is stronger, as evidenced by the greater amount of diffusion. The presence of a low base pressure also increases the losses. Both the shocks and the increased trailing edge loss contribute to increase the overall losses. This might

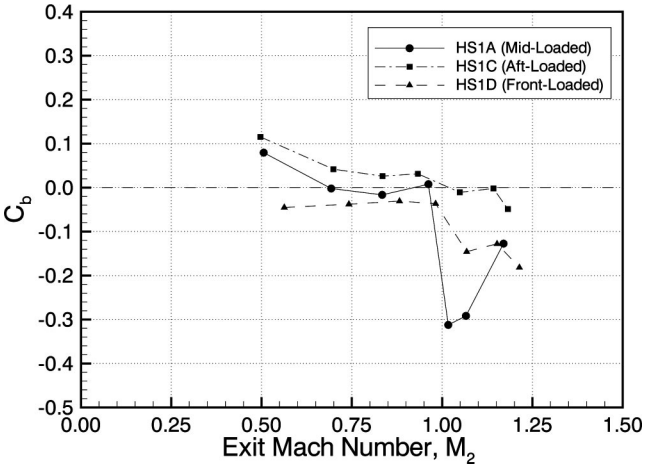


**Fig. 11 Variation of base pressure coefficient with Mach number**

explain why the mid-loaded cascade (HS1A) exhibits higher losses close to design Mach number compared to the aft-loaded cascade (HS1C).

Unlike for the other two airfoils, the base pressure coefficient for the aft-loaded blade (HS1C) was positive or near zero over most of the Mach number range investigated. Such variation of the base pressure coefficient with Mach number is typical of blades having significant rear suction side curvature. Sieverding et al. [19] suggested that higher values of unguided or uncovered turning result in higher base pressures. The uncovered turning angle for HS1C is 3.0 deg higher than that of blades HS1A and HS1D. A priori, higher base pressure coefficients may appear to be favorable for losses, as indicated by Eq. (1) and observed from **Fig. 6** where the losses for HS1C are lower than those of HS1A at the design Mach number. However, blades with strong rear suction side curvature sometimes experience a recompression around the trailing edge when the base pressure is higher than the suction side pressure before the separation point. Such diffusion close to the trailing can be seen from the Mach number distribution of HS1C. From **Fig. 10(*b*)**, it can be seen that for exit Mach numbers of 1.14 and 1.18, HS1C, unlike HS1A, is experiencing increasingly strong diffusion just before the trailing edge. The presence of the suction surface adverse pressure gradient thickens the boundary layer which probably contributes to the higher base pressure. This would help to explain why the base pressure coefficient at high Mach number for HS1C does not diminish significantly. Furthermore, the presence of a thick or separated boundary layer on the suction surface contributes directly to the increase in the losses at higher Mach numbers seen in **Fig. 6**.

For HS1D the base pressure coefficient was negative for all values of exit Mach number. The base pressure coefficient remains constant from a Mach number of 0.5 to about 1.0. At this point, the $C_p$ diminishes rapidly. The variation of the base pressure coefficient with Mach number for HS1D is similar to what is usually observed for blades with similar unguided turning angle and trailing edge wedge angle.

Although the base pressure in turbines has been investigated by a number of researchers (e.g., [19,20]), the factors determining the base pressure are still not fully understood. It is generally thought that higher values of boundary layer thickness result in higher values of base pressure. The results for the aft-loaded airfoil (HS1C) support this conclusion since it is expected to have a thick trailing-edge boundary layers at high Mach numbers and it demonstrated higher than expected values of base pressure coefficient for the highest Mach numbers investigated.

**Table 1 Variation of base pressure coefficient with mach number**

| Cascade | $M_{2s}$ | $M_{MAX}$ | $M_{MIN}$ | DFAC | $Y_t/Y_{ref}$ |
|---|---|---|---|---|---|
| HS1A | 1.06 | 1.156 | 0.995 | 0.1393 | 1.0000 |
| HS1C | 1.10 | 1.249 | 1.139 | 0.0881 | 0.8706 |
| HS1D | 1.08 | 1.256 | 1.132 | 0.0987 | 1.0021 |
| Cascade | $M_{2s}$ | $M_{MAX}$ | $M_{MIN}$ | DFAC | $Y_t/Y_{ref}$ |
| HS1A | 1.17 | 1.221 | 1.038 | 0.1499 | 1.0385 |
| HS1C | 1.20 | 1.447 | 1.252 | 0.1707 | 1.4684 |
| HS1D | 1.18 | 1.524 | 1.328 | 0.2257 | 1.1711 |
| Cascade | $M_{2s}$ | $M_{MAX}$ | $M_{MIN}$ | DFAC | $Y_t/Y_{ref}$ |
| HS1A | 1.28 | 1.409 | 1.256 | 0.1086 | 1.3059 |
| HS1C | 1.29 | 1.651 | 1.457 | 0.2187 | 1.9422 |
| HS1D | 1.25 | 1.604 | 1.433 | 0.2207 | 1.5754 |

## Diffusion Levels and Losses

The previous discussion has suggested that the level of losses at the higher Mach numbers correlates qualitatively with the amount of diffusion experienced on the aft end of the suction surface. A simple measure of the diffusion that has sometimes been used in design is a diffusion factor defined as

$$\mathrm{DFAC} = \frac{M_{MAX} - M_{MIN}}{M_{MAX}}. \tag{2}$$

$M_{MAX}$ is the maximum Mach number on the suction surface just before the impingement of the trailing-edge shock from the adjacent blade. $M_{MIN}$ is either the minimum Mach number reached immediately following the shock impingement, or if no significant flow re-acceleration is present after the shock impingement, $M_{MIN}$ is taken to be the cascade outlet Mach number, $M_2$. **Table 1** shows the values of DFAC obtained for the three cascades at three different operating points. The corresponding values of the midspan losses have been normalized by the value obtained for the baseline cascade (HS1A) at the design exit Mach number of 1.05.

For outlet Mach numbers close to 1.05 (first series in Table 1), both DFAC and the losses are lowest for the aft-loaded cascade,

**Table 2 Cascade performance data (high Re)**

| $M_{2s}$ | Re | $C_b$ | $Y_t$ | $\alpha_2$ |
|---|---|---|---|---|
| HS1A Cascade, $i-i_{des}=0.0$ deg | | | | |
| 0.59 | 514000 | 0.080 | 0.057 | 56.3 |
| 0.76 | 670000 | −0.002 | 0.057 | 56.9 |
| 0.85 | 773000 | −0.017 | 0.051 | 57.2 |
| 0.99 | 876000 | 0.008 | 0.074 | 57.6 |
| 1.06 | 955000 | −0.312 | 0.094 | 57.0 |
| 1.17 | 1019000 | −0.292 | 0.097 | 57.0 |
| 1.28 | 1069000 | −0.127 | 0.122 | 55.0 |
| HS1C Cascade, $i-i_{des}=0.0$ deg | | | | |
| 0.57 | 505000 | 0.115 | 0.053 | 55.5 |
| 0.75 | 663000 | 0.042 | 0.055 | 56.3 |
| 0.89 | 780000 | 0.026 | 0.056 | 57.0 |
| 1.01 | 871000 | 0.031 | 0.078 | 57.2 |
| 1.10 | 953000 | −0.011 | 0.081 | 56.7 |
| 1.20 | 995000 | −0.002 | 0.137 | 55.8 |
| 1.29 | 1038000 | −0.049 | 0.182 | 54.1 |
| HS1D Cascade, $i-i_{des}=0.0$ deg | | | | |
| 0.52 | 502000 | −0.045 | 0.063 | 55.6 |
| 0.71 | 685000 | −0.038 | 0.060 | 56.0 |
| 0.86 | 819000 | −0.031 | 0.050 | 56.6 |
| 0.98 | 923000 | −0.037 | 0.074 | 56.7 |
| 1.08 | 996000 | −0.146 | 0.094 | 55.9 |
| 1.18 | 1066000 | −0.128 | 0.110 | 56.0 |
| 1.25 | 1124000 | −0.182 | 0.147 | 54.7 |

**Table 3 Cascade performance data for the Reynolds number study**

| $M_2$ | Re | $Y_t$ | $\alpha_2$ |
|---|---|---|---|
| HS1A Cascade, $i-i_{des}=0.0$ deg | | | |
| 0.60 | 311000 | 0.108 | 54.5 |
| 0.60 | 443000 | 0.074 | 56.0 |
| 0.60 | 878000 | 0.054 | 56.0 |
| 0.85 | 578000 | 0.077 | 56.8 |
| 0.85 | 698000 | 0.063 | 56.9 |
| 0.85 | 1029000 | 0.056 | 57.1 |
| 0.95 | 668000 | 0.075 | 57.3 |
| 0.95 | 978000 | 0.063 | 57.4 |
| 1.05 | 1129000 | 0.101 | 56.8 |
| HS1C Cascade, $i-i_{des}=0.0$ deg | | | |
| 0.60 | 321000 | 0.114 | 54.6 |
| 0.60 | 374000 | 0.086 | 55.2 |
| 0.60 | 772000 | 0.053 | 55.6 |
| 0.85 | 590000 | 0.059 | 56.6 |
| 0.85 | 943000 | 0.054 | 56.8 |
| 0.95 | 673000 | 0.058 | 57.2 |
| 0.95 | 1003000 | 0.053 | 57.3 |
| 1.05 | 1064000 | 0.074 | 57.2 |
| HS1D Cascade, $i-i_{des}=0.0$ deg | | | |
| 0.60 | 314000 | 0.111 | 54.1 |
| 0.60 | 466000 | 0.070 | 55.4 |
| 0.60 | 646000 | 0.059 | 55.7 |
| 0.85 | 577000 | 0.069 | 56.2 |
| 0.85 | 1028000 | 0.059 | 56.5 |
| 0.95 | 663000 | 0.071 | 56.7 |
| 0.95 | 978000 | 0.061 | 56.9 |
| 1.05 | 908000 | 0.094 | 55.8 |

HS1C. The losses are nearly equal for HS1A and HS1D. However, HS1D has a much lower diffusion factor. The apparent greater sensitivity to the shock-induced diffusion for HS1D is thought to be due to the long length of mild diffusion on the forward part of the airfoil and the resulting thickening of the boundary layer. This should make the boundary layer more prone to separation when it encounters an adverse pressure gradient. This effect is not captured by the simple diffusion factor. For Mach numbers near 1.17 and 1.28, HS1A has the lowest DFAC together with the lowest losses. Both DFAC and losses are much higher for HS1C and HS1D. However, there is again no simple, direct correlation between the losses and DFAC for the three airfoils. The need to account for the effects of boundary layer thickness, which is related to the airfoil loading distribution, has already been mentioned. In addition, there may be an influence of the axial extent over which the diffusion occurs. However, there are clearly too few data available here to investigate more suitable diffusion parameters. The present study is being extended to off-design incidence and these measurements may provide the larger database that will allow such investigations.

The mixed-out loss data as well as several other parameters of interest are listed in **Tables 2, 3** to facilitate the use of these experimental data by other researchers.

## Conclusions

The paper describes an experimental study on the influence of loading distribution on the performance of HP turbine blades. Measurements have been presented for the midspan aerodynamic performance of three blades at design incidence. The airfoils tested consist of a mid-loaded blade (baseline), a front-loaded blade and an aft-loaded blade.

The aft-loaded airfoil blade yielded significantly lower losses than the baseline airfoil near the design Mach number. However, the performance of the aft-loaded airfoil deteriorated more rapidly at Mach number above design. The performance of the front-loaded airfoil was inferior to that of at least one of the two other airfoils at all operating conditions.

An attempt was made to relate the losses to the observed diffusion on the suction side of the airfoils. However, too few cases are available to establish a quantitative correlation. The study is currently being extended to off-design incidence, and it is hoped that the additional data will help to clarify the relationship between the losses and the diffusion pressure rise, its spatial extent, and the thickness of the incoming boundary layer, as determined by the airfoil loading distribution.

## Acknowledgment

The authors wish to thank Pratt & Whitney Canada Inc. for their advice and assistance in designing blades HS1C and HS1D. Financial support from Pratt & Whitney Canada, Inc., is also gratefully acknowledged.

## Nomenclature

AVDR = axial velocity density ratio, $(=\int_0^1(\rho_2 C_{(ax)_2})_{MS}d(y/s)/\int_0^1(\rho_1 C_{(ax)_1})_{MS}d(y/s))$
$a$ = leading edge ellipse major axis
$b$ = leading edge ellipse minor axis
$C$ = blade chord length
$C_b$ = base pressure coefficient, $(=(P_b-P_2)/q_2)$
$C_x$ = axial chord length
DFAC = diffusion factor
$d$ = leading edge diameter
$H$ = blade span
$i$ = incidence
M = Mach number
$O$ = throat opening
$P_b$ = base pressure
$P_o$ = total pressure
$P_s$ = static pressure
$q$ = dynamic pressure, $(1/2\rho V^2)$
Re = Reynolds number, $(\rho V_2 C/\mu)$
$s$ = blade pitch or spacing
$t$ = trailing edge thickness
$V$ = flow velocity
$We$ = wedge angle
$X$ = axial distance
$Y_t$ = midspan total pressure loss coefficient, $(=(P_{o1}-P_{o2})/q_2)$
$a$ = flow angle measured from the axial direction
$b$ = metal angle measured from the axial direction
$d^*$ = boundary layer displacement thickness
$m$ = air dynamic viscosity
$r$ = air density
$\theta$ = boundary layer momentum thickness
$\theta_u$ = uncovered turning angle
$z$ = stagger angle measured from the axial direction

### Subscripts

1 = cascade inlet
2 = cascade outlet
ax = axial
des = design
le = leading edge
MAX = maximum
MIN = minimum
MS = midspan
$s$ = isentropic
te = trailing edge

## References

[1] Mayle, R. E., 1991, "The Role of Laminar-Turbulent Transition in Gas Turbine Engines," ASME J. Turbomach., **113**, pp. 509–537.

[2] Abu-Ghannam, B. J., and Shaw, R., 1980, ''Natural Transition of Boundary Layers—The Effects of Turbulence, Pressure Gradient and Flow History,'' J. Mech. Eng. Sci., **22**, pp. 213–228.
[3] Sharma, O. P., Wells, R. A., Schlinker, R. H., and Bailey, D. A., 1982, ''Boundary Layer Development on Turbine Airfoil Suction Surfaces,'' ASME J. Eng., **104**, pp. 698–706.
[4] Gostelow, J. P., 1989, ''Adverse Pressure Gradient Effects on Boundary Layer Transition in a Turbulent Free Stream,'' *Proc. 9th Int. Symp. On Air Breathing Engines*, AIAA, Washington, DC, **2**, pp. 1299–1306.
[5] Gostelow, J. P., and Blunden, A. R., 1989, ''Investigations of Boundary Layer Transition in an Adverse Pressure Gradient,'' ASME J. Turbomach., **111**, pp. 366–375.
[6] Gostelow, J. P., Blunden, A. R., and Walker, G. J., 1994, ''Effects of Free-Stream Turbulence and Adverse Pressure Gradients on Boundary Layer Transition,'' ASME J. Turbomach., **116**, pp. 392–404.
[7] Hourmouziadis, J., 1989, ''Aerodynamic Design of Low Pressure Turbines,'' *Blade Design For Axial Turbomachines*, AGARD-LS-167.
[8] Patterson, D. J., and Hoeger, M., 1986, ''The Effect of Reynolds Number and Velocity Distribution on LP Turbine Cascade Performance,'' ASME Paper 86-GT-271.
[9] Hashimoto, K., and Kimura, T., 1984, ''Preliminary Study on Forward Loaded Cascades Designed With Inverse Method for Low Pressure Turbine,'' ASME Paper 84-GT-65.
[10] Hoheisel, H., Kiock, R., Lichtfuss, H. J., and Fottner, L., 1987, ''Influence of Free-Stream Turbulence and Blade Pressure Gradient on Boundary Layer and Loss Behavior of Turbine Cascades,'' ASME J. Turbomach., **109**, pp. 210–219.
[11] Howell, R. J., Ramesh, O. N., Hodson, H. P., Harvey, N. W., and Schulte, V., 2001, ''High Lift and Aft-Loaded Profiles for Low-Pressure Turbines,'' ASME J. Turbomach., **123**, pp. 181–188.
[12] Jouini, D. B. M., Sjolander, S. A., and Moustapha, S. H., 2001, ''Aerodynamic Performance of a Transonic Turbine Cascade at Off-Design Conditions,'' ASME J. Turbomach., **123**, pp. 511–518.
[13] Jouini, D. B. M., Sjolander, S. A., and Moustapha, S. H., 2002, ''Midspan Flow-Field Measurements for Two Transonic Linear Turbine Cascades at Off-Design Conditions,'' ASME J. Turbomach., **124**, pp. 176–186.
[14] Jeffries, M. S., 2001, ''Initial Investigations of Transonic Turbine Aerodynamics Using the Carleton University High-Speed Wind Tunnel,'' Ph.D. thesis, Department of Mechanical and Aerospace Engineering, Carleton University, Ottawa, Canada.
[15] Corriveau, D., and Sjolander, S. A., 2002, ''Impact of Flow Quality in Transonic Cascade Wind Tunnels: Measurements in an HP Turbine Cascade,'' *Proc. 23rd Int. Congress of Aeronautical Science (ICAS)*, Optimage, Ltd.
[16] Amecke, J., and Safarik, P., 1995, ''Data Reduction of Wake Flow Measurements With Injection of Other Gas,'' Technical Report DLR-FB 95-32, DLR.
[17] Moffat, R., 1988, ''Describing the Uncertainties in Experimental Results,'' Exp. Therm. Fluid Sci., **1**, pp. 3–17.
[18] Denton, J. D., 1993, ''Loss Mechanism in Turbomachines,'' ASME J. Turbomach., **115**, pp. 621–656.
[19] Sieverding, C. H., Stanislas, M., and Snoeck, J., 1980, ''The Base Pressure Problem in Transonic Cascades,'' ASME J. Eng., **102**, pp. 711–718.
[20] Xu, L., and Denton, J. D., 1988, ''The Base Pressure and Loss of a Family of Four Turbine Blades,'' ASME J. Turbomach., **110**, pp. 9–17.

# Investigation of Stator-Rotor Interaction in a Transonic Turbine Stage Using Laser Doppler Velocimetry and Pneumatic Probes

**E. Göttlich**

**F. Neumayer**

**J. Woisetschläger**
e-mail: jakob.woisetschlaeger@tugraz.at

**W. Sanz**

**F. Heitmeir**

Institute for Thermal Turbomachinery and Machine Dynamics,
Graz University of Technology,
Inffeldgasse 25,
8010 Graz, Austria

*The current paper presents steady and unsteady flow data of a transonic test turbine stage operating under flow conditions similar to modern highly loaded gas turbines. Measurements were performed between stator and rotor as well as downstream of the rotor in planes perpendicular to the rotor axis. Time-resolved axial and tangential velocities were measured by a two-component laser doppler velocimeter (LDV) to investigate unsteady phenomena, while time-averaged flow properties were measured by means of a pneumatic seven-hole probe for all three spatial directions. The time-resolved investigation done by LDV allows to present velocity fields, flow angles and turbulence data at different stator-rotor positions during one blade passing period. Averaging these results enabled comparison with the pneumatic multihole probe measurement. LDV data and stage geometry can be obtained per email request and used for computational fluid dynamics (CFD) code verification.* [DOI: 10.1115/1.1649745]

## Introduction

A sound understanding of the flow field through modern, high-pressure turbine stages is essential in order to increase the efficiency and to improve the performance of turbines.

Advanced computational fluid dynamics (CFD) techniques can help, but development of transonic turbine stages still requires intensive experimental testing to validate these CFD results, mainly because of instationary and complex three-dimensional flow effects in these machines of novel design. Moreover, unsteady three-dimensional CFD analysis of compressible turbulent flow is time consuming and needs modern computer technology of high cost.

A steady-state simulation requires less computational power but implies averaging of the flow properties at the stator-rotor-interface in circumferential direction. This means that the influence of circumferential variations on proceeding blade rows is not visible in the results of a steady-state calculation. The LDV measurement applied here delivers time-resolved and the pneumatic probe measurement time-averaged results, both containing the information on the circumferential variations of the flow. The LDV results can serve as data basis for unsteady three-dimensional CFD.

Several experimental investigations of low speed test turbines have been published, e.g., [1–3] but less literature is available for transonic stages, where the flow field of the rotor is strongly influenced by the trailing edge shocks of the stator vane, e.g., [4,5]. The direct interaction between rotating and non-rotating blade rows is dominant but in a multi stage turbine wakes are transported through the rotor blades. These wakes cause the circumferential variations mentioned above and interact with a following stator, [6].

The Institute for Thermal Turbomachinery and Machine Dynamics operates a continuously running cold flow transonic test turbine (mass flow rate up to 22 kg/s) to carry out performance tests of novel turbine stages on the one hand and to collect flow field data of more for basic research on the other hand. The facility allows testing of stages up to a diameter of approximately 800 mm. The transonic turbine stage used in this work was designed for conventional pneumatic probe measurements and is also optically accessible through large windows already used for laser Doppler velocimetry (LDV) and particle image velocimetry (PIV), [7,8].

The LDV is a nonintrusive optical method used to record instantaneous velocities at a single position in space. Therefore, the flow field has to be seeded by tiny tracer particles following the flow lag-free. These particles pass the measurement volume formed by the laser beams and provide the information on velocity needed (LDV ''burst'').

The multihole probe is an economical and robust method for determining the three-dimensional flow vector in a flow field. Measurements were conducted with a seven-hole probe and a static needle probe.

## Experimental Facility and Instrumentation

**Experimental Facility.** The transonic test turbine of the Institute for Thermal Turbomachinery and Machine Dynamics is a continuously operating cold-flow open-circuit facility which allows the testing of turbine stages with a diameter up to 800 mm in full flow similarity (corrected speed and pressure ratio) due to its modular design. Pressurized air is delivered by a separate 3 MW compressor station. The shaft power of the test stage drives a three-stage radial brake compressor. This brake compressor delivers additional air mixed to the flow from the compressor station and increases the overall mass flow. The air temperature in the mixing chamber (turbine stage inlet) can be adjusted by coolers between 40°C to 185°C. The maximum shaft speed of the test rig is limited to 11550 rpm. Depending on the stage characteristic a maximum coupling power of 2.8 MW at a total mass flow of 22 kg/s can be reached. Detailed information on the design and construction of the facility can be found in [9], on the operation in [10].

Contributed by the International Gas Turbine Institute and presented at the International Gas Turbine and Aeroengine Congress and Exhibition, Atlanta, GA, June 16–19, 2003. Manuscript received by the IGTI December 2002; final revision March 2003. Paper No. 2003-GT-38266. Review Chair: H. R. Simmons.

  

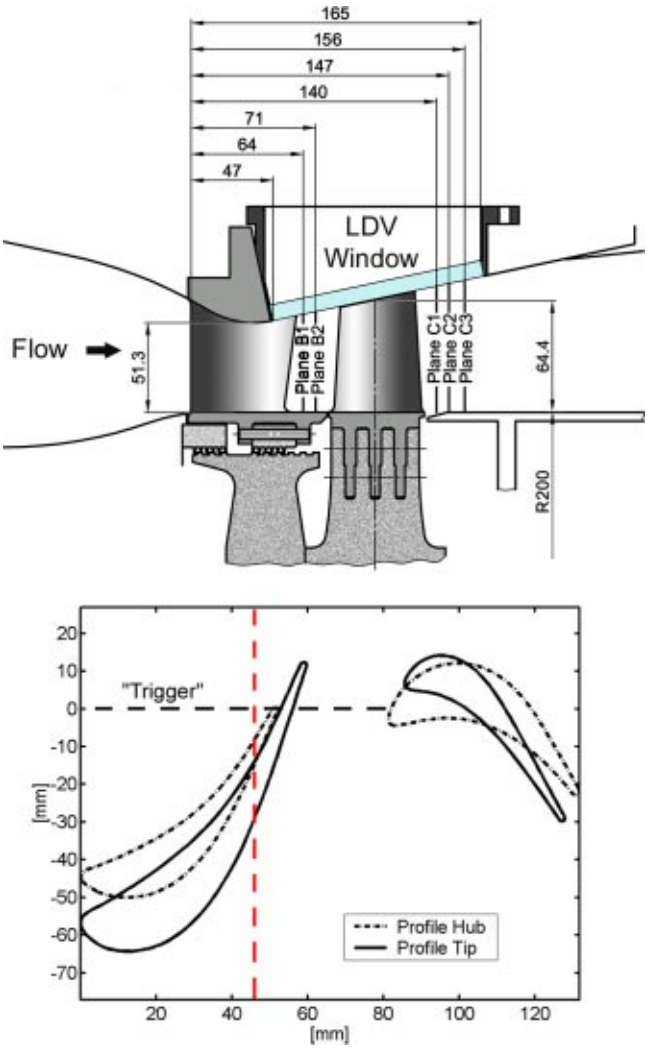


**Fig. 1 Meridional flow path and profiles at trigger zero position**

**Test Turbine Stage.** The meridional section of the applied test stage is given in **Fig. 1**. The convergent-divergent meridional flow path in the stator region is required to accelerate the flow to supersonic velocity and is obtained by a strong contraction of the shroud contour while the hub diameter is kept constant. There are 24 nozzle guide vanes and 36 rotor blades, so the guide vane–rotor blade ratio is 2:3, a ratio which was also used in [4] for the investigation of the influence of different vane blade spacings in a transonic turbine.

The optical access for LDV measurements is realized with special glass windows. The hub contour is cylindrical while the shroud contour is conical in the rotor section. The measurement planes between stator and rotor as well as downstream of the rotor are also indicated in **Fig. 1**. Some important operating conditions for this investigation and the geometrical data of the stage are given in **Table 1**.

In **Fig. 1** the vertical dotted line indicates the axial position of 46 mm from where on a gap of 0.8 mm between the nozzle guide vane tips and the outer shroud contour exists. This gap is necessary to rotate the stator ring and the guide vane casing during test run to change the relative position between vane and measurement system. The gap between rotor blade tip and shroud is 1 mm.

**Laser Doppler Velocimeter (LDV) System.** The optical velocity measurement of the flow was performed by a two-dimensional LDV-system (DANTEC Fiber Flow with BSA processors) fed by an 6W argon-ion laser from COHERENT. Optical access was realized through a small plan-parallel glass window of 9 mm thickness and $120\times23$ mm surface dimension. An antireflection coating was applied. As seeding material DEHS oil particles (Di-Ethyl-Hexyl-Sebacin-Esther, nominal diameter 0.7 $\mu$m) were added by PALLAS AGF 5D seeding generator 30 cm upstream of the stator blades using a special formed seeding pipe, [7]. These particles guarantee sufficiently high particle response at transonic flow conditions. (In the region of the trailing edge shock a smearing effect of 0.5 mm due to seeding particle inertia has to be kept in mind). The main optical parameters of the LDV system are presented in **Table 2**.

Four laser beams were emitted by the optical probe head into the measurement volume. Scattered light from the tracer particles passing through the probe volume was collected in back-scatter mode. Velocity data were recorded by point wise detection along radial lines in plane B1 and C1 (see **Fig. 1**, 0.12 mm probe volume diameter and 2.6 mm length in radial direction). The LDV system was mounted on a lightweight traverse in order to adjust the radial position of the probe head. The position in circumferential direction was changed by turning the nozzle guide vane casing. After the turning to a new position there was an allowance for the flow to settle.

The nozzle guide vanes, the rotor blades and the endwalls were covered with a high-temperature flat black paint to reduce surface reflections. To allow a rotor-phase-resolved analysis of the measured velocities in the positions traversed, a reference signal provided by the monitoring system of the turbine was used to trigger the data sampling.

**Pneumatic Probes.** The pneumatic probe measurements were performed by two different probe types: a seven-hole cone probe and a needle probe (see **Fig. 2**).

The seven-hole probe was used to determine total pressure, pitch and yaw flow angle, the needle probe to measure the undisturbed static pressure. The calibration was performed in a free jet at various Mach numbers and is described in [11,12]. The flow angle and the total pressure were determined using the calibration

**Table 1 Stage geometrical data and operating conditions**

| | |
|---|---|
| Number of nozzle guide vanes | 24 |
| Number of rotor blades | 36 |
| Nozzle chord (midspan) [mm] | 78.9 |
| Nozzle axial chord (midspan) [mm] | 56.1 |
| Geometric turning angle nozzle [deg] | 70 |
| Blade chord (midspan) [mm] | 55.9 |
| Blade axial chord (midspan) [mm] | 46.8 |
| Geometric turning angle blade [deg] | 107 |
| Nozzle height at exit [mm] | 55.1 |
| Rotor blade height at exit [mm] | 69.2 |
| Rotor tip clearance/span [%] | 1.4 |
| Vane-blade spacing [% nozzle axial chord (midspan)] | 47 |
| Pressure ratio $p_{tot,in}/p_{out}$ | 3.50 |
| Rotational speed [rpm] | 10500 |
| Inlet total temperature $T_{tot,in}$ [K] | 396 |
| Reynolds number nozzle guide vane exit | $2.57\cdot10^6$ |
| Reynolds number rotor blade exit | $1.69\cdot10^6$ |

**Table 2 Optical beam system**

| Velocity Component | $u$ | $v$ |
|---|---|---|
| Focal length [mm] | 400 | 400 |
| Wavelength [nm] | 514.5 | 488 |
| Beam spacing [mm] | 38 | 38 |
| Beam diameter [mm] | 2.2 | 2.2 |
| Focal spot diameter [$\mu$m] | 119.1 | 112.9 |
| Number of fringes | 21 | 21 |

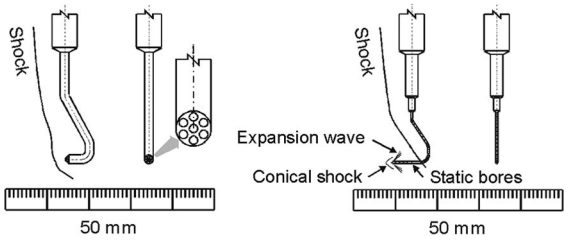


**Fig. 2 Seven-hole probe and static needle probe**

function. The pneumatic measurement grid consisted of 50 points in radial×30 points in circumferential direction in all planes indicated in **Fig. 1** and covered one nozzle guide vane pitch.

**Measurement Procedure and Data Processing.** **Figure 3** shows the LDV measurement locations in plane B1 and C1. The *z*-axis is equal to the machine axis, *x*-axis is in tangential and *y* axis in radial direction. Zero position for *z*-axis is the stator leading edge, for *y* axis the rotor axis center, for *x*-axis the trigger zero position.

LDV measurements were performed between approximately 25% and 88% relative span in B1 and 25% to 80% relative span in C1 since laser reflections from the hub and the window prevented valid burst detection closer to the endwalls. The grid behind the rotor is more wide meshed since time for measurement was limited due to the contamination of the window by seeding oil in this position.

The LDV system acquired a velocity sample each time a seeding particle crossed the LDV probe volume. A reference signal of the monitoring system of the turbine was used to sort the recorded velocity samples by the actual rotor position. Since a two-dimensional LDV was applied only the velocities in two different directions (i.e., axial and circumferential direction for plane C1) were detected. In plane B1 the LDV head was turned by 24 deg to keep the velocity components below the maximum detectable velocity of the applied optical beam system.

In each measurement position approximately 80,000 velocity bursts were collected. They were sorted with the help of the trigger signal provided by the shaft monitoring system to the proper rotor position. Thus all data recorded were reduced to one 10-deg section, i.e., one blade passing period. Thus the data presented represent the average value over 36 blades.

Velocity samples are indicated as black dots in **Fig. 4**. The blade passing period was divided into 40 evaluation windows,

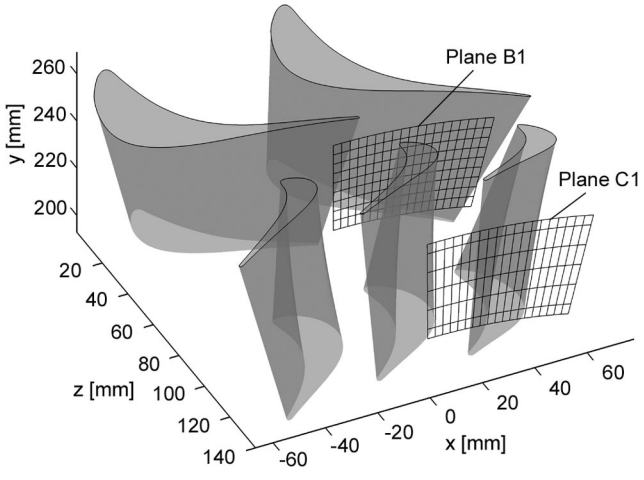


**Fig. 3 LDV measurement locations**

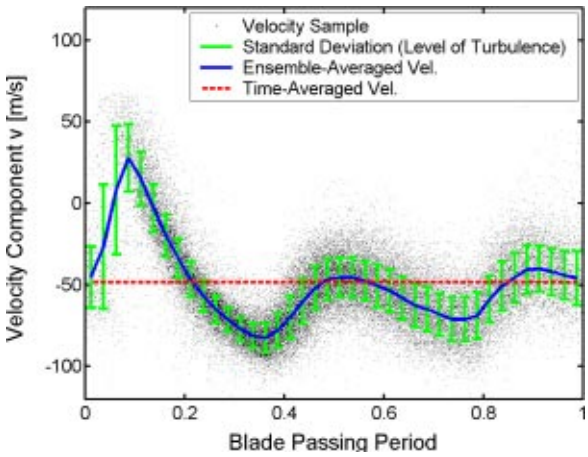


**Fig. 4 Velocity decomposition for phase averaged data**

which means that the velocity samples were assigned to 40 different stator-rotor positions per rotor blade pitch (=10 deg, due to 36 blades).

**Figure 4** shows for example the velocity decomposition of the velocity samples in circumferential direction in a point downstream the rotor at midspan (plane C1). The velocity was ensemble averaged at each evaluation window by means of the linear regression method according to [13].

The level of turbulence in each evaluation window was determined by the variance. A higher variance means a higher level of turbulence. The instantaneous velocity vector $\mathbf{V}_{k,i}$ was decomposed as follows:

$$\mathbf{V}_{k,i}=\overline{\mathbf{V}}_k+\mathbf{V}'_k=\overline{\overline{\mathbf{V}}}_k+\tilde{\mathbf{V}}_k+\mathbf{V}'_k \tag{1}$$

Where $\overline{\mathbf{V}}_k$ is the ensemble-averaged velocity, $\overline{\overline{\mathbf{V}}}_k$ is the time-averaged velocity, $\tilde{\mathbf{V}}_k$ is the periodic velocity component and $\mathbf{V}'_k$ is the unresolved velocity component (see also **Fig. 4**).

With 40 evaluation windows the number of velocity samples per window was still high enough to allow mean value and level of turbulence to be calculated with the following uncertainty. For a confidence level of 95% an uncertainty of 3.5 m/s in and 0.9 m/s outside the rotor wake for the ensemble averaged velocity as well as 11 m/s in and 2.5 m/s outside the rotor wake for the unresolved velocity was calculated.

## Experimental Results and Discussion

**Nozzle Guide Vane Exit Flow.** The time-averaged velocity field measured by the LDV system is given in **Fig. 5(*a*)** (velocity magnitude $|\overline{\overline{\mathbf{V}}}_B|$ obtained from the two velocity components recorded). The stator wake and the trailing edge shock can be seen very clearly. A sharp velocity decrease up to 90 m/s can be detected across these shocks located on the suction side. This shock starts approximately 8 mm upstream of the trailing edge at the hub (see **Fig. 5(*b*)**). A boundary layer separation occurs in this region to the trailing edge. Also the joint between two nozzle guide vanes is marked there. In **Fig. 5(*a*)** the region of low velocity on the left side of the wake near the outer endwall indicating the loss core caused by the accumulation of boundary layer fluid by the passage vortex can be seen. Most of the inner lost core is not visible due to the distance of the measurement grid from the hub. Time-resolved velocity magnitude fields $|\overline{\mathbf{V}}_B|$ are depicted in **Fig. 6**. Eight frames ($t/\tau=0$, 0.125, 0.25, 0.375, 0.5, 0.625, 0.75, 0.875) out of 40 were used to show the influence of the passing rotor blades on the stator exit flow. The view is from the low pressure side upstream onto plane B1 located at the nozzle guide vanes exit. The black

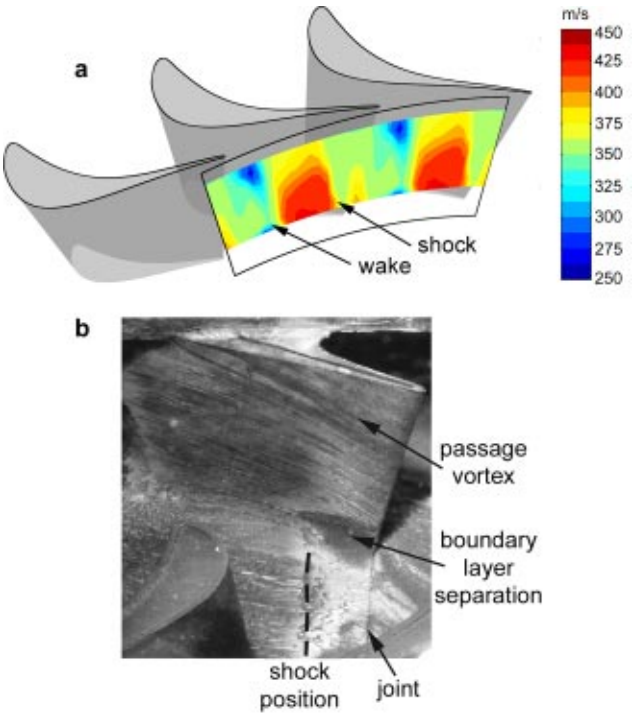


**Fig. 5** (*a*) **Time-averaged velocity field in B1 measured by LDV,** (*b*) **oil film visualization of surface flow**

lines in the field plots indicate the locations of the rotor leading edges moving from the left to the right. From one to the next picture the rotor blades moved 1.25 deg which corresponds to 1/8 of the rotor blade passing period. The arrows in **Fig. 7** indicate the direction of frame order. After one cycle the rotor blade has passed one rotor pitch (turned 10 deg).

**Figure 7** shows time-resolved flow angle distributions of the same 8 stator-rotor positions presented in **Fig. 6**. This flow angle is measured to the axial direction and represents the yaw angle (velocities were recorded in a tangential plane).

In each frame of **Figs. 6** and **7**, the flow field is presented for two nozzle pitches (30 deg). Due to the ratio number of nozzle guide vanes to the number of rotor blades of 24:36=2:3 these plots can be periodically continued all around the nozzle ring.

Although the vane-blade spacing is 47% of nozzle axial chord (at midspan) the interaction of the passing rotor blades with the stator exit flow is still clearly visible in **Fig. 6**. The shock itself remains very stable at the same position on the suction side.

In **Fig. 7**, observation of the blades during $t/\tau=0.125$ to 0.375 shows a continuous increase of the flow angle in the region between the two nozzle wakes from about 68 deg to 73 deg (see **Fig. 7**) due to the interaction with the suction side of the rotor blade. The nozzle exit flow is pressed back into the tangential direction. From $t/\tau=0.5$ on the flow switches from the SS of the rotor to its PS, this means the flow along the PS increases and the flow angle decreases continuously to 68 deg.

**Figure 8** shows the comparison of the time-averaged flow angle measured by the LDV system and the flow angle gained by pneumatic measurement. In **Fig. 8** the 0-deg position corresponds to the radial line of the grid at $x=0$ in **Fig. 3**, the dashed lines give the position of the nozzle wakes. The differences between the two types of measurement are depicted in the bottom picture. The maximum differences occur in the wake region and can be explained by the larger variation of angle in the pneumatic measurement due to the sensitivity of the applied probes to local pressure gradients (the probe head diameter is in the same order of magnitude as the thickness of the wake flow). The differences in the upper region are not fully understood and are explained by probe blockage.

The velocity defect in the nozzle wakes causes a smaller flow angle in these regions and the wake flow is more axial. The minimum angles appeared in a small area at the left side of the nozzle wake (SS of nozzle guide vane). A discontinuity created by the shock was not clearly detected.

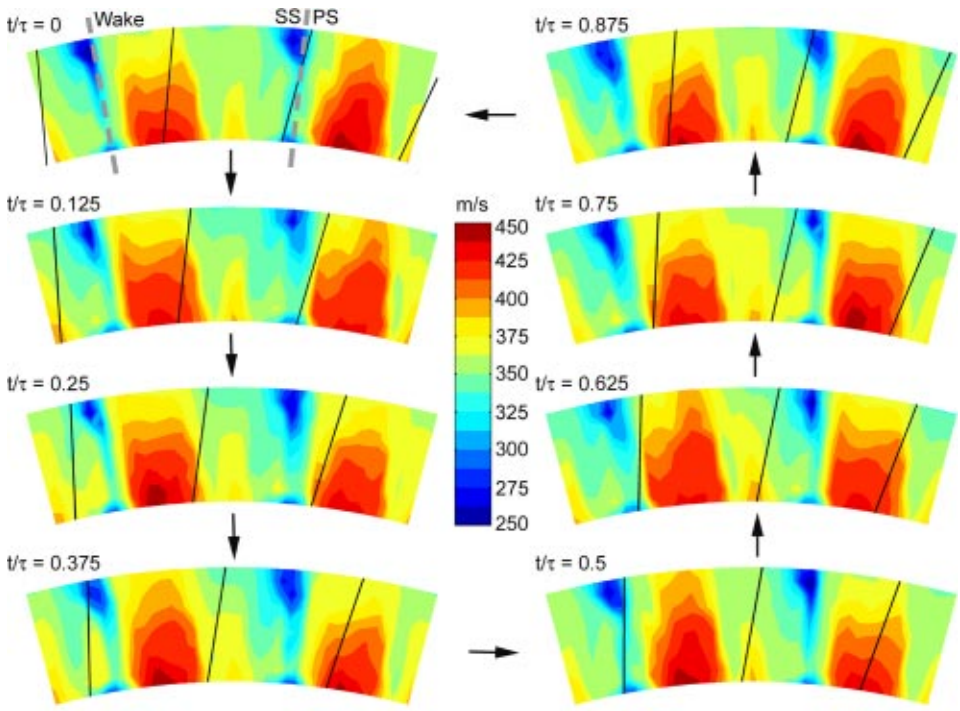


**Fig. 6 Time-resolved velocity fields in B1 measured by LDV (contour steps 12.5 m/s)**

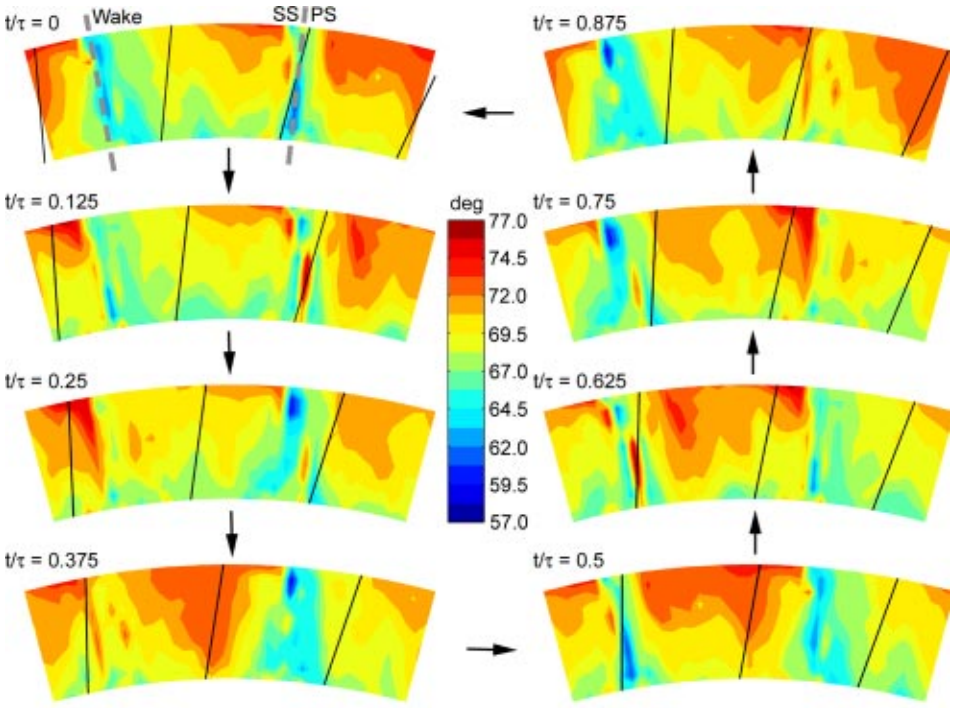


**Fig. 7 Time-resolved flow angle (yaw angle) distributions in B1 measured by LDV (contour steps 1.25 deg)**

In order to indicate zones of high losses a nondimensional coefficient $\omega$ which was used in [1] representing the ratio of total pressure loss in the stator and the averaged dynamic pressure in the measurement plane.

$$\omega = \frac{p_{\text{tot}\,A,av} - p_{\text{tot}\,B}}{p_{\text{tot}\,B,av} - p_{B,av}} \tag{2}$$

$$p_{av} = \frac{1}{A} \cdot \int p \cdot dA \tag{3}$$

**Figure 9** shows the pressure loss coefficient $\omega$ in measurement planes B1 and B2. The location of these planes is indicated in the stage meridional section in **Fig. 1**. Again in **Fig. 9** the 0 deg position corresponds to the radial line of the grid at $x=0$ in **Fig. 3**, the dashed lines give the position of the nozzle wakes.

Regions of high pressure loss result from the stator wakes which are indicated by dashed lines. The two spots of very high loss on the suction side result from the accumulation of low en-

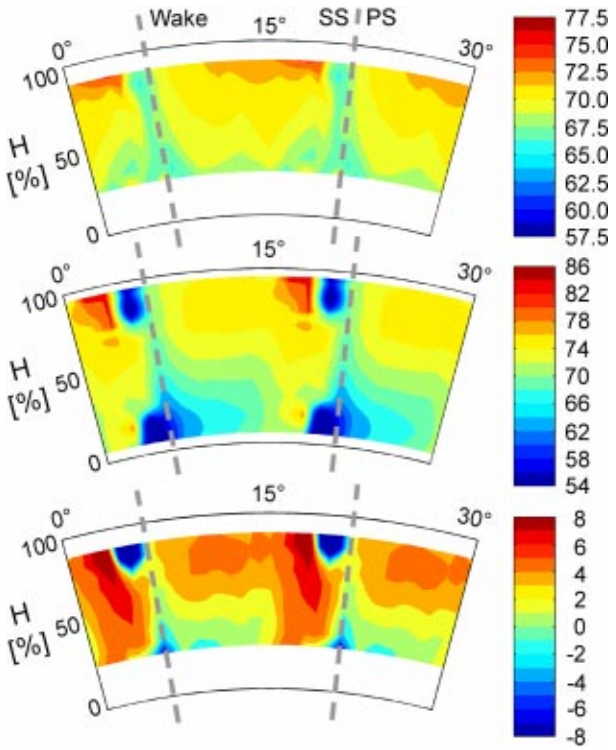


**Fig. 8 Time-averaged flow angle in B1 measured by LDV (above), flow angle by pneumatic probes (middle) and difference between two types of measurement (below)**

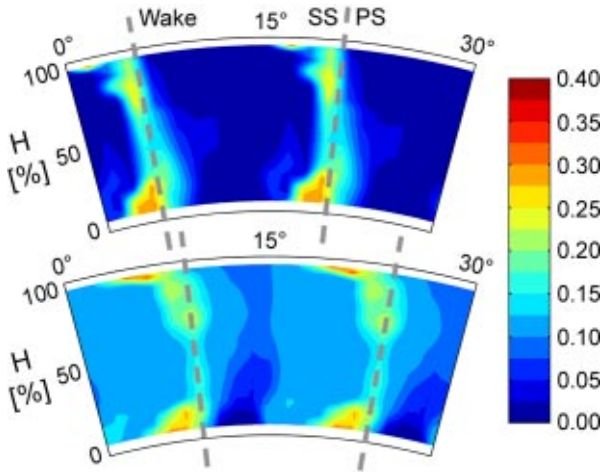


**Fig. 9 Pressure loss coefficient $\omega$ in B1 (above) and B2 (below) 0 deg correspond to $x=0$ in Fig. 3, the dashed lines give the position of the wakes (contour steps 0.025)**

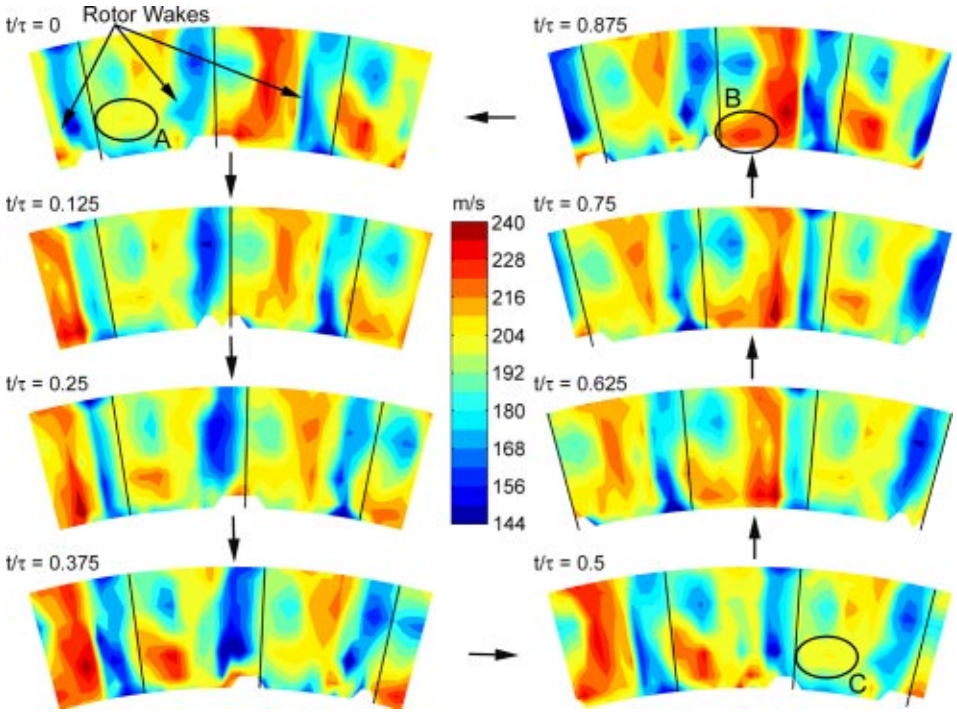


**Fig. 10 Time-resolved velocity fields in C1 measured by LDV (contour steps 6 m/s)**

ergy fluid at the endwalls by the passage vortices. The region of low total pressure at the upper endwall are larger than at the hub since the boundary layer may be thicker there. A comparison of the pictures of plane B1 and B2 shows that the wake appears circumferentially shifted and that due to mixing the total pressure distribution is smoother in plane B2. Maximums of pressure loss are higher in plane B1 than in plane B2. The total pressure loss over the nozzle vane trailing edge shock is small so that the shock cannot be detected. Regions of very high losses at the upper endwall seem to be caused by a 0.8 mm clearance between the stator vane in the trailing edge region and the casing.

**Rotor Exit Flow.** The rotor exit flow is heavily influenced by the wakes of the rotor blades passing by. In a time-averaged velocity plot variations of the velocity magnitude $|\overline{\overline{\mathbf{V}_C}}|$ were found downstream of the rotor. These variations were evoked by the non-uniform nozzle guide vane exit flow field. At midspan, a circumferential variation of velocity of approximately 30 m/s was found. For a better view onto plane B1 the plot showing the results of plane C1 is shifted in circumferential direction by two nozzle pitches.

The time-resolved measurement utilizing the LDV system allowed the investigation of flow phenomena at different stator-rotor positions. Time-resolved magnitude fields $|\overline{\mathbf{V}_C}|$ in plane C1 are presented in **Fig. 10**. Again eight frames ($t/\tau=0$, 0.125, 0.25, 0.375, 0.5, 0.625, 0.75, 0.875) are used to show the flow downstream of the rotor blades. The view is from the stage exit upstream onto plane C1. The black lines indicate the locations of the rotor trailing edges moving from the left to the right. The rotor blades move 1.25 deg from frame to frame, one whole cycle corresponds to a movement of one rotor pitch (a turning of 10 deg). As in **Figs. 6** and **7**, **Figs. 10** and **11** present the flow field for two nozzle pitches (30 deg).

**Figures 10** and **11** show the wake of the rotor blades on the left-hand side of the rotor trailing edges (black lines) moving from the left to the right. The velocity defect and the increase in flow angle can be seen very clearly. All areas in these plots, where a correct evaluation due to a lack of seeding particles was not ensured, were left white (especially at the inner radius).

On the right side of the rotor wakes a region of lower velocity and larger flow angle can be seen moving together with the rotor blades. A little more radially inward a region of higher velocity is detected. These areas of lower and higher velocity moving together with the wakes indicate secondary flow phenomena caused by the rotor blades.

When examining the encircled area "A" ($t/\tau=0$, **Fig. 10**) on the suction side of the rotor blade, it can be seen that the velocity increases in time from 205 to 230 m/s at $t/\tau=0.875$ (area "B"). During further rotation to $t/\tau=1.5$ (equal $t/\tau=0.5$) the velocity decreases back to the original value (indicated with "C"). This movement in circumferential direction corresponds to a rotation of 15 deg (one nozzle pitch). This phenomenon is effected by the stator. Similar structures can be observed in the flow angle distributions of **Fig. 11**.

Averaging over the whole blade passing period $\tau$ lead to a velocity field in **Fig. 12**. Due to the same color bar the picture can be compared to the time-resolved results of **Fig. 10**.

**Figure 13** shows the comparison of the time-averaged flow angle measured by the LDV system and the flow angle obtained by pneumatic measurement in plane C1 showing a good agreement.

The bottom picture shows the differences between both measurements. Although there are deviations between $-3$ deg and $+3.5$ deg the mean deviation is close to zero. The local differences are explained by incorrect time averaging of the probe which is not able to follow high frequent flow oscillations. The mean flow angle in plane C1 is about $-15$ deg, this means that the flow direction is in opposite direction to the rotor rotation. The extended area covered by the pneumatic probe measurement also shows the influence of the tip leakage flow to the flow angle. The difference to the mean value is up to 16 deg. The larger counter swirl at hub is evoked by secondary flow effects.

**Nozzle Wake Propagation.** Another important flow feature is the transport of the highly turbulent nozzle wakes through the rotor. When a nozzle wake enters a rotor passage, it is chopped by the rotor leading edges into individual segments and they subsequently propagate through the rotor passages independent from

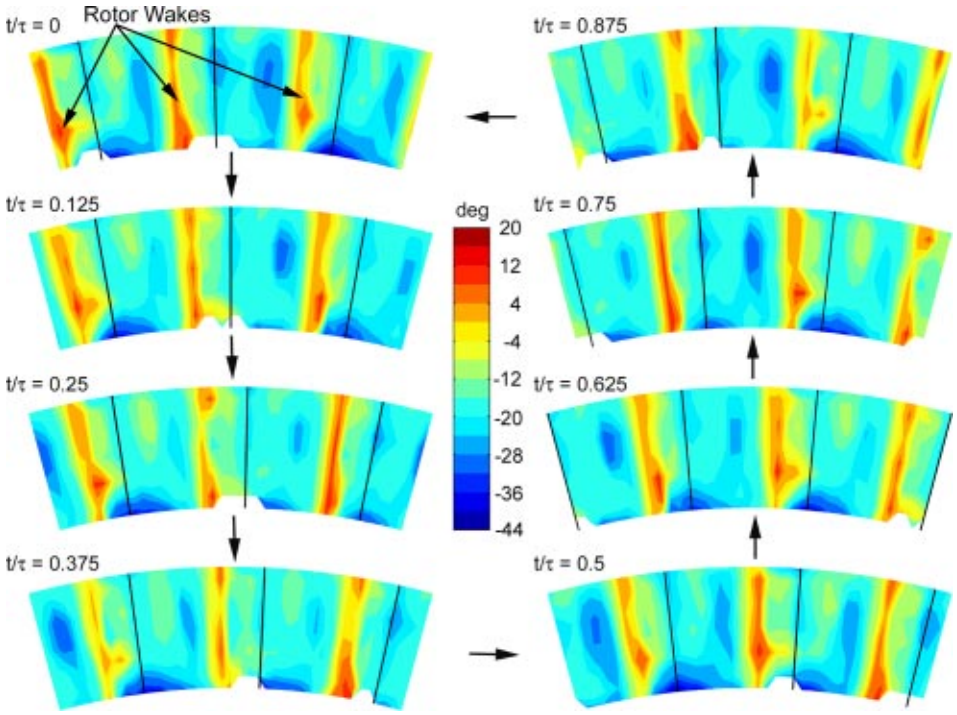


**Fig. 11 Time-resolved flow angle (yaw angle) distributions in C1 measured by LDV (contour steps 4 deg)**

each other. There is a strong mixing and a deformation of these wake fragments by the surrounding flow. The turbulent kinetic energy was used to show the turbulent segments in plane C1. The turbulent kinetic energy $k$ was calculated from the axial and circumferential velocity components $u'$ and $v'$ both measured by the LDV system by

$$k = 0.75 \cdot (u'^2 + v'^2) \tag{4}$$

and is shown in **Fig. 14**.

This equation is based on the assumption, that the radial component of fluctuating velocity not measured by the LDV system is in the same order of magnitude as the $u'$ and $v'$ components. Apart from the high turbulent kinetic energy in the wake flow of the passing turbine blades (up to 2500 $m^2/s^2$) an increase from 30 to approximately 500 $m^2/s^2$ can be seen in the regions between them. The appearing of these turbulent nozzle wake fragments is observed for example in the area between the first and second rotor wake marked with "A" in **Fig. 14**: The flow in this encircled region gets more and more turbulent till $t/\tau = 0.5$ (indicated with "B"). Then the value of turbulent kinetic energy decreases indi-

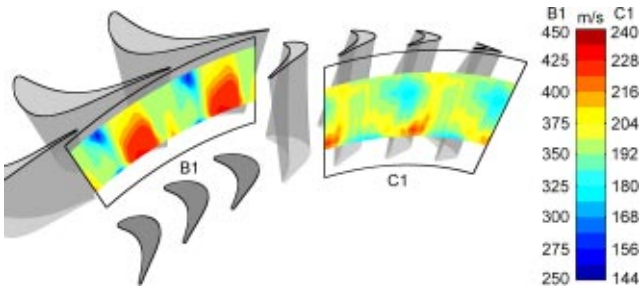


**Fig. 12 Time-averaged velocity fields measured by LDV**

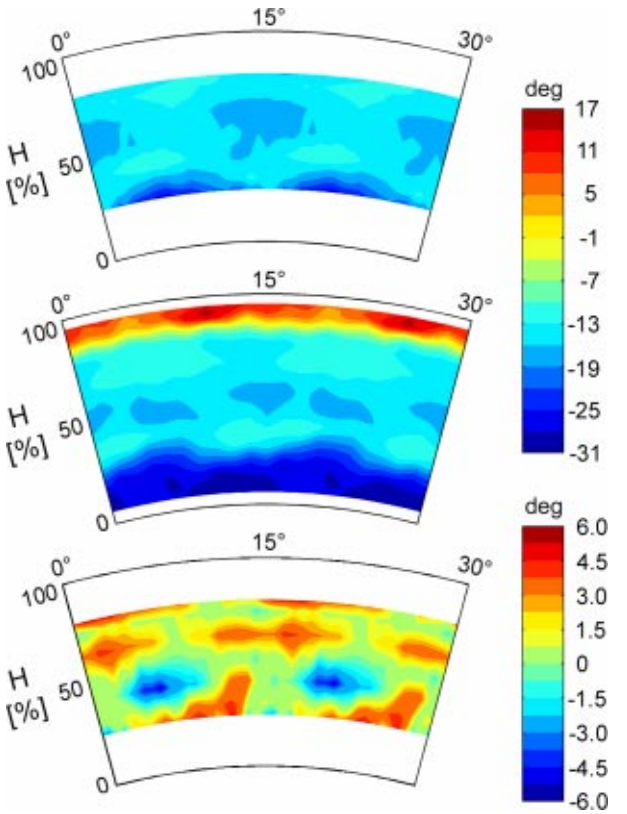


**Fig. 13 Time-averaged flow angle in C1 measured by LDV (above), flow angle by pneumatic probes (middle) and difference between two types of measurement (below)**

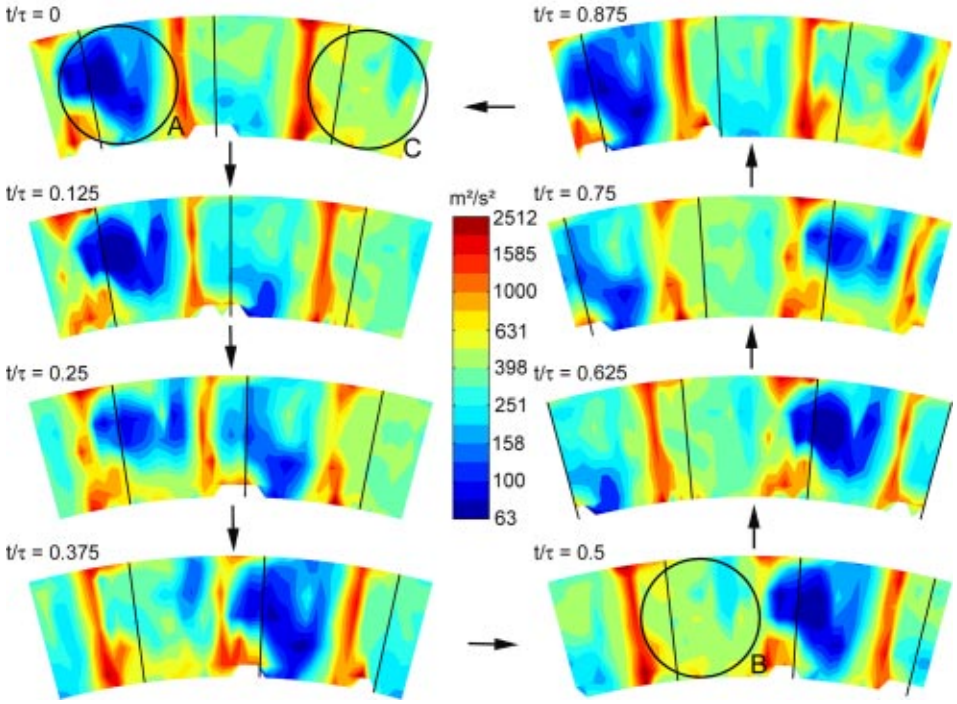


**Fig. 14 Time-resolved distributions of turbulent kinetic energy *k* in C1 measured by LDV**

cating the absence of nozzle wake fragments. The same flow situation occurs at a distance of one nozzle pitch but with a shift in time of $t/\tau = 0.5$ (marked with "C").

## Concluding Remarks

The flow in transonic turbomachines is heavily influenced by three-dimensional secondary flow phenomena which have a strong impact on their efficiency. These effects are still difficult to predict by modern CFD calculations.

Therefore the objective of this work was to provide accurate unsteady flow data in a transonic turbine stage for CFD code verification. These data were obtained by two-component laser Doppler velocimeter measurements between stator and rotor as well as downstream of the rotor in planes perpendicular to the rotor axis. The unsteady data are referred to the rotor blade passing period.

Comparisons were also performed with pneumatic probe measurements which showed an overall agreement. Differences in flow angle were observed which are contributed to the deficiencies of the probe measurement in transonic flows.

The experimental data and the stage geometry are offered to the scientific community in order to support the understanding of unsteady three-dimensional transonic flow through cooperative CFD simulation. The data can be obtained per email request.

## Acknowledgments

The authors would like to thank H. Lang and B. Hampel for their help in the taking of the LDV data. We also appreciate the help of Dr. H. P. Pirker for operating the test facility during measurement.

The support by the Austrian Science Foundation (FWF) and the Austrian Federal Ministry for Education, Science and Culture (BMBWK) within the awarded grant Y57-TEC "Nonintrusive Measurement of Turbulence in Turbomachinery" is gratefully acknowledged.

## Nomenclature

$t$ = time (s)
$PS$ = pressure surface
$SS$ = suction surface
$A$ = area of measurement planes ($m^2$)
$p$ = absolute pressure (bar)
$r$ = radial position (m)
$T$ = absolute temperature (K)
$x,y,z$ = Cartesian coordinates (m)
$u$ = velocity in axial direction (m/s)
$v$ = velocity in circumferential direction (m/s)
$\mathbf{V}$ = velocity vector (m/s)
$K$ = turbulent kinetic energy ($m^2/s^2$)
$H$ = percentage spanwise distance (%)

### Greek

$\tau$ = rotor blade passing period (s)
$\omega$ = pressure loss coefficient

### Subscripts

$i$ = instantaneous
$k$ = burst spectrum analyzer (BSA) number
tot = total
$in$ = at inlet
$av$ = averaged value
$A$ = plane A (upstream of nozzle)
$B$ = plane B (downstream of nozzle)
$C$ = plane C (downstream of rotor)

### Superscripts

$-$ = ensemble-averaged properties
$=$ = time-averaged properties
$\sim$ = periodic quantity
$'$ = unresolved fluctuating quantity

## References

[1] Zeschky, J., 1991, "Experimentelle Untersuchung der dreidimensionalen insta-

tionären Rotorströmung einer axialen Kaltluftturbine,'' Ph.D. thesis, Institute for Jet Propulsion and Turbomachinery, RWTH Aachen, Germany (in German).
[2] Joslyn, D., and Dring, R., 1992, ''Three-Dimensional Flow in an Axial Turbine. Part 1: Aerodynamic Mechanisms,'' ASME J. Turbomach., **114**, pp. 61–70.
[3] Zaccaria, M.A., 1994, ''An Experimental Investigation into the Steady and Unsteady Flow Field in an Axial Flow Turbine,'' Ph.D. thesis, Pennsylvania State University, USA.
[4] Busby, J.A., Davis, R.L., Dorney, D.J., Dunn, M.G., Haldeman, W.C., Abhari, R.S., Venable, B.L., and Delaney, R.A., 1999, ''Influence of Vane-Blade Spacing on Transonic Turbine—Part II: Time Resolved Data and Analysis,'' ASME J. Turbomach., **121**, pp. 673–682.
[5] Dénos, R., Arts, T., Paniagua, G., Michelassi, V., and Martelli, F., 2001, ''Investigation of the Unsteady Rotor Aerodynamics in a Transonic Turbine Stage,'' ASME J. Turbomach., **123**, pp. 81–89.
[6] Tiedemann, M., and Kost, F., 2001, ''Some Aspects of Wake-Wake Interactions Regarding Turbine Stator Clocking,'' ASME J. Turbomach., **123**, pp. 526–533.
[7] Lang, H., Mørck, T., and Woisetschläger, J., 2002, ''Stereoscopic Particle Image Velocimetry in a Transonic Turbine Stage,'' Exp. Fluids, **32**, pp. 700–709.
[8] Woisetschläger, J., Lang, H., Hampel, B., and Göttlich, E., 2002, ''Influence of Blade Passing on the Stator Wake in a Transonic Turbine Stage by Particle Image Velocimetry and Laser Vibrometry,'' IMechE J. Power Energy, **217** (Part A), pp. 385–391.
[9] Erhard, J., and Gehrer, A., 2000, ''Design and Construction of a Transonic Test Turbine Facility,'' ASME Paper No. 2000-GT-480.
[10] Neumayer, F., Kulhanek, G., Pirker, H.P., Jericha, H., Seyr, A., and Sanz, W., 2001, ''Operational Behavior of a Complex Transonic Test Turbine Facility,'' ASME Paper No. 2001-GT-489.
[11] Neumayer, F., Heitmeir, F., Göttlich, E., and Pieringer, P., 2002, ''Experimental Investigation of the Flow in a Transonic Turbine Stage,'' Paper No. TA08/78, *Proc. 5th European Conference on Turbomachinery, Fluid Dynamics and Thermodynamics*, M. Šťastný, C.H. Sieverding, and G. Bois, eds., Prague, Czech Republic, pp. 1061–1075.
[12] Neumayer, F., 2002, ''Measurements of Transonic Turbine Stage Characteristics and 3-D Flow Fields,'' Ph.D. thesis, Institute for Thermal Turbomachinery and Machine Dynamics, Graz University of Technology, Austria.
[13] Glas, W., Forstner, M., Kuhn, K., and Jaberg, H., 2000, ''Smoothing and Statistical Evaluation of LDV Data of Turbulent Flows in Reciprocating Machinery,'' Exp. Fluids, **29**, pp. 411–417.

**Robert Kielb**
Duke University,
P.O. Box 90300,
Durham, NC 27708-0300

**Jack Barter**
GE Aircraft Engines,
One Neumann Way,
Cincinnati, OH 45215

**Olga Chernycheva**

**Torsten Fransson**

Swedish Royal Institute of Technology,
Brinellvagen 60,
Stockholm S-10044,
Sweden

# Flutter of Low Pressure Turbine Blades With Cyclic Symmetric Modes: A Preliminary Design Method

*A current preliminary design method for flutter of low pressure turbine blades and vanes only requires knowledge of the reduced frequency and mode shape (real). However, many low pressure turbine (LPT) blade designs include a tip shroud that mechanically connects the blades together in a structure exhibiting cyclic symmetry. A proper vibration analysis produces a frequency and complex mode shape that represents two real modes phase shifted by 90 deg. This paper describes an extension to the current design method to consider these complex mode shapes. As in the current method, baseline unsteady aerodynamic analyses must be performed for the three fundamental motions, two translations and a rotation. Unlike the current method work matrices must be saved for a range of reduced frequencies and interblade phase angles. These work matrices are used to generate the total work for the complex mode shape. Since it still only requires knowledge of the reduced frequency and mode shape (complex), this new method is still very quick and easy to use. Theory and an example application are presented.* [DOI: 10.1115/1.1650380]

## Introduction

Panovsky and Kielb [1] presented a new method to conduct preliminary flutter design analysis for LPT blades. The study identified the blade mode shape as the most important contributor determining blade stability. Each mode shape is represented by three rigid-body motions (two translations and one rotation) at the spanwise location of maximum displacement. These three motions can be described by a ''pitching axis.'' The critical value of reduced frequency, $k_c$, is determined by placing this pitching axis location on the plot shown in **Fig. 1** and reading off the critical reduced frequency. The horizontal solid lines represent the location of the blade leading and trailing edges. The diagonal solid line is normal to the engine rotational axis. Blue represents a $k_c$ less than 0.1 and pink represents a $k_c$ greater than 0.5. By comparing this $k_c$ with the actual reduced frequency, the stability is determined.

Further investigation using the same approach (Tchernycheva et al. [2]) has shown that the overall stability behavior, as well as identification of the most stable and the most unstable regions as a function of blade mode shape remain remarkably similar for a rather wide range of physical and aerodynamic parameters of LPT blades with pure subsonic flow. Therefore, for preliminary design purposes CFD analyses only need to be preformed for a reference airfoil. The results are then applied to all preliminary designs. This method has been shown to be valuable in screening preliminary designs (requiring only the results of a finite element analysis) and identifying a minimal set of unsteady CFD analysis for final designs.

Flutter is typically encountered on the blades and vanes of aft LPT stages. Typical aft LPT blades (**Fig. 2**) are long and slender and contain tip shrouds that structurally couple the blades. Since this arrangement is cyclically symmetric, each eigenvalue has a complex mode shape that can be represented by two real mode shapes that are commonly called the cosine and sine modes. These two modes are phase shifted by 90 deg. As a result, direct application of the Panovsky-Kielb (P-K) method (never intended to handle cyclic symmetry modes) results in two pitching axis locations for each eigenvalue. The use of **Fig. 1** then results in two values for $k_c$. Although this can easily be done, it is theoretically incorrect, and experience has shown that it is ultra-conservative. That is, virtually all designs are judged to be unstable.

Another approach is to take advantage of the fact that the cosine and sine modes are not unique and can be ''clocked'' circumferentially to maximize the amplitude ratio between these two modes. This approach is commonly referred to as the ''antinode'' method. The higher amplitude mode shape is used to determine the pitching axis location to use with **Fig. 1** for determining stability. The lower amplitude mode is ignored. The example given later in this paper shows that this method is also overly conservative. In addition, design experience has shown that this approach is typically overly conservative with respect to actual engine experience. This paper presents an extension to the Panovsky-Kielb method that eliminates these conservatisms, and is useful for preliminary flutter design of shrouded LPT blades.

## Panovsky-Kielb Method

In the Panovsky-Kielb method, two dimensional computational fluid dynamics (CFD) (usually inviscid) analyses must be performed for a reference airfoil for a range of reduced frequencies and interblade phase angles. The interblade phase angle is

$$\beta_l = \frac{2\pi l}{N_b} \tag{1}$$

where $l$ is the number of nodal diameters and $N_b$ is the number of blades. For each interblade phase angle the unsteady pressures on the blade surface are calculated for three rigid body mode shapes; translation in $\xi$, translation in $\eta$, and rotation about the leading edge ($\xi$ and $\eta$=0, see **Figs. 1** and **3**). The blade surface unsteady pressures are combined with the mode shapes to calculate the work per cycle matrix.

$$b_l = \begin{bmatrix} w_{\xi\xi} & w_{\xi\eta} & w_{\xi\alpha} \\ w_{\eta\xi} & w_{\eta\eta} & w_{\eta\alpha} \\ w_{\alpha\xi} & w_{\alpha\eta} & w_{\alpha\alpha} \end{bmatrix}.$$

Contributed by the International Gas Turbine Institute and presented at the International Gas Turbine and Aeroengine Congress and Exhibition, Atlanta, GA, June 16–19, 2003. Manuscript received by the IGTI Dec. 2002; final revision Mar. 2003. Paper No. 2003-GT-38694. Review Chair: H. R. Simmons.

  

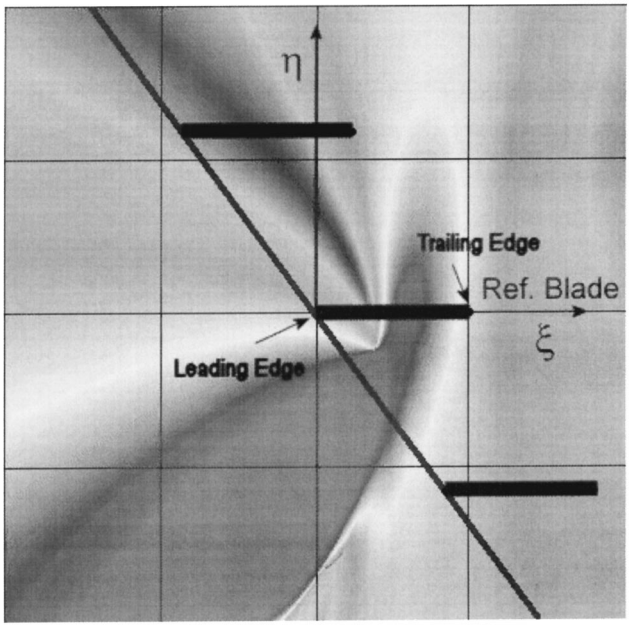


**Fig. 1 Critical reduced frequency "tiedye" plot**

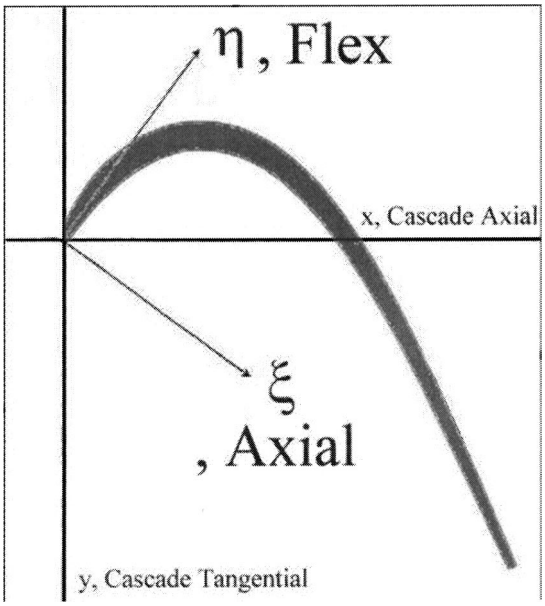


**Fig. 3 Blade coordinate system**

The diagonal terms represent work done by the unsteady pressures acting on the mode shapes producing these unsteady pressures. The off-diagonal terms represent the work done by the unsteady pressures acting on the other mode shapes.

The work for any two-dimensional rigid-body mode shape can then be determined from

$$w_l = \{a\}^T [b_l] \{a\}$$

where

$$\{a\} = \begin{Bmatrix} h_\xi \\ h_\eta \\ \alpha \end{Bmatrix}$$

$h_\xi$ is the rigid-body displacement in the $\xi$-direction
$h_\eta$ is the rigid-body displacement in the $\eta$-direction
$\alpha$ is the rotation about the leading edge.

Thus, for any given mode shape (or location of pitching axis) the stability can be determined by considering all interblade phase angles. The tie-dye plot (**Fig. 1**) is created by determining $k_c$ for a fine grid of $\xi$, $\eta$ pitching axis locations. An efficient method of obtaining the $k_c$s is presented in Panosky and Kielb [1].

## Cyclic Symmetry Method

As in the Panovsky-Kielb method the same work matrices $b_l$ are generated for a range of reduced frequencies and interblade phase angles. A finite element method is usually used to determine the frequencies and complex mode shapes as a function of nodal diameter. Also, as in the P-K method, the spanwise location of maximum displacement is used for the stability evaluation. For each mode the real cosine and sine mode shapes can be converted into two-dimensional rigid-body mode shapes represented by

$$\{a_{lc}\} = \begin{Bmatrix} h_{\xi lc} \\ h_{\eta lc} \\ \alpha_{lc} \end{Bmatrix} \quad \text{and} \quad \{a_{ls}\} = \begin{Bmatrix} h_{\xi ls} \\ h_{\eta ls} \\ \alpha_{ls} \end{Bmatrix}$$

Although the amplitude of the mode shapes is arbitrary, it is important to retain the amplitude ratios of the cosine and sine modes. The work for the cosine and sine modes can then be individually calculated and summed to obtain the combined work

$$w_{lc} = \{a_{lc}\}^T [b_l] \{a_{lc}\}$$

$$w_{ls} = \{a_{ls}\}^T [b_l] \{a_{ls}\}$$

$$w_{l,\text{comb}} = w_{lc} + w_{ls}\,.$$

Note that this approach does include the "off-diagonal" work terms. That is, the unsteady pressures due to the cosine mode applied to the sine mode and vice versa. Although some very limited data has shown these terms to be small. There is no theoretical reason to expect that they should be insignificant. Therefore, this effect needs to be studied.

The equations above represent the work in the forward traveling wave with l nodal diameters. For example, the $l$ nodal diameter modes of a rotor with $N_b$ blades results in a forward traveling mode with an interblade phase angle given by Eq. (1). However, the mode shapes $a_{lc}$ and $a_{lc}$ are also valid for the backward traveling wave that can be represented by $-l$ nodal diameters. For this mode the interblade phase angle is

$$\beta_{-l} = -2\pi l / N_b\,.$$

Therefore, the same cosine and sine mode shapes can be used to calculate the work for the backward traveling wave by

$$w_{-lc} = \{a_{lc}\}^T [b_{-l}] \{a_{lc}\}$$

$$w_{-ls} = \{a_{ls}\}^T [b_{-l}] \{a_{ls}\}$$

$$w_{-l,\text{comb}} = w_{-lc} + w_{-ls}\,.$$

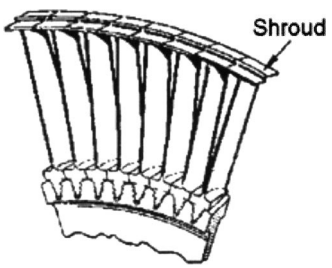


**Fig. 2 Typical aft LPT shrouded blades (pie section)**

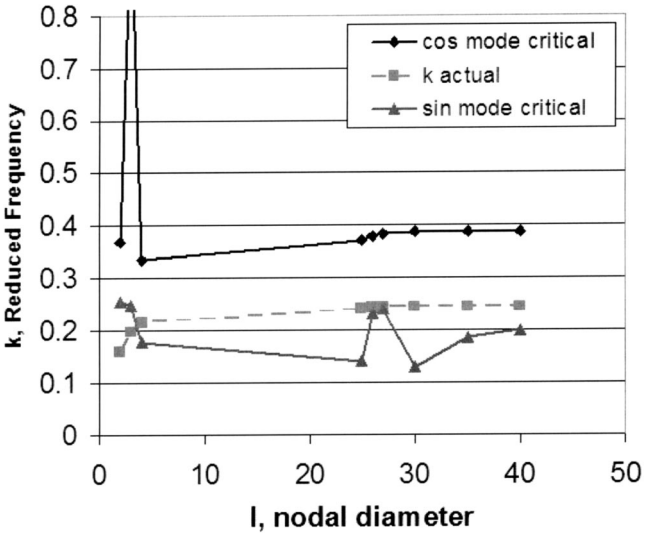


**Fig. 4 Evaluation using traditional P-K method**

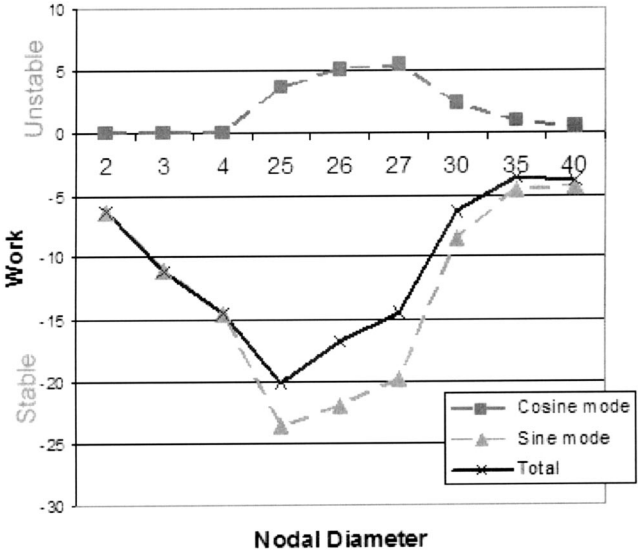


**Fig. 5 Forward traveling wave—cosine, sine, and total work**

Given the frequencies and mode shapes for a range of nodal diameters, the work for both the forward and backward traveling waves can be easily determined. It is usually more meaningful to put the results in terms of damping.

$$\zeta = \frac{-W}{4\pi E_{\max}} \quad \text{(critical damping ratio)}$$

where $E_{\max}$ is the maximum kinetic energy.

## Example Problem

The frequencies and mode shapes of an LPT blade ($N_b = 176$) were determined for nine different nodal diameters. Directly applying the traditional P-K method separately for the cosine and sine modes to determine the stability gives the results shown in **Fig. 4**. When the critical value is greater than the actual value the mode is unstable. Therefore, for this case all cosine modes are unstable and two of the sine modes are judged to be unstable.

The cyclic method was applied to the same problem. For the 35 nodal diameter case the finite element cyclic symmetry analysis resulted in the following frequencies and rigid-body mode shapes:

$$k = 0.246$$

$$a_{35c} = \begin{Bmatrix} -0.00304 \\ -0.00399 \\ 0.01285 \end{Bmatrix}$$

$$a_{35s} = \begin{Bmatrix} -0.19467 \\ 0.44450 \\ 0.03671 \end{Bmatrix}.$$

The pitching axis locations ($\xi, \eta$-coordinates) are $(0.31, -0.24)$ and $(-12.1, -5.3)$ for the cosine and sine modes, respectively. By plotting the cosine pitching axis location on **Fig. 1** results in a $k_c$ of approximately 0.39. Notice that this pitching axis location is in a high gradient region. To evaluate the $k_c$ of the sine mode requires a zoomed out tie-dye plot showing pitching axis locations farther from the blade leading edge. The resulting $k_c$ is approximately 0.18. These critical reduced frequency values are shown in **Fig. 4**, where it can be seen that the cosine mode is unstable and the sine mode is stable. However, as can be seen from the rigid-body mode shapes, the sine mode has significantly larger amplitude. The cyclic symmetry method results in the following values of work per cycle:

Forward Traveling Wave, $\beta = 71.6$

$$w_{35c} = 0.87$$

$$w_{35s} = -4.55$$

$$w_{35,\text{comb}} = -3.68$$

Backward Traveling Wave, $\beta = -71.6$

$$w_{-35c} = -3.25$$

$$w_{-35s} = -17.99$$

$$w_{-35,\text{comb}} = -21.24$$

Indeed the forward traveling cosine mode is unstable, but it is overwhelmed by the larger amplitude sine mode that is stable.

Cyclic symmetry method results for all nodal diameters studied are shown in **Fig. 5** and **Fig. 6**. For the 2, 3, and 4 nodal diameter modes the amplitude of the sine components is significantly larger than that of the cosine mode. As a result the work for the 2, 3, and 4 nodal diameter cosine modes is insignificant. For the forward traveling wave the cosine modes are unstable for the higher nodal

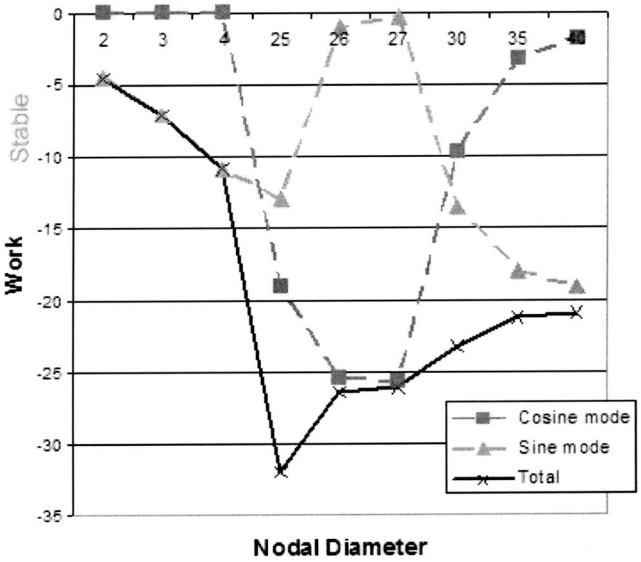


**Fig. 6 Backward traveling wave—cosine, sine, and total work**

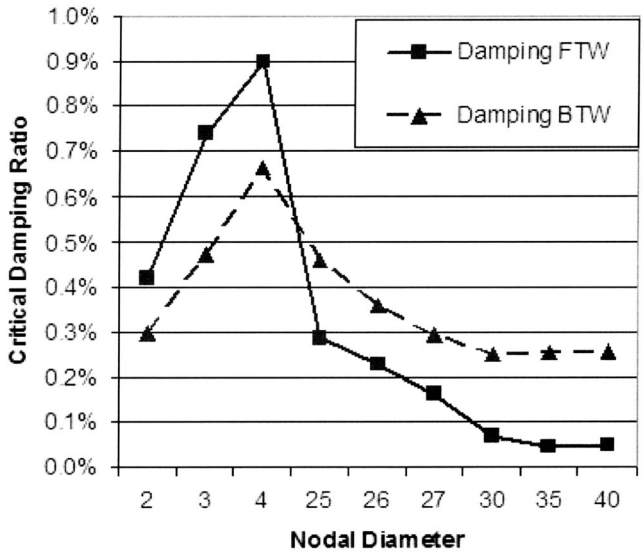


**Fig. 7 Damping versus nodal diameter**

diameters. However, the sine modes are stable for all nodal diameters and result in the total work to be stable for all nodal diameters. This is an excellent example of the problem of applying the P-K method to cyclic symmetry cases. For the backward traveling wave the work is stable for all cosine and sine modes. Therefore, the forward and backward traveling waves for all nodal diameters are judged to be stable.

In **Fig. 7** the work results have been converted to critical damping ratios, and again are predicted to be stable for all nodal diameters considered. This is in subjective agreement with the actual engine test that showed the blade to be stable. Damping values were not measured. A future publication will compare these damping values with those of full three-dimensional CFD flutter analysis.

The results in **Figs. 4** through **7** also display the error of the anti-node method. In this case the 2, 3, 4, 35, and 40 nodal diameter mode shapes are heavily dominated by the sine mode. In other words, the sine mode is essentially the anti-node mode. From **Fig. 4** the antinode method predicts that the actual reduced frequency is lower than the critical value (unstable) for the 2 and 3 nodal diameter modes. Whereas **Figs. 5** through **7** show that these modes are stable for both forward and backward traveling waves. The primary reason for this error is the assumption in the tie-dye plot that all nodal diameters are possible. Also, note that for these nodal diameters we know that the off-diagonal terms are small because the cosine mode has low relative amplitude.

In this particular example the blade design is judged to be stable. However, the aerodynamic damping of the 35 and 40 nodal diameter forward traveling wave is very small (0.05%). Therefore, a detailed flutter analysis is recommended for at least one of these cases.

## Summary and Conclusions

Application of the traditional Panovsky-Kielb preliminary design analysis method for LPT blades with tip shrouds has been found to be overly conservative. This paper presents an extension to this method that considers the cyclic symmetry mode shapes. As demonstrated in the example problem this new cyclic symmetry method eliminates this conservatism, but does not require any additional input information or CFD analysis. Future work will include the off-diagonal terms in the work matrix and compare the predicted damping with that of full three-dimensional CFD flutter analysis.

## Acknowledgments

The authors wish to acknowledge GE Aircraft Engines for financial support and for the permission to publish this work.

## Nomenclature

$E_{\max}$ = maximum kinetic energy
$N_b$ = number of blades
$V$ = exit relative velocity
$W$ = work per cycle
$a$ = rigid-body displacement vector
$b_l$ = baseline work matrix for $l$ nodal diameters
$c$ = blade chord
$h_\xi$ = rigid-body displacement in $\xi$-direction
$h_\eta$ = rigid-body displacement in $\eta$-direction
$k=\omega c/(2V)$ = reduced velocity
$k_c$ = critical reduced velocity
$l$ = number of nodal diameters
$w_{\xi\xi,\ldots}$ = baseline work terms
$w_{lc}$ = cosine mode work for $l$ nodal diameters
$w_{ls}$ = sine mode work for $l$ nodal diameters
$w_{l,\mathrm{comb}}$ = combined mode work for $l$ nodal diameters
$\alpha$ = angle of pitching about leading edge
$\beta_l$ = interblade phase angle
$\xi$ = distance along blade chord
$\eta$ = distance normal to blade chord
$\zeta$ = critical damping ratio
$\omega$ = vibration frequency

## References

[1] Panovsky, J., and Kielb, R. E., 1998, "A Design Method to Prevent Low Pressure Turbine Blade Flutter," ASME Paper No. 98-GT-575.
[2] Tchernycheva, O. V., Fransson, T. H., Kielb, R. E., and Barter, J., 2001, "Comparative Analysis of Blade Mode Shape Influence on Flutter of Two-Dimensional Turbine Blades," ISABE-2001-1243, XV ISOABE Conference, Sept. 2–7, Bangalore, India.

**P. Cinnella**
Dipartimento di Ingegneria dell'Innovazione,
Universita di Lece,
Via Monteroni,
73100 Lecce, Italy
e-mail: paola.cinnella@unile.it

**P. De Palma**
e-mail: depalma@poliba.it

**G. Pascazio**
e-mail: pascazio@poliba.it

**M. Napolitano**
e-mail: napolita@poliba.it

Dipartimento di Ingegneria Meccanica e
Gestionale and Centro di Eccellenza in
Meccanica Computazionale,
Politecnico di Bari,
via Re David 200,
70125 Bari, Italy

# A Numerical Method for Turbomachinery Aeroelasticity

*This work provides an accurate and efficient numerical method for turbomachinery flutter. The unsteady Euler or Reynolds-averaged Navier-Stokes equations are solved in integral form, the blade passages being discretised using a background fixed C-grid and a body-fitted C-grid moving with the blade. In the overlapping region data are exchanged between the two grids at every time step, using bilinear interpolation. The method employs Roe's second-order-accurate flux difference splitting scheme for the inviscid fluxes, a standard second-order discretisation of the viscous terms, and a three-level backward difference formula for the time derivatives. The dual-time-stepping technique is used to evaluate the nonlinear residual at each time step. The state-of-the-art second-order accuracy of unsteady transonic flow solvers is thus carried over to flutter computations. The code is proven to be accurate and efficient by computing the 4th Aeroelastic Standard Configuration, namely, the subsonic flow through a turbine cascade with flutter instability in the first bending mode, where viscous effect are found practically negligible. Then, for the very severe 11th Aeroelastic Standard Configuration, namely, transonic flow through a turbine cascade at off-design conditions, benchmark solutions are provided for various values of the inter-blade phase angle.* [DOI: 10.1115/1.1738122]

## Introduction

In modern turbomachinery design and development, it is crucial to predict the blade vibratory stresses arising from self-excitation or inlet flow distortion. This is particularly true for aircraft compressor and fan blade rows, that may work at highly loaded off-design conditions, but also for the last stages of steam and gas turbines. The prediction of the unsteady pressure loads on the blading may involve the computation of shock waves, shock/boundary layer interaction and boundary layer separation, which could not be accounted for in early approaches based on potential methods, see e.g., [1]. Therefore, time-linearized methods have become very popular for turbomachinery aeroelastic computations, since they take into account such strongly nonlinear phenomena, at least for the steady flow field, see, e.g., [2,3]. However, these methods, which are very reliable when the blade vibrations add only a small disturbance to the steady flow, are clearly inadequate when studying the fluid/structure interaction and the blade displacements are not known a priori. In order to remove this limitation, a time-accurate solver of the Euler, thin layer, or complete Reynolds-averaged Navier-Stokes (RANS) equations is to be used, depending on the nature of the phenomena of interest. Recently, several researchers have developed and applied numerical methods for solving such equations, using different spacial and time discretisations, see, e.g., [4–8]. However, none of them employs all state-of-the-art features of current unsteady compressible flow solvers. In this paper, a second-order-accurate state-of-the-art RANS solver is extended to flutter computations to provide a significant accuracy improvement over existing codes when strongly nonlinear phenomena are present in the flow field. Moreover, the proposed approach, using a dual-time-stepping technique, is very apt to ultimately solve the full system of aeroelastic equations for both fluid and solid. It is noteworthy that the code can solve the Euler and the thin-layer RANS equations, by simply switching off the appropriate terms. However, only the full RANS equations are considered for the present viscous computations, insofar as they provide a more complete description of the flow, with a minimal additional cost.

The proposed method is applied to compute two aeroelastic test cases, for which detailed experimental data are provided by Bölcs and Fransson [4] and Fransson et al. [9], respectively (details about the experimental setup together with the electronic files containing the experimental data are available at: http://www.egi.kth.se). The first test case is the 4th Aeroelastic Standard Configuration, i.e., the subsonic flow through a turbine cascade with flutter instability in the first bending mode, where no separation occurs and the pressure loads are well predicted by the Euler equations. The second test case is the very severe 11th Aeroelastic Standard Configuration, i.e., a transonic off-design flow through a turbine cascade, where both leading-edge separation and shock/boundary layer interaction are present. For both test cases, the experimental data and the numerical solutions available to date are not in good agreement, so that the present thorough numerical investigation is warranted to validate the experimental data and to provide benchmark numerical solutions.

## Governing Equations

The two-dimensional unsteady RANS equations for compressible flow are written for a moving control volume $\Omega(t)$ with boundary $\Gamma(t)$, as

$$\frac{d}{dt}\int_{\Omega(t)} w d\Omega + \oint_{\Gamma(t)} (\mathbf{f}^e - \mathbf{f}^v - w\mathbf{s})\cdot\mathbf{n} d\Gamma = 0. \tag{1}$$

In Eq. (1), $w$ is the conservative variable vector based on the components of the absolute velocity vector in the fixed reference frame, $\mathbf{s}$ is the speed of the surface $\Gamma(t)$, $\mathbf{n}$ is the outer normal to $\Gamma(t)$, and $\mathbf{f}^e$ and $\mathbf{f}^v$ are the inviscid and viscous fluxes, given in Cartesian coordinates as

$$f_x^e = \begin{pmatrix} \rho u \\ p+\rho u^2 \\ \rho uv \\ \rho uH \end{pmatrix}, \quad f_y^e = \begin{pmatrix} \rho v \\ \rho uv \\ p+\rho v^2 \\ \rho vH \end{pmatrix}, \tag{2}$$

Contributed by the International Gas Turbine Institute (IGTI) of THE AMERICAN SOCIETY OF MECHANICAL ENGINEERS for publication in the ASME JOURNAL OF TURBOMACHINERY. Paper presented at the International Gas Turbine and Aeroengine Congress and Exhibition, Amsterdam, The Netherlands, June 3–6, 2002; Paper No. 2002-GT-30321. Manuscript received by IGTI, December 2001, final revision, March 2002. Associate Editor: E. Benvenuti.

  

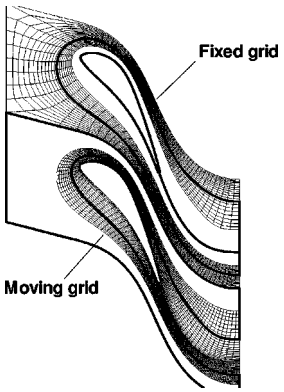


**Fig. 1 Moving grid strategy and boundary conditions**

$$f_x^v = \begin{pmatrix} 0 \\ \tau_{xx} \\ \tau_{xy} \\ b_x \end{pmatrix}, \quad f_y^v = \begin{pmatrix} 0 \\ \tau_{yx} \\ \tau_{yy} \\ b_y \end{pmatrix}, \tag{3}$$

where

$$\tau_{xx} = \mu[2\partial u/\partial x - (2/3)(\partial u/\partial x + \partial v/\partial y)],$$

$$\tau_{xy} = \tau_{yx} = \mu[\partial u/\partial y + \partial v/\partial x],$$

$$\tau_{yy} = \mu[2\partial v/\partial y - (2/3)(\partial u/\partial x + \partial v/\partial y)],$$

$$b_x = u\tau_{xx} + v\tau_{xy} + k\partial T/\partial x,$$

$$b_y = u\tau_{yx} + v\tau_{yy} + k\partial T/\partial y.$$

The above formulation can treat both fixed and moving grid blocks covering the computational domain. The viscous flux also contains the contribution of turbulent stresses, evaluated using either the Baldwin-Lomax [10] algebraic model or the Spalart-Allmaras [11] one-equation model:

$$\frac{\partial \tilde{\nu}}{\partial t} = -\mathbf{u}\cdot\nabla\tilde{\nu} + c_{b1}S\tilde{\nu} + \frac{1}{\sigma\,\mathrm{Re}}[\nabla\cdot((\nu+\tilde{\nu})\nabla\tilde{\nu}) + c_{b2}(\nabla\tilde{\nu})^2] - \frac{1}{\mathrm{Re}}\left[c_{w1}f_w - \frac{c_{b1}}{k^2}f_{t2}\right]\left[\frac{\tilde{\nu}}{d}\right]^2, \tag{4}$$

where $\tilde{\nu}$ is the modified kinematic eddy viscosity coefficient and the right-hand-side terms represent convection, production, diffusion, and destruction, respectively, see [11], for details.

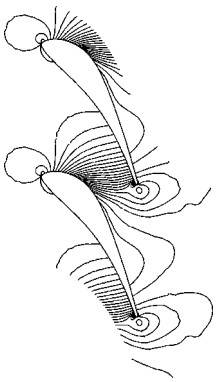

**Fig. 2 4th Standard Configuration, steady solution. Pressure coefficient contours ($\Delta C_p = 0.05$).**

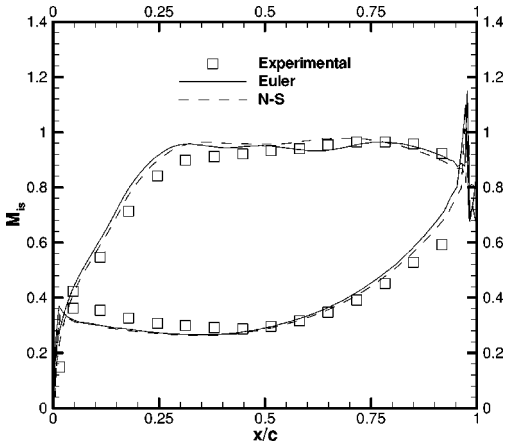


**Fig. 3 4th Standard Configuration, steady solution. Isentropic Mach number distributions at the wall**

## Numerical Method

The system of conservation laws (1) and (4) is discretised using a cell-centered finite volume method for structured multiblock grids. Equations (1) and (4) are written for each cell of the computational mesh, which can move with respect to a fixed reference frame. The convective fluxes at the cell interfaces are evaluated using Roe's approximate Riemann solver, [12], with a fully upwind unlimited second-order-accurate MUSCL extrapolation. The eigenvalues of Roe's matrix are corrected as in [13] to allow

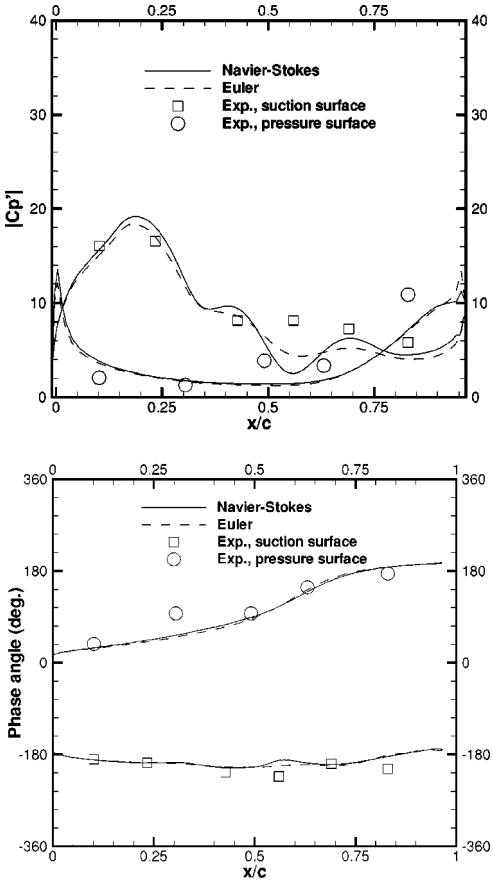


**Fig. 4 4th Standard Configuration. Amplitude (upper) and phase (lower) distributions of the pressure first harmonic, IBPA = −90 deg.**

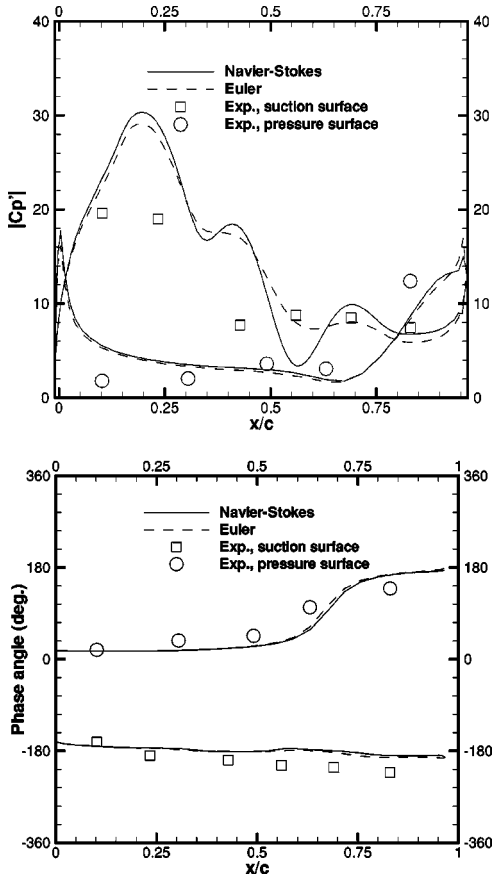


**Fig. 5 4th Standard Configuration. Amplitude (upper) and phase (lower) distributions of the pressure first harmonic, IBPA=180 deg.**

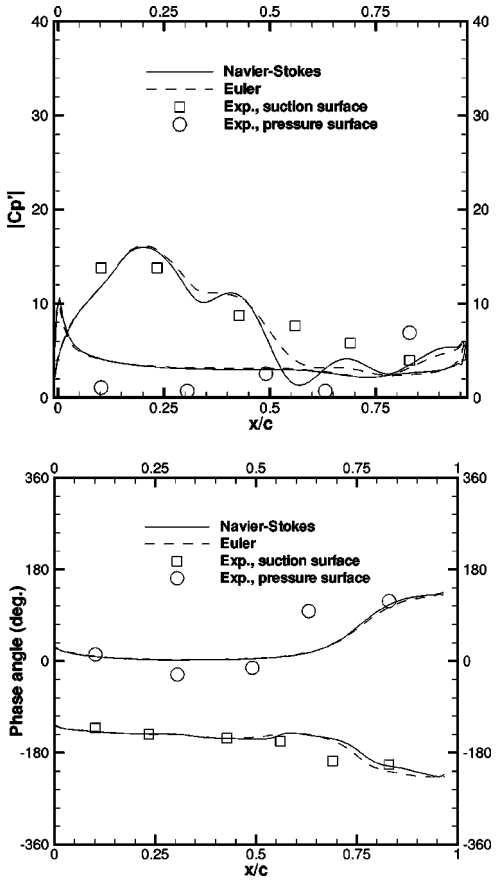


**Fig. 6 4th Standard Configuration. Amplitude (upper) and phase (lower) distributions of the pressure first harmonic, IBPA=90 deg.**

enough dissipation at the sonic points. A standard centered second-order-accurate approximation is used for the viscous fluxes.

For steady flows, the solution is marched in time using the four-stage Runge-Kutta scheme proposed by Jameson et al. [14]. Local time stepping, implicit residual smoothing, and multigrid, [15], are used to speed up the convergence. The turbulence-closure equation (4), when employed, is solved at every local iteration after Eq. (1). For unsteady flow computations, the time derivative is discretised using a three-level second-order-accurate backward difference scheme and the dual time stepping technique, [16], is used to advance the solution in time. Such a strategy guarantees the nonlinear coupling of Eq. (1) and (4) at every physical time level; moreover, within a general procedure for aeroelastic computations, it would simplify the implicit coupling of the flow and structural solvers with respect to approximate factorization schemes, [6,8].

For turbomachinery flutter calculations, two main difficulties arise: the blade is moving with respect to the flow net and each blade may vibrate with a constant phase difference, called inter-blade phase angle (IBPA). In this work such difficulties are overcome as follows. Each blade passage is covered with a background fixed C-grid, which allows to easily impose the inlet, outlet, and inter-passage conditions, and a body-fitted moving C-grid, with an overlapping region, as shown in **Fig. 1**, inter-block boundary conditions being imposed by bilinear interpolation of the variables at the overlapping boundaries; a similar procedure has been employed in [17]. A multipassage computational domain is employed, using a number of blade passages, $n_p (n_p > 1)$, given as

$$n_p = \frac{360° z}{|\mathrm{IBPA}|}, \quad \mathrm{IBPA} \neq 0,$$

where $z$ is the minimum integer which leads to an integer value for $n_p$. Such an approach is more general than the *direct store* method proposed in [18], used to employ a single passage also for IBPA$\neq 0$, insofar as it allows to compute mistuned oscillating cascades.

## Results

**4th Standard Configuration.** The experimental data for the 4th Standard Configuration refer to an annular turbine cascade in which the blades are sinusoidally oscillated in the first bending mode. The same oscillation amplitude and frequency are imposed for all blades, whereas several IBPAs are considered, [4]. The flow is subsonic, with isentropic exit Mach number equal to 0.9, and the inlet flow is inclined 45 deg downward with respect to the axial direction. The Reynolds number, based on the chord length and the inlet conditions, is equal to $8.2 \times 10^5$. C-grids with $256 \times 32$ and $384 \times 48$ cells have been used to compute the inviscid and viscous steady solutions, respectively. These meshes have been selected after an appropriate mesh-refinement study, which is not reported for brevity. For the viscous flow computation the average value of $\eta^+$ for the first cell near the wall equals 5. **Figure 2** provides the pressure coefficient contours for the inviscid computation. In **Fig. 3** the experimental isentropic Mach number distribution at the wall is compared with the numerical results obtained by solving the Euler equations and the RANS equations closed by the Baldwin-Lomax turbulence model. The agreement with the experimental data is good, considering that no attempt is

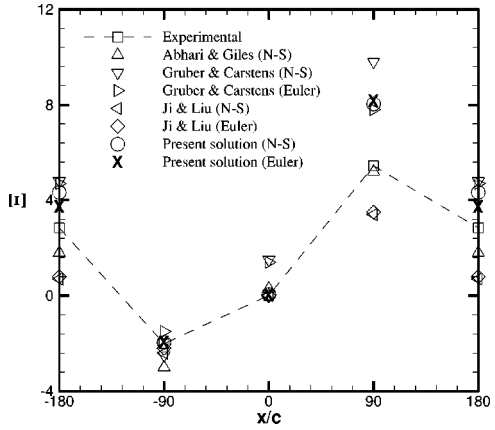


**Fig. 7 Aerodynamic damping coefficient (Ξ) versus IBPA for the 4th Standard Configuration**

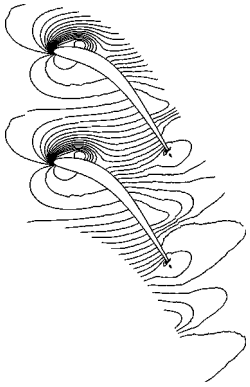

**Fig. 8 11th Standard Configuration, steady solution. Pressure coefficient contours ($\Delta C_p = 0.075$).**

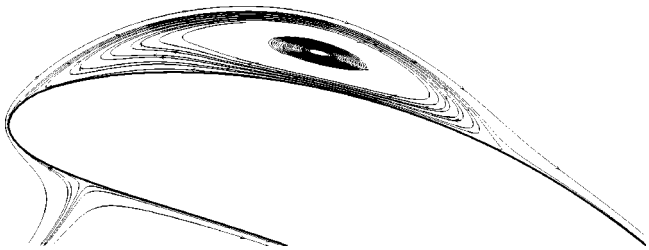

**Fig. 9 11th Standard Configuration, steady solution. Streamlines at the leading edge.**

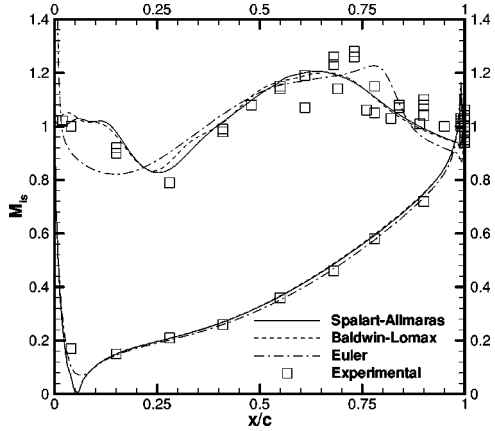


**Fig. 10 11th Standard Configuration, steady solution. Isentropic Mach number distributions at the wall.**

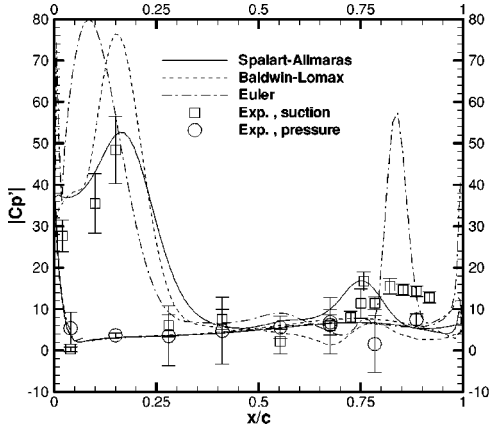


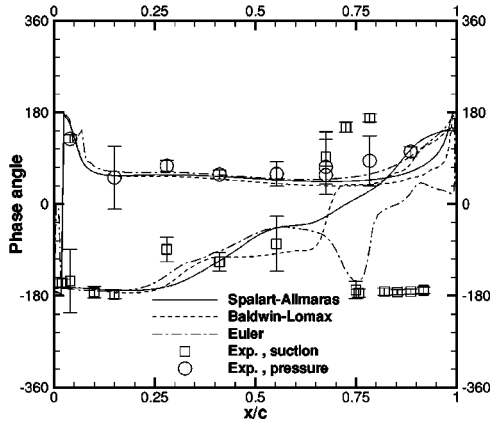


**Fig. 11 11th Standard Configuration. Amplitude (upper) and phase (lower) distribution of the pressure first harmonic, IBPA = 180 deg.**

made to take into account the varying thickness of the streamtubes (quasi-three-dimensional approximation). The results also compare well with those provided in [5–7]. The influence of viscous effects is quite small. The steady solution is used as the initial condition for the unsteady computations. For the inviscid computations, each blade passage has been discretised using an inner block with 256×20 cells and an outer block with 128×20 cells. For turbulent flow computations, the two blocks have 384×40 cells and 256×14 cells, respectively. The oscillation amplitude, *h*, is equal to 0.33% of the chord length and the reduced frequency, *k*, based on the half-chord length and the outlet flow conditions, is equal to 0.107. The bending direction is 60 deg with respect to the chord. Eighty physical time-steps have been used to compute each cycle, the corresponding $\Delta t$ providing grid convergence in time. **Figure 4–6** show the normalized amplitude and the phase of the first harmonic of the pressure time history for three values of the IBPA. The solutions agree reasonably well with the experimental data, and indicate that viscous effects have some influence only on the suction surface amplitude. The numerical results provided in [5–7], not reported in the figures, are fairly spread out, so that the present RANS solutions are considered to date's benchmark for the present test case. This is confirmed by the results of **Fig. 7**, which provides computed and experimental damping coefficients versus the inter-blade phase angle. The present results are the closest to the experimental ones and confirm them, e.g., the instability at IBPA = −90 deg, except for IBPA equal to 90 deg. Nonetheless, the good agreement between the present Euler and RANS results may suggest that the experimental data are the inaccurate ones for such a case.

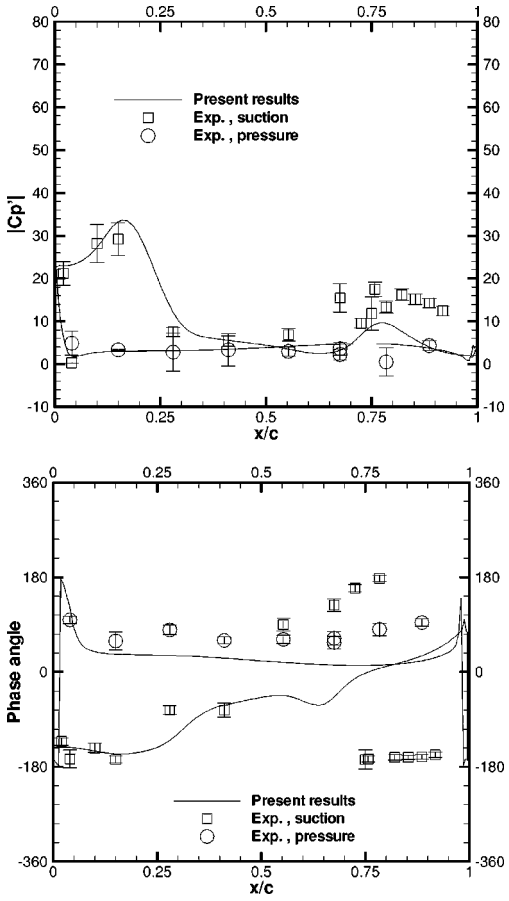


**Fig. 12 11th Standard Configuration. Amplitude (upper) and phase (lower) distributions of the pressure first harmonic, IBPA=108 deg.**

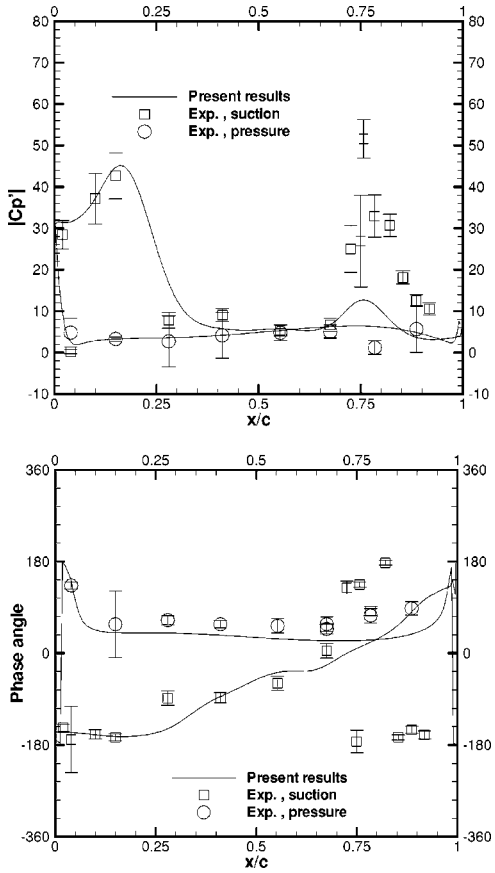


**Fig. 13 11th Standard Configuration. Amplitude (upper) and phase (lower) distributions of the pressure first harmonic, IBPA=144 deg.**

**11th Standard Configuration.** The very severe 11th Standard Configuration is a transonic flow through a turbine cascade at off-design conditions. The isentropic exit Mach number is equal to 0.99 and the inlet flow is inclined 34 deg upward with respect to the axial direction. The Reynolds number, based on the chord length and inlet conditions, is equal to $1.2\times10^6$. For such flow conditions, the stagnation point is located at about 6% of the chord on the pressure surface of the blade. The flow strongly accelerates around the sharp leading edge forming a tiny supersonic region. The flow then separates on the suction side of the blade from the leading edge to 30% of the chord. After reattachment, the flow accelerates again to supersonic speed and a shock occurs at about 75% of the chord. Steady inviscid and viscous computations have been performed using grids with $288\times32$ and $288\times48$ cells, respectively. For the viscous flow computation the average value of $\eta^+$ for the first cell near the wall equals 1. For the unsteady computations, the moving and fixed blocks are always composed of $288\times20$ and $144\times20$ cells, respectively. **Figure 8** provides the pressure coefficient contours for the steady viscous computation, whereas the streamlines at the leading-edge separation region are shown in **Fig. 9**. In **Fig. 10**, the steady isentropic Mach number distributions obtained by solving the Euler equations and the RANS equations closed by the Baldwin-Lomax and the Spalart-Allmaras turbulence models are compared with the experimental data. The inviscid solution is very far from the experiments in the front part of the suction side, due to separation. The viscous solution is in good agreement with the experimental data, especially when the Spalart-Allmaras model is employed. For the unsteady case, the blades oscillate in the first bending mode, with bending angle equal to 90 deg with respect to the chord direction, oscillation amplitude equal to 0.0035 *c*, and a reduced frequency, based on the half-chord length and the outlet conditions, equal to 0.1545. Also for this case, grid convergence in time is achieved using 80 physical time-steps per period. Experimental data are available for ten equally spaced values of the IBPA, from 36 deg to 360 deg [9], whereas numerical results are provided by Fransson et al. [9], Sbardella and Imregun [3], and Campobasso and Giles [19] only for IBPA=180 deg. First, for such a well-documented case, the present calculations of the amplitude and the phase distribution of the first harmonic of the pressure time history are given in **Fig. 11**, together with the experimental results. It appears that the present Euler and Baldwin-Lomax RANS computations are clearly inadequate, which is well known to happen in the presence of a large separation bubble (see **Fig. 9**). On the other hand, the results obtained using the RANS equations with the Spalart-Allmaras turbulence model compare reasonably well with the experimental data, except in the rear part of the suction side. Furthermore, the experimental results cannot be considered very reliable, insofar as, for some values of the IBPA their 95% confidence interval is about half of the mean value. And in fact, the experimental data for the aerodynamic damping, given in [9], show large differences for similar flow conditions, due to local changes on the blade surface in the shock region, which result in a large influence on the aerodynamic damping because of the discrete integration points. For such a reason, Fransson et al. [9] recommend to consider only the experimental local pressure values for comparing the numerical results. Therefore, although one cannot be certain that the Spalart-Allmaras turbulence model is fully adequate for the flow under consideration, the present code remains a state-of-the-art tool for validating numerical as well as experimental results. At this purpose the present Navier-Stokes code has been used to provide

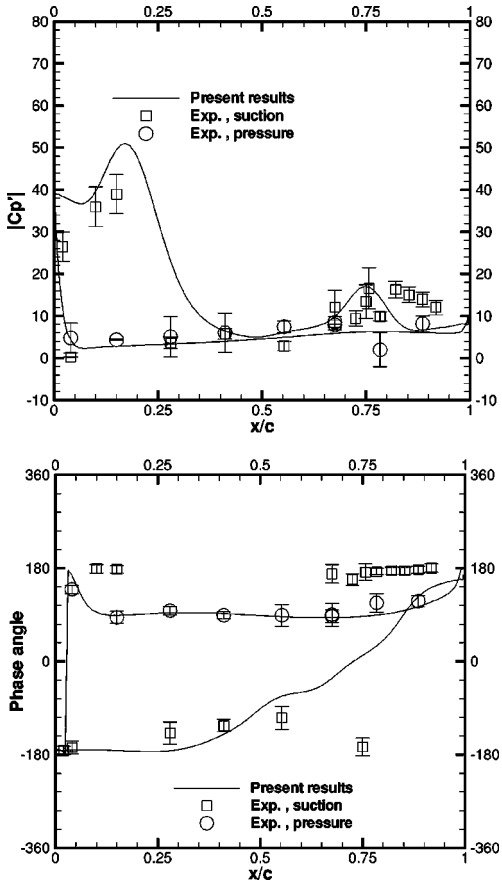


**Fig. 14 11th Standard Configuration. Amplitude (upper) and phase (lower) distributions of the pressure first harmonic, IBPA=216 deg.**

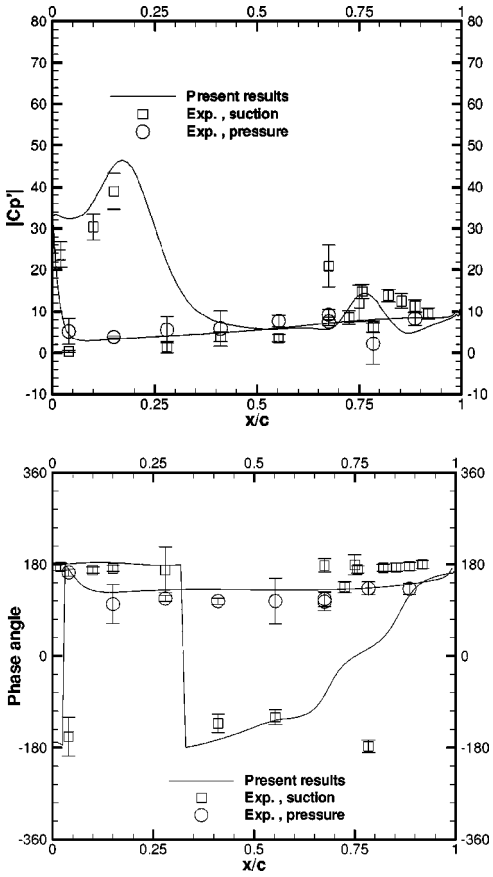


**Fig. 15 11th Standard Configuration. Amplitude (upper) and phase (lower) distributions of the pressure first harmonic, IBPA=252 deg.**

*benchmark solutions* for the following values of IBPA: 108 deg, 144 deg, 216 deg, and 252 deg, in addition to the 180 deg case, for which the experimental data are less unreliable. Such results are given in **Fig. 12**, **13**, **14**, and **15**, together with the experimental data. Once again, a quite nice agreement with the experimental data is found, the numerical solution being always located within the experimental error bars, except for the phase distribution at the rear part of the suction side. This behavior has been also observed in the other numerical results available in the literature. The discrepancies could be due to the turbulence model inadequacy to accurately predict the shock/boundary layer interaction but, just as likely, to the inaccuracy of the experimental data. For completeness, the results for the aerodynamic damping coefficient are presented in **Fig. 16**. According to the present Spalart-Allmaras RANS solutions, the configuration is stable for almost all considered IBPAs, is marginally stable (aerodynamic damping close to zero) for IBPA=315 deg, and is unstable for IBPA=324 deg and IBPA=337.5 deg.

## Conclusions

A numerical method has been developed for solving the compressible Euler and Reynolds averaged Navier-Stokes (RANS) equations for flows through two-dimensional oscillating cascades. The method has been used to solve the well-documented 4th Standard Aeroelastic Configuration, namely, the subsonic flow through a turbine cascade with flutter instability in the first bending mode, where the very good agreement between the present Euler and RANS solutions and the experimental data demonstrates their benchmark accuracy. Then, the very severe 11th Aeroelastic Standard Configuration, i.e., a transonic off-design flow through a turbine cascade, has been considered. For such a problem, only the RANS equations with the Spalart-Allmaras turbulence model compare reasonably well with the experimental data. In particular, the amplitude and phase of the pressure first harmonic at the blade surface, computed for several values of the inter-blade phase angle (IBPA), lay almost everywhere within the experimental error bars, except in the rear part of the suction side, where a moving shock-wave impinges on the boundary layer. In this region, the use of a linear turbulence model for computing the shock/boundary layer interaction can be inappropriate; on the other hand, experimental data are affected by considerable uncertainties.

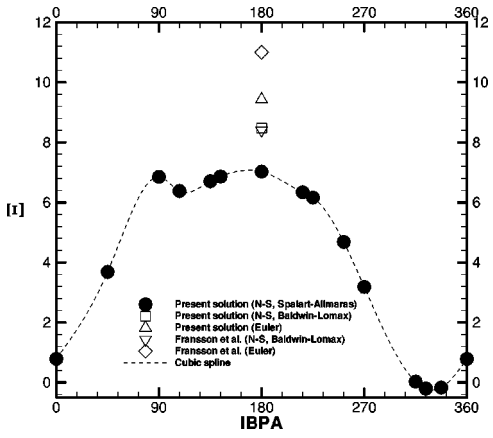


**Fig. 16 Aerodynamic damping coefficient (Ξ) versus IBPA for the 11th Standard Configuration**

In order to complete the experimental data set, the damping coefficient was computed for several values of the IBPAs, providing benchmark data to be used for code validation. The electronic files with the results of the 11th Aeroelastic Standard Configuration are available at http://cemec.poliba.it/cfd4.htm.


## Acknowledgments

This research has been supported by CofinLab2000 and Cofin2001.


## Nomenclature

$c$ = chord length
$C_p$ = $p-p_1/p_{t1}-p_1$=pressure coefficient
$C_p'$ = amplitude of the first harmonic of the pressure coefficient normalized with respect to the vibration amplitude
$f$ = vibration frequency
$\mathbf{f}^e$ = inviscid flux vector
$\mathbf{f}^v$ = viscous flux vector
IBPA = inter-blade phase angle
$h$ = ratio of the bending amplitude to the chord length
$H$ = specific total enthalpy
$k$ = $2\pi fc/2v_2$=reduced frequency
$k$ = thermal conductivity
M = Mach number
$\mathbf{n}$ = instantaneous outer normal to a cell
$p$ = pressure
$\mathbf{s}$ = control surface velocity
Re = Reynolds number
$t$ = time
$T$ = temperature
$\mathbf{u}$ = velocity vector
$u,v$ = velocity components
$x, y$ = Cartesian coordinates
$w$ = conservative variable vector
$\Gamma$ = control surface
$\eta^+$ = characteristic wall coordinate
$\mu$ = dynamic viscosity
$\nu$ = kinematic viscosity
$\Xi$ = aerodynamic damping
$\rho$ = density
$\tau_{ij}$ = stress tensor component
$\phi$ = phase of the first harmonic of the pressure coefficient
$\Omega$ = control volume

### Subscripts

1 = inlet
2 = outlet
*is* = isentropic
$t$ = stagnation condition
$x, y$ = Cartesian components

## References


[1] Whitehead, D. S., and Newton, S. G., 1985, "A Finite Element Solution of Unsteady Two-Dimensional Transonic Flows in Cascades," Int. J. Numer. Methods Fluids, **5**, pp. 115–132.
[2] Hall, K. C., 1999, "Linearized Unsteady Aerodynamics," VKI-LS 1999-05, von Karman Institute for Fluid Dynamics.
[3] Sbardella, M., and Imregun, M., 2001, "Linearized Unsteady Viscous Turbomachinery Flows Using Hybrid Grids," ASME J. Turbomach., **123**, pp. 568–582.
[4] Bölcs, A., and Fransson, T. H., 1986, "Aeroelasticity in Turbomachines—Comparison of Theoretical and Experimental Cascade Results," Communication du Laboratoire de Thermique Appliquée et de Turbomachines, No. 13, EPFL, Lausanne, Switzerland.
[5] Abhari, R. S., and Giles, M., 1997, "A Navier-Stokes Analysis of Airfoils in Oscillating Transonic Cascades for the Prediction of Aerodynamic Damping," ASME J. Turbomach., **119**, pp. 77–84.
[6] Grüber, B., and Carstens, V., 1998, "Computation of the Unsteady Transonic Flow in Harmonically Oscillating Turbine Cascades Taking Into Account Viscous Effects," ASME J. Turbomach., **120**, pp. 104–120.
[7] Ji, S., and Liu, F., 1999, "Flutter Computation of Turbomachinery Cascades Using a Parallel Unsteady Navier-Stokes Code," AIAA J., **37(3)**, pp. 320–327.
[8] Weber, S., and Platzer, M. F., 2000, "A Navier-Stokes Analysis of the Stall Flutter Characteristics of the Buffum Cascade," ASME J. Turbomach., **122**, pp. 769–776.
[9] Fransson, T. H., Jöker, M., Bölks, A., and Ott, P., 1999, "Viscous and Inviscid Linear/Nonlinear Calculations Versus Quasi 3D Experimental Cascade Data for a New Aeroelastic Turbine Standard Configuration," ASME J. Turbomach., **121**, pp. 717–725.
[10] Baldwin, B. S., and Lomax, H., 1978, "Thin Layer Approximation and Algebraic Model for Separated Turbulent Flows," AIAA Paper 78-257.
[11] Spalart, P. R., and Allmaras, S. R., 1992, "A One-Equation Model for Aerodynamic Flows," AIAA Paper 92-0439.
[12] Roe, P. L., 1981, "Approximate Riemann Solvers—Parameter Vectors and Difference Schemes," J. Comput. Phys., **43**, pp. 357–372.
[13] Harten, A., and Hyman, J. M., 1983, "Self Adjusting Grid Method for One-Dimensional Hyperbolic Conservation Laws," J. Comput. Phys., **50**, pp. 235–269.
[14] Jameson, A., Schmidt, W., and Turkel, E., 1981, "Numerical Solutions of the Euler Equations by Finite Volume Methods Using Runge-Kutta Time Stepping," AIAA Paper 81-1259.
[15] Jameson, A., and Baker, T., 1983, "Solution of the Euler Equations for Complex Configurations," AIAA Paper No. 83-1929.
[16] Jameson, A., 1991, "Time-Dependent Calculations Using Multigrid, With Applications to Unsteady Flows Past Airfoils and Wings," AIAA Paper 91-1596.
[17] Tuncer, I. H., Weber, S., and Sanz, W., 1998, "Investigation of Periodic Boundary Conditions in Multi-Passage Cascade Flows Using Overset Grids," ASME J. Turbomach., **121**, pp. 341–347.
[18] Erdos, J. I., and Alzner, E., 1977, "Numerical Solution of Periodic Transonic Flow Through a Fan Stage," AIAA J., **15**, pp. 1559–1568.
[19] Campobasso, M. S., and Giles, M. B., 2003, "Effects of Flow Instabilities on the Linear Analysis of Turbomachinery Aeroelasticity," J. Propul. Power, **19(2)**, pp. 250–259.

# Study on Crack Propagation Tendencies of Non-Repaired and Repaired Nozzles

**Tomoharu Fujii**

**Takeshi Takahashi**

CRIEPI,
2-6-1 Nagasaka
Yokosuka,
Kanagawa 240-0196,
Japan

*A system designed to control and predict the length of cracks that generate in the first-stage nozzles of E and F class gas turbines was developed. This system consists of three programs for (1) inputting cracks, (2) displaying cracks, and (3) predicting cracks, and a database consisting of approximately 350,000 cracks generated in first-stage nozzles taken from past repair records of five power plants operating in Japan. The database also contains data on operating time and number of starts of gas turbines. The distinctive features of this system are described below. (1) The crack data can be entered on the nozzle drawing as a picture by using the mouse. (2) The accumulated data allows the sections of nozzles in which cracks have generated most frequently to be identified. (3) The correlation formula of cracks and operating time or number of starts can be obtained simply. (4) By entering the scheduled operating time or number of start-ups to the time of the next scheduled inspection in the correlation formula, the length of cracks in optional sections and propagating in optional directions can be predicted. Using this system, the statuses of cracks generated in non-repaired and repaired nozzles of E class gas turbines were compared. The comparison focused on 11 patterns with comparatively long cracks selected from the cracks propagating together with the increase in operating time or number of starts. The propagation of cracks covering a period of approximately two years, which corresponds to the inspection interval of power plants in Japan, was also compared. The results showed that the extent of crack propagation tends to increase with the increase in the number of repairs. Furthermore, the propagation of cracks in repair nozzles is about two times greater than that in non-repair nozzles. It was also found that the system could identify the sections in which the longest cracks are generated.* [DOI: 10.1115/1.1650378]

## Introduction

Because of its high efficiency and outstanding operability, the gas turbine combined cycle is being introduced into existing facilities and new plants. Since measures are also being developed to raise the temperature of the combustion gas, the parts installed in the hot gas path of gas turbines must be inspected, and repaired or replaced very frequently.

Since the first-stage nozzles of gas turbines are exposed to hot gases, many cracks are found during inspection. However, since the nozzle is a static part, nozzles with cracks found to be within certain criteria at inspection are kept in use as is. Cracks exceeding the criteria are weld-repaired to allow re-use. For this reason, accurate control or prediction of crack propagation will permit effective repairs and reduce maintenance and repair costs. However, since vanes are integral with the side walls to form a segment structure and since wall thickness differs by sections, the temperature and thermal stress distributions in the nozzle are complex. Therefore, in order to accurately grasp and analytically predict the status of crack propagation, very large facilities and high costs are necessary. Gas turbine makers and research organizations are therefore developing models for predicting crack propagation based on empirical models which themselves are based on actual crack data, [1–4].

Since 1997, the present authors have conducted studies on techniques to efficiently digitize nozzle crack-related data and highly accurate crack propagation prediction techniques in order to develop a system for predicting crack propagation in nozzles, [5].

Contributed by the International Gas Turbine Institute and presented at the International Gas Turbine and Aeroengine Congress and Exhibition, Atlanta, GA, June 16–19, 2003. Manuscript received by the IGTI Dec. 2002; final revision Mar. 2003. Paper No. 2003-GT-38351. Review Chair: H. R. Simmons.

## General Description of the System

The system is used for digitizing the vast amounts of crack data owned by power plants and operating records of gas turbines in order to construct databases. Based on such databases, the correlation of operating time or number of starts was analyzed to obtain a correlation formula. The operating time or the number of starts scheduled in the future is entered in the formula to predict the crack propagation. This method assumes that factors which depend on the operating time such as high-temperature creep or the factors which depend on the number of starts such as low-cycle fatigue are related to the propagation of cracks, [2,4]. The major functions of the system are described below.

## Function for Inputting Crack Data

Crack data are entered by using figures illustrating the outside and inside walls of nozzles, and two vanes, respectively, on the pressure side and suction side and divided into six sections. The crack input screen of the outside wall of the first-stage nozzles installed on the F class gas turbine is shown in **Fig. 1** as an example. Using this input screen, the positions of crack generation and end points can be pinpointed with the mouse. By entering only the length from the keyboard, the coordinates of crack generation and end point positions, direction of crack propagation, and length of cracks are automatically digitized. The operating time or number of starts of the gas turbine resulting from the propagation of cracks is entered on another screen and consolidated with the stored crack data.

This method has made it possible to construct a crack database for approximately 350,000 cracks of first-stage nozzles installed on E and F class gas turbines.

  

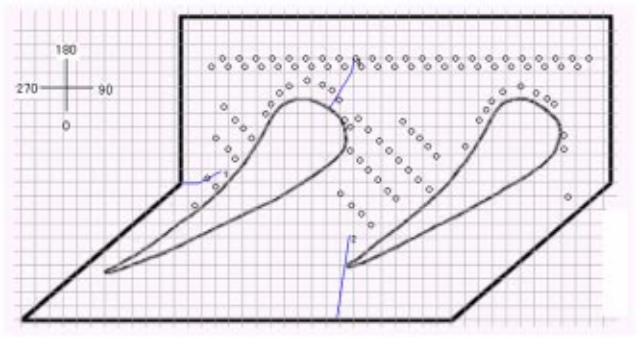


**Fig. 1 Example of crack input screen**

## Function for Displaying Crack Data

As shown in **Fig. 2**, the entered crack data can be displayed in one-segment units. In order to grasp the tendency of crack propagation in the same gas turbine, the crack data of nozzles installed in a gas turbine can be superposed and displayed on the same screen as shown in **Fig. 3**. This method permits the sections in which cracks are generated, direction of propagation, and frequency of generation to be qualitatively grasped.

## Function for Analyzing Crack Data

As shown in **Fig. 4**, as the first step before the targeted cracks can be selected for analysis, after blocking in the scope of positions of generated cracks with the mouse, the direction of propagation when viewed from the direction of gas flow must be entered. This method allows the patterns of cracks propagating in the optional direction in the optional sections to be analyzed. On selecting the crack patterns, two types of analyses can be performed as described below.

The first type is an analysis of the tendency of crack propagation based on average crack length. Due to fluctuations in the manufacture and distribution of combustor outlet gas temperature, the length of cracks generated in the same section of each nozzle is not always consistent, [1]. For this reason, the system calculates

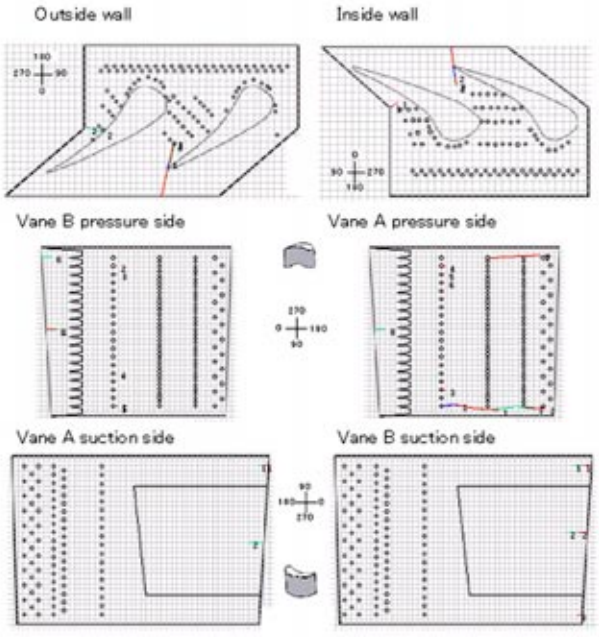


**Fig. 2 Example of crack display screen**

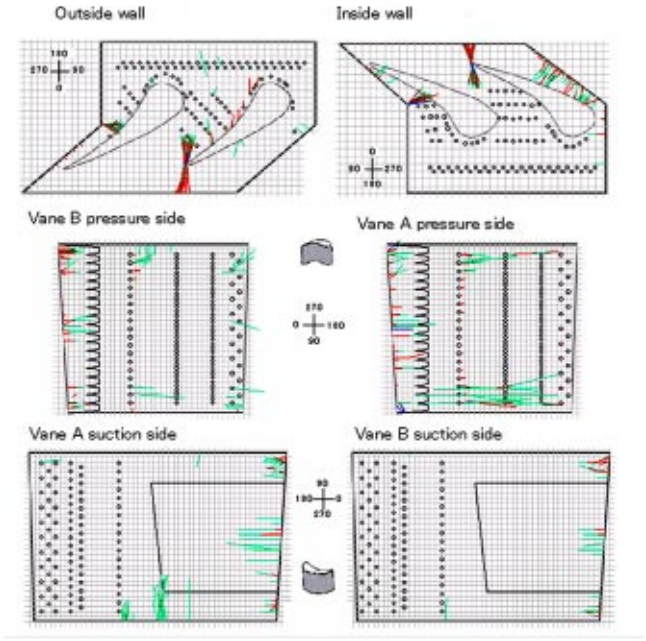


**Fig. 3 Example of crack display screen of a gas turbine**

the averaged crack length of a gas turbine from the crack patterns. Correlation analysis is carried out on the average crack length and operating time or number of starts of the gas turbine to obtain the correlation formula. The predicted average crack length is generated upon entering the operating time or number of starts scheduled in the future. Furthermore, the average rate of crack propagation can be calculated by calculating the amount of propagation per unit operating time or unit number of starts.

The second type is an analysis of the crack propagation tendency by maximum crack length. In this respect, the key point is the maximum length by crack patterns. The maximum crack length here is defined as the maximum crack length that has propagated according to a certain crack pattern during a certain period of time. In other words, if the scheduled inspection interval is two years, the maximum value of cracks actually measured every two years is set as the maximum length irrespective of the operating conditions of the gas turbine and cracks generated in whichever nozzles during that time. The maximum crack length is used to control and predict the maximum crack length by inspection frequency.

As a typical analysis of cracks using the functions just mentioned, the analytical results of crack data of a certain power plant are shown in **Fig. 5**. In the case of this crack pattern, the average

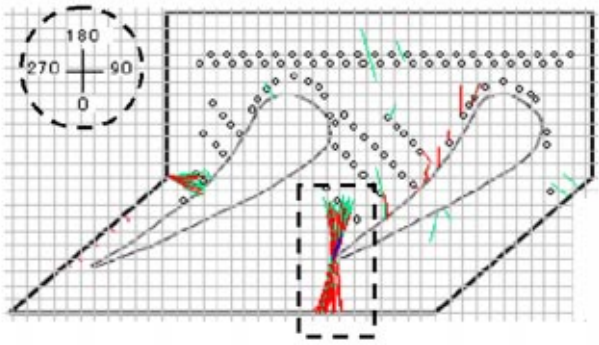


**Fig. 4 Selection method of crack pattern**

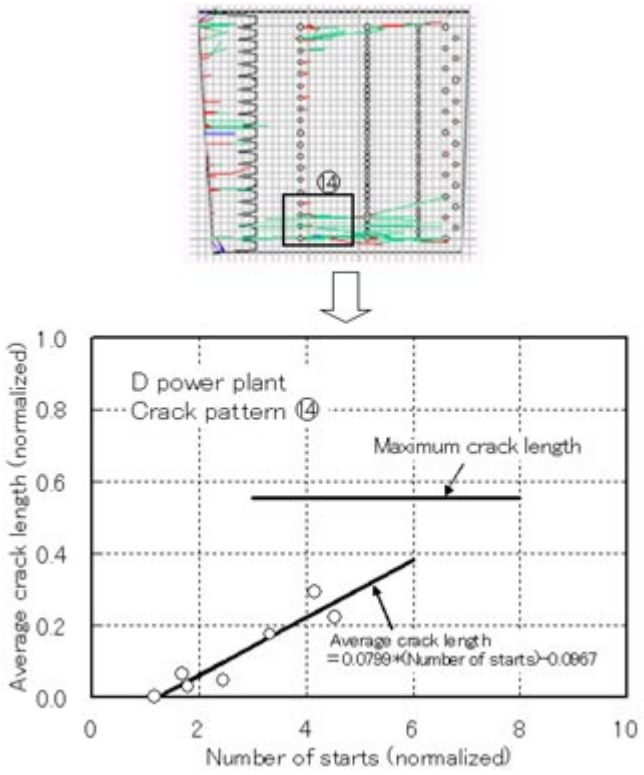


**Fig. 5 Example of crack propagation analysis**

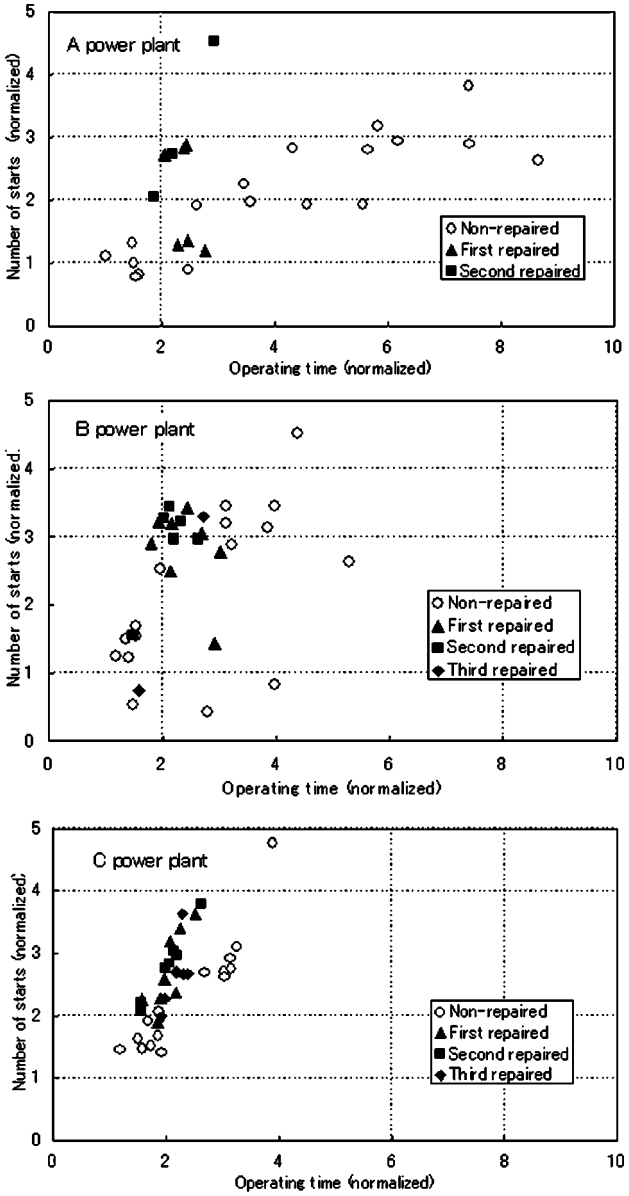


**Fig. 6 Operating conditions of gas turbines**

crack length indicates a high degree of correlation with the number of starts of the gas turbine and shows that propagation increases as the number of starts increase. The figure also shows the maximum crack length of the crack pattern under the operating conditions used for the analysis. The propagation of cracks generated in the pattern can be predicted by the correlation formulas and maximum crack values.

## Comparison of Crack Propagation Tendency of Non-Repaired and Repaired Nozzles

Since the nozzles are used by repairing them frequently, the system was used to analyze how the repair frequency affects the propagation of cracks. The first-stage nozzles installed on three E class gas turbines operating in Japan were analyzed.

The operation history of the three gas turbines selected for analysis is shown in **Fig. 6**. The vertical and horizontal axes were normalized with the annual average number of starts and operating time of all gas turbines selected for analysis. The open symbols indicate the operation history of gas turbines equipped with non-repaired nozzles, while the solid symbols indicate that of gas turbines equipped with repaired nozzles. In Japan, new nozzles installed on gas turbines are normally used up to the second or third scheduled inspection. Thereafter, the cracks are generally weld-repaired at each scheduled inspection. In this figure, the operating time and number of starts are accumulated for nozzles used continuously, but when the nozzles are repaired, that point in time is established as zero and the operating time and number of starts are accumulated afresh. In Japan, parts are generally controlled by assuming the nozzle segment of one gas turbine as a group, and the usage history is also controlled by groups. The nozzle group of power plant A is continuously used without repairs up to the time of the third inspection. Thereafter, the nozzles are repaired at each scheduled inspection. On the other hand, the nozzle groups of power plants B and C were continuously used without repairs up to the time of the second scheduled inspection. Thereafter, the nozzles were repaired at each scheduled inspection. The nozzles of respective power plants were inspected approximately every two years.

As an example of qualitative analytical results of crack propagation, cracks generated in a total of 18 segments of nozzle group B2 of power plant B were superposed. The results are shown in **Figs. 7** and **8**. The cracks are weld-repaired at each scheduled repair. Thereafter, the entire segment is heat-treated which produces a finish that is practically the same as that of a non-repaired nozzle. As a result, the increase in the number of repairs tends to increase the density of hair cracks, but it is assumed that the sections in which cracks are generated are approximately the same. The authors have already clarified the propagation of propagation-type cracks with the operating time or number of starts of E class gas turbines, [5]. The cracks of 11 patterns are comparatively long as shown in **Fig. 9**. Accordingly, the extent of the propagation of cracks of 11 patterns was compared.

## Analysis by Average Crack Length

The method of calculating crack propagation is shown in **Fig. 10**. Since the cracks of 11 patterns selected for analysis propagate

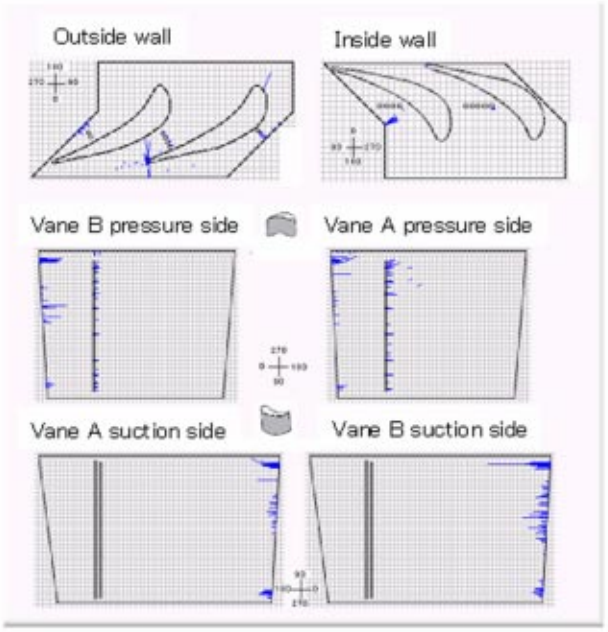


(a) Non-repaired nozzle (first use)

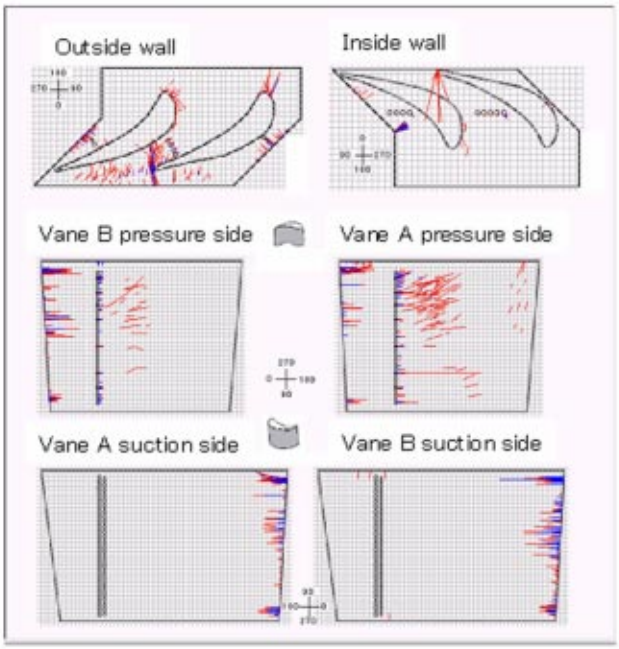


(b) Non-repaired nozzle (second use)

**Fig. 7 Crack propagation of non-repaired nozzle; (*a*) non-repaired nozzle (first use), (*b*) non-repaired nozzle (second use)**

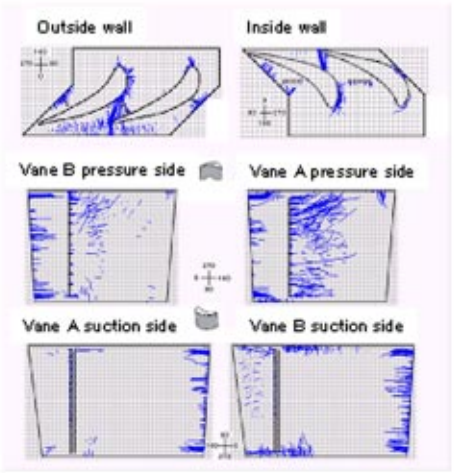


(a) First repaired

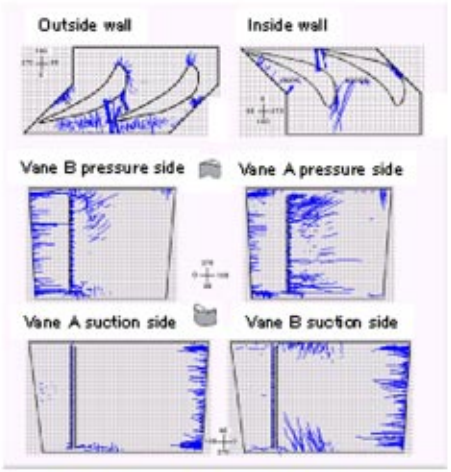


(b) Second repaired

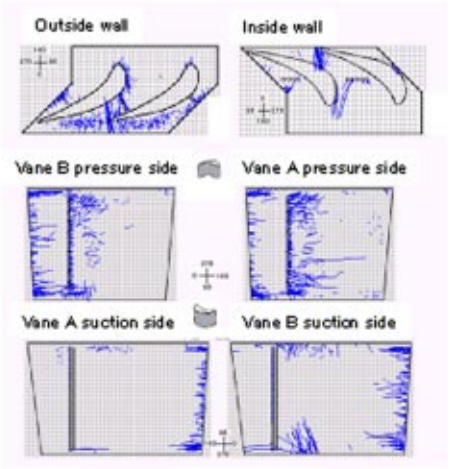


(c) Third repaired

**Fig. 8 Crack propagation of repaired nozzle**

together with the operating time or number of starts of gas turbines, two methods of calculating the propagating rate were devised: (1) using the operating time as the base and (2) using the number of starts as the base. Accordingly, the average propagation rates of the cracks of 11 patterns were calculated for each repair by using the average crack length of several nozzle groups. The average crack propagating rate was multiplied by the average operating time or the average number of starts between scheduled inspections of three power plants and compared with the value normalized by the maintenance criterion repair length of each crack pattern indicated in **Fig. 11**. This value corresponds to the crack length measured at the next scheduled inspection when new nozzles or repaired nozzles are installed on the gas turbine.

As an example, the calculated average crack length using the number of starts is compared in **Fig. 12**. The value of 1 on the

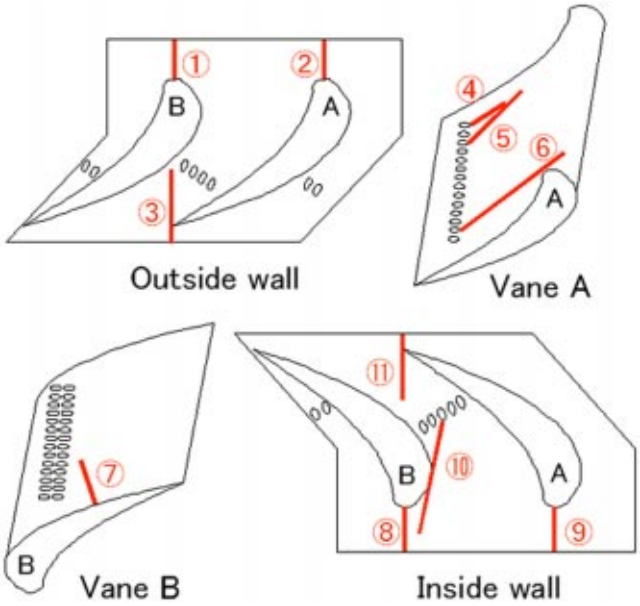


**Fig. 9 Typical crack pattern**

vertical axis corresponds to the maintenance criterion length. The results indicate that the calculated average crack length is approximately 20 to 30% of the maintenance criterion length in any of the crack patterns. When compared with the non-repaired nozzles, the extent of crack propagation of the repaired nozzles was larger.

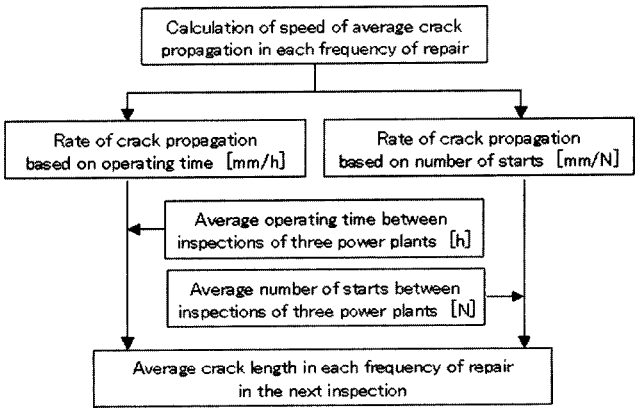


**Fig. 10 Calculation method of crack propagation**

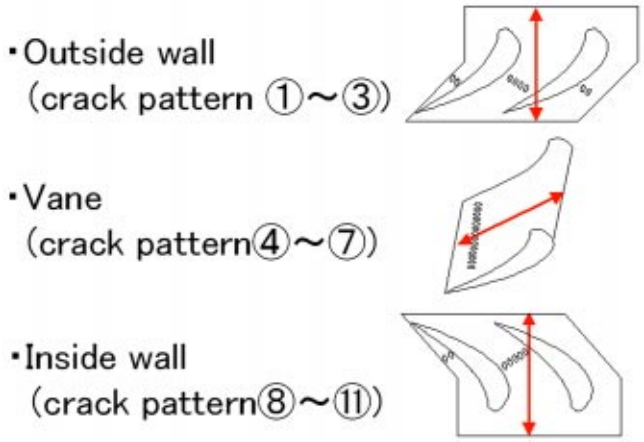


**Fig. 11 Maintenance criterion length**

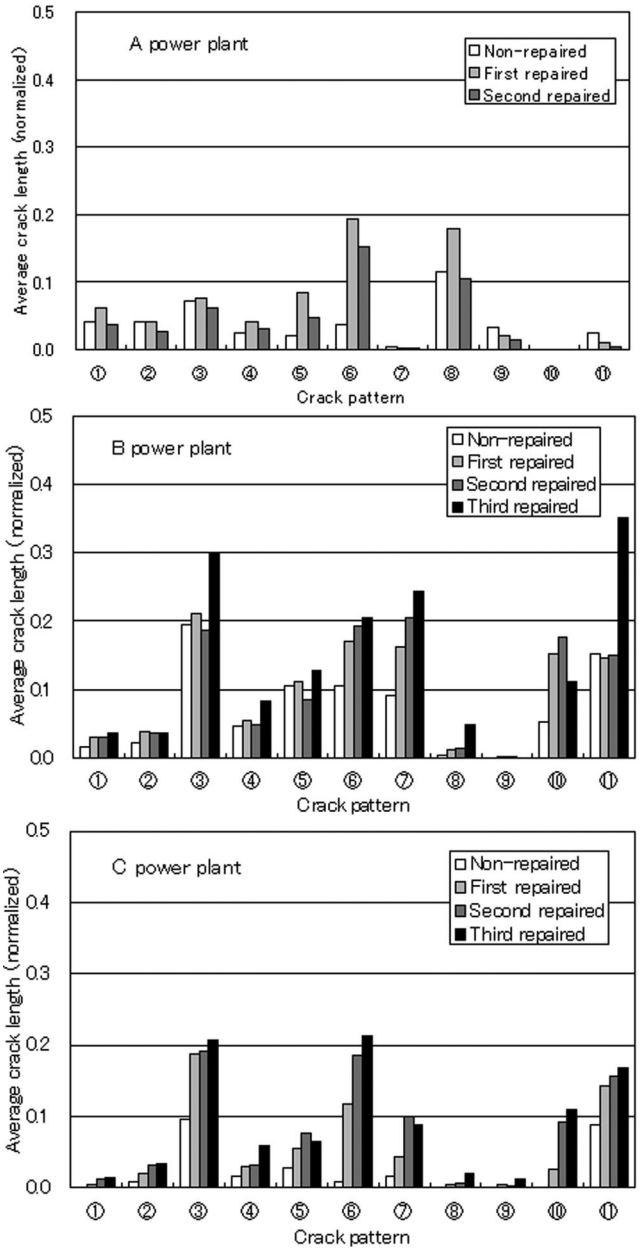


**Fig. 12 Comparison of average crack lengths**

When cracks with a maintenance criterion length of 10% or more were selected for analysis, the maximum extent of crack propagation was approximately 2.3 times greater. Therefore, it is considered that the non-repaired and repaired nozzles cannot be handled in the same manner from the standpoint of controlling the crack propagating tendency. Furthermore, it was found that the rate of crack propagation tends to rise as the repair frequency increases. The causes are considered to be: (1) high rate of crack propagation in weld sections as compared to the base metal, (2) heat treatment is carried out at each repair, but the material structure has failed to completely restore itself to the initial stage, and (3) since fine cracks cannot be completely repaired by the weld-repair method, the fine cracks connect together, thus increasing the rate of propagation as can be observed visually. In order to clarify the causes, it is necessary to perform in-depth material tests and analyze the material structure.

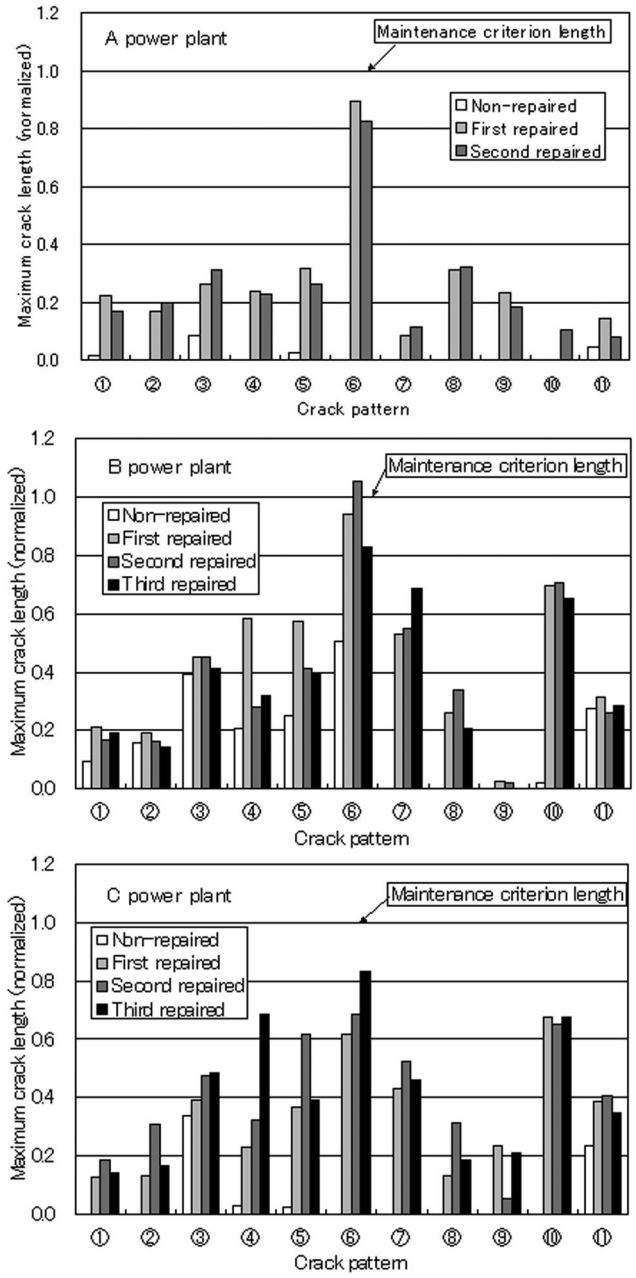


**Fig. 13 Comparison of maximum crack lengths**

## Analysis by Maximum Crack Length

The maximum crack length differs from the average crack length, and is determined without considering the operating time or number of starts of gas turbines. For this reason, comparisons were made on the basis of maximum crack length with nozzles used up to the time of the next scheduled inspection after installed on the gas turbine without considering the rate of crack propagation. The comparison of maximum crack length normalized with maintenance criterion length is shown in **Fig. 13**. The extent of propagation of repaired nozzles as compared to non-repaired nozzles is larger. When it is assumed that cracks have a length of more than 10% of the maintenance criterion length, the extent of crack propagation is 2.8 at maximum. The extent of crack propa gation of pattern 6 is the largest. Therefore, the cracks exceed the maintenance criterion length. Cracks other than those of pattern 6 are approximately 60 to 70% of the maintenance criterion length. Therefore, propagation of large cracks that exceeded the maintenance criterion length was not observed.

Although the extent of crack propagation is small, a close look at the maximum value of individual cracks reveals that the cracks of pattern 6 are the only ones that exceed the maintenance criterion length. Therefore, the repair work can be simplified provided the cracks of pattern 6 are repaired on a priority basis.

Furthermore, since the extent of crack propagation of non-repaired nozzles as compared to repaired nozzles is smaller, the nozzles can be continuously used over a long period of time. It is also possible to extend the scheduled inspection intervals.

## Conclusion

A Crack Propagation Prediction System to control and predict the length of cracks generated in the first-stage nozzles of E and F class gas turbines was developed. The system was used to compare the extent of the propagation of cracks generated in non-repaired and repaired nozzles. The results indicated the following:

(1) As compared to non-repaired nozzles, the extent of the propagation of average and maximum cracks in repaired nozzles was the largest. The propagation of cracks with a length of more than 10% of the maintenance criterion length generated in repaired nozzles was 2.3 times greater than that of non-repaired nozzles for average cracks, while the propagation of maximum cracks was 2.8 times at maximum.

(2) The extent of propagation of cracks of pattern 6 was the largest and they were the only ones that exceeded the maintenance criterion length. Therefore, repairing the cracks of pattern 6 on a priority basis is expected to simplify the repair work.

A new crack propagation prediction system for analyzing the stresses of first-stage nozzles will be constructed in the future.

## References

[1] Bernstein, H. L., McClung, R. C., Sharron, T. R., and Allen, J. M., 1994, ''Analysis of General Electric Model 7001 First-Stage Nozzle Cracking,'' ASME J. Eng. Gas Turbines Power, **116**, pp. 207–216.

[2] Hayasaka, Y., Isobe, N., Sakurai, S., and Kumata, K., 1999, ''Life Management System for Hot-Gas-Path Components of Gas Turbines,'' ASME Paper 99-GT-428.

[3] Yau, J., and Kuang, H., 2002, ''An Empirical Model for Predicting Crack Growth Behavior of Gas Turbine Stage 1 Nozzles,'' ASME Paper GT-2002-30302.

[4] Soechting, F. O., Kallianpur, V., Koff, S. G., Lee, J. H., and Tomita, Y., 2002, ''A Review of Damage Accumulation Rules Applied to Maintenance Scheduling of Advanced Industrial Gas Turbines,'' ASME Paper GT-2002-30296.

[5] Fujii, T., and Takahashi, T., 2001, ''Development of a Crack Growth Prediction System for First Stage Nozzle of Gas Turbine,'' ASME Paper 2001-GT-0470.

# Design of Industrial Axial Compressor Blade Sections for Optimal Range and Performance

**Frank Sieverding**
Sulzer Innotec,
Sulzer Markets and Technology,
CH-8401 Winterthur, Switzerland

**Beat Ribi**
MAN Turbomaschinen AG Schweiz,
Hardstrasse 319,
CH-8005 Zurich, Switzerland

**Michael Casey**
Institut für Thermische
Strömungsmaschinen (ITSM),
Universität Stuttgart,
D-70569 Stuttgart, Germany

**Michael Meyer**
MAN Turbomaschinen AG Schweiz,
Hardstrasse 319,
CH-8005 Zurich, Switzerland

*Background: The blade sections of industrial axial flow compressors require a wider range from surge to choke than typical gas turbine compressors in order to meet the high volume flow range requirements of the plant in which they operate. While in the past conventional blade profiles (NACA65 or C4 profiles) at moderate Mach number have mostly been used, recent well-documented experience in axial compressor design for gas turbines suggests that peak efficiency improvements and considerable enlargement of volume flow range can be achieved by the use of so-called prescribed velocity distribution (PVD) or controlled diffusion (CD) airfoils. Method of approach: The method combines a parametric geometry definition method, a powerful blade-to-blade flow solver and an optimization technique (breeder genetic algorithm) with an appropriate fitness function. Particular effort has been devoted to the design of the fitness function for this application which includes non-dimensional terms related to the required performance at design and off-design operating points. It has been found that essential aspects of the design (such as the required flow turning, or mechanical constraints) should not be part of the fitness function, but need to be treated as so-called "killer" criteria in the genetic algorithm. Finally, it has been found worthwhile to examine the effect of the weighting factors of the fitness function to identify how these affect the performance of the sections. Results: The system has been tested on the design of a repeating stage for the middle stages of an industrial axial compressor. The resulting profiles show an increased operating range compared to an earlier design using NACA65 profiles. Conclusions: A design system for the blade sections of industrial axial compressors has been developed. Three-dimensional CFD simulations and experimental measurements demonstrate the effectiveness of the new profiles with respect to the operating range.* [DOI: 10.1115/1.1737782]

## Introduction

The blade sections of industrial axial flow compressors require a wider range from surge to choke than typical gas turbine compressors in order to meet the high-volume flow-range requirements of the plant in which they operate. For motor-driven units it is often necessary to have a large number of variable stators to meet these requirements. In addition, the compressors are usually assembled from a limited set of standardized stages and casings to meet the particular customer specifications. These can vary substantially from machine to machine to cope with completely different requirements in terms of mass flow, pressure ratio and gas properties—and therefore of rotor size, number of stages, Mach numbers, and Reynolds numbers.

It is normal practice in such compressors to use so-called repeating stages, whereby several successive stages have the same blades for the rotors and stators but the span of the blade rows are shortened by cropping the tips. The requirements of axial matching determines the local meridional flow channel and defines the height of the blades, see Goede and Casey [1]. Normally there are different styles of repeating stage design for the front, middle, and end stages, whereby the following design criteria are used for these:

Front stages

- insensitive to high Mach number
- sensitive to variable IGV setting angles
- low hub/tip ratio

Middle stages

- high efficiency
- high work input per stage
- wide range without variables

End stages

- low flow coefficient giving high span
- low exit swirl

In general these requirements lead to designs of 50 to 60% reaction stages at the front, 70 to 80% in the middle and zero swirl (90% reaction) at the end. The stage in consideration in this paper is in the middle section of the compressor, where more or less sound repeating conditions are given.

This type of standardization of the design forbids several design features that are often encountered in axial compressors for gas turbines. Transonic blades are excluded, as the operating range would be too small and the axial matching of the sections would be too sensitive to cropping. The variation of blade height through cropping also impedes a refinement of the aerodynamics in the endwall region, although a treatment of the blade roots alone could be considered. The shift of the rotor and stator blade sections relative to each other through cropping (the rotor is shortened from the casing section and the stator from the hub section) also precludes any fine optimization of the design through the axial matching of the blade sections. To alleviate this problem, the middle stage considered here is designed with a constant exit flow angle from the stator across the span. Any improvement in performance is therefore primarily focused on the reduction of profile losses and improvement of the operating range of the section to allow it to cope with the severe aerodynamic maltreatment through cropping.

For this type of axial compressor, conventional blade profiles (NACA65 or C4 profiles) at moderate Mach number have mostly

Contributed by the International Gas Turbine Institute and presented at the International Gas Turbine and Aeroengine Congress and Exhibition, Atlanta, GA, June 16–19, 2003. Manuscript received by the IGTI December 2002; final revision March 2003. Paper No. 2003-GT-38036. Review Chair: H. R. Simmons.

  

been used as the availability of well-documented correlations allow the influence of changes in design parameters to be assessed with ease (Casey [2] and Casey and Hugentobler [3]). However, recent well-documented experience in axial compressor design for gas turbines suggests that peak efficiency improvements and considerable enlargement of volume flow range can be achieved by the use of so-called prescribed velocity distribution (PVD) or controlled diffusion (CD) airfoils. These types of bade sections are already widely used in compressors in jet engines and in stationary gas turbines and have also been applied in industrial compressors (Eisenberg [4]). Hobbs and Weingold [5] describe several features of the profiles whose advantages over conventional profiles have been proven. These features can be summarized as follows (see also Cumpsty [6]):

- a very rapid acceleration near the leading edge to avoid premature laminar boundary layer separation or transition,
- a deceleration region, beginning very steep, but relaxing so as to keep the boundary layer form parameter $H_k$ approximately constant, and
- for the pressure side a nearly constant subsonic Mach number distribution.

The most promising approach for the design of controlled diffusion style of airfoils has been documented in two recent ASME papers by DLR and Siemens (Köller et al. [7] and Küsters et al. [8]) and this paper documents the transfer and adaptation of this technology to industrial compressors.

## Description of Design System

The blade shapes of PVD or CD profiles are almost arbitrary and the number of degrees-of-freedom is high so an efficient design system without correlations is called for. A design system consisting of a parameterized geometry description, a fast two-dimensional flow solver and an optimization tool has proved to be an efficient way to evaluate the optimal set of parameters for given boundary conditions. Due to the two-dimensional optimization, three-dimensional effects such as secondary flow and tip leakage flow are neglected. This concession has to be made as the available three-dimensional Navier-Stokes codes are still too time-consuming to be coupled with optimization algorithms, although three-dimensional Euler codes which are adequate for water turbine designs can be incorporated, see Sallaberger et al. [9]. Instead, the three-dimensional geometry of the blade is defined by the radial stacking of three planar sections (hub, root-mean-square (rms), and casing), each of which is optimized separately using the procedure shown in **Fig. 1**.

The geometry of one section is defined by a set of parameters given by the genetic algorithm (i.e., breeder genetic algorithm (BGA)). Once the geometry has been generated by the geometry program (GEOM), preliminary checks are performed to ensure that vital mechanical aspects such as cross section area, moment of inertia or limitations concerning the curvature of the blade shape are not violated. If any of these checks is not passed successfully, the individual is marked as a ''bad'' individual and no further evaluation is done—it is effectively killed off without further consideration. Similarly, designs which do not achieve the required outlet flow angle—and therefore violate the specific work and flow turning required for the axial matching of the sections—are also eliminated by this ''killer'' criteria.

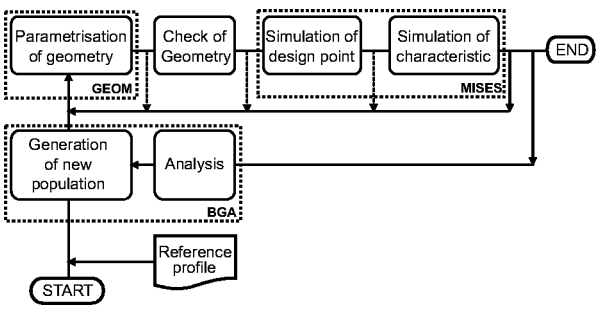


**Fig. 1 Design system**

Optimizing with respect to the whole characteristic (at design and off-design operating points) strongly increases the turnaround time for one optimization. The calculations of the characteristic are conducted up to an operating point that shows a doubled profile loss compared to the design point. To reduce the effort, the flow simulation is split into two steps, the simulation of the design point (i.e., evaluating of the exit flow angle at the design point) and—only if the exit flow angle is within the given limits—the simulation of the characteristic. Nevertheless, the elapsed time for a complete section is, in the worst case, about 14 days.

In this case, the development of a new blade sections is based on an already existing design (NACA65) which is to be improved. A reference profile, which closely represents the current design, is included in the optimization process in the start population to ensure that current knowhow and experience are taken into account. Although this might accelerate the process of optimization, it is important to note that it does not affect the result of the optimization itself. Test runs have led to the same result with and without including the reference profile.

## Parameterization of Blade Section Geometry

The challenge for the geometry program is to provide an accurate and flexible parameterization by using a low number of parameters so as the effort of optimizing is reduced. The implemented solution uses the concept of superposition of a camber line and a thickness distribution. This was necessary so that the new sections could be incorporated into the available design system which uses this technique, following Casey [10]. Both distributions are described by four patches, two central Bezier patches of order 4 and two linear patches for the leading and the trailing edge (see **Fig. 2**). In case of the thickness distribution the leading edge patch is replaced by an ellipse.

Altogether, the geometry model ends up with 20 parameters, 10 for the camber line and 10 for the thickness distribution for each blade section. Each parameter is directly or indirectly related to the chord length. By scaling with the chord length, the final design can therefore easily be obtained.

Some of the parameters are not object of the optimization, such as the chord length and the trailing edge radius (actually rTE/c), others are restricted or used as an initial value, such as the parameters p7 to p10, because they are not independent of each other. With the parameters p3 and p5 position and slope of the first point of patch 2 are defined. The position of the last point of patch 2 is

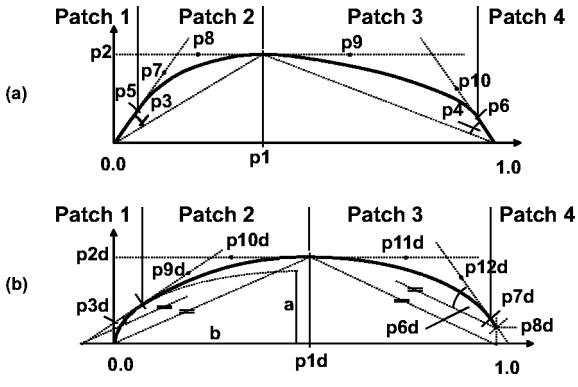


**Fig. 2 Parameterization of (*a*) camber line and (*b*) thickness distribution**

given by p1 and p2 and, as this is the point of maximal camber, the slope is also known. Parameters p7 and p8 finally specify the inner polygon points. In the same manner, the second Bezier patch (i.e., patch 3) is described. Arbitrary combinations of the parameters p1 to p10 will result in a discontinuity of the curvature at the transition of patch 2 to 3. Therefore p7 to p10 are varied in an internal loop until continuity of the curvature is achieved.

What has so far been described for the camber line, is also true for the thickness distribution, save that the first polygon point of patch 2 is defined as the location at which the ellipse with a minor to major axis ratio of 0.3 shows the same slope as p3d.

## Two-Dimensional Flow Solver

The quasi-three-dimensional blade-to-blade solver MISES V2.4.1 (Youngren and Drela [11]) has been chosen as the flow code for the optimization. This fast code describes the inviscid flow using the steady Euler equations, while the viscous effects are modeled by the integral boundary layer equations. The coupled system of nonlinear equations is solved by a Newton-Raphson technique.

The boundary conditions are defined by those of the existing NACA stage. Beginning at the design point the inlet angle is varied while keeping the inlet Mach number constant. For the stages in consideration the turbulence level is typically 5% and higher. According to Abu-Ghannam and Shaw [12], there is no further influence of turbulence on bypass transition for levels above 3%, so that the turbulence level is set to 5%.

For all calculations the radius of the section is taken as constant and the AVDR is set to unity, which means that both, stator and rotor sections, can be optimized with no rotation. Adjustments for noncylindrical flow channel and therefore nonconstant radius and AVDR$>$1 are made by modification of the desired exit flow angle.

## Breeder Genetic Algorithm

The breeder genetic algorithm (BGA), developed by Mühlenbein and Schlierkamp-Voosen [13,14], is based on the evolution theories of Darwin and the genetics of Mendel. A population of individuals changes over a number of generations using the mechanisms of selection, recombination and mutation, whereby the best individual is always transferred unchanged to the next generation (elitism).

According to the findings of former projects using this optimization tool (see Sallaberger [9] for details) the parameters for the optimization process were chosen to be 0.20 for the selection threshold, $[-0.20,1.20]$ for the recombination interval and $[-0.25,0.25]$ for the mutation interval. Starting with a population size of 500 individuals, each following generation consists of 50 individuals, which compromises the calculation time for one generation and the number of generations needed until the optimum is found.

It is worth noting here that the stringent convergence criteria applied in the optimization process (see below) indicate that a true optimum is found, and in this sense the results are independent of the actual optimization algorithm that is used. Other systems of optimization have been examined (including gradient methods and neural networks) but none were found to be consistently better than the breeder genetic algorithm.

## Fitness Function

Experience obtained from former projects has led to the following conclusions:

- Every term of the fitness function has to be associated to suitable reference values so that the contributions to the fitness value are all of the same order of magnitude.
- The distinction has to be made between goals which are essential and goals which are desirable. Only the latter should be included in the fitness function.

**Fig. 3 Influence of moment of inertia on resulting profiles (dashed line: original; solid line: cross section area and moment of inertial taken into account)**

Typically, the terms of the fitness function are of different types, like loss coefficients or angles. Without relating them to reference values, the numerical values of flow angles (in units of degrees) would outweigh any improvement in the loss coefficient (typically 0.03), as long as it is not compensated by a well-chosen weighting factor. With reference values each component in the fitness function has the same order of magnitude and the choice of appropriate weighting factors is much simplified. Suitable reference values can be obtained from experience or from existing profiles.

By definition, essential criteria have to be fulfilled without exception. If they were included in the fitness function, their corresponding weighting factors would have to be set at very high levels, and—as explained above—the criteria would become so dominant that required criteria would no longer be relevant. This type of criteria is called ''killer criteria'' and checked beforehand.

In the present case of an industrial axial compressor four killer criteria have been identified:

- the exit flow angle,
- the moment of inertia,
- the cross-section area, and
- the number of turning points on suction and pressure side.

The first of these is related to the achievement of the required specific work and appropriate axial matching of the sections, and, the second and third take into account the bending and centrifugal stresses, and the fourth is related to manufacturing requirements.

Strictly speaking, the cross-section area concerns only the rotor, but in order to develop a standardized method for rotor and stator it is checked for the stator as well. The effect of taking into account the cross section area and the moment of inertia is demonstrated in **Fig. 3**. Optimizing without these criteria leads to a profile with little camber, with the maximum thickness close to the leading edge and a very thin trailing edge. On the other hand, the resulting profile with respect to the stress criteria shows increased camber and a more regular thickness distribution. The previous shape might be superior in terms of loss coefficient and operating range, but is of no technical interest.

So far the exit flow angle has been described and classified as a killer criteria. This classification will now be examined in more detail. A design which meets the exact exit flow angle is only an

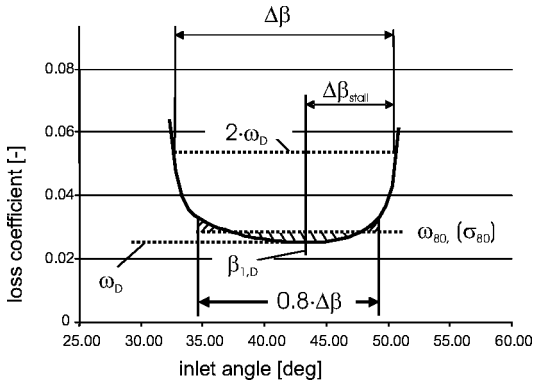


**Fig. 4 Parameter of the characteristic for the evaluation by the fitness function**

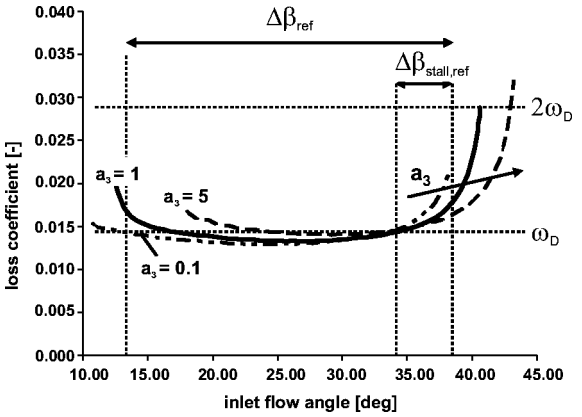


**Fig. 5 Influence of weighting factor $a_3$ on $\Delta\beta_{stall}$**

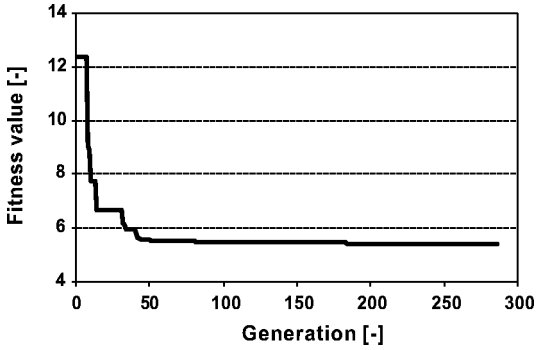


**Fig. 6 "Convergence" behavior of the optimization process of the stator casing section**

academic task, the designer will rather allow a defined tolerance, especially as the methods for prediction of exit angle are not perfect. Thus, we have to distinguish between two cases. If the exit flow angle is outside of the specified tolerance, it is interpreted as a killer criteria and therefore the affected individuals excluded. But, if the exit flow angle is within the tolerance, it is no longer a killer criteria. On the contrary, the exit flow angle is now an object of the optimization to meet the requirements as accurate as possible. For this reason, it is part of the fitness function, but the fitness value is only analyzed for those individuals whose exit flow angle is within the tolerance.

The components of the fitness function to describe position and shape of the characteristic have been chosen according to the proposal of Köller et al. [7] and are sketched in **Fig. 4**. For the design point $\beta_{1,D}$ the profile shows a design loss coefficient of $\omega_D$. When decreasing or increasing the inlet flow angle, the losses will eventually start to rise until a loss coefficient double that of the design point is reached. This range is defined as the operating range and the difference between the stall point and the design point is known as the safety against stall. For the inner 80% of the operating range the average value $\omega_{80}$ and the standard deviation $\sigma_{80}$ are used to assess the flatness and the homogenity of the loss characteristic.

Altogether, the fitness function consists of 6 components

$$F = a_1\left(\frac{\omega_D}{\omega_{D,\mathrm{ref}}}\right)^{e_1} + a_2\left(\frac{\Delta\beta_{\mathrm{ref}}}{\Delta\beta}\right)^{e_2} + a_3\left(\frac{\Delta\beta_{\mathrm{stall,ref}}}{\Delta\beta_{\mathrm{stall}}}\right)^{e_3} + a_4\left(\frac{\omega_{80}}{\omega_{80,\mathrm{ref}}}\right)^{e_4} + a_5\left(\frac{\sigma_{80}}{\sigma_{80,\mathrm{ref}}}\right)^{e_5} + a_6\left(1+\left|\frac{\beta_2-\beta_{2,\mathrm{ref}}}{\beta_{2,\mathrm{ref}}}\right|\right)^{e_6} \quad (1)$$

whereby ref refers to values of the reference profile used to make each term nondimensional. It is interesting to note that because the blade-to-blade code of MISES is able to predict the operating range and the loss coefficients, there are no elements of the fitness function which are related to the specification of optimum velocity distributions or boundary layer distributions.

Each component is associated with a weighting factor $a_i$ and an exponent $e_i$. The exponent factors $e_i$ have not been used and are all set to unity. It has been found expedient to examine the influence of each of the weighting factors $a_i$ separately. As an example, the influence of $a_3$ (responsible for the safety against stall) is shown in **Fig. 5**.

Increasing the weighting factor $a_3$ gives a higher margin against stall through an increased stagger angle and leads to less incidence for high inlet flow angles. Furthermore, the leading edge is thickened, so that the profile is less sensitive to incidence. Both measures improve the safety against stall. On the other side, due to the higher incidence for small inlet flow angles, the losses are increased and the operating range towards choke is substantially reduced.

It is interesting to note here that studies of the effect of the weighting factors $a_4$ and $a_5$ did not substantially affect the design of the sections, indicating that the fullness and the width of the characteristic close to low loss is probably similar for all axial compressor sections and is related to the global features of the flow rather than detail of the profile shape.

## Time Frame of Optimization Process

The optimization process is regarded as ''converged,'' if the best individual has not changed for more than 70 generations or the 400th generation is reached (see **Fig. 6**). There can, of course, be no proof that with more generations a better individual would not be found. To test the risk of this, several sections have been optimized starting from different reference profiles and, with the convergence criteria given above, no differences in the optimized profile could be identified even when starting from quite different starting profiles.

This optimization process for one section typically requires about two weeks on a single DEC ALPHA ES40 processor, whereby the characteristic is only calculated if all geometrical requirements are fulfilled and the exit flow angle is within the given limits for the design point.

The time frame strongly depends on the section that is to be optimized. Rotor sections generally take longer than stator sections. This is due to the boundary conditions (higher Mach numbers) which require longer convergence times in MISES (especially if shocks occur). The system has not been made parallel to improve its speed, but on a multiprocessor machine different blade sections can be optimized in different processors at the same time.

## Results of Optimization of Sections

The features of the optimized sections are in good agreement with the expected velocity profiles and boundary layer development expected for PVD and CD profiles (see introduction), even though no specific aspect of the fitness function is related to velocity distributions or boundary layer parameters. Clearly, the physics of the flow included in MISES is able to identify that the typical velocity boundary layer distributions automatically minimize the fitness function chosen, which examines only losses and operating range.

One example of the results for the casing section of the stator is given in **Figs. 7–11**. In these comparisons the reference data are the MISES calculation for the original NACA profile. In many cases the MISES simulation identifies problems that occur in this reference section that could probably have been avoided by using a different NACA65 profile with different camber and stagger. The original design was carried out without the MISES results using the procedure outlined by Casey and Hugentobler [3] so that the improvements given by the optimization process include some effects due to the poor selection of the original reference profile.

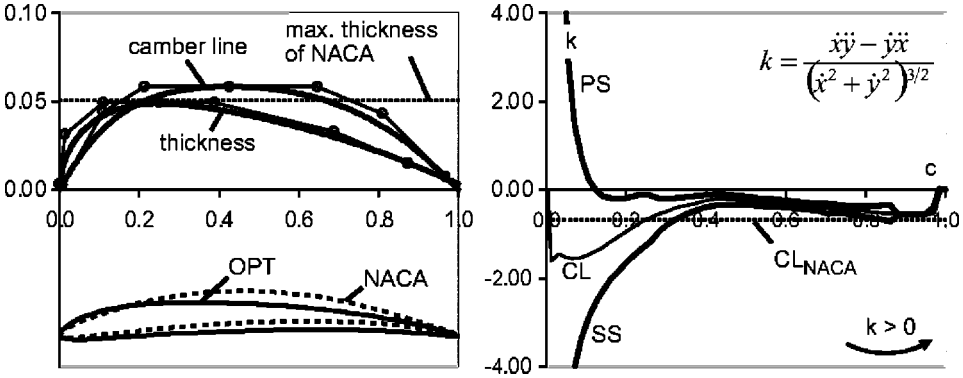


**Fig. 7 Stator casing section. Camber and thickness distribution showing polygon points (upper left), geometry without stagger (lower left), and curvature (right).**

**Geometric Features.** On the right side of **Fig. 7** the curvature of the optimized camber line (CL) is compared with that of the NACA profile whose camber is approximately a circular arc. The curvature in the front part of the optimized profile is increased, while it is less over the rear 75% of the section, leading to the typical shape of CD profiles with a relatively low curvature towards the rear of the blade. Additionally, the location of the maximum thickness, which is at 40% of the chord length for the NACA profile, has been moved forwards (**Fig. 7** upper left) and is now very close to its lower limit of 25% chord length, which has been set to avoid too blunt leading edges. Finally, the new blade has a lower stagger angle than that of the NACA blade.

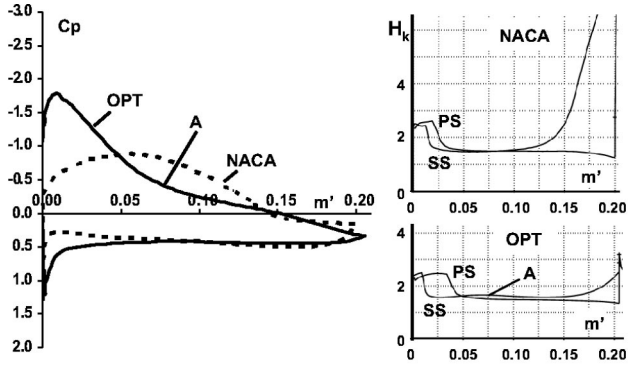


**Fig. 8 Pressure distribution and form factor *Hk* of stator casing section at design point**

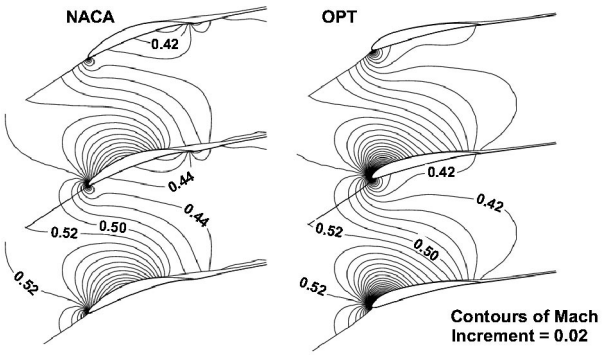


**Fig. 9 Mach number distribution of stator casing section at design point**

In this case all of the geometric ''killer'' criteria are fulfilled, i.e. the number of turning points (pressure side: 1; suction side: 0; **Fig. 7** right) and the cross section area and the moment of inertia (both approx. 3% above their lower limit).

**Flow Features in Design Point.** The positive effect of high camber and thickness close to the leading edge is demonstrated in **Fig. 8**. The flow at the suction side of the NACA profile is continuously accelerated up to a maximum at about 30% chord length (i.e. $m' = 0.05-0.06$ in **Fig. 8**) followed by a deceleration whose gradient becomes increasingly steeper towards the trailing edge. When the adverse pressure gradient is too strong for the flow to overcome, separation occurs (**Fig. 9**). Consequently, the deviation of the exit flow angle lies outside the desired tolerance and the overall pressure rise is lower.

For the optimized profile the flow on the suction side is highly accelerated and reaches its peak value shortly after the leading edge at about 5% chord length. The deceleration which follows starts with a strong gradient as in this region the boundary layer is still thin and uncritical. When the conditions start to become critical, the gradient is weakened in order to stabilize the boundary layer. This form of pressure distribution, often called ''ski-slope'' is typical for PVD and CD profiles.

The effect of stabilization can also be seen on the boundary layer form factor distribution Hk (**Fig. 8** right). After the transition, which occurs at the suction side right after the leading edge, the form factor starts to rise slowly. With the reduction of the deceleration gradient, the *Hk*-curve is flattened again and separation avoided, even though the stagger angle of the optimized profile is less than that of the NACA blade. The resulting exit flow angle is within a 0.2-deg tolerance of the desired value.

While the flow at the pressure side of the NACA blade is decelerated, the optimized profile shows an almost constant pressure distribution with a slight acceleration in the front part of the blade, which delays the transition at the pressure side and reduces the losses.

**Flow Features at Off-Design.** With increasing flow angle, the velocity on the suction side close to the leading edge rises as well and, in the case of the optimized profile, becomes transonic (**Fig. 10**). The higher velocity of the new profile is due to the lower stagger angle and the thickened leading edge, but, as a thicker leading edge results in less sensitivity to incidence, the velocity peak is not as distinct as for the NACA profile. The effects of the optimized pressure distribution, which have already been described for the design point (ski slope), are even more emphasized, the pressure gradient at the rear part of the blade is very small. Still, separation cannot be completely averted, but compared to the NACA blade the separation is much smaller and results in lower losses.

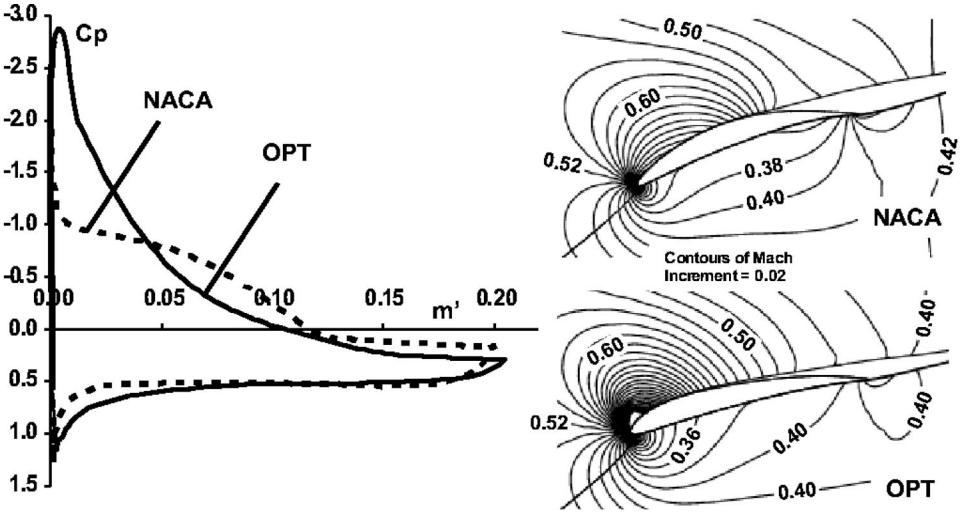


**Fig. 10 Pressure and Mach number distribution of stator casing section at high inlet flow angle**

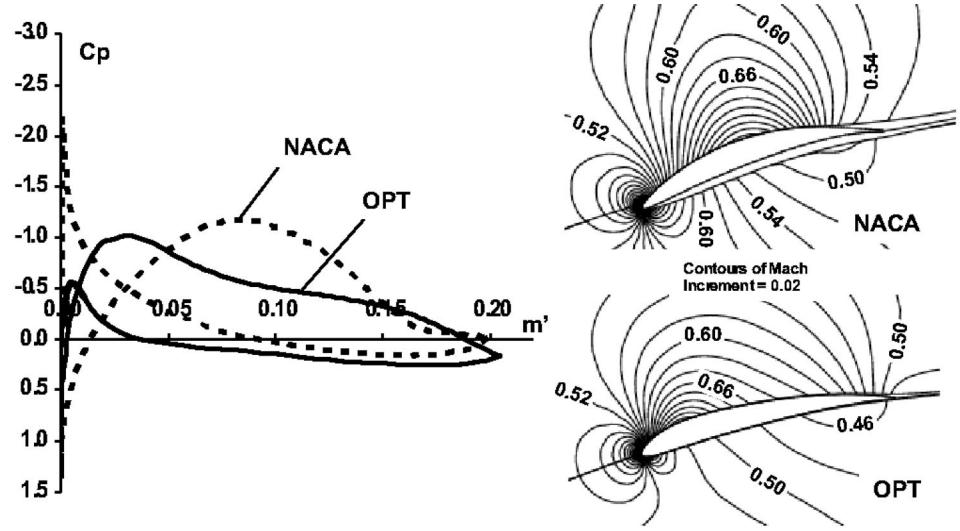


**Fig. 11 Pressure and Mach number distribution of stator casing section at small inlet flow angle**

The lower stagger angle of the new profile, which has been a disadvantage at high inlet flow angles, becomes advantageous for small inlet flow angles (**Fig. 11**). Due to the higher stagger angle and the thin leading edge the flow at the pressure side of the NACA blade separates immediately after the leading edge and sets therefore the lower limit of the operating range. At this point, the new blade is still working perfectly. Thanks to the smaller stagger angle and the thicker leading edge, the predicted operating range is increased by more than 50%.

**Loss Coefficients.** Similar results were obtained for the remaining stator and rotor sections. The loss coefficients of all sections, each compared to the corresponding NACA65 profile, are given in **Fig. 12**. For all sections the losses have been reduced significantly and the operating range increased. For the rotor hub section, it is clear that the original choice of the NACA65 profile was not at all good. The loss curve of the optimized profile is now in the desired range, while a shift to higher inlet flow angles can be found at the casing section of the rotor.

## Blade Stacking

To build up the three-dimensional geometry, the centers of gravity are typically used as the stacking line for NACA65 profiles. This is possible, since all sections are members of the same profile family and their shape, and therefore the location of the center of gravity, is similar. The optimized profiles tend to have a different location of the center of gravity relative to the chord length for different sections over the span and so they are stacked over the mean value for all sections instead.

Originally, optimizations were performed for seven sections across the span of each blade. This required a lot of computing time, and the resulting shape of the blade turned out to be slightly irregular across the span. The question arose, how many sections for a proper definition of the blade were needed. To answer the question, both the rotor and the stator blades have been built up by using only the hub, midspan, and casing sections. At the span values corresponding to the four nonused sections the resulting profiles have been generated by interpolation and their loss coef-

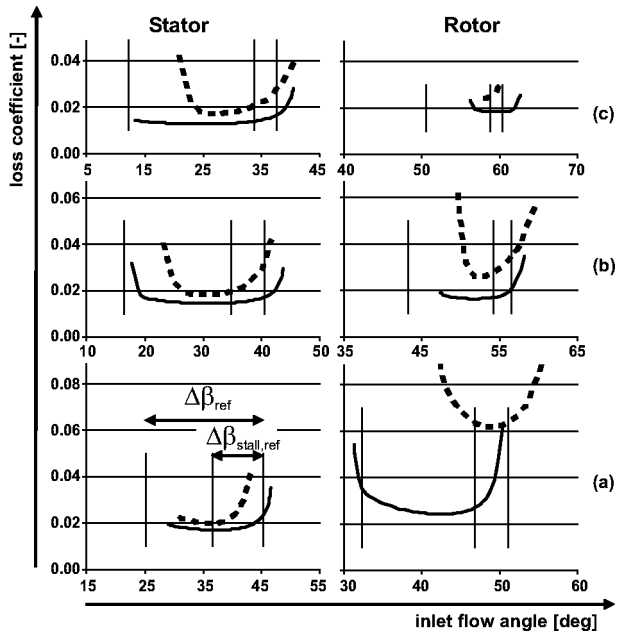


**Fig. 12 Loss coefficient for (*a*) hub, (*b*) midspan, and (*c*) casing section of stator and rotor for existing (dotted) and optimized profile**

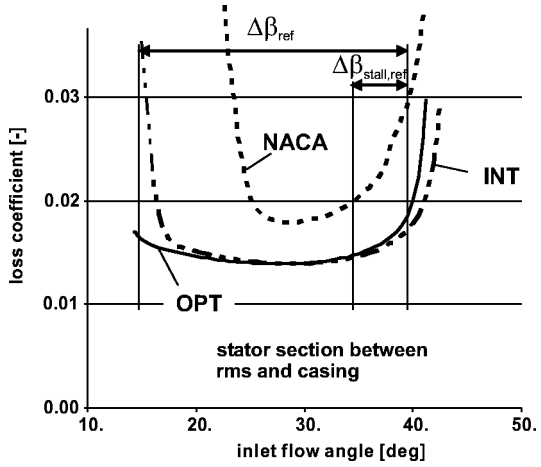


**Fig. 13 Influence of number of sections used for the blade (OPT: optimized profile; INT: profile generated by interpolation)**

ficients compared to those of the optimized profiles. As can be seen by the example of the stator (**Fig. 13**), the difference is only small which means that three sections per blade are sufficient for the definition of the blade.

## Comparison With Three-Dimensional Navier-Stokes Simulation

In order to test the performance of the newly developed profiles, calculations were carried out using the commercial CFD package Fine/Turbo from Numeca. The geometrical model takes into account all 4 $\frac{1}{2}$ stages of the axial compressor test rig at Sulzer Innotec as well as the inlet and exit part of the machine and the tip clearances.

The mathematical model employs a steady, three-dimensional viscous turbulent Navier-Stokes solver with the Baldwin-Lomax turbulence model incorporated. Furthermore, a central discretization scheme and first order extrapolation on rotor-stator interfaces are used. The mesh consists of $\sim$2 million nodes with four possible multigrid levels. This results in average $y+$ values of $\sim$3,

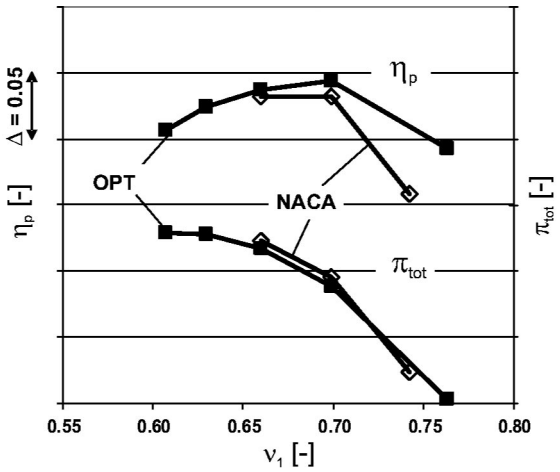


**Fig. 14 Three-dimensional Navier Stokes simulations. Overall polytropic efficiency $\eta_p$ and total pressure rise $\pi_{tot}$ for the existing (filled squares) and the new design (diamonds).**

which is required for the Baldwin-Lomax model. The calculations were performed for a machine Mach number of Mu=0.5 with total pressure and temperature inlet and a massflow outlet boundary condition, respectively. The calculations were considered to be converged if the difference between inlet and outlet massflow is less than 1‰, which took an average calculation time per operating point of 27 hours on an SGI octane.

The guide vane stagger angle of the existing NACA stage was chosen to be 60 deg, since this value was found by the measurements to give the highest efficiencies. For the new stage, the optimal guide vane stagger angle is not known in advance. Therefore, as an initial guess it was assumed that the difference between its design and optimum stagger angle is the same as for the NACA stage, which leads to a value of 65 deg. This assumption has to be checked by the measurements.

The overall polytropic efficiency and the total pressure rise (calculated for the 4 $\frac{1}{2}$ stages) of the existing and the new stage are presented in **Fig. 14**. The peak efficiency of the new stage is higher with a flattened characteristic and as a result an increased operating range.

## Comparison With Measurements

Experimental validation of the optimised blading has been carried out in the large high-speed 4 1/2 stage axial compressor ''Palue'' in Sulzer Innotec, which has a hub diameter of 400 mm. This compressor was also used for the measurements of the original NACA 65 blading and for these new tests the annulus geometry, and all instrumentation remained unchanged, the compressor was simply fitted with a new set of blades. The instrumentation included measurement of the volume flow in a calibrated nozzle, inlet and outlet conditions (static pressures and total temperatures) upstream and downstream of the blading, and static pressures between each blade row.

Tests in this compressor follow a standard, and well-established procedure whose objective is to derive measured stage characteristics for repeating stage conditions at different stator vane stagger angle settings. In these measurements the inlet guide vane and stator vane setting angles of all blade rows are adjusted to provide a geometry that repeats through the compressor. The annulus is designed following Goede and Casey [1], and under these conditions there is one speed of the compressor which leads to repeating stage conditions through the machine at the best operating point. The establishment of repeating stage conditions can be confirmed from the static pressure measurements on the casing. At the given speed, the repeating stage conditions are then more or less retained as stall is approached, but deviate from this as choke is approached with the last stages operating at a lower relative pres-

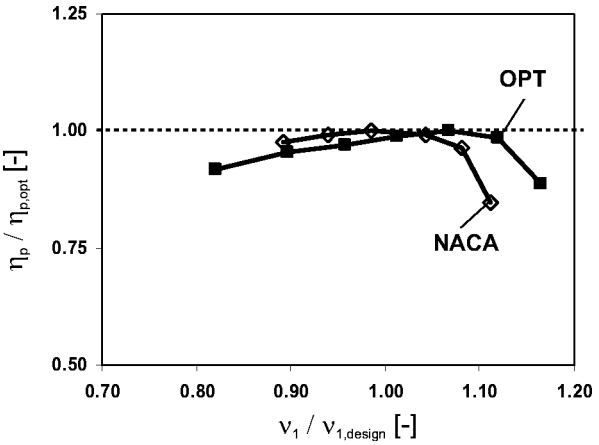


**Fig. 15 Measured polytropic efficiency $\eta_p/\eta_{p,\mathrm{opt}}$ of the existing (diamonds) and the new stage (filled squares)**

sure rise. Note that at higher stagger angles a lower speed is needed to attain repeating stage conditions as the stage produces a higher work input.

The measurements on this stage were completed in December 2002, during the submission process for this paper. The results, which are summarized in **Figs. 15** and **16**, are highly satisfactory with regard to the operating range of the stage, but unfortunately the optimized blading did not achieve a better efficiency than the NACA 65 blading. In the short time available since the completion of the tests it has not been possible to find an explanation for the poor efficiency of the optimised stage. Work is continuing on this.

**Figure 15** shows a nondimensionalized plot of the efficiency characteristic at the design stagger angle of the optimised and the NACA 65 blading. It can be seen that the operating range of the optimised stage is significantly wider (with more than 30% more variability in flow) than that of the NACA 65 blading. **Figure 16** demonstrates that the optimized stage achieves a similar wider operating range than the NACA 65 blading at all stagger angles and speeds that have been tested. In this figure the operating range is denoted by the flow range defined as the difference between the flow coefficient at the point where the stage has 90% of its peak efficiency ($\nu_{1,90}$) and the flow coefficient at stall ($\nu_{1,\mathrm{stab}}$) divided by the design flow coefficient ($\nu_{1,\mathrm{design}}$).

$$\Delta\nu' = \frac{\nu_{1,90} - \nu_{1,\mathrm{stab}}}{\nu_{1,\mathrm{design}}} \tag{2}$$

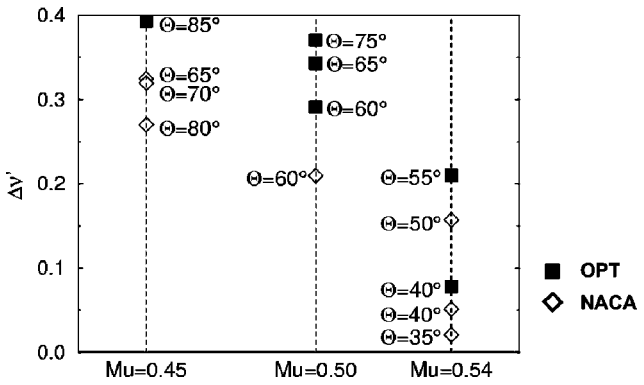


**Fig. 16 Relative increase of operating range for original (NACA) and optimized (OPT) design at blade Mach number Mu=0.45, 0.50, and 0.54 and different stagger angles Θ**

## Conclusions

A design system for the blade sections of industrial axial compressors has been developed. The method combines a parametric geometry definition method, a powerful blade-to-blade flow solver (MISES) and an optimization technique (breeder genetic algorithm) with an appropriate fitness function. Particular effort has been devoted to the design of the fitness function for this application:

- All terms in the fitness function are nondimensional with respect to reference values.
- Essential aspects of the design (such as the required flow turning, or mechanical constraints) should not be part of the fitness function, but need to be treated as so-called ''killer'' criteria in the genetic algorithm.
- It has been found worthwhile to examine the effect of the weighting factors of the fitness function to identify how these affect the performance of the sections.
- The fitness function only includes terms related to the required performance at design and off-design operating points. Nevertheless the optimized sections have the typical velocity and boundary layer distributions associated with CD and PVD profiles.

The system has been tested on the design of a repeating stage for the middle stages of an industrial axial compressor. The resulting profiles show an increased operating range compared to an earlier design using NACA65 profiles. Three-dimensional CFD simulations and experimental measurements demonstrate the effectiveness of the new profiles with respect to the operating range.

## Acknowledgments

The authors wish to thank Dr. Ernesto Casartelli for the geometry program, Rudi ter Harkel and Paul Stadler for FINE calculations, Christian Güdel for measurements, Dr. Bernhard Eisenberg for his advices.

## Nomenclature

AVDR = axial velocity density ratio $=\rho_2 C_{x2}/\rho_1 C_{x1}$
$CL$ = camber line
$Cp$ = static pressure rise coefficient $=(p-p_1)/q$
$C_x$ = axial velocity [m/s]
$Hk$ = form factor $=\delta^*/\theta$
INT = interpolated profile
OPT = optimized profile
PS = pressure side
SS = suction side
$U_h$ = blade speed at hub (m/s)
$a_i$ = weighting factor of fitness function
$e_i$ = weighting exponent of fitness function
$k$ = curvature
$m'$ = meridional coordinate $=\int[\sqrt{(dr^2+dz^2)}/r]$
$p$ = pressure ($N/m^2$)
p1–p10 = parameter of camber line
p1d–p10d = parameter of thickness distribution
$q$ = dynamic pressure at inlet ($N/m^2$)
$r$ = radius (m)
$rTE$ = trailing edge radius (m)
$t$ = temperature (K)
$x$ = coordinate in chordwise direction (m)
$y$ = coordinate perpendicular to chordwise direction (m)
$z$ = coordinate in axial direction (m)
$\beta$ = flow angle with respect to axial direction (deg)
$\gamma$ = ratio of specific heat capacities
$\Delta\beta$ = operating range (deg)

$\Delta\beta_{stall}$ = safety against stall (deg)
$\Delta\nu'$ = dimensionless operating range$=(\nu_{1,90}-\nu_{1,stab})/\nu_{1,design}$
$\delta^*$ = boundary layer displacement thickness (m)
$\eta_p$ = polytropic efficiency (total-total)$=\gamma-1/\gamma\ \ln(p_{02}/p_{01})/\ln(t_{02}/t_{01})$
$\Theta$ = stagger angle with respect to circumferential direction (deg)
$\theta$ = boundary layer momentum thickness (m)
$\nu$ = flow coefficient$=C_x/U_h$
$\rho$ = density (kg/m$^3$)
$\pi_{tot}$ = stage pressure ratio$=p_{02}/p_{01}$
$\sigma$ = standard deviation
$\omega$ = loss coefficient$=(p_{02,is}-p_{02})/(p_{01}-p_1)$

**Subscripts**

0 = stagnation value
1 = inlet plane
2 = outlet plane
80 = inner 80% of $\Delta\beta$
90 = 90% of peak efficiency
$D$ = design point
$is$ = isentropic
ref = reference value
stab = at stall

**Superscripts**

$'$ = 1st deviation
$''$ = 2nd deviation

## References


[1] Goede, E., and Casey, M. V., 1988, "Stage Matching in Multistage Industrial Axial Compressors With Variable Stagger Stator Vanes," VDI-Ber., **706**, pp. 229–243.
[2] Casey, M. V., 1987, "A Mean Line Prediction Method for Estimating the Performance Characteristic of an Axial Compressor Stage," *Turbomachinery—Efficiency Prediction and Improvement*, Robinson College, Cambridge, UK, ImechE, London, Paper C264/87.
[3] Casey, M. V., and Hugentobler, O., 1988, "The Prediction of the Performance of an Axial Compressor Stage With Variable Stagger Stator Vanes," VDI-Ber., **706**, pp. 213–227.
[4] Eisenberg, B., 1994, "Development of a New Front Stage for an Industrial Axial Flow Compressor," ASME J. Turbomach., **116**, pp. 596–604.
[5] Hobbs, D., and Weingold, H., 1984, "Development of Controlled Diffusion Airfoil for Multistage Compressor Application," ASME J. Eng. Gas Turbines Power, **106**, pp. 271–278.
[6] Cumpsty, N. A., 1989, *Compressor Aerodynamics*, Longman, London.
[7] Köller, U., Möning, R., Küsters, B., and Schreiber, H.-A., 1999, "Development of Advanced Compressor Airfoils for Heavy-Duty Gas Turbines, Part I: Design and Optimization," ASME Paper No. 99-GT-95.
[8] Küsters, B., Schreiber, H.-A., Köller, U., and Möning, R., 1999, "Development of Advanced Compressor Airfoils for Heavy-Duty Gas Turbines, Part II: Experimental and Theoretical Analysis," ASME Paper No. 99-GT-96.
[9] Sallaberger, M., Fisler, M., Michaud, M., Eisele, K., and Casey, M. V., 2000, "The Design of Francis Turbine Runners by 3-D Euler Simulations Coupled to a Breeder Genetic Algorithm," 20th IAHR Symposium on Hydraulic Machinery and Systems, Charlotte, NC, Aug.
[10] Casey, M. V., April 1983, "A Computational Geometry for the Blades and Internal Flow Channels of Centrifugal Compressors," ASME J. Eng. Gas Turbines Power, **105**, pp. 288–295.
[11] Youngren, H., and Drela, M., 1991, "Viscous/Inviscid Method for Preliminary Design of Transsonic Cascades," Paper No. AIAA-91-2364.
[12] Abu-Ghannam, B., and Shaw, R., 1980, "Natural Transition of Boundary Layers. The Effects of Turbulence, Pressure Gradient and Flow History," J. Mech. Eng. Sci., **22**, pp. 213–228.
[13] Mühlenbein, H., and Schlierkamp-Voosen, D., 1993, "Predictive Models for the Breeder Genetic Algorithm I. Continuous Parameter Optimisation," Evol. Comput., **1**, pp. 25–49.
[14] Mühlenbein, H., and Schlierkamp-Voosen, D., 1994, "The Science of Breeding and Its Application to the Breeder Genetic Algorithm," Evol. Comput., **1**, pp. 335–360.